To the Graduate Council:

I am submitting herewith a dissertation written by Cheng-chien Liu entitled "On-line Experimental Study And Theoretical Modelling Of Tubular Film Blowing." I have examined the final copy of this dissertation for form and content and recommend that it be accepted in partial fulfillment of the requirements for the degree of Doctor of Philosophy, with a major in Polymer Engineering.

Joseph E. Spruiell, Major Professor

We have read this dissertation
and recommend its acceptance:

Accepted for the Council:

Associate Vice Chancellor
and Dean of The Graduate School

ON-LINE EXPERIMENTAL STUDY AND THEORETICAL MODELLING OF TUBULAR FILM BLOWING

A Dissertation

Presented for the

Doctor of Philosophy

Degree

The University of Tennessee, Knoxville

Cheng-chien Liu

August 1994

Copyright 1994 by Cheng-chien Liu

All rights reserved

Dedicated to my parents

Mr. Liang-sheng Liu
(劉 亮 生)
and
Mrs. Pi-yun Tsai
(蔡 碧 雲)

who make my education possible

and also to my wife

Shao-fang Kuang

for her support

ACKNOWLEDGMENTS

The author wish to express his sincere gratitude to his advisors, Professor Joseph E. Spruiell and Professor Donald C. Bogue for their guidance, support and patience during the course of this work. Appreciation is extended to Professor Edward S. Clark and Professor Marion G. Hansen, who served on his committee.

The author thanks the Center for Materials Processing and the Department of Materials Science and Engineering at the University of Tennessee for stipend support. Also the author would like to express his sincere thanks to Professor Gary Harrison of College of Charleston for invaluable help and discussion in this work.

The author thanks the Dow Chemical Company and Dr. R. M. Patel of the Dow Chemical Company for the supply of experimental materials and information. Finally, thanks are offered to the staffs of the electronics and machine shops for providing technical help.

ABSTRACT

The literature on tubular film blowing is contradictory, even on such basic matters as to whether increasing inflation pressure increases or decreases the bubble radius. To provide a solid experimental base for physical understanding and theoretical modelling, detailed on-line measurements of the tubular film blowing process were made using three polyethylenes (a low density, a linear low density and a high density material, all of melt index 1.0). The measurements included blow-up ratio as a function of inflation pressure and take-up ratio; the extrusion temperature and the air flow rate were also varied. On-line distributions of radius, thickness, velocity and temperature along the machine direction were made in some runs. For the most part these data showed an "intuitive" effect of inflation pressure on blow-up ratio; that is, increasing the pressure caused the final radius (the blow-up ratio) to increase. However, at high blow-up ratios (typically values of 3 ~ 4, depending on the material and processing conditions), regimes having a "counter-intuitive" relationship were observed in some cases. There were not substantial differences among the three materials except that

the low density material was less prone to instabilities at high blow-up ratios. The detailed on-line data indicates that at a fixed take-up ratio all the deformation rates in the three principal directions increase with an increase in blow-up ratio. This phenomenon is used as a means of explaining the deformation-thinning associated with "counter-intuitive" pressure effect.

The validity of the two existing theoretical models (the earlier model of Pearson and Petrie and the newly proposed model in the author's M.S. thesis) are examined by making qualitative comparisons with experimental data. It is found that prediction of the new model agrees with the basic trend of data but that of Pearson-Petrie does not.

Furthermore, the newly proposed theoretical model based on treating the bubble as "quasi-cylindrical" at each point (neglecting curvature in the axial direction) and incorporating a deformation-thinning viscosity equation (which is motivated by experimental results) explained all of the essential features of the data. The viscosity function required to fit the blown film data were in plausible agreement with viscosity data (complex viscosity data) measured independently. The predicted passage from an "intuitive" regime to a "counter-intuitive" regime,

qualitatively in agreement with the data, comes about from the thinning behavior of the viscosity model.

Comparisons with the earlier model of Pearson and Petrie were also made. This model, based on thin-shell theory, disagrees with the data in several essential ways when the analysis is done as a problem in fluid mechanics: it predicts "counter-intuitive" results as regards the effect of inflation pressure and melt viscosity on bubble radius. These unusual effects come about from an axial curvature term in the thin-shell formulation. In a free-boundary fluid mechanics analysis, the theory *predicts* the shape of the bubble. If, however, one does the analysis as one would in solid mechanics — in which the shape of the bubble is known *a priori* — there are not substantial differences between the predictions of the Pearson-Petrie model and that of the present paper. The reasons for this difference are not clearly understood.

TABLE OF CONTENTS

CHAPTER PAGE

CHAPTER PAGE

LIST OF TABLES

LIST OF FIGURES

CHAPTER 1

INTRODUCTION

The tubular film blowing process is becoming more and more important in the polymer processing industry for producing thin thermoplastic films. The existing blown film lines number about 2,300 in North America, and over 80 new processing lines are built every year [1]; that is, there is a 3.5% annual increase of the present blown film market. The reason blown film extrusion represents such a developing potential is that tubular film has better physical properties than that of a film produced by the other techniques of fabrication, such as casting of film. The better performance of blown film is mainly due to its biaxially oriented molecular structure which gives more balanced mechanical properties to the film. For example, for the same kind of material, the thickness of a cast film, without being re-oriented, is required to be twice that of a blown film to achieve the same performance [2]. Thus, in order to obtain a detailed and a better understanding of the tubular film

blowing process, experimental on-line study and theoretical analysis are needed.

In the past 24 years a mathematical description, which was first given by Pearson and Petrie [3,4] and then developed by other investigators [5,6], has been widely used in the analysis of the blown film process. In the same period, various experimental studies and on-line measuring techniques have been reported [7-24]. However, due to the complexity of the experimental data collection and the mathematical simulation for the blown film process, few investigations could provide a complete picture of the theoretical as well as the experimental aspects of this process. Thus, some key relationships between processing conditions and tubular films are still not well established by either the mathematical simulation or the experimental study. For example, the influence of the inflation pressure on the final bubble radius is not clear. Experimental observations on this point are mixed. Kanai et al. [14] and Kwack et al. [25] note an inverse effect in their data; that is, the higher inflation pressure produces the smaller bubble. Wagner [26,27] and Liu [28] find the "intuitive" effect for most of their data; that is, increasing pressure shows an increase in radius, except a nearly constant pressure seems to be required at blow-up ratios (defined as the ratio of final to initial radius of

bubble) greater than about two; whereas Han and Park [11] find both situations (radius increasing and decreasing with pressure), depending on the material and processing conditions. On the other hand, the original mathematical model, originally set down by Pearson and Petrie [3,4], always predicts an inverse effect of pressure on the final radius of the bubble [4-6,29,30].

Based on the statements in the above paragraph, one can find that not only the results of mathematical analysis disagree with the experimental observation, but also the basic qualitative trends of data measured by different investigators are mixed. These difficulties were discussed in the present author's M.S. thesis [28]. It should be emphasized that there is still no satisfactory explanation given, so far, either for the mixed experimental results, or for the discrepancy between the experimental observation and the theoretical analysis. In summary, lack of systematic on-line data that provides a solid basis for comparison of the results of mathematical modelling caused the entire physical picture to be ambiguous.

Systematic comparisons between on-line studies and mathematical simulations were carried out by the present author in earlier work. Since obvious discrepancies between the experimental observations and (Pearson-Petrie) model predictions were found, a new mathematical model based on a

new physical approach was proposed, in the present author's M.S. thesis [28]. According to the preliminary results then, the new model looked promising.

Therefore, the first objective of the present research was to obtain extensive experimental data for three types of polyethylenes (high density, low density and linear low density polyethylene) under a wide range of film blowing conditions. The processing parameters to be varied were the blow-up ratio, the take-ratio, the extrusion temperature and the flow rate of cooling air; and the variables to be measured were the inflation pressure, the on-line profiles of radius, thickness, velocity, temperature and the principal deformation rates. These data should provide us a clear physical picture as well as a better understanding of the tubular film blowing process.

The second objective was to establish a valid mathematical model which is able to correctly describe the blown film process. To achieve this objective, two existing mathematical analyses (that is, the model of Pearson and Petrie [3,4] and the model of the present author [28]) were examined via qualitative comparisons to experimental observations. Since the predictions of the present model agree with the basic trends of the experimental data, quantitatively checking the present model was carried out; and

the results show that there is a good agreement between the predictions and data. Thus, a further exploration of the film blowing process by means of the present model was carried out. This exercise not only shows that the present model incorporated with a deformation-thinning viscosity equation is able to describe all of the essential features of the data, but also provides a satisfactory explanation for the mixed experimental observations in the literature. Finally, a physical explanation of the difference between these two theoretical analyses and resolving the difficulties of the Pearson-Petrie model were attempted. The scheme of this research is illustrated by the flow chart, as shown in Figure 1-1.

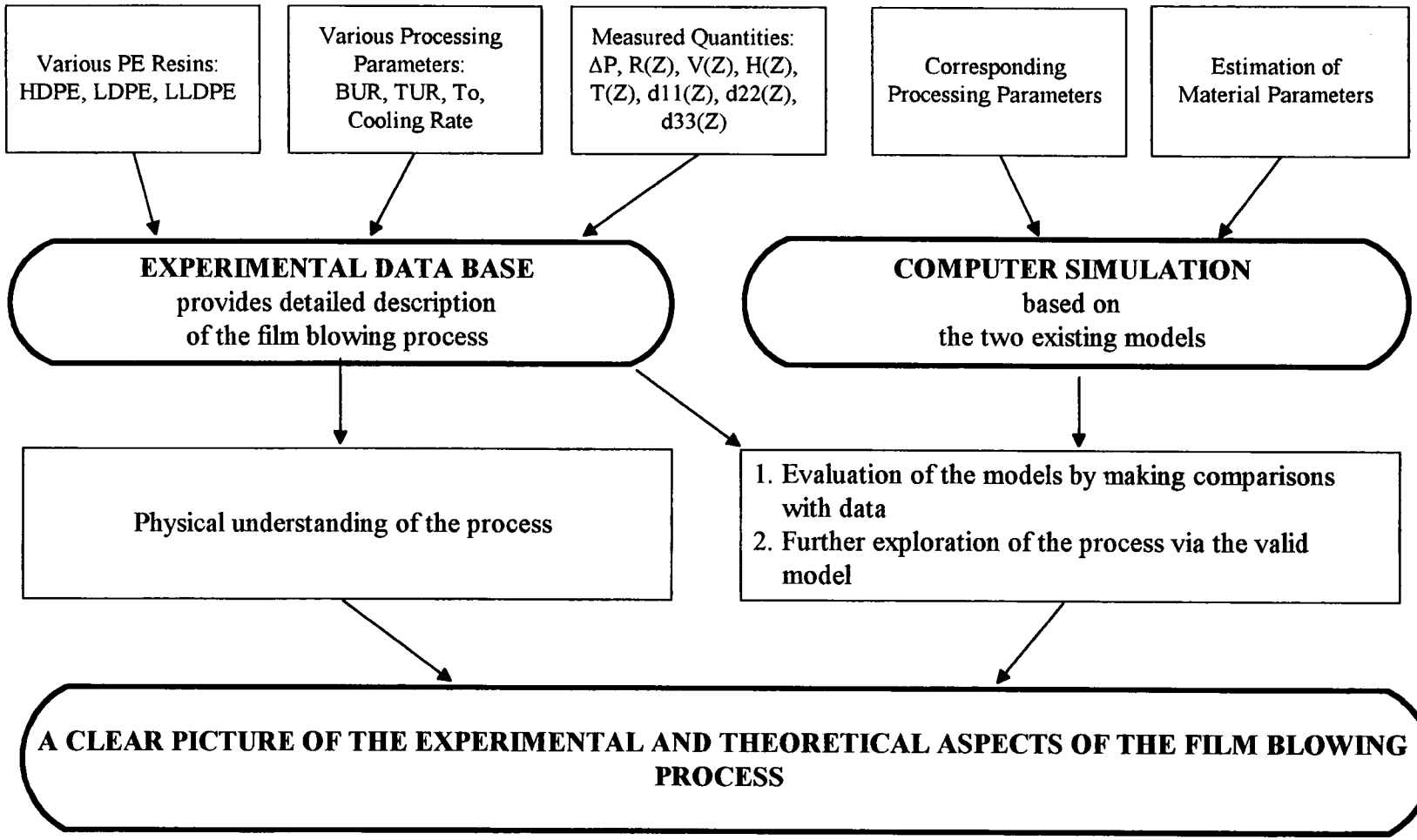

Figure 1-1 The outline diagram for the scheme of the present research.

CHAPTER 2

BACKGROUND

2.1 TUBULAR FILM BLOWING PROCESS

The tubular film blowing process is one of the most important polymer processes and is quite complex because the material is subjected to a complicated stress field. A sketch of the blown film process is shown as Figure 2-1. The polymer melt is extruded by an extruder through an annular slit die. The molten polymer exits from the die and is formed into a tubular shape just above the die exit. This tubular melt is drawn upward by a take-up device. At the same time, air from the center of the die is introduced into this melt tube in order to inflate it to form a bubble of thin film. The air being blown into the bubble is adjustable to control the inside pressure, i.e., the pressure difference across the film.

An air cooling ring is installed around the bubble to cool and solidify the tubular film. Thus, the height of the frost line (i.e., the position where the melt becomes solidified) can be controlled by adjusting the velocity of

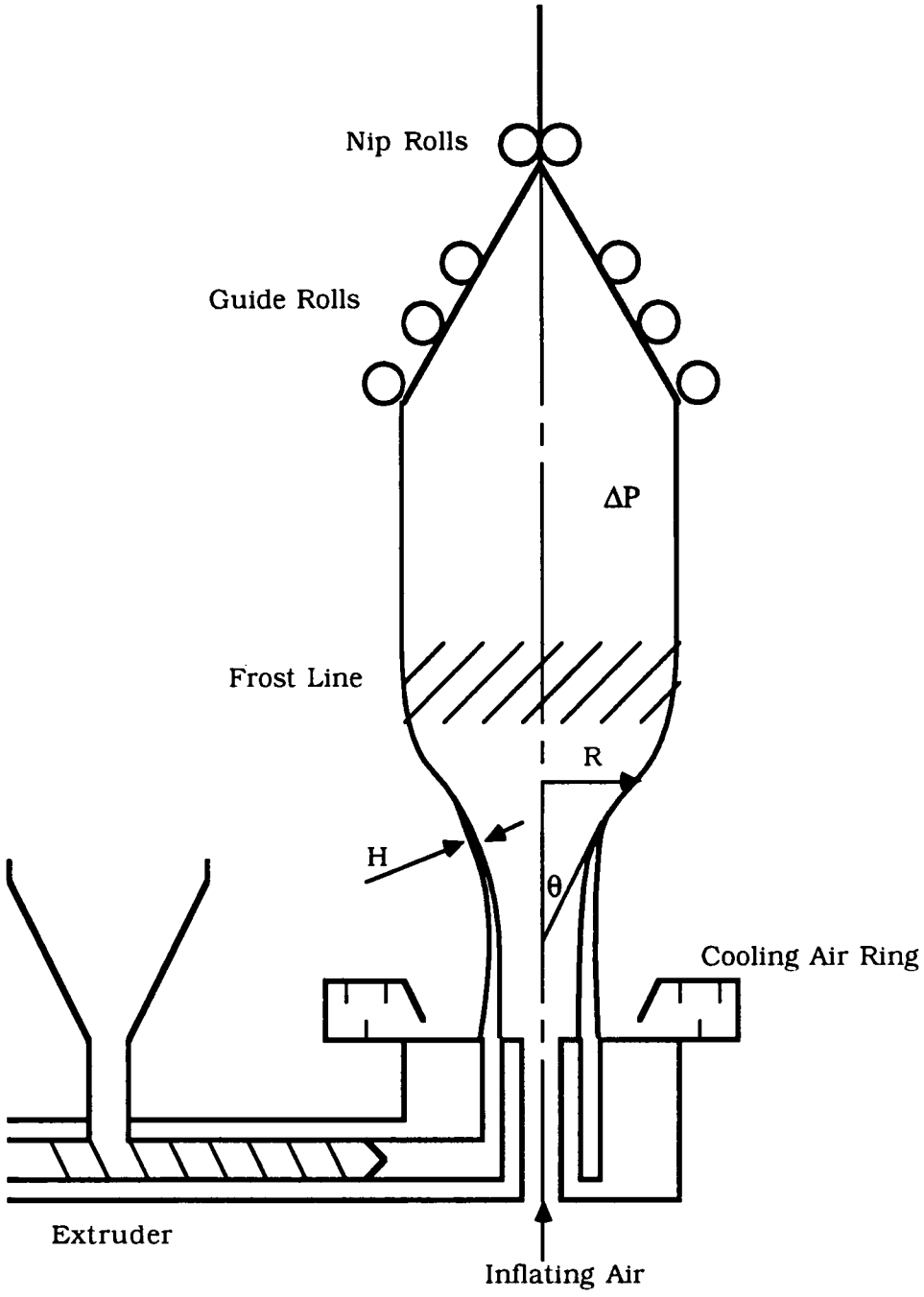

Figure 2-1 Blown film extrusion process.

cooling air which blows both perpendicular and parallel to the machine direction. Another function of the cooling air ring is to help stabilize the tubular film shape. The inflated tubular film is guided to pass through nip rolls by a series of guide rolls. The nip rolls are controlled by a motor which provides variable speeds to produce different draw-down ratios.

2.2 ON-LINE MEASUREMENT TECHNIQUES

In order to obtain a better understanding of the blown film process, on-line measurements are essential. Various on-line experimental observation and measuring techniques for radius, velocity, thickness and temperature were reported separately [7-17]. Probably due to the high complexity of the blown film extrusion itself and on-line data collection, few investigations provided a complete set of on-line measured results. The following sections will review the measuring techniques reported in the literature.

2.2.1 Radius

Measurement of the radius by contacting with a caliper or similar device is not very accurate or practical. This inaccuracy is mainly due to the fact that the film bubble is in a dynamic condition, rather than a static one. Since the film is in motion, the friction between the ruler and the bubble will cause this measurement to become ineffectual.

The main techniques suggested by the literature are either to photograph the bubble [5] or to record it with a video camera [8,28,31], as illustrated in Figure 2-2. Besides recording the shape of bubble, it is necessary to photograph a piece of paper with a grid, which is placed at the same position as the bubble, to obtain the so-called "average image expansion factor" [31]. This factor is the ratio of the values of an actual scale to the corresponding values on the recorded image. Thus, the actual radius of the bubble can be obtained by multiplying the measured value on the recorded image with the average image expansion factor. The accuracy of this technique was examined by measuring several static tubular films with various known diameters; and an average error of 1.74% was reported [28].

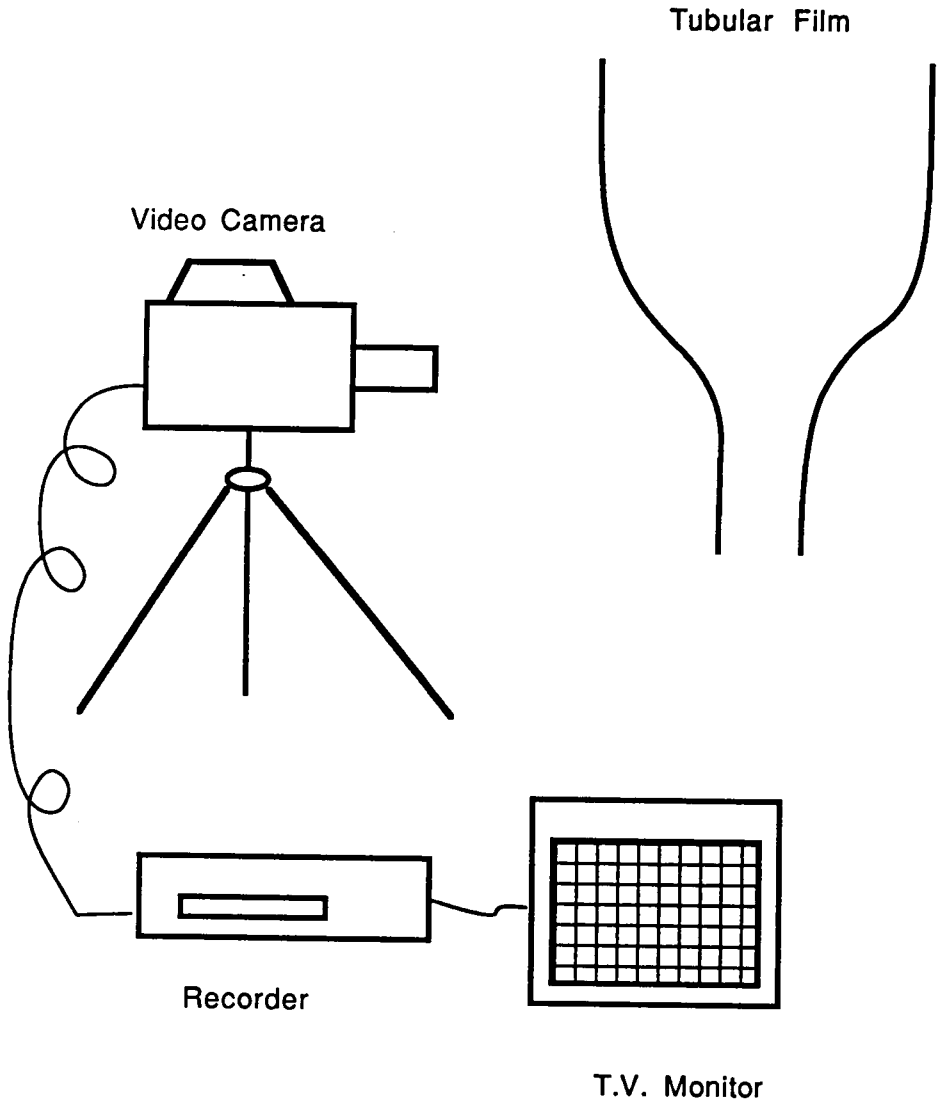

Figure 2-2 Video camera system for on-line measurement in the tubular film blowing process.

2.2.2 Thickness

Han and Park [11] suggested that after cutting and cooling the tubular film in the region between the annular die and the nip rolls, the distribution of the thickness of film along the machine direction could be obtained by directly measuring it. However, owing to the phenomena of thermal shrinkage and elastic relaxation, the thickness of the film after being cut and cooled will be different from that during processing, in which stresses and heat are applied to the whole film [15,31].

Hence, an alternative method was later suggested by Huang and Campbell [28] to obtain the thickness profile via the conservation of mass. Inspecting the following continuity equation for the blown film process,

$$W = 2\pi\rho RHV \qquad (2\text{-}1)$$

one can find that the mass flow rate W, density ρ, radius R and velocity V are needed in order to calculate the on-line thickness H. The mass flow rate can be obtained by collecting and weighing the extruded film for a predetermined time interval. The density of a polymer material is a function of temperature T when it is in the molten state. (The experimental observations reported in the literature [28]

showed that the bubble dimension stopped changing when significant solidification occurred.) Therefore, the effect of crystallization on density in the film blowing part, which is the major concern of this process, can be neglected. The temperature dependent density for polyethylene can be estimated by the following equation [32,33]:

$$\rho = [\ 1.135 + 0.00104(T-273)\ ]^{-1} \qquad (2\text{-}2)$$

where T is in units of Kelvin. The measuring techniques to obtain the radius profile have been discussed in the previous section; the techniques for the measurements of the film velocity and temperature will be given in the following paragraphs.

2.2.3 Velocity

A detailed description of the technique for on-line velocity measurement was given by Farber [34], Farber and Dealy [8], and Huang and Campbell [31]. Generally the apparatus used for on-line velocity measurement includes a video or movie recording system and a timer.

During processing, either a small piece of label is gently attached on the surface of the bubble [8,34], or a wax pencil is used to mark the bubble [31]. Thus, the piece of

label or the colored mark can be traced and recorded by a video camera system. The initial point at which the label could be observed is the position just above the air cooling ring. Monitoring and recording the displacement and the corresponding time interval progressed by the label (or the colored mark), the local velocity can be obtained by differentiating the measured curve of displacement vs. time with respect to time.

The reliability of this on-line measuring technique for velocity was tested and discussed by Liu [28]. Since the actual take-up velocity could be obtained by collecting and measuring the length of the film during a predetermined time interval, it became possible to compare this take-up velocity with the final velocity, which was measured by the video camera tracing technique at the take-up position. Several film blowing experiments with various take-up velocities were tested, and the results showed that the average error was 1.62%.

2.2.4 Temperature

Due to the bubble of thin film being in a dynamic condition during processing, the temperature of the film cannot be measured by contact-type measurement devices, such as, a thermometer or thermocouple. It can be understood that

a very soft running bubble, which is in a molten state during processing, will not support the friction produced by contacting with these devices. For this reason, the remote infrared sensing technique was used for the on-line temperature measurement [14,35-37]. The infrared sensing technique is based on the measurement of the thermal (or infrared) energy emitted from the target object. Then, the measured thermal energy can be converted into temperature on the basis of the Stefan-Boltzmann law and knowledge of the emissivity value.

For the on-line temperature measurements with the infrared sensing technique, there are two methods suggested by Fischer [9]: "Method I", in which a black body is placed behind the bubble, and "Method II", in which a black tube is vertically placed within the bubble. Since "Method II" will cause much more experimental difficulty, "Method I" has been mostly used to measure and correct the temperature readings from an infrared measurement device [7,13,28].

(A) Theoretical Analysis

According to Fischer's analysis, for the "Method I" the total radiant energy, R_{total}, received by an infrared thermometer is given by

$$R_{total} = [\varepsilon+\varepsilon\tau+\varepsilon\tau\rho+(\rho^2+\rho^3+\rho^4+\rho^5+...)]R_f + [\tau^2+\tau^2(\rho^2+\rho^4+...)]R_b + [\rho+\rho\tau^2+\tau^2(\rho^3+\rho^5+...)]R_e \quad (2\text{-}3)$$

in which the subscripts "f", "b" and "e" respectively denote the film, black body and environment; and ε, τ and ρ are the emissivity, transmissivity and reflectivity of the film, respectively.

However, Cao, Sweeney and Campbell [7] thought of the whole bubble as one film, and considered that the total amount of thermal radiation, R_{total}, received by the detector is composed of the radiation directly emitted from the bubble itself $\varepsilon^* R_f(b)$, the radiation of black body transmitted through the film, $\tau^* R_b$, and the ambient radiation reflected by the film $\rho^* R_e$. Cao et al. proposed the following equation for the total thermal radiation, R_{total}

$$R_{total} = \varepsilon^* R_f(b) + \tau^* R_b + \rho^* R_e \quad (2\text{-}4)$$

where $R_f(b)$ is thermal radiation from an absolute (ideal) black body at temperature of the film; ε^*, τ^* and ρ^* are apparent emissivity, transmissivity and reflectivity of the bubble, respectively. Thus, from the slope and the intercept in the plot of R_{total} versus R_b, the temperature of the film

can be found. However, since Equation(2-4) was derived by considering the whole bubble as one film, the emissivity obtained from the above equation is an apparent value rather than a value for a single piece of film.

Based on the conceptional approach of Cao et al., Equation(2-4) was developed and modified to obtain the emissivity and temperature values for a single piece of film by Liu [28]. In his analysis, it was assumed that the bubble is composed of two parallel plain films which are separated by a distance of the local diameter of the bubble. Moreover, it was allowed in Liu's analysis that these two pieces of films may have different temperature, emissivity, transmissivity and reflectivity. Then, based on the approach depicted in Figure 2-3, the total radiation received by the infrared detector could be expressed as the following equation

$$R_{total} = \varepsilon_1 R_{f1}^{(b)} + \tau_1\rho_2\varepsilon_1 R_{f1}^{(b)} + \tau_1\varepsilon_2 R_{f2}^{(b)} + \tau_1\tau_2 R_b + \rho_1 R_a + \tau_1^2\rho_2 R_a \qquad (2\text{-}5)$$

where the subscripts "1" and "2" denote the two plain films. With the further assumption that the bubble is axisymmetric, and its thickness and temperature are homogeneous and only depend on the position in the machine direction, i.e., both the film 1 and film 2 are identical, we have

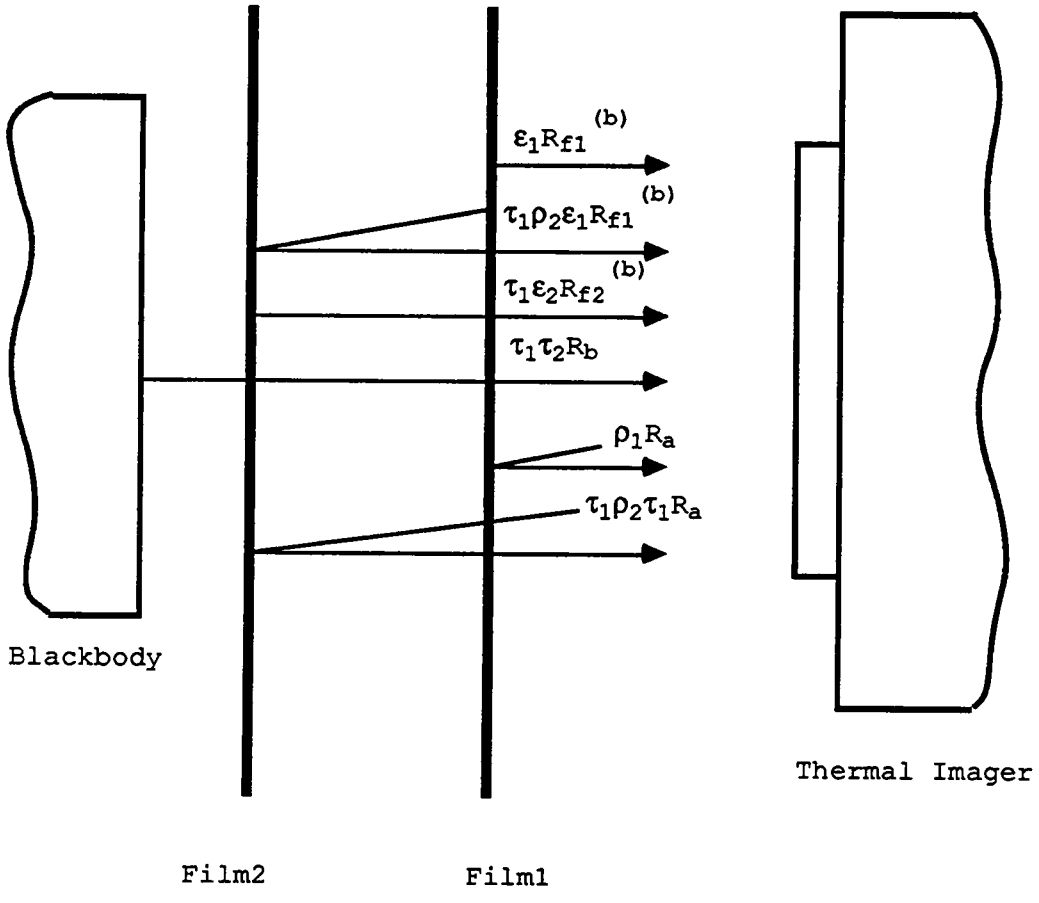

Figure 2-3 Schematic diagram of the total thermal radiant energy received by the detector of thermal imaging system.

$$\varepsilon = \varepsilon_1 = \varepsilon_2 \qquad (2\text{-}6a)$$

$$\tau = \tau_1 = \tau_2 \qquad (2\text{-}6b)$$

$$\rho = \rho_1 = \rho_2 \qquad (2\text{-}6c)$$

$$R_f(b) = R_{f1}^{(b)} = R_{f2}^{(b)} \qquad (2\text{-}6d)$$

Finally, with Equations(2-6a) ~ (2-6d), Equation(2-5) can be simplified into the following form

$$R_{total} = \varepsilon(1+\tau+\tau\rho)R_f^{(b)} + \tau^2 R_b + \rho(1+\tau^2)R_a \qquad (2\text{-}7)$$

Furthermore, a detailed comparison of Equation(2-3) with Equation(2-7) shows that the latter is an approximate form of the former. Equation(2-7) neglected the secondary (minor) reflection in the closed bubble, i.e., the serial terms within each parentheses of Equation(2-3). For the case of polyethylene whose reflectivity is very small (ρ = 0.04), the secondary reflection becomes insignificant when compared with the other primary terms. It was reported that about 1.15 ^{o}C difference existed between the temperatures of the film computed by Equations(2-3) and (2-7), respectively [28].

Equation(2-3) can be rewritten in the following compact form

$$R_{total} = \varepsilon\left(1 + \frac{\tau}{1-\rho}\right)R_f^{(b)} + \left(\frac{\tau^2}{1-\rho^2}\right)R_b + \rho\left(1 + \frac{\tau^2}{1-\rho^2}\right)R_a \tag{2-8}$$

If the following apparent quantities are defined as

$$\varepsilon^* = \varepsilon\left(1 + \frac{\tau}{1-\rho}\right) \tag{2-9a}$$

$$\tau^* = \left(\frac{\tau^2}{1-\rho^2}\right) \tag{2-9b}$$

$$\rho^* = \rho(1+\tau^*) \tag{2-9c}$$

then, Equation(2-8) can be expressed by the further compact form

$$R_{total} = \varepsilon^* R_f^{(b)} + \tau^* R_b + \rho^* R_a \tag{2-10}$$

Thus, with the further analysis, which will be given in the following section, Equations(2-8) ~ (2-10) provide us a possibility to obtain the actual temperature profile of the tubular film during processing.

(B) Data Analysis

As stated in the above paragraphs, the temperatures read from an infrared sensing device are merely apparent values, and they need a further calibration on the basis of infrared radiation theory and Equation(2-10) in order to obtain actual temperature values.

The classical Stefan-Boltzmann law for the total black body radiation, E_b, is written as

$$E_b = \sigma T^4 \qquad (2\text{-}11)$$

where $\sigma = 5.6696 \times 10^{-8}$ W/m^2K^4 is the Stefan-Boltzmann constant and T is the temperature of black body in units of Kelvin. Equation(2-11) can be derived from Planck's expression for the energy distribution in the wavelength of a black body

$$E_{b\lambda} = \frac{dE_b}{d\lambda} = \frac{m_1}{\lambda^5\left[\exp\left(\frac{m_2}{\lambda T}\right)-1\right]} \qquad (2\text{-}12)$$

where $E_{b\lambda}$ is the spectral or wavelength distribution of black body radiant energy, m_1 and m_2 are constants which are calculated from the speed of light, Boltzmann's constant and Planck's constant. Integrating $E_{b\lambda}$ with respect to λ at a constant temperature T, we have

$$E_b = \int_0^{\infty} E_{b\lambda}(\lambda, T)\, d\lambda = \sigma T^4 \qquad (2\text{-}13)$$

Thus, it is very clear that the Stefan-Boltzmann constant σ is just a combination of the spectrum constants m_1 and m_2. Hence, we know that Equation(2-11) is correct only for the condition of the whole spectrum (i.e., $\lambda = 0 \rightarrow \infty$) being under consideration. However, for different infrared sensing devices they have their own specified sensitive spectral range. Therefore, a fractional function, f_e, should be introduced into the expression of Stefan-Boltzmann law, Equation(2-11), to calculate the black body radiant energy contained within a finite-wavelength band

$$f_e(\lambda, T) = \frac{E_b(0 \rightarrow \lambda T)}{Eb(0 \rightarrow \infty)} = \frac{E_b(0 \rightarrow \lambda T)}{\sigma T^4} \qquad (2\text{-}14)$$

Knowledge of this function allows us to calculate the black body radiant energy emitted in any finite-wavelength band ($\lambda_1 \rightarrow \lambda_2$) at any temperature T by

$$E_b(\lambda_1 T \rightarrow \lambda_2 T) = (f_{e2} - f_{e1})\sigma T^4 = F_e(T)\sigma T^4 \qquad (2\text{-}15)$$

where $F_e(T)$ is equal to $(f_{e2} - f_{e1})$, and the values of f_{e1} and f_{e2} with respect to $\lambda_1 T$ and $\lambda_2 T$ are available elsewhere [38].

Inserting Equation(2-15) into Equation(2-10) then dividing it by the Stefan-Boltzmann constant σ, we have

$$F_e(T_{total})T_{total}^4 = \varepsilon^* F_e(T_f)T_f^4 + \tau^* F_e(T_b)T_b^4 + \rho^* F_e(T_a)T_a^4 \qquad (2\text{-}16)$$

where T_f is the actual temperature of the film, and T_{total}, T_b and T_a are the apparent black body temperatures of the total radiation, the black body and the environment, respectively. Here the apparent black body temperature is defined as the temperature at which an ideal black body would give the same amount of thermal radiant energy [39].

For the case of steady state, it can be assumed that the values of temperature, emissivity, transmissivity and reflectivity of the axisymmetric film are only dependent on the position along the machine direction. Thus, Equation(2-16) shows that a linear relationship exists between $F_e(T_{total})T_{total}^4$ and $F_e(T_b)T_b^4$. In other words, by changing the apparent black body temperature of the heater behind the bubble, the values of $F_e(T_{total})T_{total}^4$ have a linear response to that of $F_e(T_b)T_b^4$. Hence, from a series of data, a straight line can be obtained in the plot of $F_e(T_b)T_b^4$ vs. $F_e(T_{total})T_{total}^4$, and its slope and intercept at y-axis are given as

$$\text{Slope} = \tau^* = \left(\frac{\tau^2}{1-\rho^2}\right) \tag{2-17}$$

$$\text{Intercept at y-axis} = \varepsilon^* F_e(T_f) T_f^4 + \rho^* F_e(T_a) T_a^4 \tag{2-18}$$

(C) Calibration

The accuracy and reliability of the above analysis were examined by Liu [28]. The experimental setup, as shown in Figure 2-4, was created in his testing. Two flat films with the same thickness were separately hung above a furnace which was used to heat the cold air from its bottom up to a certain temperature. Thus, a mild hot air current with homogeneous temperature came out from the top of this furnace and kept those two small films at a constant temperature. A thermocouple was used to directly measure the temperature of the film by contacting. At the same time, the technique of on-line measurement on the basis of the above analysis was used to measure the temperature of the position where the thermocouple was measuring. Thus, comparing the results from two independent methods becomes possible; and an average difference of ±2.53 ^{o}C was reported. However, the limitation of this calibration is that the experiment has to be carried

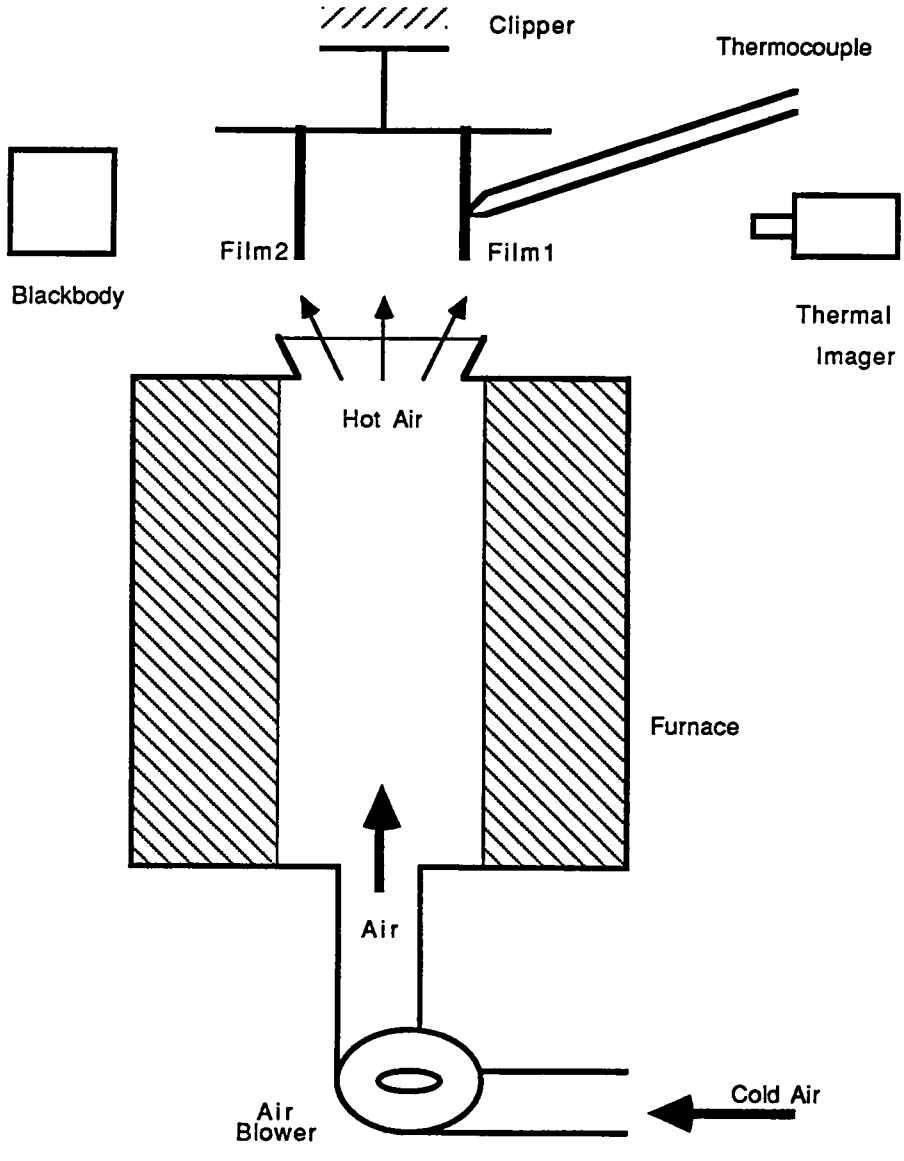

Figure 2-4 Experimental setup for the test of the on-line temperature measuring technique.

out at a temperature lower than the melting temperature of the film. Nevertheless, according to the results of the measurement of melt emissivity carried out by Hajji [40], it is found that the radiant properties are hardly affected by the variation of temperature; and within the experimental error, it was unaffected by the change in state on melting or freezing. Hence, it is believed that the accuracy and reliability of the technique for on-line temperature measurement in the molten state will be similar to that in the solid state.

2.3 RHEOLOGY

Shear viscosity and elongational viscosity are two important measures of performance of polymer melt during processing. The main factors that affect the viscosity of polymer melts are molecular structures (e.g. molecular weight, degree and type of molecular chain branching, molecular weight distribution, and as crystallization progresses in the film blowing process, the degree of crystallinity) and the processing conditions (e.g. processing temperature and deformation rate).

2.3.1 Influence of Molecular Structure on Rheological Behavior

With regard to the influence of molecular weight on viscosity, Fox and Flory [41,42] found that the zero-shear viscosity μ_o is proportional to $\bar{M}_w^{3.4}$ under the condition of $\bar{M}_w > Mc$ (the critical molecular weight for entanglements of chains). Nevertheless, for the sake of practical reason, the effects of molecular weight and long chain branching have to be considered for a typical polydisperse polymer [43,44]. Atalla and Romanini [45] proposed an empirical equation describing the isothermal behavior of elongational viscosity under the influences of molecular weight and long chain branching

$$\log\eta_E = 2.18\log\left\{\left[\frac{(\eta_o)br}{(\eta_o)lin}\right]^{\frac{1}{2.84}}\beta\bar{M}_w\right\} - 7.87 \qquad (2\text{-}19)$$

where β is the polydispersity index and η_o is the measured zero-shear-rate viscosity from the molten sample. From this equation, it is found that the effect of long chain branching is to lower the elongational viscosity for the same values of $\beta\bar{M}_w$, "molecular weight times polydispersity".

Furthermore the influence of the molecular structure on the melt extensibility for polyethylene resins were studied by Constantin [46], Acierno et al. [47], and Mantia et al. [48].

Constantin found that the lack of long chain branching leads to good extensibility. Acierno et al. discovered that for different samples, HDPE, LDPE, and LLDPE (i.e., high density, low density, and linear low density polyethylene), the breaking stretch ratio increases with melt index while the melt strength decreases with the increase of melt index. Moreover, Mantia et al. concluded that the substitution of LDPE by the blend of 25% LLDPE with LDPE shows a good performance during processing of the blown film extrusion.

In a series of studies Han et al. [49], Han and Kwack [50], and Kwack and Han [51] established a good understanding of the relationship between rheological properties and processing conditions for polyethylene resins with different molecular structures. They found that the resin with a narrower molecular weight distribution and less degrees of long chain branching increases the ability to blow a large diameter film, and the lower elongational viscosity leads to larger draw-down ratios.

2.3.2 Rheological Modelling

In the earliest mathematical analysis for the blown film extrusion, an isothermal Newtonian fluid was assumed [3,52]. Thus, under this assumption, the viscosity value of the polymeric material would remain constant through the whole

processing. However, for a non-Newtonian fluid, the main factors affecting its viscosity are temperature, deformation rate and the previous kinematic history [53].

In the tubular film blowing process, the kinematics are basically the elongational type rather than the shear one [54]. Hence, Han and Park [11] determined the elongational viscosity by force balance equations. They carried out the experiments under an isothermal condition to eliminate the influence of temperature. By controlling the inside pressure of the bubble, the uniaxial and biaxial elongational flow were investigated. Their experimental results showed that the elongational viscosity may decrease or increase with the elongation rate, and even may be independent of elongational rate. Moreover, they concluded that the data of elongational viscosity obtained from the blown film under the condition of uniaxial stretching (i.e., $\Delta P = 0$) is consistent with the data of elongational viscosity obtained from the melt spinning process [55-59].

Beside the elongational rate, the variation of temperature may be the dominating factor to effect the value of viscosity in processing. Hence, an Arrhenius type equation which describes the temperature dependence of melt viscosity was given as [60]

$$\eta = \eta_o \exp\left[\frac{E_a}{R_g T}\right] \qquad (2\text{-}20)$$

where R_g is the gas constant, E_a is the viscosity activation energy and η_o is a constant, the reference viscosity, which depends on an arbitrarily selected reference temperature. Therefore, in the second part of a series of papers by Han and Park [5], they expressed the elongational viscosity by the Arrhenius-type function of temperature and the second invariant of deformation rate tensor for the non-isothermal blown film extrusion

$$\eta(T, II) = \eta_o \exp\left[\frac{E_a}{R_g}\left(\frac{1}{T} - \frac{1}{T_o}\right)\right]\left[\frac{II_d}{2}\right]^{\frac{n-1}{2}} \qquad (2\text{-}21)$$

where η_o is the elongational viscosity at the reference temperature T_o, T is the temperature of the film, II_d is the second invariant of the rate-of-strain tensor, and n is the power law index. Equation(2-21) was used in the computer simulation for tubular film blowing process by Han et al. [5] and Yamane [61].

Generally speaking, the materials most frequently used to produce tubular films are semi-crystalline, e.g. polyethylene and polypropylene [62]. Thus, Kanai and White [6] included a term of crystallinity in the viscosity equation. Considering that the occurrence of crystallization

causes a resistance to deformation, the viscosity equation was given by

$$\eta = \eta_o \exp\left[\frac{E_a}{R_g}\left(\frac{1}{T} - \frac{1}{T_o}\right)\right] \exp(GX) \qquad (2\text{-}22)$$

in which X is the fraction of crystallinity and G is a material constant obtained from experimental results [14]. In a later paper, Kanai [63] used a more complete rheological model to analyze the high molecular weight HDPE tubular film process. The viscosity equation included the factor of temperature, the second invariant of deformation rate tensor, the power law index and the fraction of crystallinity

$$\eta(T, II_d, X) = \eta_o \exp\left[\frac{E_a}{R_g}\left(\frac{1}{T} - \frac{1}{T_o}\right) + GX\right] [II_d]^{\frac{n-1}{2}} \qquad (2\text{-}23)$$

2.4 INSTABILITIES IN TUBULAR FILM BLOWING

Only a few studies investigated the instability of the bubble and the reasons for this phenomenon are still unclear. Most of the investigations focused their attention on the qualitative description. Han and Park [64] experimentally

observed that a type of instability similar to draw resonance occurred under uniaxial stretching, and a surface wave-type instability was found in biaxial stretching. Later, Han and Shetty [12] had a further observation that a disturbance from the take-up speed would cause a much more severe instability than that of inflating air pressure did. Moreover, they also found that the decrease of melt temperature might help to stabilize the bubble.

Kanai and White [14], Minoshima [65], and Minoshima and White [66] studied the relationship between the processing variables, such as, draw-down ratio, blow-up ratio and frost line height, and the materials, such as, different kinds of resins, rheological properties and molecular structures. Minoshima et al. proposed a more detailed qualitative description of instabilities by four types of unsteady state behavior.

In a later paper a video system which could be used to investigate the extent of instability of bubble more quantitatively during processing was introduced by Sweeney, Campbell and Feeney [67]. They also found that LDPE, i.e., polyethylene with long chain branching, made the blown film processing of polyethylenes more stable.

Apparently only two reports [68,69] deal with the instable phenomena in a quantitative manner. Yeow [68]

analyzed the stability of an isothermal Newtonian model by the methods of linear hydrodynamic stability. Cain and Denn [69] made an extensive quantitative analysis to correlate the operation variables with the process stability by two different rheological models, the Newtonian and Maxwell model. They concluded that the increase of melt viscosity by cooling is a significant stabilizing factor, and that the theoretical stability depends on the selection of control variables.

2.5 PREVIOUS MATHEMATICAL ANALYSIS OF THE BLOWN FILM PROCESS

2.5.1 Kinematics

The kinematics of the tubular film blowing process were first analyzed by Pearson [52] and were detailed in a series of studies by Pearson and Petrie [3,4]. The following assumptions were made in their development:

(1) The polymer melt behaves as a Newtonian fluid.

(2) The film is thin enough, so that variations in the flow field across it are negligible.

(3) Comparing with the other dimensions of the tubular film, the curved film is thin enough to be approximated by a plane film, i.e., thickness H <<

R_i where R_i is the radius of curvature of the bubble in direction i.

(4) The tubular film is axisymmetric about the Z axis, which is along the machine direction.

The coordinate system is depicted as Figure 2-5, in which "1" is the machine direction, "2" is the circumferential (transverse) direction, and "3" is the direction normal to the film (i.e., the thickness direction). For a point P embedded in the inner surface of the bubble, its rectangular Cartesian coordinates (ξ_1, ξ_2, ξ_3) can be related to the cylindrical coordinate system (R, θ, Z), as shown in Figure 2-5, where θ is the angle between the bubble profile and the Z-axis. The rate-of-strain tensor is written as

$$d = \begin{vmatrix} d_{11} & 0 & 0 \\ 0 & d_{22} & 0 \\ 0 & 0 & d_{33} \end{vmatrix} \qquad (2\text{-}24)$$

Let (V_1, V_2, V_3) be the velocity components in the coordinates (ξ_1, ξ_2, ξ_3), then from the definition

$$d_{ij} = \frac{\partial V_j}{\partial x_i} + \frac{\partial V_i}{\partial x_j} \qquad (2\text{-}25)$$

we have

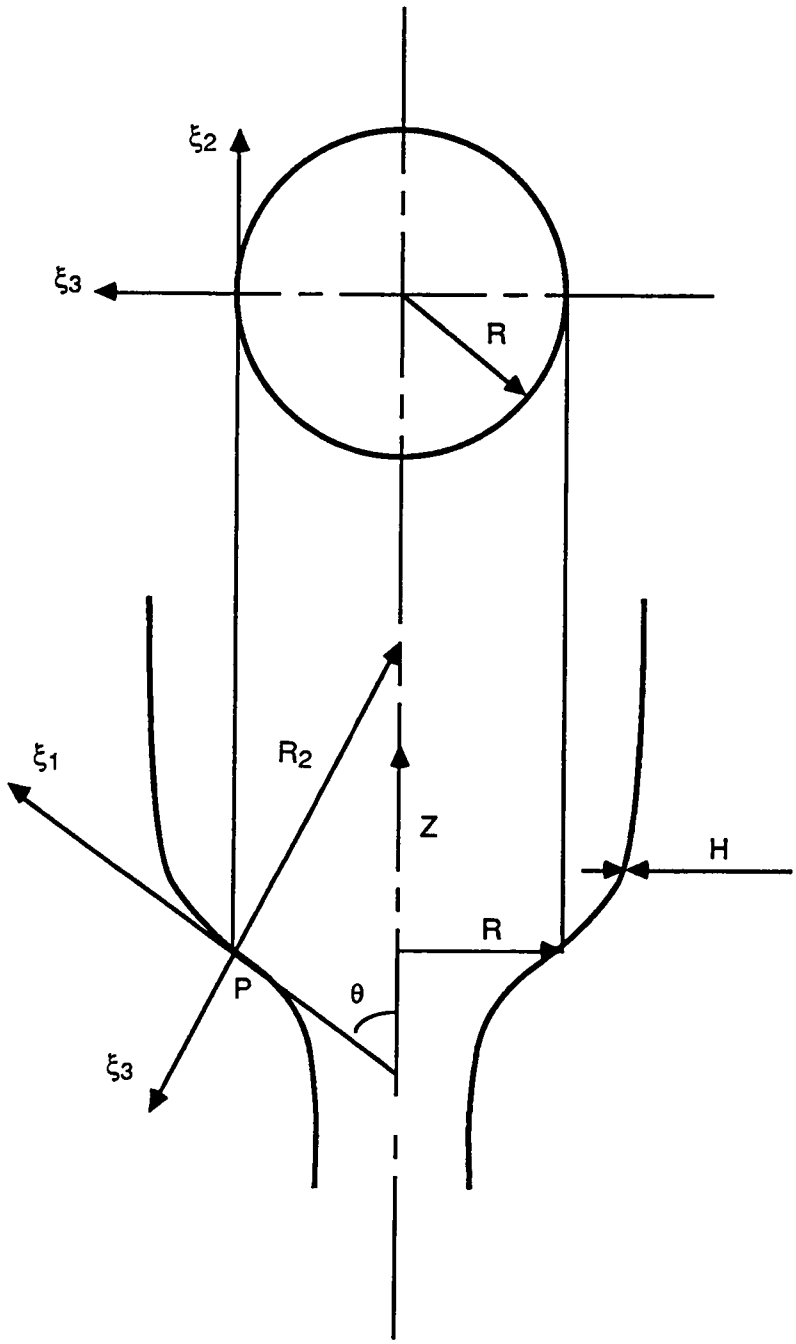

Figure 2-5 Coordinate systems of a tubular film.

$$d_{11} = 2 \frac{\partial v_1}{\partial \xi_1} \tag{2-26a}$$

$$d_{22} = 2 \frac{\partial v_2}{\partial \xi_2} \tag{2-26b}$$

$$d_{33} = 2 \frac{\partial v_3}{\partial \xi_3} \tag{2-26c}$$

Based on the above assumptions and through the following two relationships:

$$v_1 = \frac{d\xi_1}{dt} \tag{2-27a}$$

$$d\xi_1 = \frac{1}{\cos\theta} dZ \tag{2-27b}$$

d_{22} and d_{33} may be expressed as

$$d_{22} = \frac{2}{R} \frac{dR}{dt} = 2v_1 \cos\theta \frac{1}{R} \frac{dR}{dZ} \tag{2-28}$$

$$d_{33} = \frac{2}{H} \frac{dH}{dt} = 2v_1 \cos\theta \frac{1}{H} \frac{dH}{dZ} \tag{2-29}$$

where t is the time.

Under the assumption that the polymer is an incompressible fluid, $d_{11} + d_{22} + d_{33} = 0$, we have

$$d_{11} = -2V_1\cos\theta \left(\frac{1}{R} \frac{dR}{dZ} + \frac{1}{H} \frac{dH}{dZ} \right) \qquad (2\text{-}30)$$

Furthermore, the velocity component V_1 can be easily expressed in terms of R, H, and Q

$$V_1 = \frac{Q}{2\pi RH} \qquad (2\text{-}31)$$

where Q is the volumetric flow rate. Finally, Equations(2-28),(2-29) and (2-30) are rewritten as:

$$d_{11} = \frac{-Q\cos\theta}{\pi RH} \left(\frac{1}{R} \frac{dR}{dZ} + \frac{1}{H} \frac{dH}{dZ} \right) \qquad (2\text{-}32)$$

$$d_{22} = \frac{Q\cos\theta}{\pi RH} \frac{1}{R} \frac{dR}{dZ} \qquad (2\text{-}33)$$

$$d_{22} = \frac{Q\cos\theta}{\pi RH} \frac{1}{H} \frac{dH}{dZ} \qquad (2\text{-}34)$$

From the above kinematic analysis, Han and Park [11] developed two special cases: (1) uniaxial stretching, $2d_{22} = 2d_{33} = -d_{11}$, and (2) uniform biaxial stretching, $2d_{11} = 2d_{22} = -d_{33}$. Furthermore, Choi, White and Spruiell [70] correlated the processing variables, blow-up ratio BUR = R_L/R_o and take-up ratio TUR = V_L/V_o, with several special cases of kinematics:

(1) Uniaxial extension

$$d_{22} = d_{33} \tag{2-35a}$$

$$\frac{1}{R}\frac{dR}{dZ} = \frac{1}{H}\frac{dH}{dZ} \tag{2-35b}$$

Integrating Equation(2-35b) from die exit to the take-up position, we have

$$\frac{V_L}{V_o} = \frac{1}{BUR^2} \tag{2-36}$$

where the subscript "L" and "o" represent the positions of take-up device and die exit, respectively.

(2) Planar extension

$$d_{22} = 0 \tag{2-37a}$$

$$\frac{1}{R}\frac{dR}{dZ} = 0 \tag{2-37b}$$

Then the following can be obtained

$$BUR = \frac{R_L}{R_o} = 1 \tag{2-38a}$$

$$\frac{V_L}{V_o} = \frac{H_L}{H_o} \tag{2-38b}$$

(3) Equal biaxial extension

$$d_{11} = d_{22} \tag{2-39a}$$

$$\frac{-1}{H}\frac{dH}{dZ} - \frac{1}{R}\frac{dR}{dZ} = \frac{1}{R}\frac{dR}{dZ} \tag{2-39b}$$

Integration of Equation(2-39b) leads to

$$\frac{V_L}{V_O} = BUR \tag{2-40}$$

That is, under the processing condition of the take-up ratio being equal to the blow-up ratio, an uniform biaxially stretched film can be obtained.

2.5.2 Force Balance

A precise dynamic analysis for the tubular film blowing process would be very complicated because of the bubble being stretched in two directions. Alfrey [71] may be the earliest one to develop the force balance equations from membrane theory. Nevertheless, a more detailed and deeper discussion was in a series of studies by Pearson and Petrie [3,4,29]. By neglecting the inertial, gravitational force and surface tension, they made a mechanical analysis for an isothermal

Newtonian flow of a thin tubular film. Then, Petrie [72] reconsidered this tubular film as an Oldroyd type of viscoelastic fluid under an isothermal condition. In a later paper, Petrie [73] carried out the calculation of his model for a non-isothermal Newtonian and an isothermal elastic flow, and he made a comparison with the published experimental results [34,35,74]. Han and Park [5] argued the importance of the effect of gravity during the process, and added a term for gravitational force into the force balance equations.

The force balances for blown film extrusion can be split into two directional considerations.

(A) In the Machine Direction

An overall force balance in longitudinal direction is given by

$$F_{rheo} = F_L - F_{grav} - F_{drag} - F_{surf} - F_{inert} - \pi(R_L^2 - R^2)\Delta P \qquad (2\text{-}41)$$

where

F_{rheo} = the rheological force in the film,

F_L = the take-up force being applied on the film,

F_{grav} = the gravitational force due to the film's weight,

F_{drag} = the drag force between the air and the film surface,

F_{surf} = the surface tension of the bubble,

F_{inert} = the inertial force required to accelerate the fluid,

ΔP = the pressure difference across the film,

i.e., $\Delta P = (P_{inside} - P_{outside})$.

Comparing with the magnitude of the total force acting in the machine direction, the contributions of surface tension are insignificant, and the inertial and drag force become unimportant for the reason of low take-up speed. Thus, neglect of the F_{drag}, F_{surf} and F_{inert} terms is very reasonable, and the remaining terms in Equation(2-41) are expressed as

$$F_{rheo} = 2\pi RH\sigma_{11}\cos\theta \qquad (2\text{-}42)$$

$$F_{grav} = 2\pi\rho_m g \int_{Z}^{Z_F} RH\sec\theta \, dZ + 2\pi\rho_s gRH(Z_L - Z_F) \qquad (2\text{-}43)$$

where

σ_{11} = the normal stress in the machine direction,

ρ_m = the density of polymer in the molten state,

ρ_s = the density of polymer in the solid state,

Z_L = the height of the take-up position,

Z_F = the height of the frost line,

g = the standard acceleration of gravity.

(B) In the Circumferential Direction

Based on the considerations in the above statements and the membrane theory [75,76], the force balance equation in the transverse direction is given by

$$\Delta P = \frac{H\sigma_{11}}{R_1} + \frac{H\sigma_{22}}{R_2} - \rho g H \sin\theta \qquad (2\text{-}44)$$

where σ_{22} is the normal stress in the hoop direction, and R_1 and R_2 are the principal radii of curvature of the film in the direction "1" and "2", respectively. From the geometrical relationships the two principal radii can be expressed as

$$R_1 = \frac{-\sec^3\theta}{\frac{d^2R}{dZ^2}} \qquad (2\text{-}45a)$$

$$R_2 = \frac{R}{\cos\theta} \qquad (2\text{-}45b)$$

For an incompressible fluid, the total stress σ can be expressed by two separate terms, the isotropic pressure p and the deviatoric stress τ. Hence the component of total stress is given by

$$\sigma_{ij} = -p\delta_{ij} + \tau_{ij} \qquad (2\text{-}46)$$

where δ_{ij} is the component of the Kronecker delta and i is 1, 2, or 3. In the tubular film blowing process, the stress at the free surface is equal to atmospheric pressure, and we have

$$\sigma_{33} = -p + \tau_{33} = 0 \qquad (2\text{-}47)$$

That is, being relative to atmospheric pressure σ_{33} is zero. Finally, the expression for both of the total stresses acting in the machine and hoop directions are obtained

$$\sigma_{11} = \tau_{11} - \tau_{33} \qquad (2\text{-}48)$$

$$\sigma_{22} = \tau_{22} - \tau_{33} \qquad (2\text{-}49)$$

2.5.3 Energy Balance

The earlier theoretical analyses [3,4,29,52,72] of blown film extrusion lacked any consideration of the influence of temperature, that is, an isothermal condition was assumed. In a later study by Petrie [77], the mathematical modelling of heat transfer in film blowing was qualitatively discussed, then he [73] developed a mathematical model to simulate the

flowing behavior of non-isothermal Newtonian fluid merely by adding a temperature term into the viscosity and the density equations. However, there was no energy balance involved in his analysis, and the temperature profiles were taken from published data [34,35,74].

The first quantitative description of the occurrence of heat transfer in the film blowing process was established by Han and Park [5]. The following assumptions were made in their theoretical analysis:

(1) The heat transfer between the inner surface of film and the inflating air inside the bubble is negligible.

(2) The heat transfer between the tubular film and the environment is primarily controlled by convection and radiation, and the heat conduction of the film may be neglected.

(3) The heat generation due to the frictional force is small enough to be neglected.

(4) The heat of crystallization is negligible even if the material is semi-crystalline.

Thus, the energy balance equation was given as

$$\rho C_p \left(\frac{Q\cos\theta}{2\pi R}\right)\frac{dT}{dZ} = -U(T-T_{air}) - \varepsilon\sigma(T^4-T_r^4) \qquad (2\text{-}50)$$

in which

ρ = the density of material,

C_p = the specific heat capacity,

T = the temperature of the film,

T_{air} = the temperature of cooling air,

T_r = the room temperature,

ε = the emissivity of the film,

σ = the Stefan-Boltzmann constant.

As mentioned in the previous section, the semi-crystalline polymers are the most frequently used to produce tubular films. Moreover, some of these semi-crystalline polymers have high values of final crystallinity. Thus, the amount of the crystallization energy, which is released while the crystalline phase appears, would be so large that its influence on the film's temperature is very significant [14]. Hence, Kanai and White [6,14] established the energy balance equation more completely by adding a term for crystallization into Equation(2-50), and it becomes

$$\rho C_p\left(\frac{Q\cos\theta}{2\pi R}\right)\frac{dT}{dZ} = -U(T-T_{air}) - \varepsilon\sigma(T^4-T_r^4) + \rho\Delta H_f\left(\frac{Q\cos\theta}{2\pi R}\right)\frac{dX}{dZ} \qquad (2\text{-}51)$$

in which ΔH_f is the heat of fusion, and X is the fraction of crystallinity.

2.5.4 Heat Transfer Coefficient

In the practical processing condition, the tubular film is cooled by forced convection by the ambient cooling air. Moreover, according to the experimental analysis of Menges and Predohl [15], the amount of heat transfer by radiation is about 15 percent of the total amount of overall heat transfer. Thus, the cooling rate of the film is dominated by the heat convection term in Equation(2-51), and the determination of the overall heat transfer coefficient U is certainly important.

Menges and Predohl [15,78] proposed an empirical equation to correlate the velocity of cooling air to the heat transfer coefficient

$$U = 3.3(V_{max})^{1.5} \qquad (2\text{-}52a)$$

and for thicker plastic bags

$$U = 3.04(V_{max})^{1.3} \qquad (2\text{-}52b)$$

in which V_{max} is the characteristic (maximum) air velocity along the machine direction. V_{max} is a function of position and can be estimated by

$$V_{max} = V_{max,F} \left(\frac{Z_F}{Z} \right)^{0.74} \qquad (2\text{-}53)$$

where $V_{max,F}$ is the maximum parallel air velocity at the position of frost line, Z_F.

Kanai and White [14] have carried out an on-line measurement for temperature; and from the temperature profiles they concluded that

$$\text{at} \quad Z < Z_c , \qquad U = k_1 \qquad (2\text{-}54a)$$

$$\text{at} \quad Z > Z_c , \qquad U = \frac{k_2}{Z^{\gamma}} \qquad (2\text{-}54b)$$

where Z_c is a critical position and equal to 8 cm in their study, and k_1, k_2 and γ are constants. In other words, the value of heat transfer coefficient remains constant from the die exit to a critical position Z_c, then starts to decrease along the machine direction. The values of k_1, k_2 and γ would vary with cooling air velocity.

Kanai et al. [14] also carried out a dimensionless analysis for the apparent heat transfer coefficient. The correlation between Reynolds number, Nusselt number and Prandtl number was given by [79,80]

$$\frac{UL}{k_{air}} = m_i \left[\frac{LV_{air}\rho_{air}}{\eta_{air}} \right]^{m_j} \left[\frac{C_{pair}\eta_{air}}{k_{air}} \right]^{m_k} \qquad (2\text{-}55)$$

where k is the thermal conductivity, m_i, m_j and m_k are constants, and the subscript "air" refers to the values for air. They found the above equation is more suitable for the case of the lower frost line height, and obtained the following empirical relationship

$$\frac{UL}{k_{air}} = 0.043 \left[\frac{LV_{air}\rho_{air}}{\eta_{air}}\right]^{0.76} \qquad (2\text{-}56)$$

Also, Kanai et al. successfully correlated the V_{max} and U by the form proposed by Menges et al.

$$U = 2.5\ V_{max}^{1.6} \qquad (2\text{-}57)$$

from the experimental data above the frost line.

2.5.5 System Equations of Mathematical Model

Although various considerations and material equations were used in the theoretical simulation of the blown film process, the primary system equations were generally similar in principle. Hence, based on the analysis of kinematics, dynamics, and energy balance in the above sections, the governing system equations of non-isothermal tubular film

blowing for a semi-crystalline material can be derived and shown as follows.

Under the assumptions that the surface tension of the bubble, the inertial force, the air drag force and the gravitational force are negligible compared to the rheological force, the following differential equations can be derived from the force balance equations, Equations(2-41) and (2-44), incorporated with kinematic and geometrical analysis.

$$\frac{dR}{dZ} = \tan\theta \tag{2-58}$$

$$\frac{dH}{dZ} = \frac{-H}{2R}\tan\theta - [\ A+BR^2\ ]\frac{H\sec^2\theta}{4\eta} \tag{2-59}$$

$$\frac{d\theta}{dZ} = \frac{1}{R(A+BR^2)}\left[\frac{A-3BR^2}{2} + \frac{3\eta\sin\theta\cos\theta}{R}\right] \tag{2-60}$$

where

$$A = \frac{F_L-\pi R_L^2\Delta P}{Q} \tag{2-61}$$

$$B = \frac{\pi\Delta P}{Q} \tag{2-62}$$

Assuming that both the heat conduction and heat generation due to the frictional force are negligible, the differential equation regarding temperature variation during

processing can be obtained from the energy balance equation, Equation(2-51).

$$\frac{dT}{dZ} = -CR\sec\theta(T-T_{air}) - DR\sec\theta(T^4-T_r^4) + FX_fKRH\sec\theta\left(1-\frac{X}{X_f}\right) \tag{2-63}$$

where

$$C = \frac{2\pi U}{\rho C_p Q} \tag{2-64}$$

$$D = \frac{2\pi\sigma\varepsilon}{\rho C_p Q} \tag{2-65}$$

$$F = \frac{2\pi\Delta H_f}{C_p Q} \tag{2-66}$$

In Equation(2-63) X and K are the local crystallinity and the crystallization rate constant, respectively. For the case of semi-crystalline material, the crystallinity change along the machine direction may be estimated by the following equation:

$$\frac{dX}{dZ} = \frac{X_f K}{V}\left(1 - \frac{X}{X_f}\right) \tag{2-67}$$

where V is the velocity in the machine direction. The detailed derivation of Equations(2-67) was given by Liu [28].

2.6 PREDICTION OF PREVIOUS MATHEMATICAL MODEL

Based on the fundamental system equations described above, many investigations regarding mathematical simulation of the tubular film blowing process have been reported. Since 1970, the fundamental kinematic and dynamic analysis for the isothermal case was first established by Pearson and Petrie. In order to make this mathematical description closer to the practical process, this model was developed and improved to describe the non-isothermal processing conditions for semi-crystalline materials by taking energy balance equation [5,6,14,28,30,81], various types of rheological models [30,81-87] and crystallization [6,28] into consideration.

Most of the simulation shows that the shape of the profiles, such as, radius, thickness, velocity and temperature, predicted by the previous model qualitatively agree with the experimental observations. However, unfortunately, probably due to high complexity and difficulty of the mathematical simulation and experimental data collection, prediction of this mathematical model was rarely systematically or quantitatively tested by comparing to the on-line measured data. Hence, the capability of prediction of the previous model has not been fully revealed.

Moreover, several unexpected phenomena that appeared in the simulation have been repeatedly reported, and still no satisfactory interpretation is available [5,29,30]. For example, the most obvious one, mathematical prediction shows that the radius of the bubble decreases with the increase of ΔP [5,29,30]. This phenomenon was previously interpreted as due to the effects of the surface tension forces between the inflated bubble and the air, i.e., a larger ΔP is required for a bubble with smaller radius (ΔP = surface tension / radius of a bubble) [5,29]. However, this explanation seems not satisfying, because the surface tension term was not considered when the force balance equations were established. On the other hand, the experimental observations on the relationship between ΔP and blow-up ratio are mixed. Kanai and White [6,14] found an inverse pressure effect both in their experimental data and theoretical analysis. However they did not give a physical interpretation. Han and Park [11] found both situations (i.e., radius increasing and decreasing with the inside pressure); whereas Wagner [26,27] found the "intuitive" effect for most of his data (that is, small increases in the pressure caused large increases in the radius). There was not any analysis, however, in either of these studies. According to Wagner's results, a significant intuitive effect was shown in the cases of low blow-up ratio;

however, a nearly constant pressure appeared in the cases of blow-up ratio greater than about two. Several experimental observations similar to Wagner's results were also reported in a recent study by Liu [28].

Based on the above discussion, the mathematical model first established by Pearson and Petrie appears to have some difficulty to correctly predict the influence of the inside pressure, one of the important processing parameters, on the dimension of the tubular film. This problem was first explicitly raised and discussed by Liu [28]. Furthermore, Liu also found that there exists a huge discrepancy between the prediction of this mathematical model and his on-line measured data. Finally, the discrepancies stated above were greatly improved by the new mathematical model proposed in his analysis. This new model is going to be discussed in the following section.

2.7 NEWLY PROPOSED MATHEMATICAL MODEL

2.7.1 Modified Physical Approach and Proposed Equations

In Liu's analysis [28], the tubular film blowing process was reconsidered and approached from another point of view. His modified physical approach to describe the film blowing

process is depicted in Figure 2-6. When the polymeric melt emerges from the exit of an annular slit die with a constant flow rate, its shape appears to be a small, short "tube" with constant radius. As the blowing process is being carried out, this short "tube" is being acted on by two principal forces in two different directions: one is an effective take-up force F in the machine direction; the other one is a pressure difference ΔP across the wall of this "tube". In other words, the whole tubular film in processing is considered as being composed of many infinitesimal tubular (cylindrical) elements, which are schematically shown as Figure 2-6. Thus, based on this physical model, two force balance equations for a tubular element with unit length can be obtained and expressed as

$$F = 2\pi RH\sigma_{11} \tag{2-68}$$

$$\Delta P = \frac{H\sigma_{22}}{R} \tag{2-69}$$

where R and H are the radius and thickness of the tubular element, respectively, and the normal stresses, σ_{11} and σ_{22}, are given by

$$\sigma_{11} = \frac{-\Delta P}{2} - \tau_{33} + \tau_{11} = \frac{-\Delta P}{2} + \eta(d_{11}-d_{33}) \tag{2-70}$$

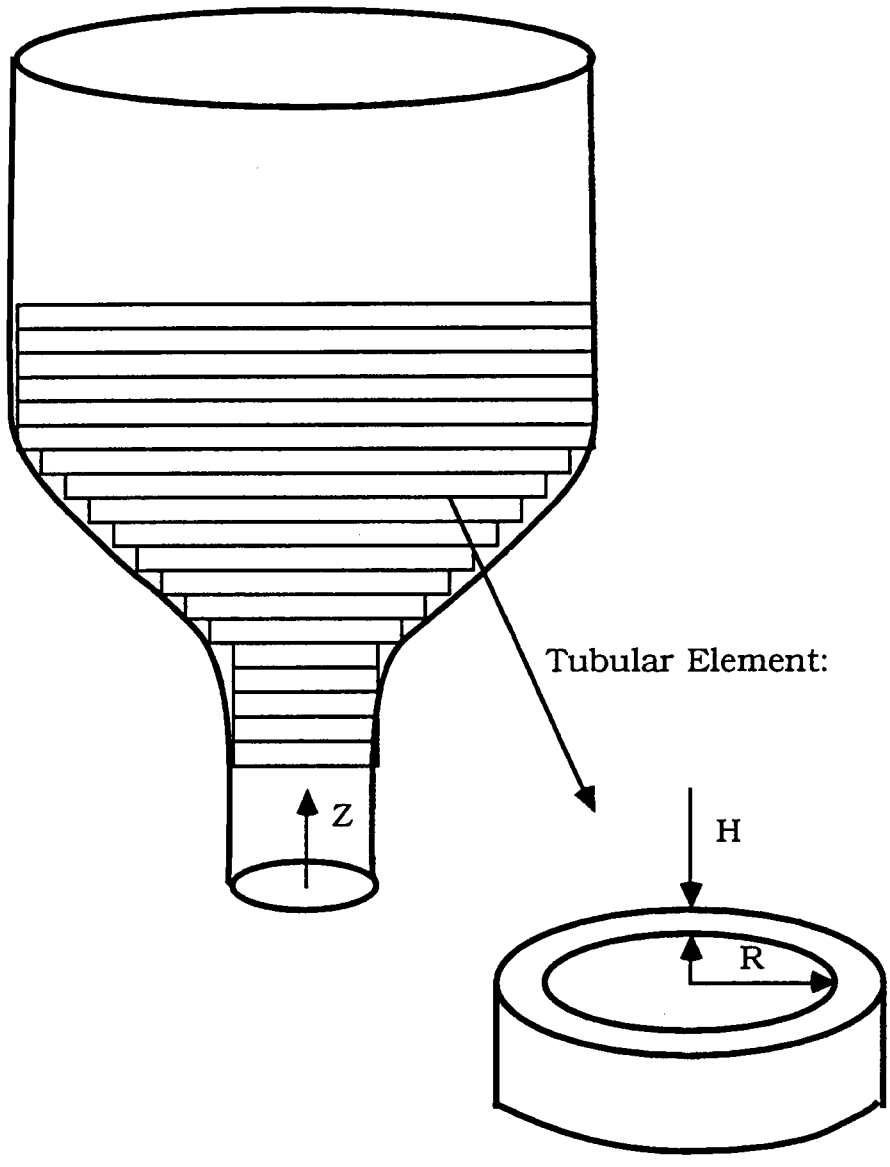

Figure 2-6 Schematic diagram of the modified physical approach to describe the tubular film blowing process.

$$\sigma_{22} = \frac{-\Delta P}{2} - \tau_{33} + \tau_{22} = \frac{-\Delta P}{2} + \eta (d_{22}-d_{33}) \quad (2\text{-}71)$$

The expressions of the deformation rates d_{11}, d_{22}, and d_{33} in three principal directions can be obtained by kinematic analysis for the physical modeel, as shown in Figure 2-6. The detailed derivation was given by Liu [28], and the final equations are expressed as the following.

$$d_{11} = \frac{-Q}{\pi R H} \left(\frac{1}{H} \frac{dH}{dZ} + \frac{1}{R} \frac{dR}{dZ} \right) \quad (2\text{-}72)$$

$$d_{22} = \frac{Q}{\pi R^2 H} \frac{dR}{dZ} \quad (2\text{-}73)$$

$$d_{33} = \frac{Q}{\pi R H^2} \frac{dH}{dZ} \quad (2\text{-}74)$$

Furthermore, the energy balance equation for an unit tubular element can be obtained

$$\rho C_p \left(\frac{Q}{2\pi R} \right) \frac{dT}{dZ} = -U(T-T_{air}) - \varepsilon\sigma(T^4-T_r^4) + \rho \Delta H_f \left(\frac{Q}{2\pi R} \right) \frac{dX}{dZ} \quad (2\text{-}75)$$

if the following conditions are assumed:

(1) Compared with the major heat transfer by convection and radiation, the conductive heat transfer in the film is negligible.

(2) The film is thin enough so that the temperature variation across it can be neglected.

(3) The heat generation due to the frictional force and the viscous dissipation are small enough to be neglected.

Finally, the following system of equations can be obtained on the basis of the above analysis

$$\frac{dH}{dZ} = \frac{-H}{6\eta Q}[\ 2\pi R\Delta P(R+H) + F\ ] \tag{2-76}$$

$$\frac{dR}{dZ} = \frac{R}{6\eta Q}[\ \pi R\Delta P(4R+H) - F\ ] \tag{2-77}$$

$$\frac{dT}{dZ} = -CR(T-T_{air}) - DR(T^4-T_r^4) + FX_fKRH\left(1 - \frac{X}{X_f}\right) \tag{2-78}$$

where

$$C = \frac{2\pi U}{\rho C_p Q} \tag{2-79}$$

$$D = \frac{2\pi\sigma\varepsilon}{\rho C_p Q} \tag{2-80}$$

$$F = \frac{2\pi\Delta H_f}{C_p Q} \tag{2-81}$$

2.7.2 Prediction and Characteristics of the New Model

According to the comparison between prediction of the new model and the on-line data, this new proposed model provides a better agreement with the on-line measured profiles. This obvious improvement can be seen in Figure 2-7, in which the measured and predicted profiles of radius, thickness, velocity and temperature are compared. In Figure 2-7, the solid lines represent the predictions using the new model; the dashed lines show the predictions using the previous model (i.e., the Pearson-Petrie model). In simulation, the take-up force and pressure were used as arbitrary input parameters to allow the calculated final radius to approach to the experimental result.

Besides the semi-quantitative agreement with the data, this new model also successfully correlates the behavior of radius change with two major processing parameters, F and ΔP. Under the assumption of $R >> H$, Equation (2-77) can be simplified to

$$\frac{dR}{dZ} = \frac{R}{6\eta Q}[\ 4\pi R^2 \Delta P - F\ ] \qquad (2\text{-}82)$$

Thus, a dimensionless grouping ($F/4\pi R^2\Delta P$) which governs the nature of subsequent film behavior can be generated from Equation(2-82). If this group is less than unity, the radius

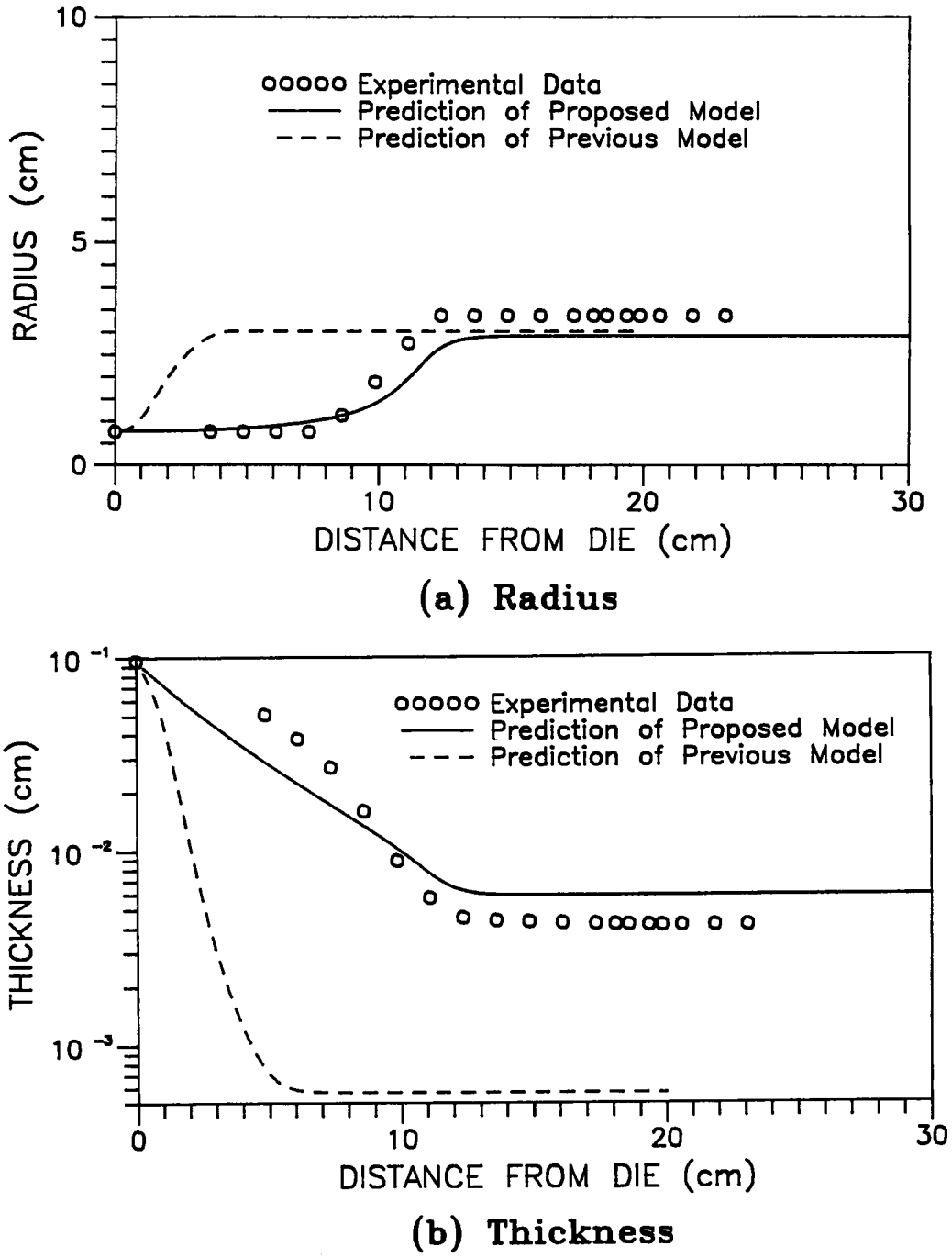

Figure 2-7 Comparisons of the on-line measured data and the predictions of the proposed model and the previous model.

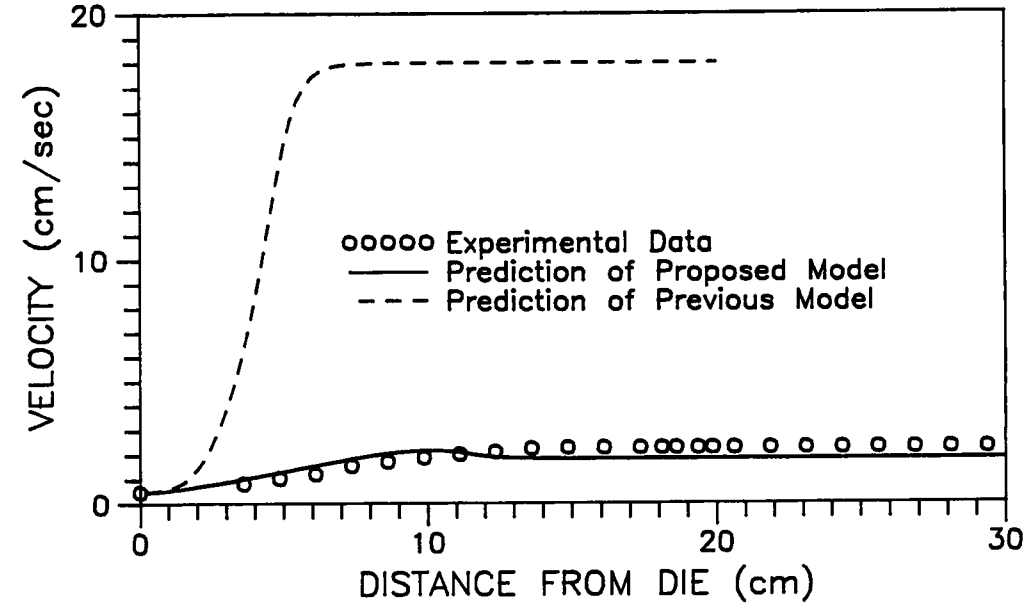

(c) Velocity

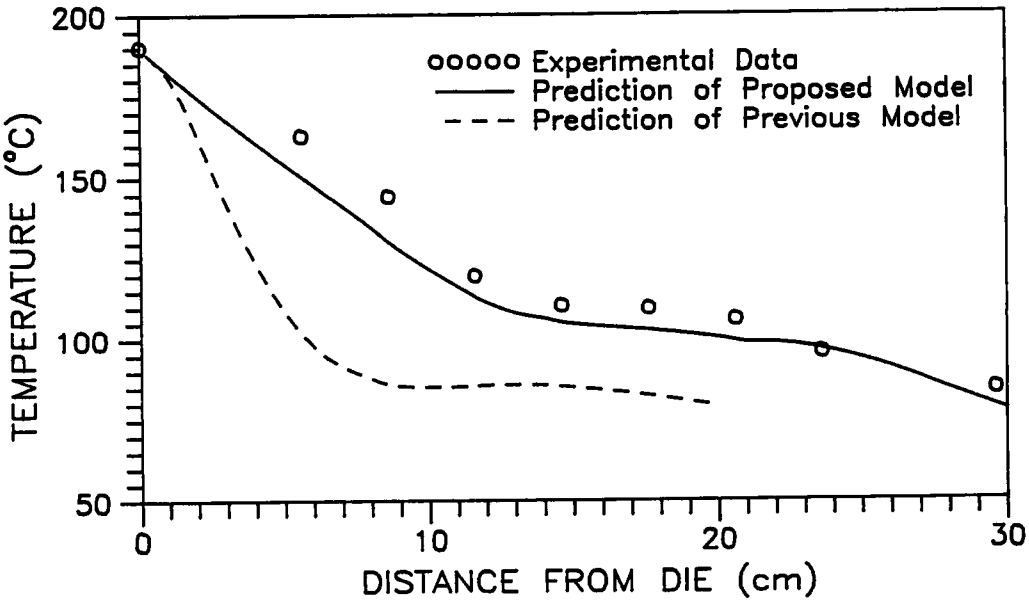

(d) Temperature

Figure 2-7 (Continued)

increases (i.e., the film blows up); if it is equal to unity, the radius remains constant; and if it is greater than unity, radius decreases. Furthermore, from the above statements regarding discussion of the dimensionless group ($F/4\pi R^2\Delta P$), it becomes very obvious that this new model predicts the intuitive effect of inside pressure on radius, rather than the counter-intuitive ΔP effect predicted by the original model.

2.8 SUMMARY

The major advantages of mathematical modelling are to provide deeper understanding of the physical system described as well as to reduce the scope of experiments. Thus, before its corresponding predicted results are accepted, any mathematical model should be tested against experiments qualitatively as well as quantitatively.

For the tubular film blowing process, much effort has been made separately on both the experimental aspects and the mathematical modelling. However, few investigations can provide a complete test of the model against data either qualitatively or quantitatively. Hence, the capability of prediction of the original model first established in the early 1970's is still ambiguous. The first trial to

quantitatively test the original model was carried out by Liu. Owing to several obvious discrepancies between prediction and data being found, a new modified model was proposed in Liu's study. After comparing to experimental results, this proposed new model showed great improvement on the extent of agreement with experimental observations.

CHAPTER 3

EXPERIMENTAL MATERIALS AND PROCEDURES

3.1 MATERIALS

Since polyethylenes are currently the most frequently used resins in blown film extrusion, three different types of polyethylene resins were used: low density polyethylene (LDPE), linear low density polyethylene (LLDPE), and high density polyethylene (HDPE). Each of these resins was supplied by Dow Chemical Company. Several properties of these three resins, including melt flow index, density, weight-average molecular weight $\bar{M}_w$, and number-average molecular weight $\bar{M}_n$, were also supplied by Dow Chemical Company and are summarized in Table 3-1. All of these three polyethylenes have the same melt index of 1.0. These three types of polyethylenes are suitable for use in the tubular film blowing process because of their low melt flow index.

Furthermore, the data of complex viscosity versus deformation rate at various temperatures (i.e., 160 ^{o}C, 170 ^{o}C, 180 ^{o}C and 190 ^{o}C) for the three polyethylenes were also

Table 3-1 Identification and properties of polyethylene resins.

Resin Type	Melt Index	Density (g/cm^3)	$\bar{M}_w$	$\bar{M}_n$	$\bar{M}_w/\bar{M}_n$
LDPE	1.0	0.919	84,100	18,600	4.52
LLDPE	1.0	0.935	109,900	32,100	3.42
HDPE	1.0	0.959	97,800	24,600	3.98

supplied by Dow Chemical Company. Using a parallel-plate oscillatory rheometer, the measured complex viscosity in a frequency (ω) range of 10^{-1} ~ 10^{2} rad/sec are plotted in Figures 3-1, 3-2 and 3-3 for LDPE, LLDPE, and HDPE, respectively. Comparing these three figures, it can be seen that LLDPE shows the least non-linearity in the melt viscosity; LDPE shows the largest degree of deformation-rate thinning.

3.2 EXPERIMENTAL PROCEDURES

3.2.1 Tubular Film Blowing

(A) Apparatus of Blown Film Extrusion

A Kissam single screw extruder (manufactured by Kissam Manufacturing, Inc., Mountainside, NJ), shown schematically in Figure 2-1 in Chapter 2, was used in the film blowing experiments. The diameter of the screw is 3/4 inch (L/D = 20). Just underneath the hopper, the barrel throat is fitted with a cooling water sleeve to prevent the resin from melting too quickly and possibly clogging the feed area. An annular blown film die with an inside diameter of 1.40 cm and an outside diameter of 1.59 cm is mounted on the end of the

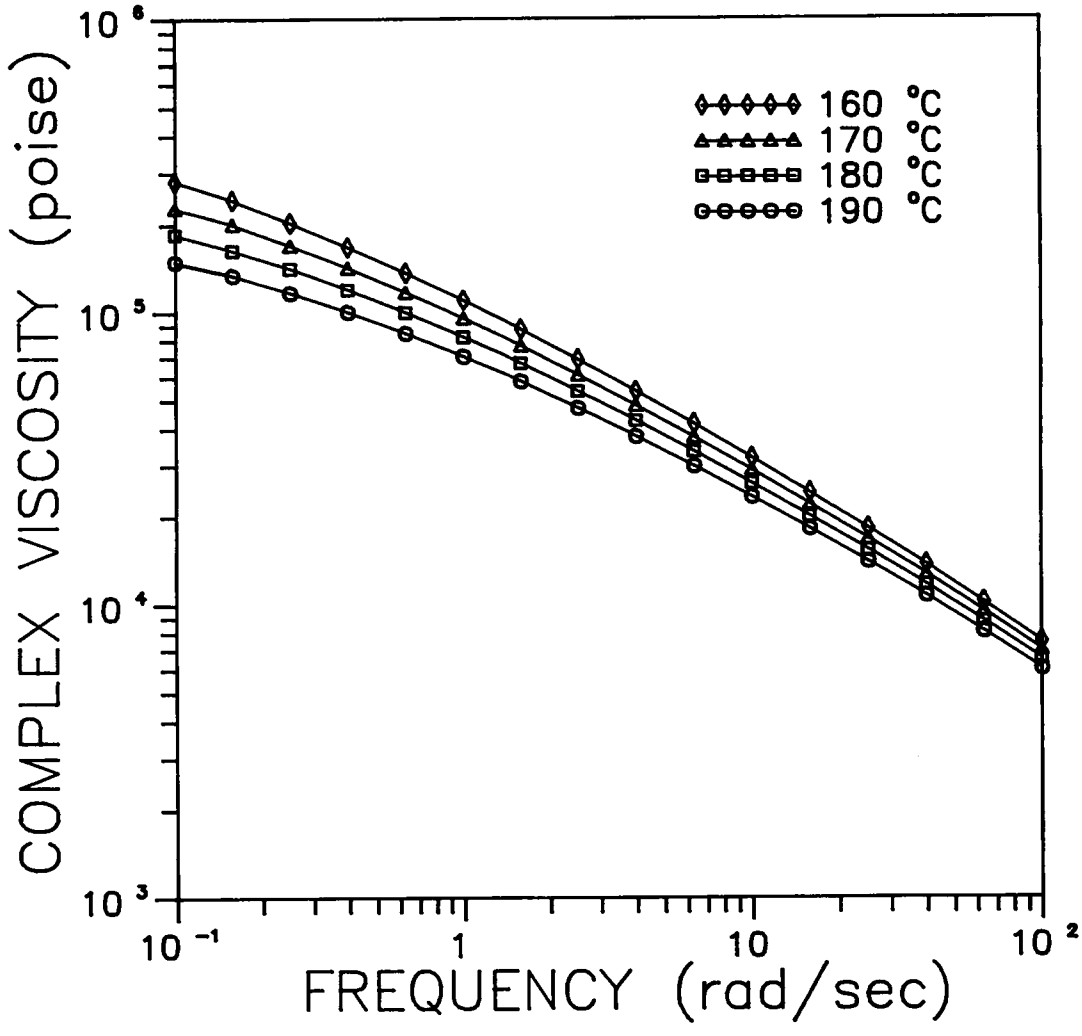

Figure 3-1 Measured complex viscosity of LDPE at various temperatures.

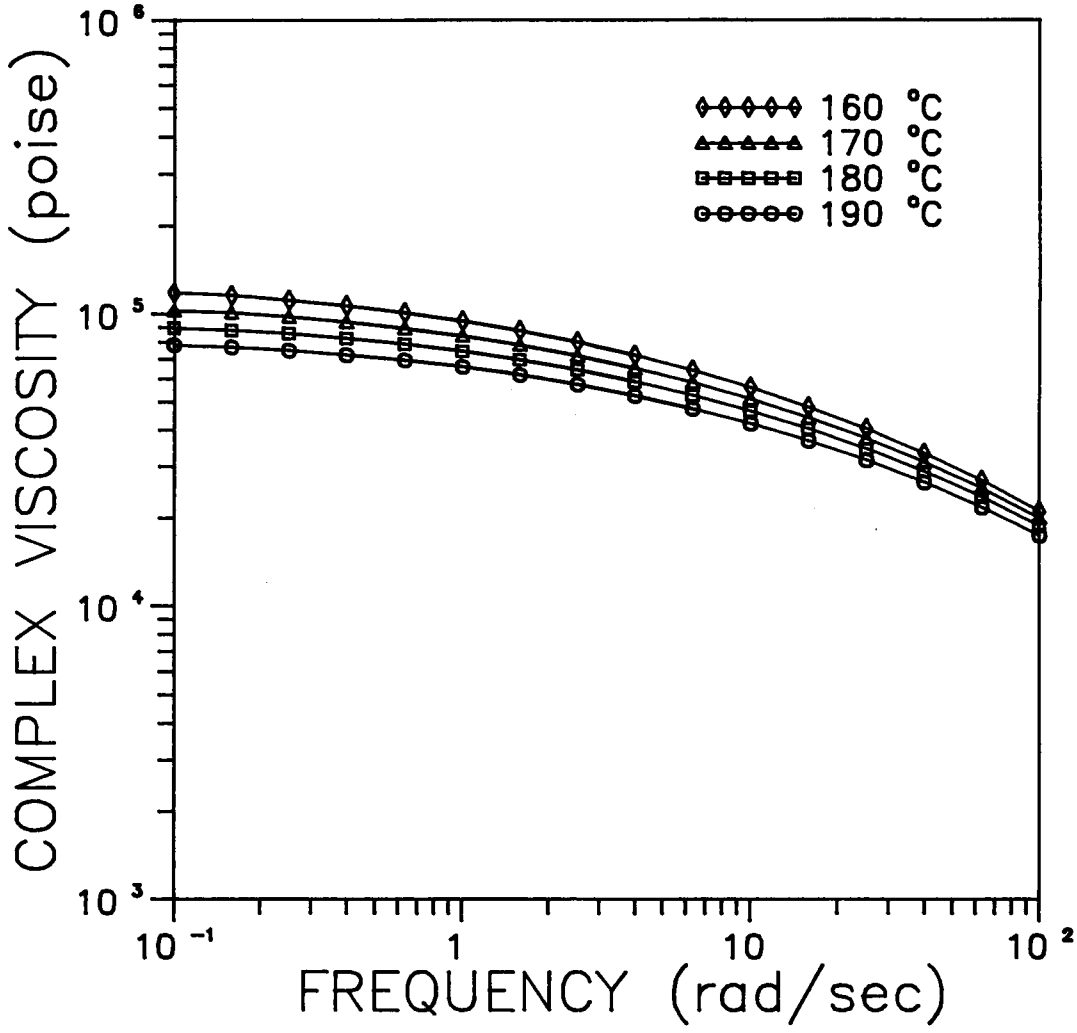

Figure 3-2 Measured complex viscosity of LLDPE at various temperatures.

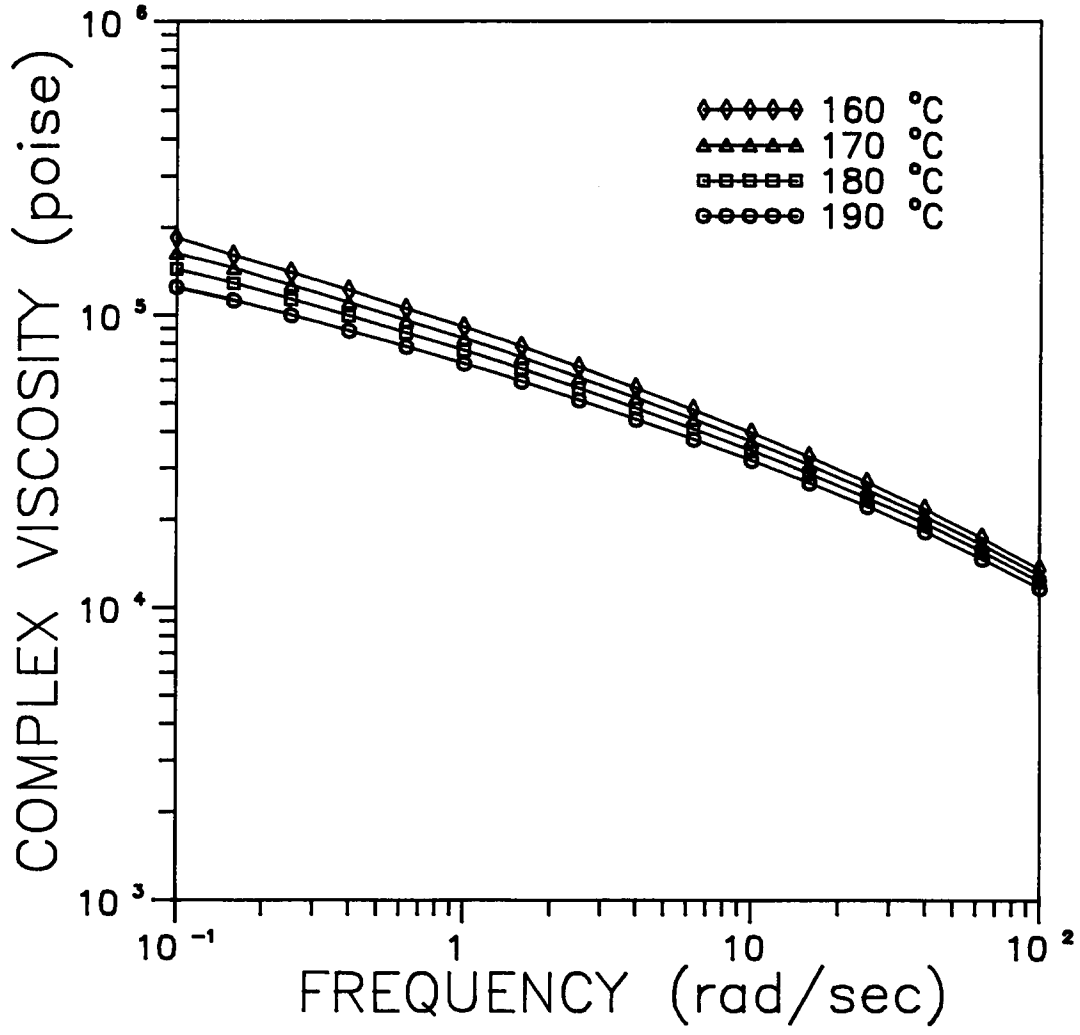

Figure 3-3 Measured complex viscosity of HDPE at various temperatures.

barrel of the screw, and a sketch of this die is given in Figure 3-4.

The temperature inside the barrel is maintained by two independently controlled band-type heaters. For the annular die, two band-type heaters and one heating tape are used to maintain the temperature of the die at the desired extrusion temperature. Also, these heaters are independently controlled by three thermocouples to ensure that the temperature is uniform through the entire die.

In order to cool and solidify the tubular film, an air cooling ring with five-centimeter diameter is installed directly on the top of the annular die. On the top of this equipment a set of nip rolls is used to flatten and seal the bubble to keep the inside inflation pressure constant. Between the nip-roll set and the annular die, several sets of guide rolls are used to make the tubular film pass through the nip rolls smoothly and minimize the possible sliding motion of the bubble. Two sets of take-up rolls, which are able to provide a variable take-up speed, are located beyond the nip-roll set.

During processing, the final velocity and radius of the bubble can be controlled by the speed of the take-up rolls and the amount of inflation air, respectively. The cooling rate

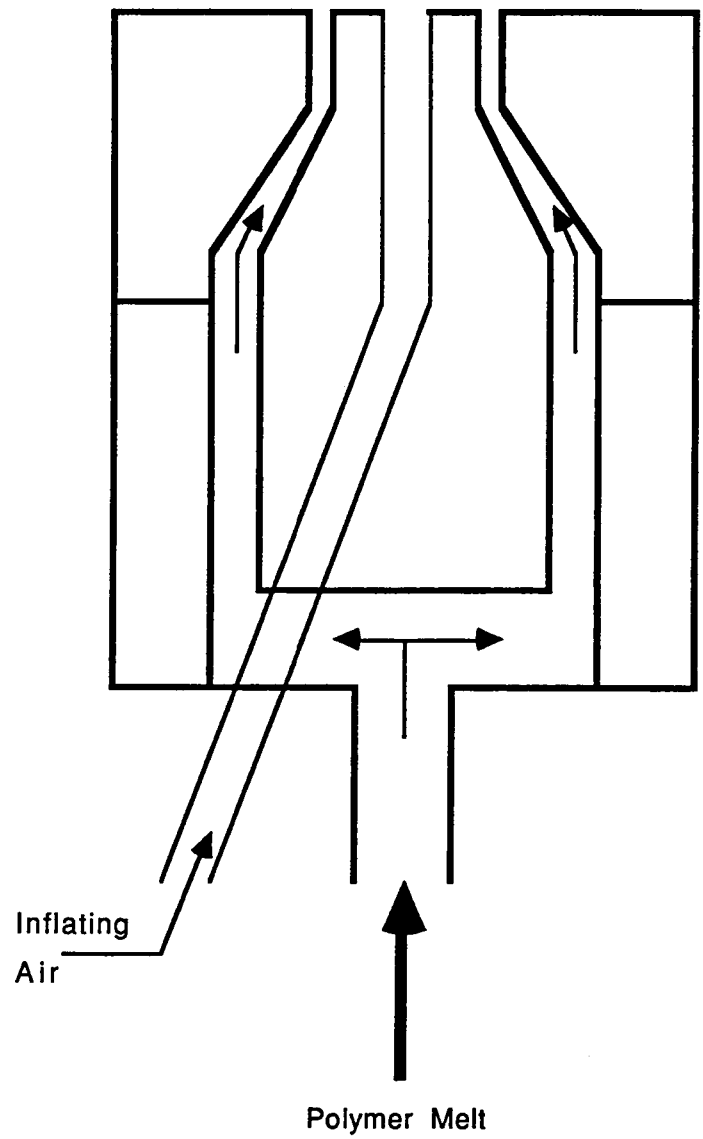

Figure 3-4 Schematic diagram of the annular die.

of the tubular film is controlled by adjusting the flow rate of cooling air.

(B) Film Blowing Procedure

Before starting the extruder, all the heaters were turned on to warm up the machine; the cooling water was circulated in the mean time. It takes approximately one hour to allow the entire system to come to a stable condition and to ensure that all residual polymer in the system has been melted. At the beginning, a very low screw speed and take-up speed were used to allow the melt (without inflation pressure) successfully and smoothly to pass through the entire system. Then, the screw speed and the take-up speed were gradually increased to the desired values; in the mean time, the inflation air was also allowed to enter into the tube until it reached the desired radius.

For the purpose of obtaining a stable bubble under the same processing conditions for all the three polyethylenes, several trial runs were carried out in order to determine appropriate processing parameters. The resulting appropriate processing conditions are summarized in Table 3-2, which includes the temperature of each heating zone in the extruder, the extruder screw speed, the extrusion temperature, the throughput and the flow rate of cooling air. These

Table 3-2 Summary of the processing conditions for the three polyethylenes.

Temperature Settings			Extruder Screw Speed (RPM)	Mass Flow Rate (g/sec)	Cooling Air Volumeric Flow Rate (ft^3/min)
Barrel Region I (^oC)	Barrel Region II (^oC)	Annular Die Zone (^oC)			
140	175	190	28	0.15	4.0

processing parameters were used for the major part of experimental work, that is, the interaction between the take-up ratio, the blow-up ratio and the inflation pressure, and the detailed on-line profiles of bubble. Furthermore, in order to examine the influences of the extrusion temperature and the flow rate of cooling air as well, the values listed in Table 3-2 were varied for certain cases; the details will be given in Chapter 4.

3.2.2 On-line Measurements and Data Collection

The quantities which were measured during processing are the internal pressure and the on-line profiles of radius, thickness, velocity and temperature. The pressure inside the tubular film was measured with an inclined-tube manometer because the pressure difference across the thin film is very small. The profile of the bubble was recorded with a video camera system, which is schematically shown in Figure 2-2 in Chapter 2. The on-line velocity distribution was measured by the video camera tracing technique, which has been described in Section 2.2.3 in Chapter 2; and its measuring procedures are summarized in Figure 3-5. The temperature profile of the tubular film was measured with a remote infrared sensing technique which was discussed in detail in Chapter 2. A Hughes PROBEYE 3300 thermal imaging system, whose measuring

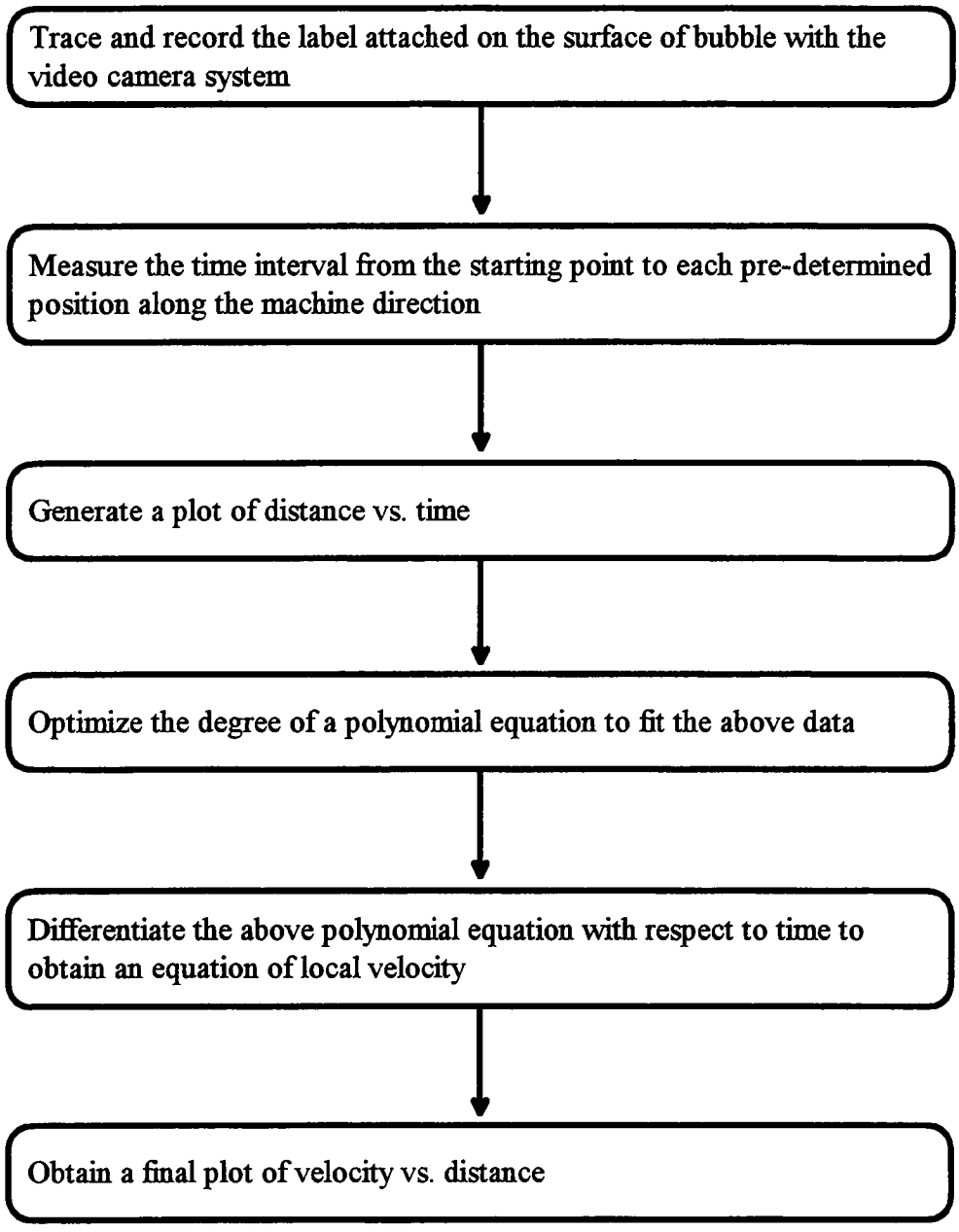

Figure 3-5 Flow chart of the procedures for determining the on-line velocity profile.

range is from -20 °C to 950 °C [88], was used for the temperature measurement; and the experimental setup is schematically shown in Figure 3-6. Based on the results of theoretical analysis, Equations(2-16), (2-17) and (2-18), the corresponding measuring procedures are summarized in the flow chart as shown in Figure 3-7. Finally, the local thickness variation along the machine direction was obtained by the continuity equation, Equation(2-1) in Chapter 2, incorporated with the on-line measured radius, velocity, mass flow rate and temperature (which was used to estimate the temperature-dependent density of the melt via Equation(2-2)).

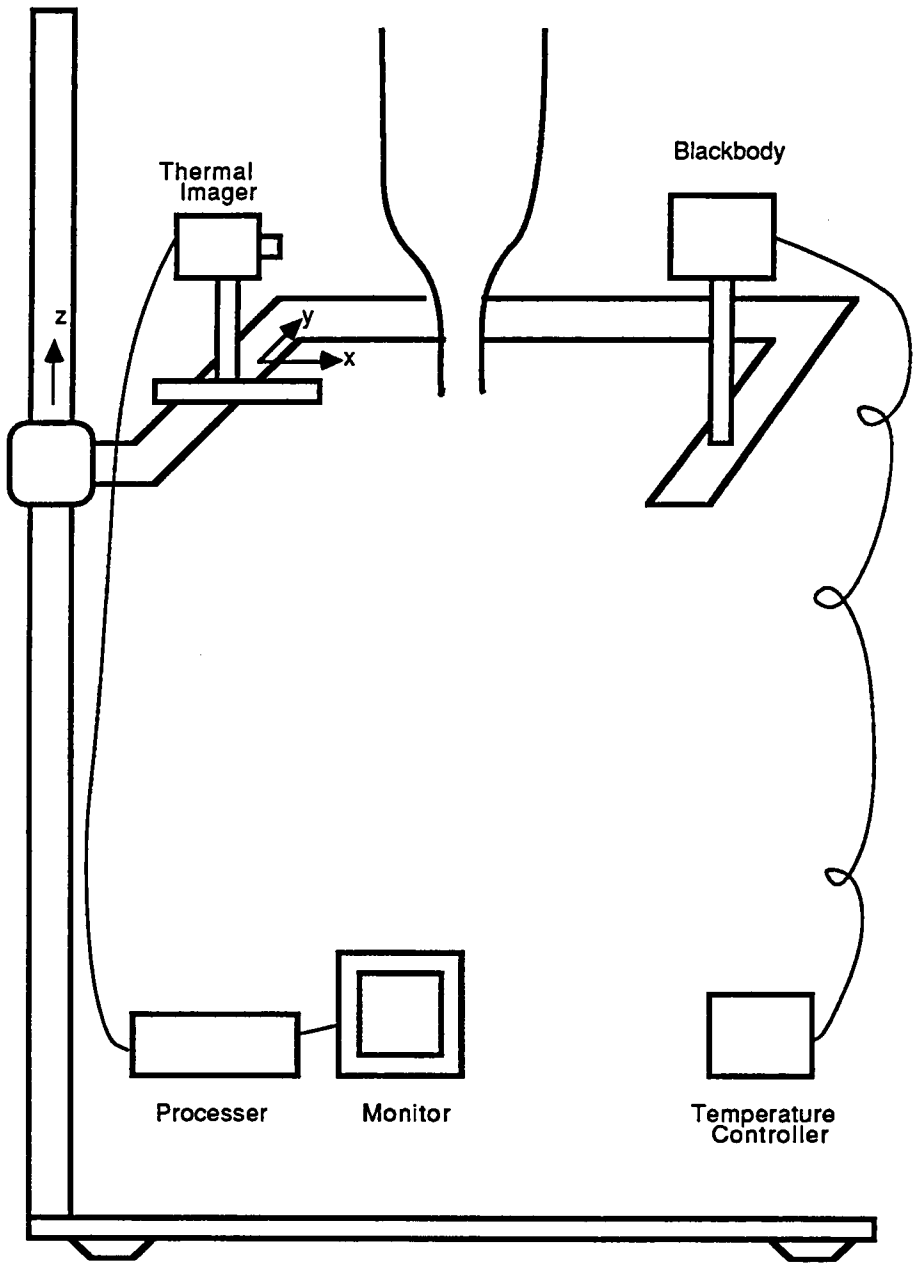

Figure 3-6 Schematic diagram of on-line temperature measurement in the tubular film blowing process.

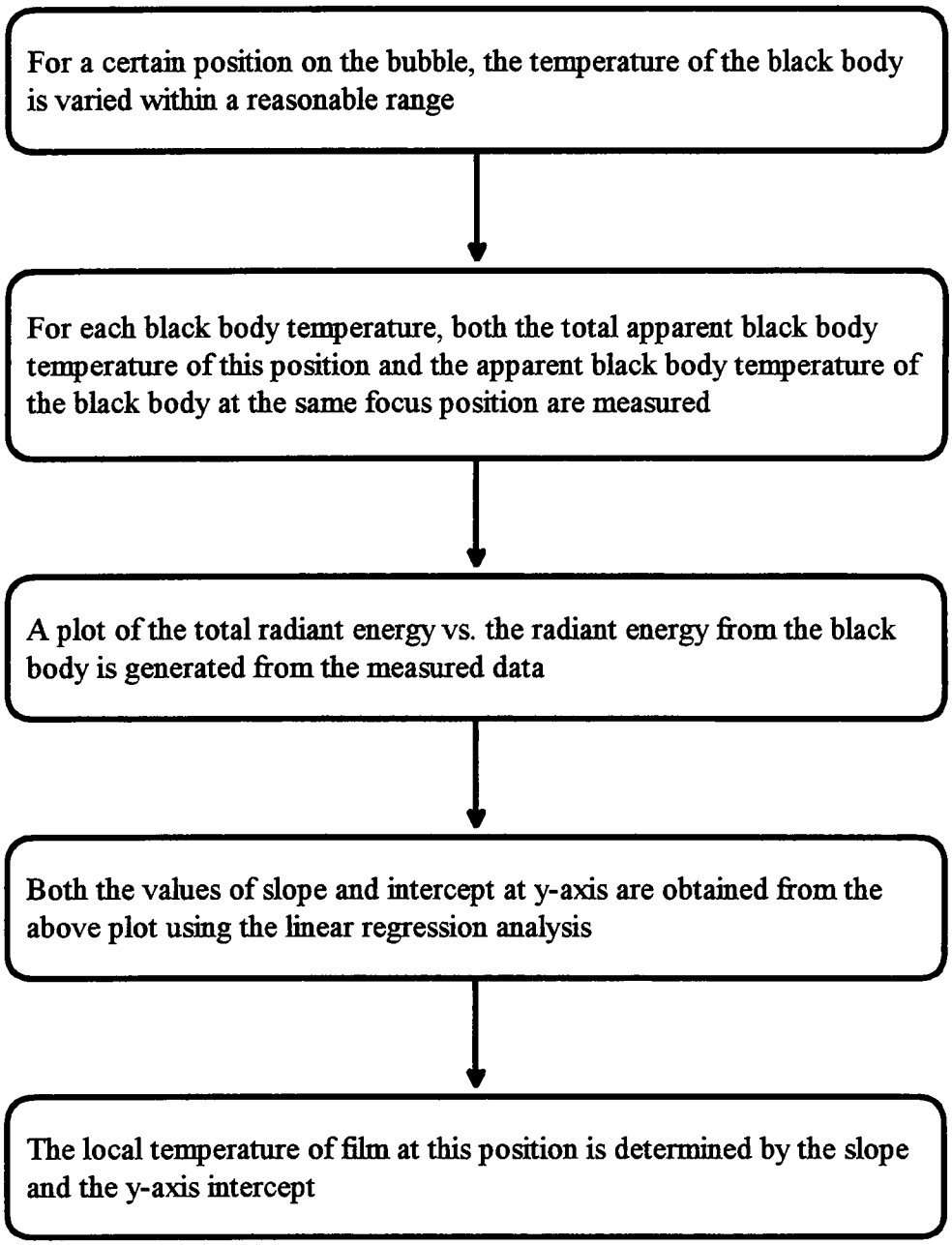

Figure 3-7 Flow chart of the procedures for determining the on-line temperature distribution.

CHAPTER 4

EXPERIMENTAL RESULTS

Using the measuring techniques described in Chapter 3, inflation pressure, on-line profiles of radius, velocity and temperature for three polyethylene resins (that is, LDPE, LLDPE, and HDPE, as listed in Table 3-1) were measured under the processing conditions, as summarized in Table 3-2. The processing conditions shown in this table were used for the major part of the experimental investigations: the effect of the inflation pressure and the take-up ratio on the blow-up ratio for three polyethylenes, and the detailed on-line profiles of the bubbles for LDPE and LLDPE. Moreover, in order to examine the influences of the extrusion temperature and the flow rate of cooling air as well, the values listed in Table 3-2 were varied for some certain cases; the details will be given later.

These experimental results can provide a better understanding of the tubular film blowing process. The behavior of the bubble under this broad range of processing

conditions will be described and discussed in the following sections.

4.1 INFLUENCE OF INFLATION PRESSURE

Inflation pressure is one of the most important processing parameters. It controls the variation of extensional stresses and bubble radius during processing and also determines the ultimate radius of the tubular film. For three different polyethylenes, LDPE, LLDPE and HDPE, the pressure difference across the thin film, ΔP, was measured under the conditions of various take-up ratios (TUR) as well as various blow-up ratios (BUR). The ranges of take-up ratios and blow-up ratios, which were varied, are limited by the stability of the bubble. Under various fixed take-up ratios, the curves of blow-up ratio versus measured ΔP for LDPE, LLDPE and HDPE are shown in Figures 4-1, 4-2 and 4-3, respectively. Examining all these curves, it is found that most of the results show the "intuitive" effect of ΔP on the blow-up ratio; that is, a higher inflation pressure produces a larger bubble. Only in a few cases, especially in the region of high blow-up ratio and high take-up ratio, the data show a slight inverse influence of ΔP on the radius of the bubble; that is,

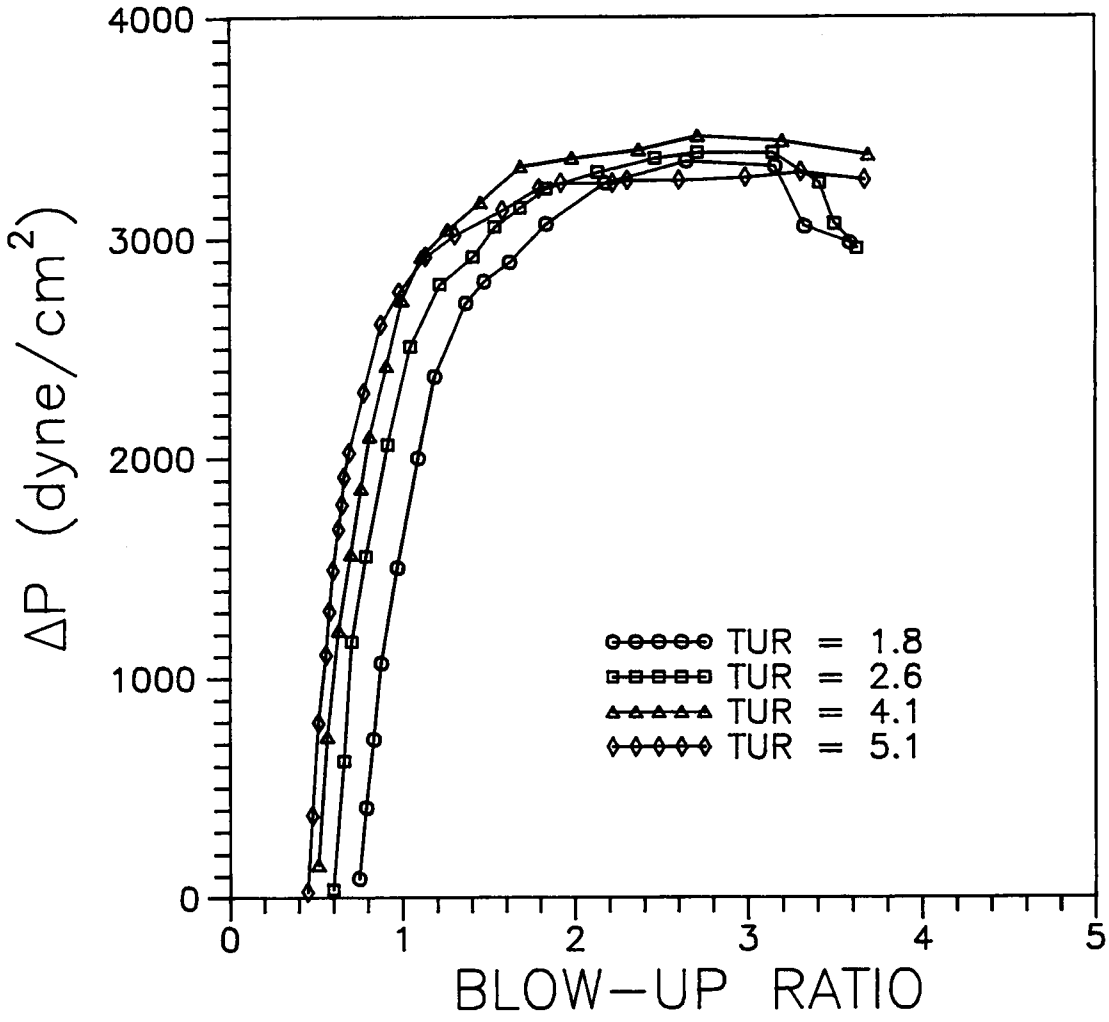

Figure 4-1 Experimentally observed relationship between inflation pressure and blow-up ratio at various take-up ratios for LDPE resin.

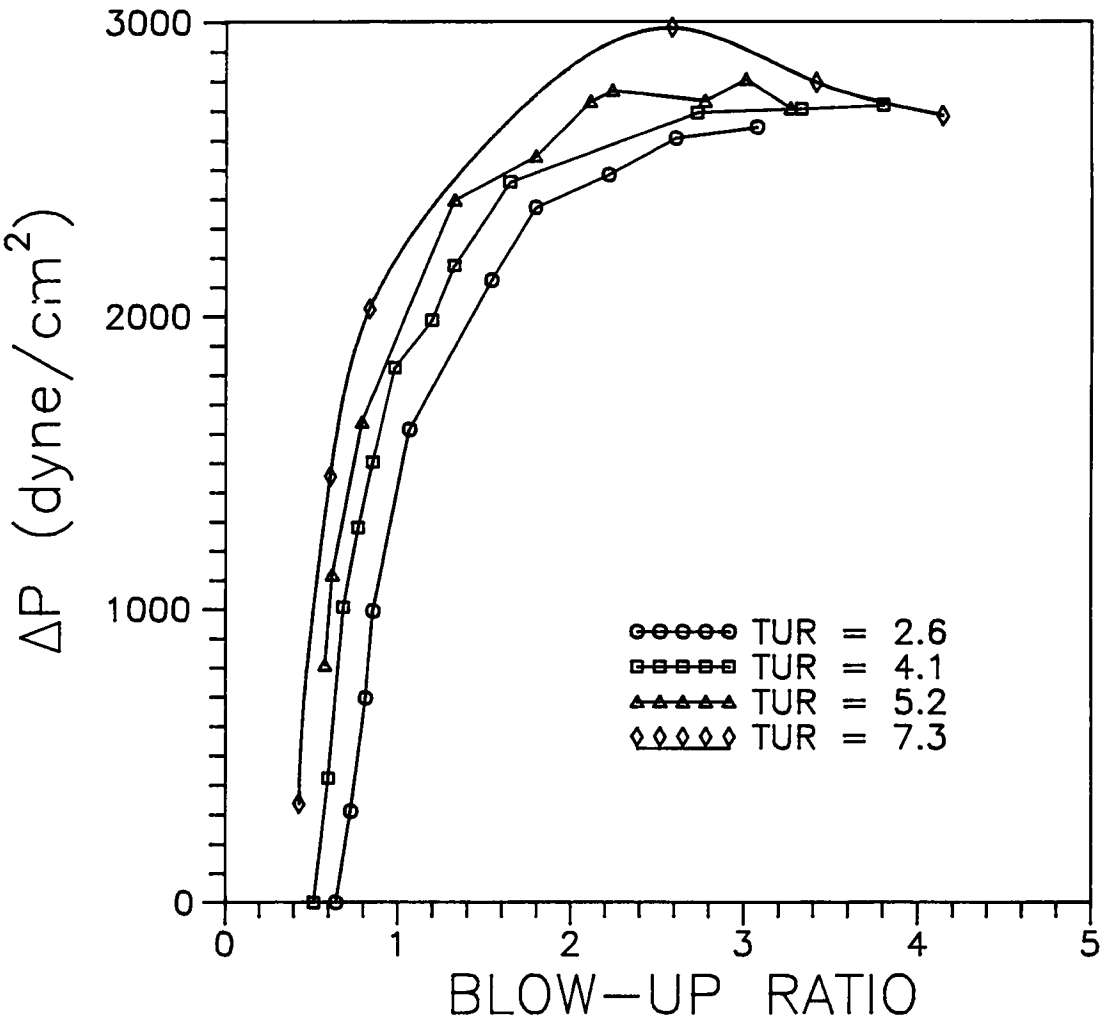

Figure 4-2 Experimentally observed relationship between inflation pressure and blow-up ratio at various take-up ratios for LLDPE resin.

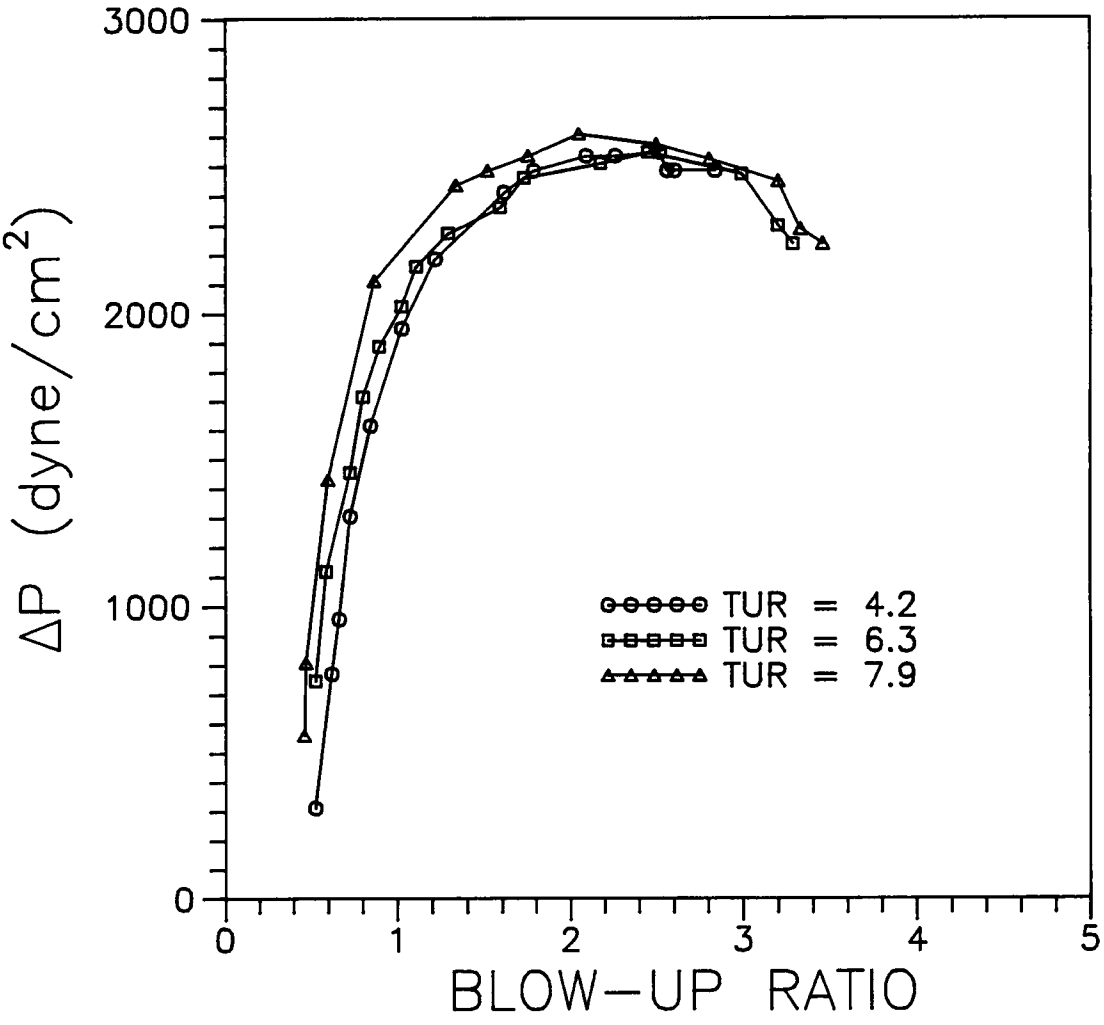

Figure 4-3 Experimentally observed relationship between inflation pressure and blow-up ratio at various take-up ratios for HDPE resin.

an increase in the radius of bubble corresponds with a slight decrease in the measured pressure. This "counter-intuitive" pressure effect is most likely due to the effect of deformation thinning. The phenomenon of deformation thinning nature of polymer melts during processing has been reported [89-91]. For example, for Nylon 6 the computed spinline elongational viscosity is lower than the Trouton viscosity data [92] in Patel's investigation [91]; the same observation for polypropylene was also reported in Hajji's study [40]. This reasoning will be further supported in the following chapter from a theoretical point of view.

Further, comparing the blow-up ratio (BUR) versus ΔP curves for three polyethylenes, it can be seen that the shapes of the curves, qualitatively speaking, are very similar to each other. In the region of low blow-up ratios, generally smaller than about 1.5, all of the curves are very steep; in other words, to obtain a larger final radius the inflation pressure must be increased steeply. However, for the cases of higher blow-up ratios, usually beyond 1.5, the final radius is becoming more sensitive to the increase of pressure. Hence, slopes of these curves decrease rapidly, and a near plateau shape is observed. Furthermore, quantitatively speaking, all of the measured BUR vs. ΔP curves for the three polyethylenes are of the same order of magnitude. This is not surprising

because these three polyethylenes all have the same melt flow index, 1.0, as shown in Table 3-1.

4.2 INFLUENCE OF TAKE-UP RATIO

From the order of the curves in Figures 4-1, 4-2 and 4-3, it can be found that the BUR vs. ΔP curves shift upwards with increasing take-up ratio. In other words, at higher take-up ratios, a higher inflation pressure is required to reach the same blow-up ratio. This is due to a competition between stretching in the machine direction and extension in the hoop direction. Under the restriction of the continuity equation, as expressed in Equation(2-1), the higher velocity of a film results from a decrease of the thickness and radius of the tubular film. Therefore, in order to maintain the same blow-up ratio at higher take-up speeds, a higher inflation pressure is required.

It should be noticed that for LDPE at TUR = 5.1 a part of the measured BUR vs. ΔP curve (the part of curve with higher blow-up ratios) crosses over the others instead of shifting upwards, as shown in Figure 4-1. This is probably due to the influence of deformation thinning of the viscosity.

This reasoning will be discussed further in the following chapter.

4.3 INFLUENCE OF EXTRUSION TEMPERATURE

Extrusion temperature affects the properties of the melt at the die exit (such as melt viscosity), and the processing conditions that are needed to reach a desired final radius. To understand these effects, three different die temperatures, 170 ^{o}C, 190 ^{o}C and 210 ^{o}C, were chosen. In this experiment LDPE was used and the take-up ratio is fixed at 2.6. Under these three different extrusion temperatures, the final film radii and the required inflation pressures are shown in Figure 4-4. As shown in Figure 4-4, to reach a certain blow-up ratio, the required inflation pressure (or pressure difference, ΔP) is higher as one decreases the die temperature. In other words, with a fixed inflation pressure, a larger film can be obtained by increasing the extrusion temperature. This is due to the strong dependence of melt viscosity on temperature: the higher temperature, the lower viscosity. Furthermore, comparing the three curves in Figure 4-4, it can be found that an extrusion temperature of 210 ^{o}C provides a wider processing window than the other two; that

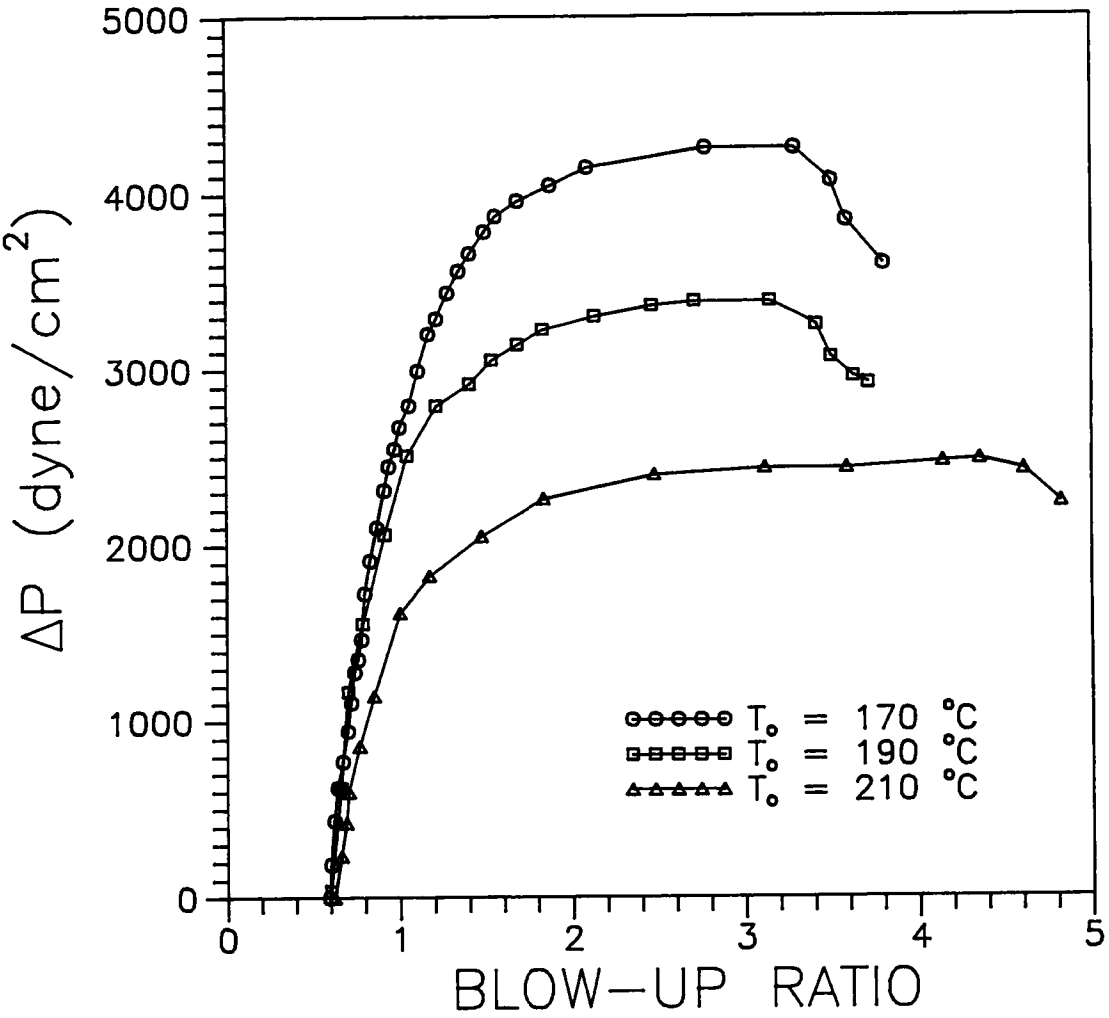

Figure 4-4 Experimentally observed relationship between inflation pressure and blow-up ratio at various extrusion temperatures for LDPE resin.

is, among the three temperatures, the temperature of 210 ^{o}C is able to produce a larger stable film. It should also be noticed that even under various extrusion temperatures, most of the experimental results still show an "intuitive" pressure effect on the radius, except that at the extreme right of the curves a slight inverse pressure effect can be seen. This feature is very similar to that of Figures 4-1, 4-2 and 4-3.

4.4 INFLUENCE OF FLOW RATE OF COOLING AIR

The cooling rate is another of the important processing parameters. As described in the previous chapter, the entire tubular film is cooled by air from a cooling ring and the cooling rate can be controlled by adjusting the flow rate of air. To understand the effect of air flow rate on the relationship between pressure and blow-up ratio, two different volumetric flow rates of cooling air, 3.5 and 4.0 ft^3/min, were chosen. The influence of the air flow rate on inflating the film is shown in Figure 4-5. This figure indicates that the flow rate of cooling air has a significant influence on the inflation pressure (in the region of the blow-up ratio larger than one); that is, to reach a certain blow-up ratio, a higher inflation pressure is required for the case with a

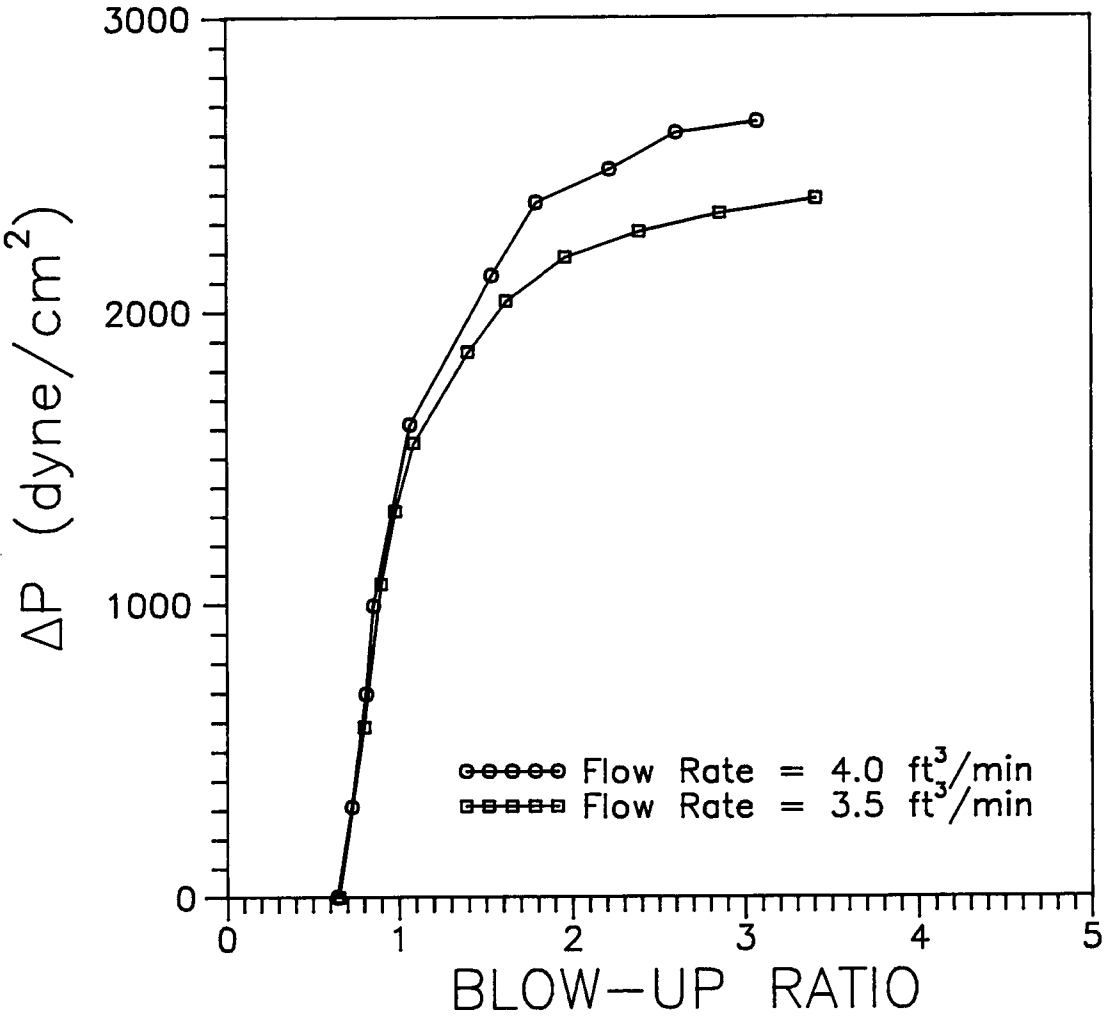

Figure 4-5 Experimentally observed relationship between inflation pressure and blow-up ratio under two different flow rates of cooling air for LLDPE resin.

higher air flow rate. This is attributed to the fact that increasing the air flow rate causes the convective heat transfer to be higher. An increase of the heat transfer coefficient with air flow rate has been reported by Kanai and White [14]. Therefore, it becomes clear that a higher cooling rate will result in a higher melt viscosity (which is strongly temperature dependent), hence a higher inflation pressure is required. Furthermore, according to the energy balance, as expressed by Equation(2-51), the influence of the heat transfer coefficient (U) on the cooling rate ($\frac{dT}{dZ}$) is enhanced by an increase of the bubble radius (R). Thus, this reasoning can be used to explain that there is not detectable difference between two curves in the region of low blow-up ratio (BUR < 1), as shown in Figure 4-5.

4.5 ON-LINE PROFILES OF THE TUBULAR FILMS

Two polyethylenes, LDPE and LLDPE, were used in the measurements of detailed profiles of certain on-line quantities, namely, radius, thickness, temperature and velocity. The measuring techniques described in Chapter 3 were followed for collecting these on-line data; the processing conditions summarized in Table 3-2 were used to

produce three basic film shapes: BUR < 1 (especially $\Delta P = 0$), BUR ≈ 1, and BUR > 1. These three different bubble shapes are defined as case(A), case(B), and case(C), respectively; they will be referred to in the following discussion. For LDPE and LLDPE, the measured on-line profiles of radius, velocity, temperature and thickness of these three cases are given and discussed in the following sections.

4.5.1 Radius

The radius profiles measured under different conditions of blow-up ratio are shown in Figures 4-6 and 4-7 for LDPE and LLDPE, respectively.

For the case of no inflation pressure ($\Delta P = 0$ dyne/cm^2), case(A), the radius profiles of both polyethylenes decrease; that is, the tubular films are contracted by drawing in the machine direction. For the second case, case(B), BUR ≈ 1, a small inflation pressure (i.e., 1590 and 1242 dyne/cm^2 for LDPE and LLDPE, respectively) is required to prevent significant contraction in the hoop direction; also the curves show that the radii are almost constant. For the third case, case(C), BUR > 1 (in which even higher pressures were applied: 3477 and 2608 dyne/cm^2 for LDPE and LLDPE, respectively), it can be observed that the melt comes from the annular die in the shape of a "tube" and the radii remain approximately

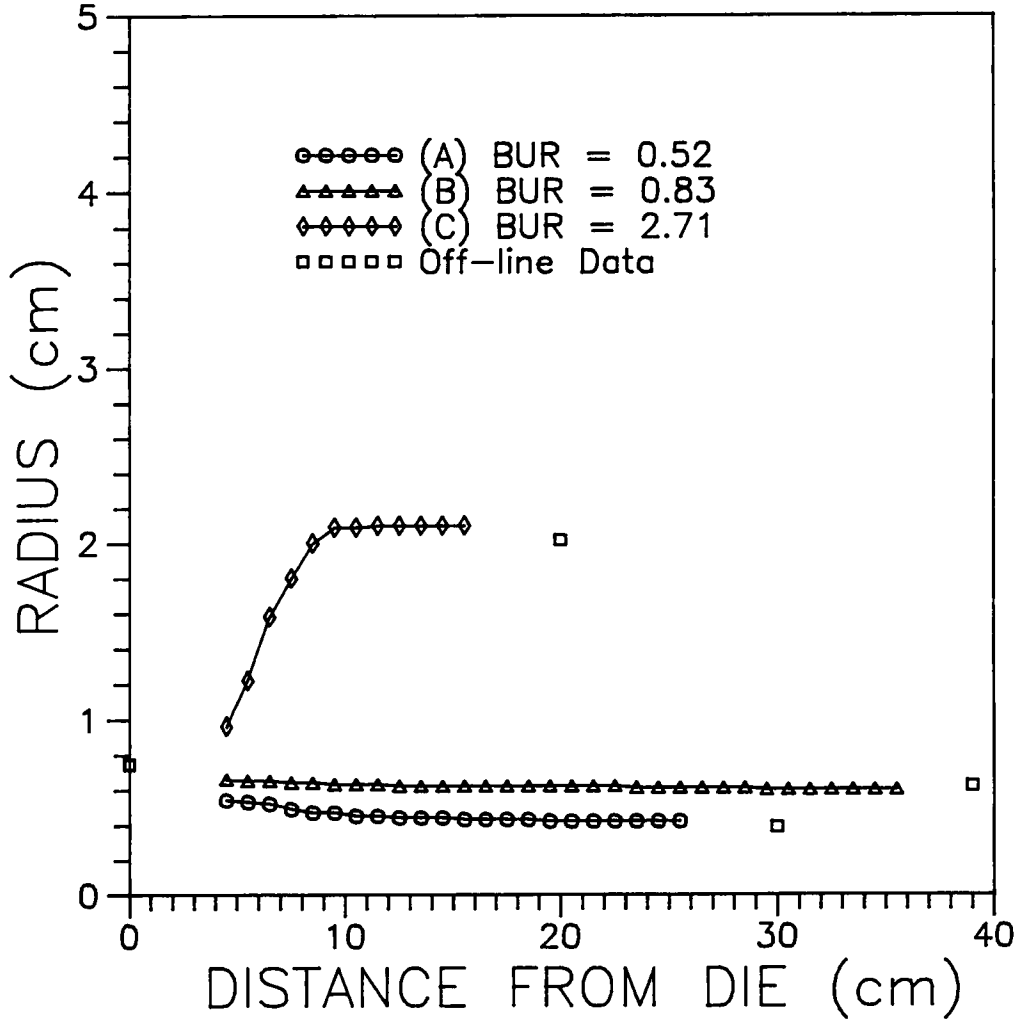

Figure 4-6 On-line measured radius profiles for the three cases for LDPE resin.

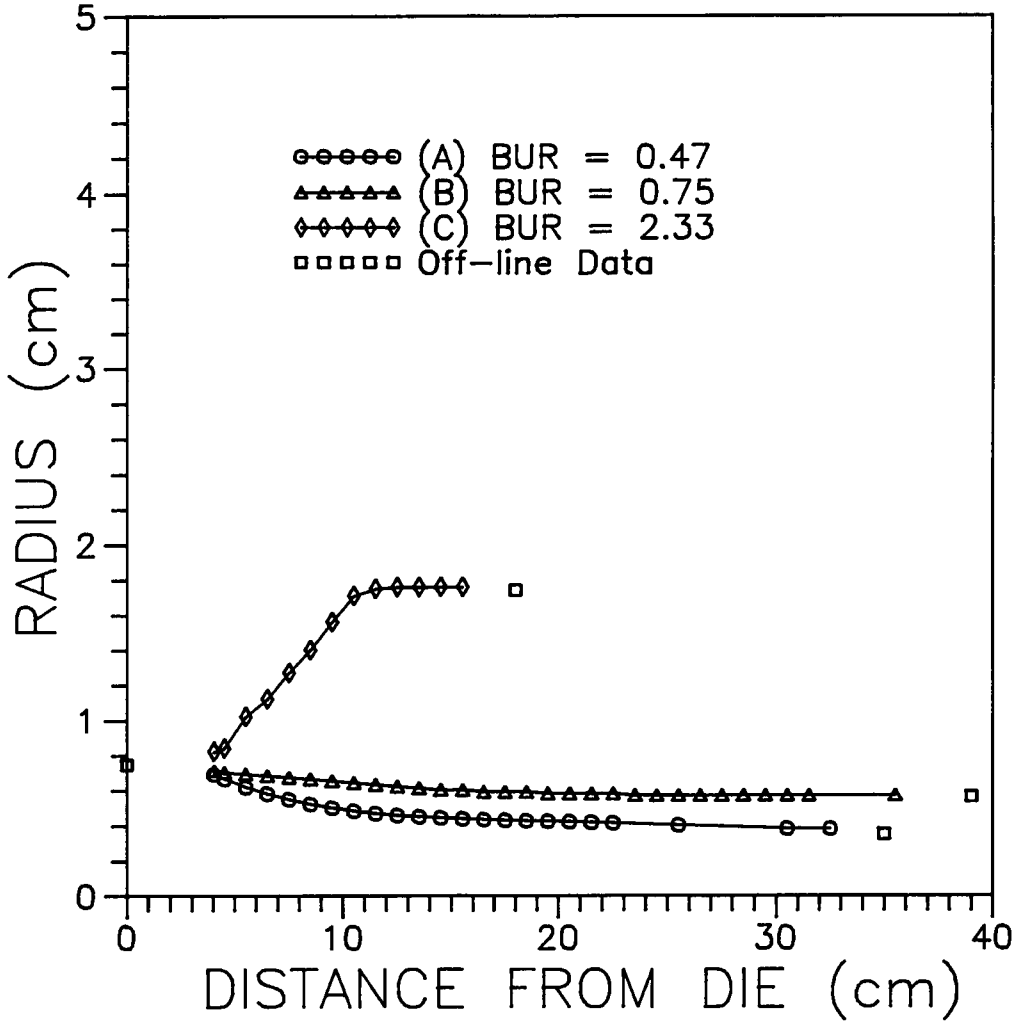

Figure 4-7 On-line measured radius profiles for the three cases for LLDPE resin.

constant up to a short distance; then the radii start to increase. Qualitatively speaking, there is no basic difference between LDPE and LLDPE as to the shape of the bubble.

Furthermore, it should be noticed that all these six runs were carried out at the same pre-set take-up speed, that is, 1.6 cm/sec. Hence, associating the applied inflation pressures with the resulting radius profiles and blow-up ratios, it can be seen that the shape of the film is primarily controlled by competition between the extension in the machine direction and in the circumferential direction.

Finally, the accuracy of the on-line measured radius profiles can also be examined in Figures 4-6 and 4-7. In each figure the square symbol at the left (at Z = 0 cm) is the radius of the annular die; the square symbol on the right side of each curve represents the directly measured final radius of each film (that is, the off-line data). Hence, it can be seen that the on-line measured initial and final radii are in good agreement with the directly measured values.

4.5.2 Velocity

The velocity variations along the machine direction for the three shapes of films (with different blow-up ratios) are plotted in Figures 4-8 and 4-9 for LDPE and LLDPE, respectively.

Generally speaking, all the velocity curves shown in Figures 4-8 and 4-9 indicate that the film velocity increases rapidly immediately after the die under the influence of the take-up force; then they remain constant after reaching the take-up speed. With further inspection, it can be seen that films with higher blow-up ratios have steeper velocity curves before reaching the plateau, which is the pre-set take-up speed (the same in all cases). In other words, the blow-up ratio is not only directly related to the radius profile (as described in the preceding section, Section 4.5.1) but also has a significant effect on the local velocity in the machine direction (even under the same take-up conditions). This phenomenon is most likely due to the fact that the position of the frost-line varies with the ultimate bubble radius. As reported in the literature [14,26,93], the height of the observed frost line decreases with an increase in blow-up ratio. This phenomenon was also observed in the present study, as shown in Figure 4-10. Furthermore, as indicated in the author's prior study [28] and other investigations

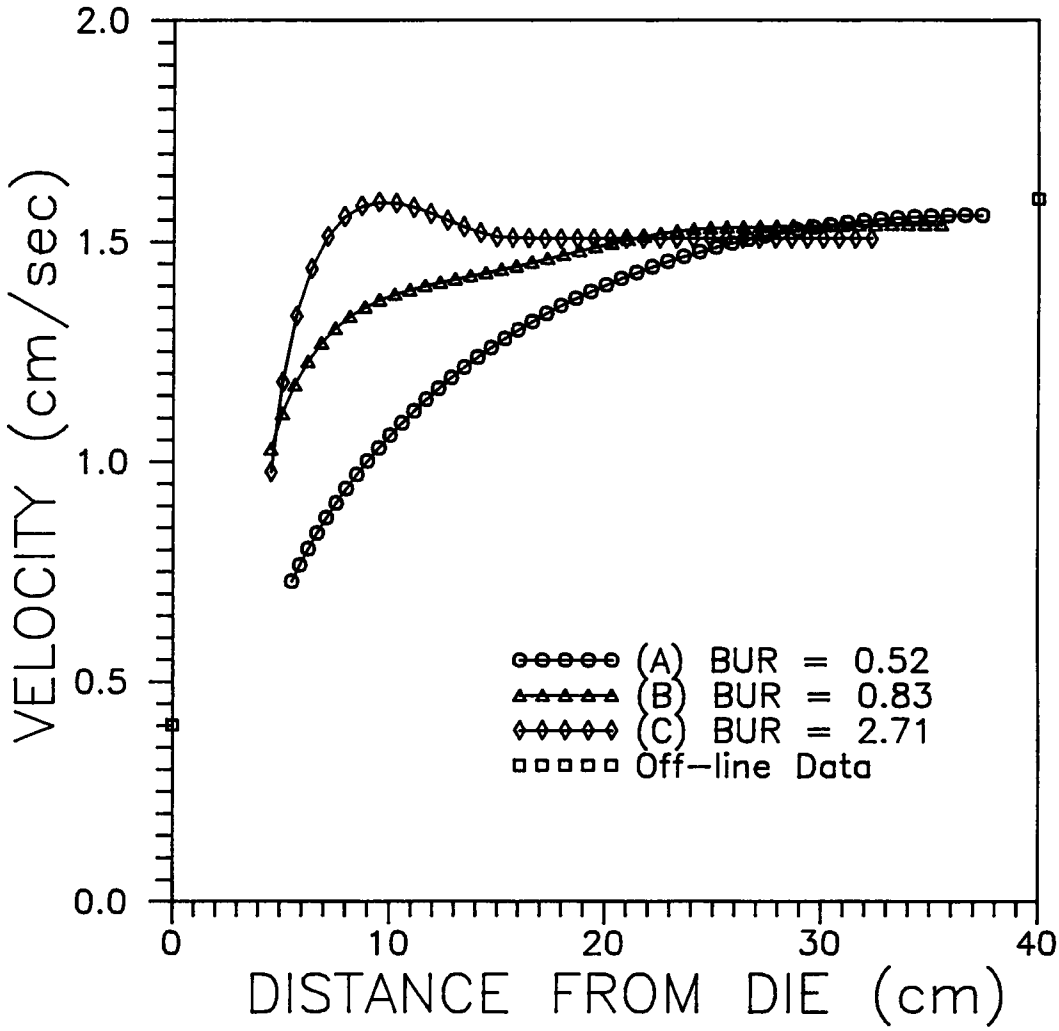

Figure 4-8 On-line measured velocity profiles for the three cases for LDPE resin.

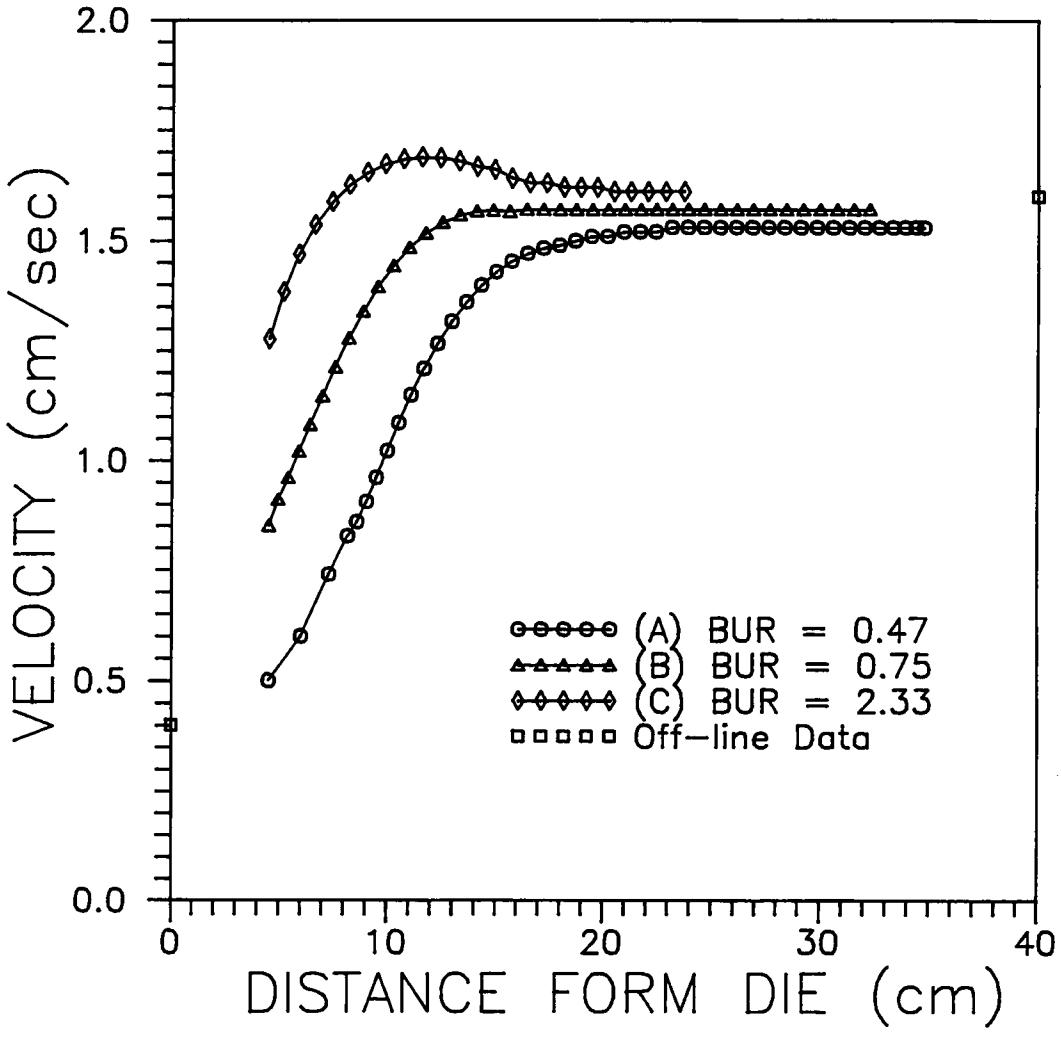

Figure 4-9 On-line measured velocity profiles for the three cases for LLDPE resin.

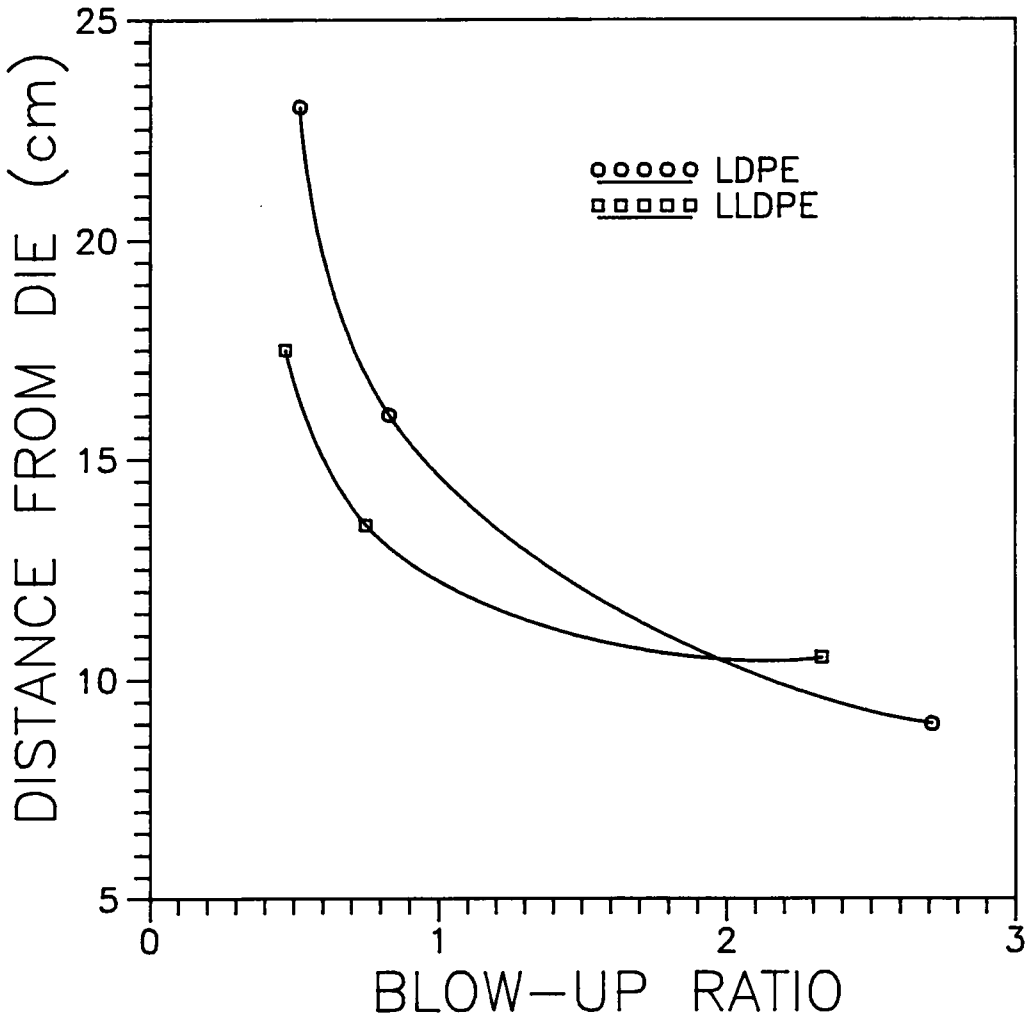

Figure 4-10 On-line observed relationship between the frost line height and the blow-up ratio for LDPE and LLDPE resins.

[14,26,63,94], no significant change in the radius, thickness or velocity was seen beyond the frost line. Therefore, in order to reach a pre-set take-up speed before solidification, a larger bubble, which has a lower frost line, requires a larger initial rate of change of velocity.

Finally, beside providing information on the velocity, both Figures 4-8 and 4-9 show that the on-line measured velocity profiles are reliable. Both figures show that the on-line velocity curves fall between two boundary conditions: the velocity at the die exit (Z = 0 cm), shown by the square symbol at the left, is the initial velocity obtained by calculation from the known flow rate; the square symbol on the right side represents the pre-set take-up speed.

4.5.3 Temperature

The on-line temperature profiles with different blow-up ratios are shown in Figures 4-11 and 4-12 for LDPE and LLDPE, respectively. Both figures show that the cooling rate increases with an increase of blow-up ratio. However, it should be emphasized that each case has the same volumetric flow rate of cooling air, that is, 4.0 ft^3/min. Therefore, the observed increase in the cooling rate with the blow-up ratio is due to an increase in the outside bubble surface area, an important parameter in heat transfer.

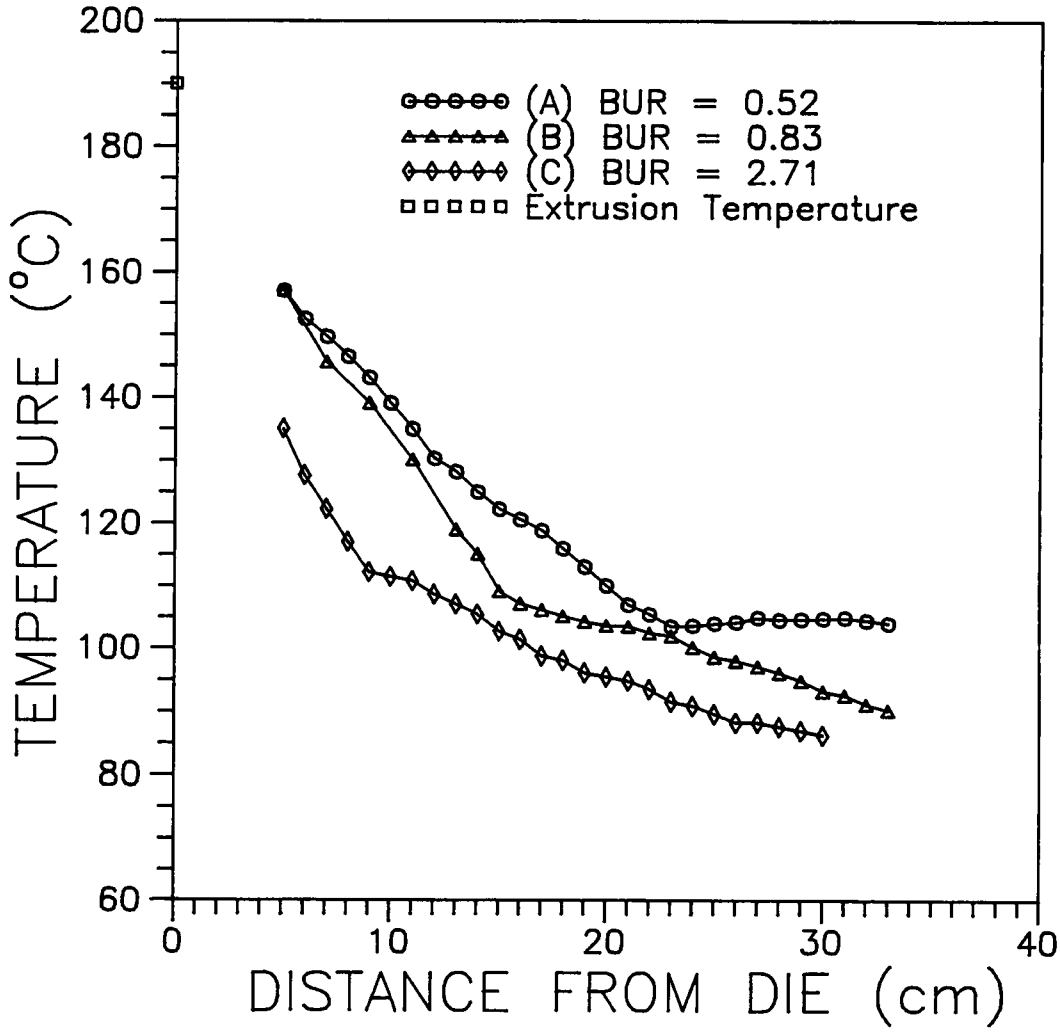

Figure 4-11 On-line measured temperature profiles for the three cases for LDPE resin.

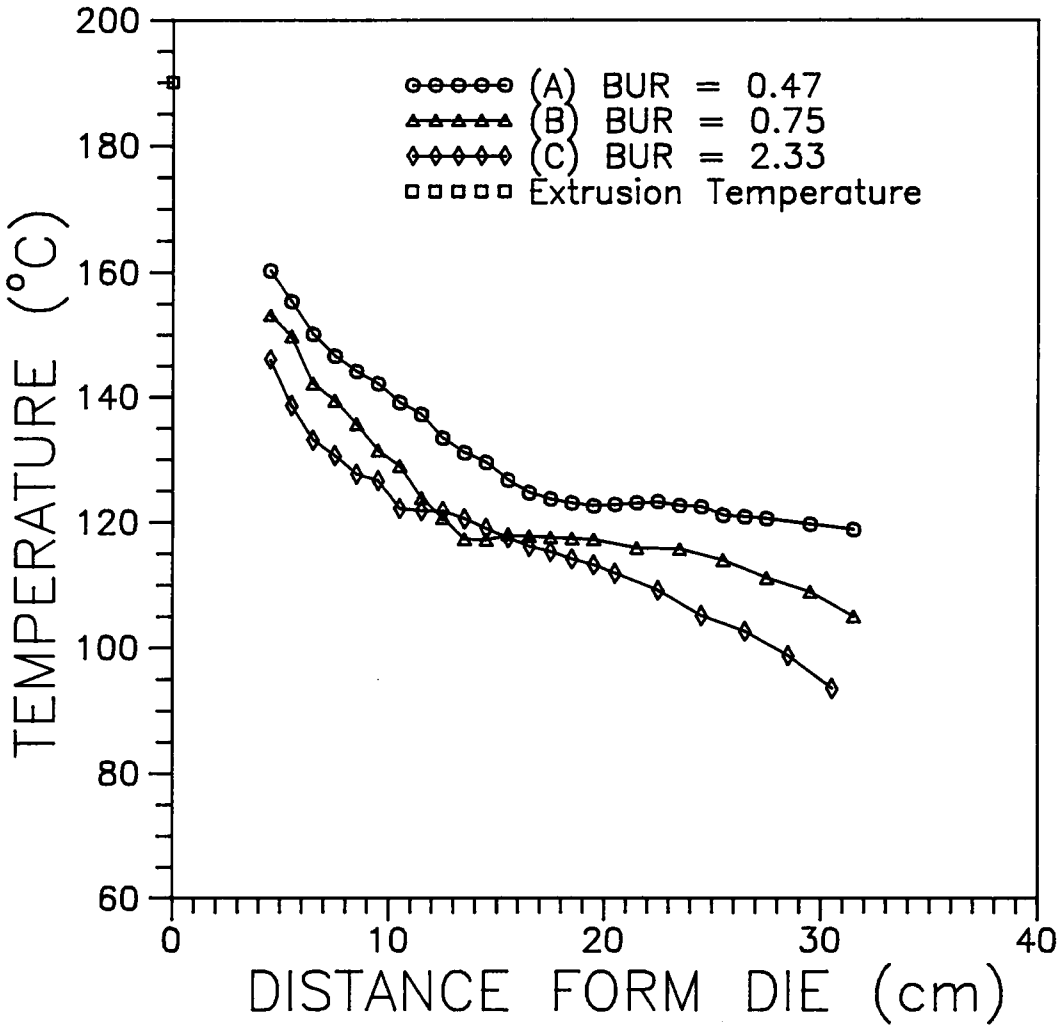

Figure 4-12 On-line measured temperature profiles for the three cases for LLDPE resin.

Further inspection of Figures 4-11 and 4-12, shows that there are significant temperature plateaus for case(A) and case(B); however, for case(C), the temperature plateaus are less significant. Since both LDPE and LLDPE are semi-crystalline materials, the occurrence of a temperature plateau is primarily due to the heat of fusion released from the crystallization process and it competes with the outside cooling rate. Therefore, according to the temperature curves in both Figures 4-11 and 4-12, the first case (case(A)), which has the lowest cooling rate, shows the most significant temperature plateau.

Furthermore, examining the plateau temperatures for case(A) for both materials LDPE and LLDPE, it can be seen that the plateau temperature of LDPE (about 104 ^{o}C) is lower than that of LLDPE (about 122 ^{o}C). Similar results can also be seen in the data of other investigators [14,37]. This could be explained by the difference in density between the two materials, as shown in Table 3-1. In general, the lower density is associated with the lower melting point [95,96]; also, it is well-known that crystallization occurs at temperatures below the melting point. Thus, it is reasonable that for LDPE, which has a lower density, the crystallization process would occur in a lower temperature range.

4.5.4 Thickness

The thickness distribution of the tubular films for the three cases is shown in Figure 4-13 for LDPE and in Figure 4-14 for LLDPE. Both Figures 4-13 and 4-14 show that the thickness always decreases along the machine direction, then remains constant. Moreover, the entire curve shifts downward with increasing blow-up ratio. That is, the final film thickness decreases with increasing blow-up ratio.

Furthermore, in both Figures 4-13 and 4-14, the condition at the die exit (Z = 0 cm), shown by a square symbol, represents the gap of the annular die; the square symbols on the right end are the final thickness measured directly with a micrometer. It can be seen that the extrapolated thickness plateaus are in good agreement with the final (directly measured) values.

4.5.5 Overview of On-line Data

In the preceding paragraphs, consideration and discussion of each type of on-line quantity is made separately. The interaction between these quantities becomes evident when the various profiles are combined in one figure. A combination of radius, velocity, temperature and thickness for case(C) (for LLDPE) is shown in Figure 4-15. The vertical dashed line represents the position of the observed frost

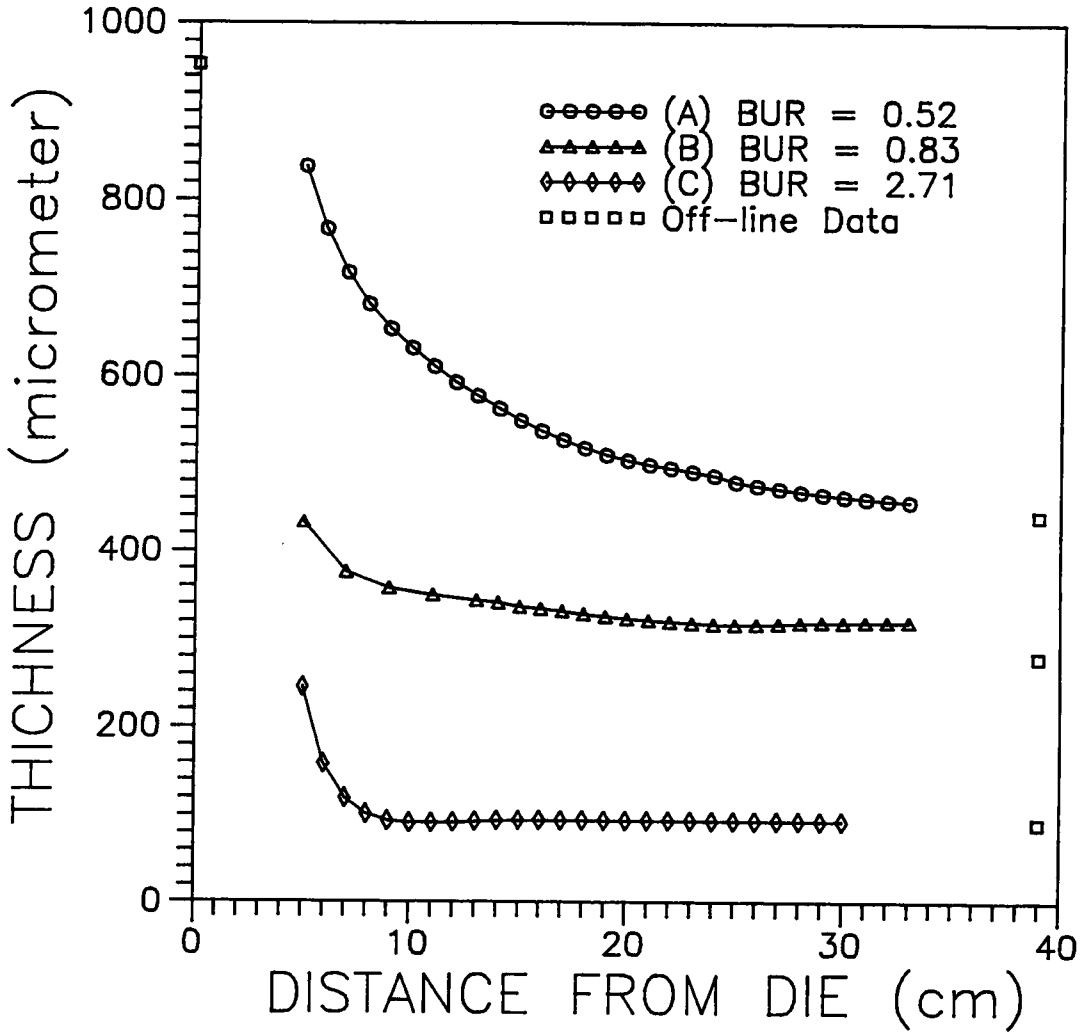

Figure 4-13 Calculated thickness profiles on basis of the on-line data for LDPE resin.

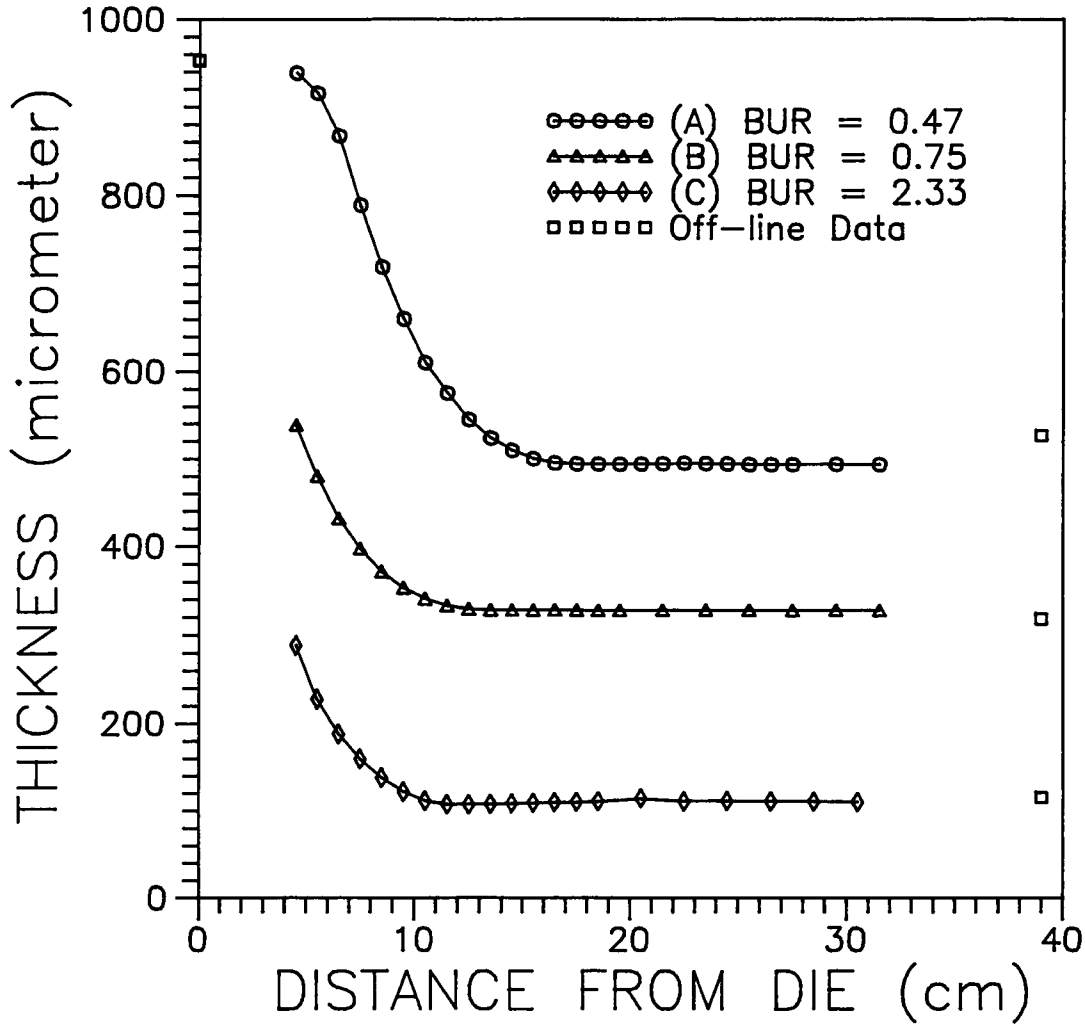

Figure 4-14 Calculated thickness profiles on basis of the on-line data for LLDPE resin.

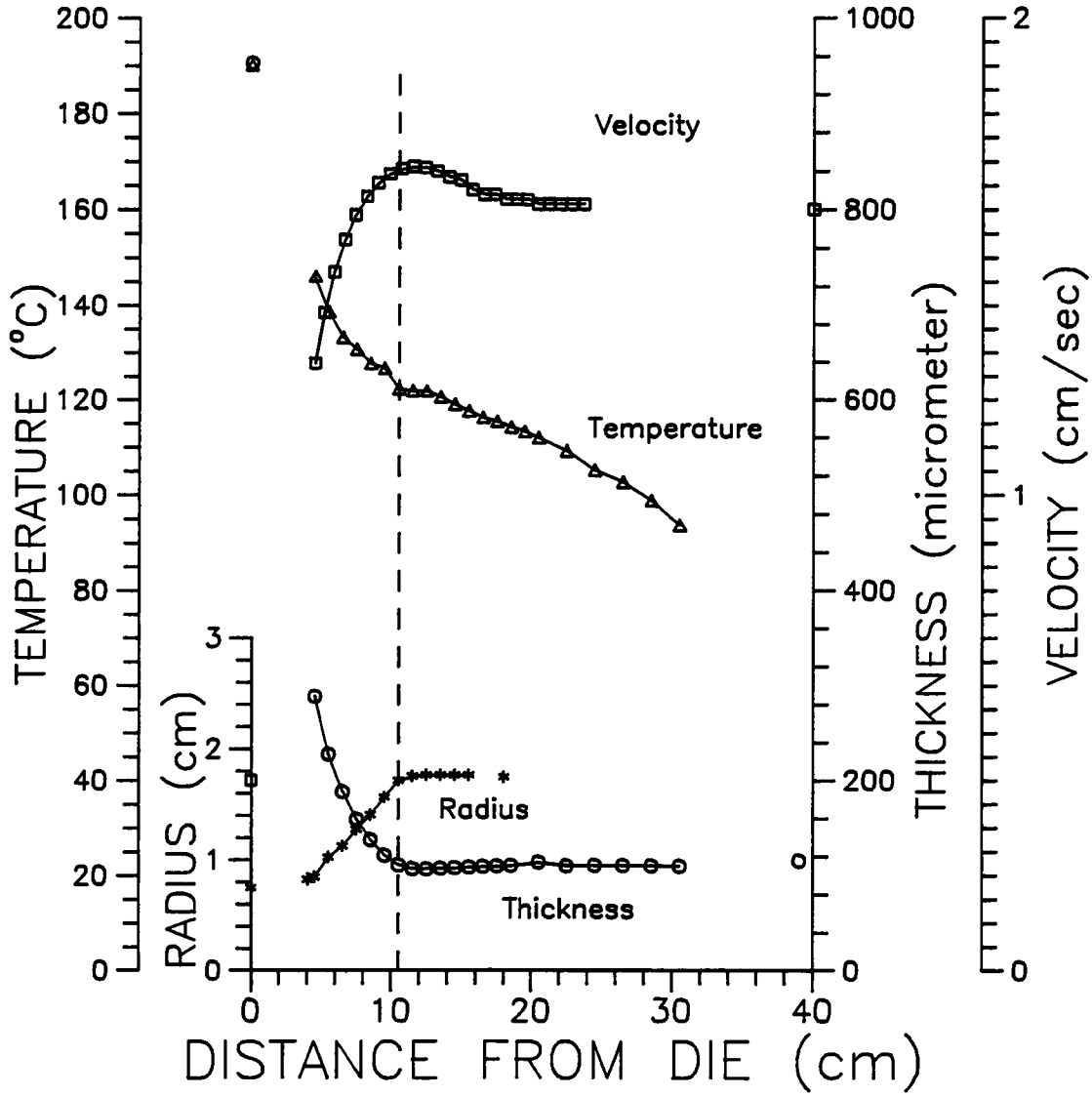

Figure 4-15 Combination of the on-line profiles of radius, velocity, temperature and thickness, and the on-line observed frost line height for case(C) using LLDPE resin.

line. This figure indicates an important result about the frost line: namely, that the radius, velocity and thickness almost stop changing there; and that a temperature plateau (or, in this particular case (semi-crystalline material), the start of temperature plateau) occurs. Similar results can be found in case(C) for LDPE, as shown in Figure 4-16, also in the rest of other cases for LLDPE and LDPE, as shown in Appendix A.

4.5.6 Deformation Rate

The deformation rate is an important factor describing the rheological behavior. The deformation rates in the machine direction (d_{11}), in the circumferential direction (d_{22}) and in the normal direction (d_{33}) can be expressed by the following equations derived from the kinematic analysis:

$$d_{11} = 2\frac{dV}{dZ} \tag{4-1}$$

$$d_{22} = \frac{2V}{R}\frac{dR}{dZ} \tag{4-2}$$

$$d_{33} = \frac{2V}{H}\frac{dH}{dZ} \tag{4-3}$$

in which R, H and V are the bubble radius, thickness and velocity along the machine direction, respectively. Hence,

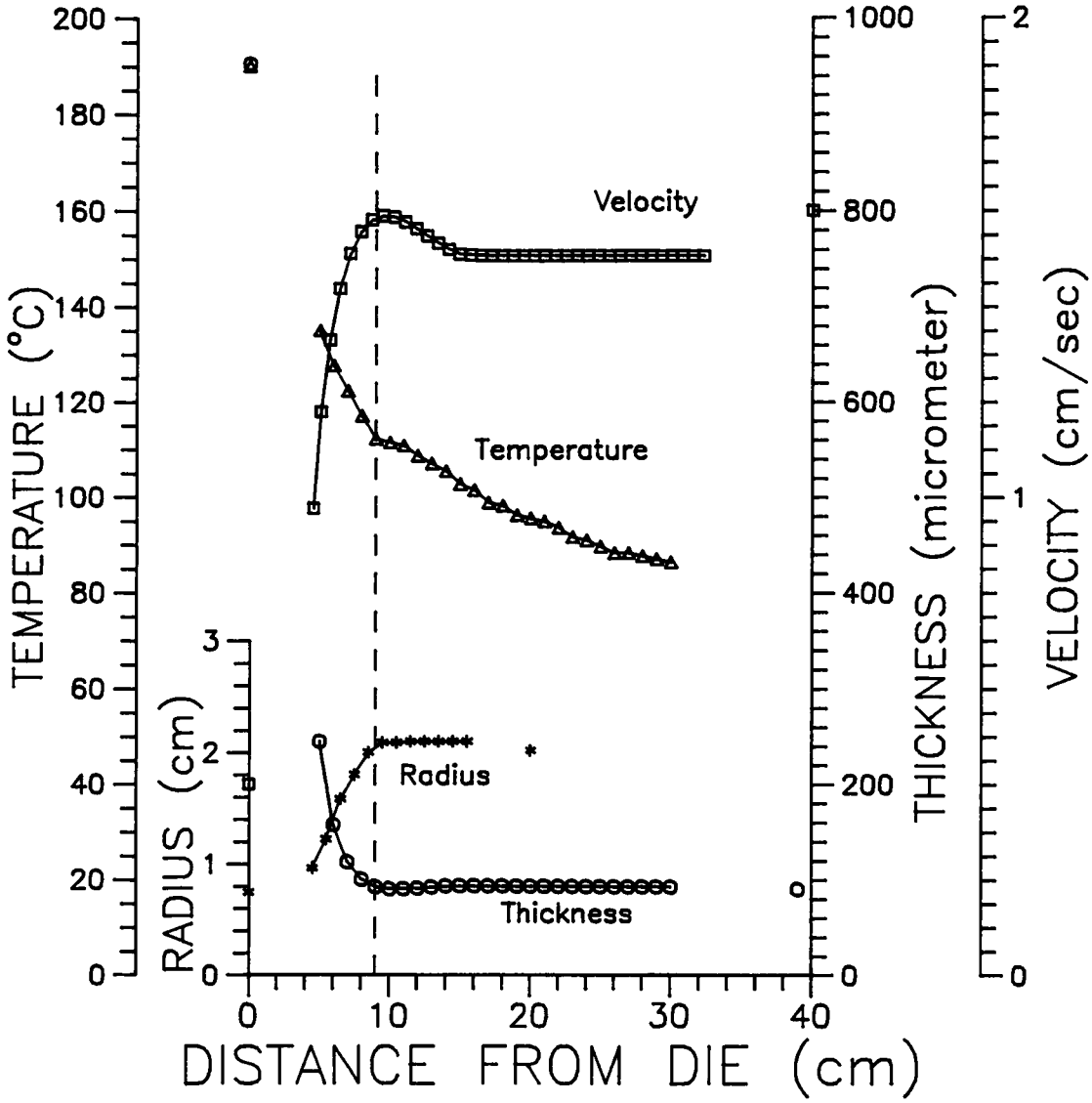

Figure 4-16 Combination of the on-line profiles of radius, velocity, temperature and thickness, and the on-line observed frost line height for case(C) using LDPE resin.

the distribution of the deformation rates in the three principal directions can be determined from the on-line collected profiles shown previously.

For LDPE, the variation of the deformation rates, d_{11}, d_{22} and d_{33}, for the three cases are plotted in Figures 4-17, 4-18 and 4-19, respectively. It should be noted that the only difference between these three cases, case(A), case(B) and case(C), is the blow-up ratio. Hence, the influence of blow-up ratio on the deformation rate in each principal direction can be seen in Figures 4-17 ~ 4-19. Naturally, due to the change of blow-up ratio, one can expect a significant effect in the deformation rate in the hoop direction, d_{22}, as shown in Figure 4-18. In this figure the curve of case(C), which has the highest blow-up ratio, has the largest variation on the deformation rate d_{22}; and the absolute value at the peak of case(C) is much higher than that of the other two cases.

Furthermore, inspecting Figure 4-17, it is very interesting that changing the blow-up ratio has a remarkable effect on d_{11}. (It should be emphasized that the tubular films of these three cases have the same take-up ratio.) The deformation rate in the machine direction, d_{11}, significantly increases with an increase in the blow-up ratio. This phenomenon may be attributed to the fact that increasing the blow-up ratio lowers the frost-line height, as it was

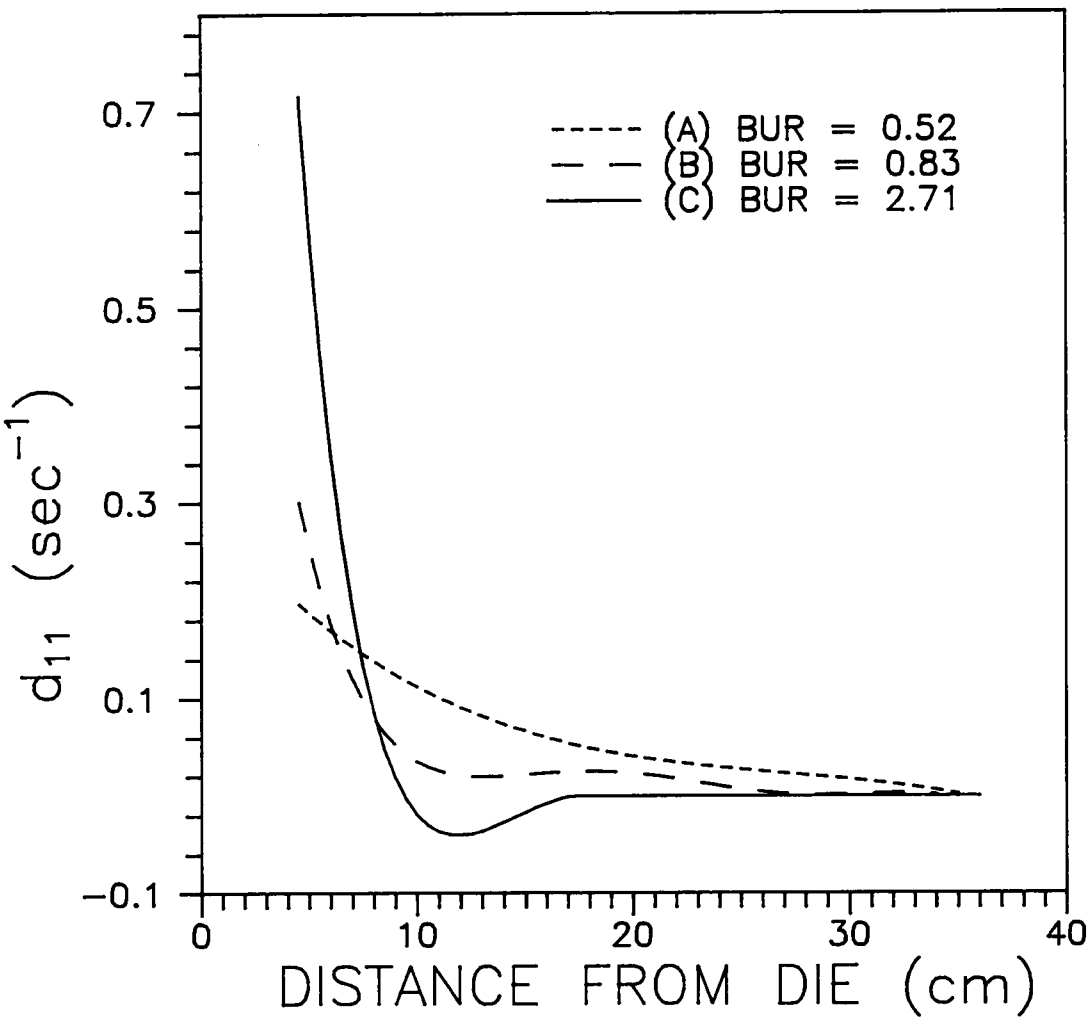

Figure 4-17 Calculated profiles of the deformation rates in the machine direction for three cases on basis of the on-line measured velocity profiles for LDPE.

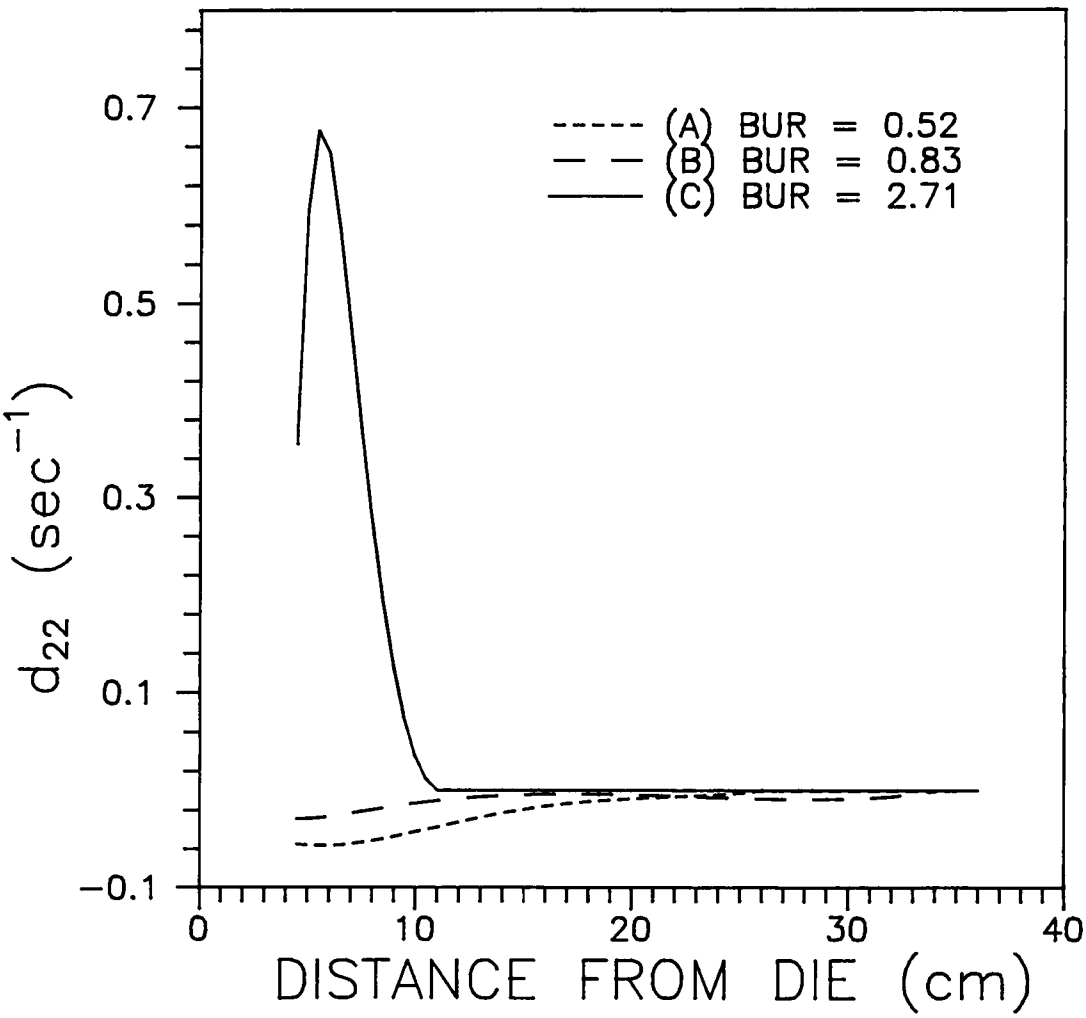

Figure 4-18 Calculated profiles of the deformation rates in the circumferential direction for three cases on basis of the on-line measured radius profiles for LDPE.

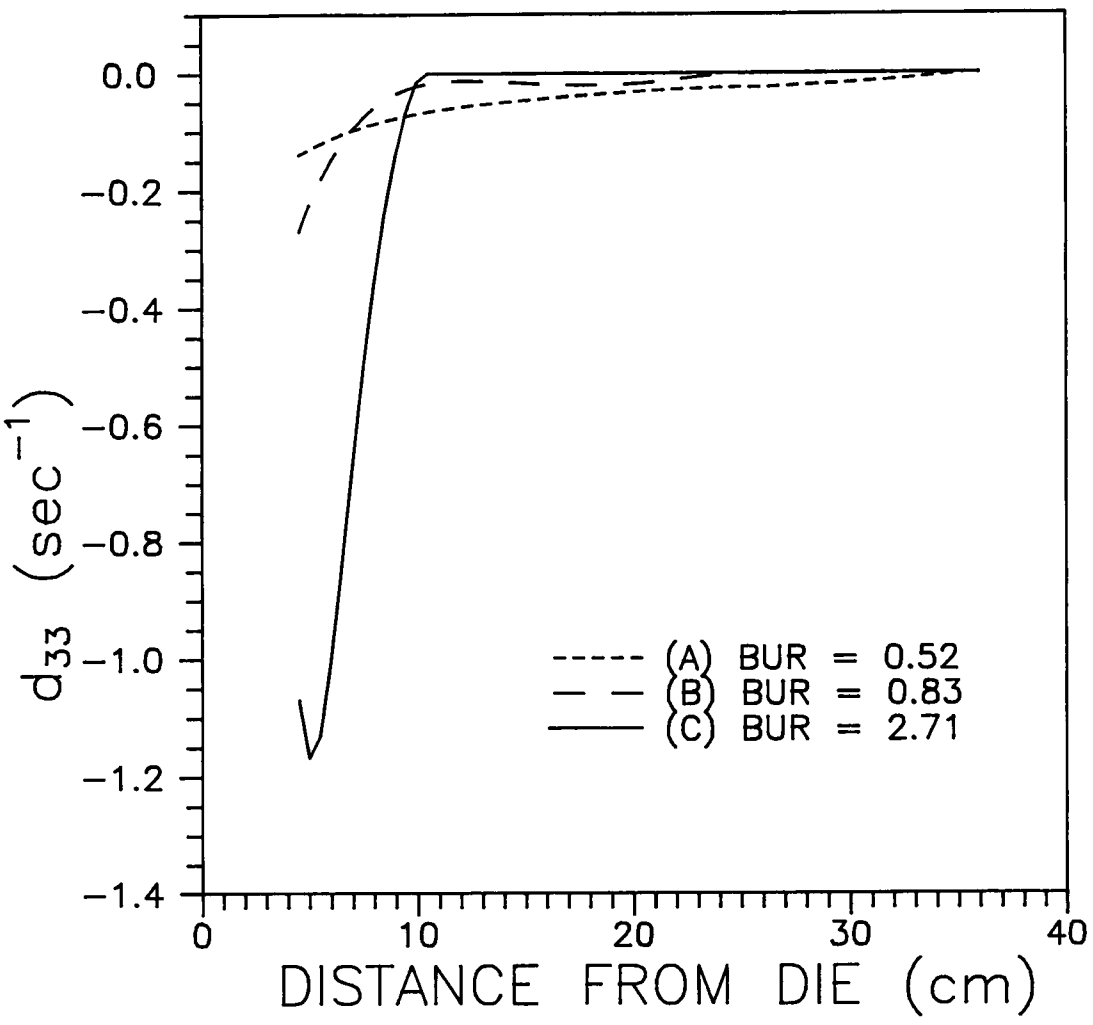

Figure 4-19 Calculated profiles of the deformation rates in the normal direction for three cases on basis of the on-line thickness profiles for LDPE.

indicated in Figure 4-10. Therefore, it becomes evident that the tubular film with a larger blow-up ratio requires a more rapid increase in velocity to reach the pre-set take-up speed due to its lower frost line height. Moreover, it is not surprising (using the mass conservation law) that case(C) has the largest variation of deformation rate in the direction of film thickness, d_{33}, as shown in Figure 4-19.

Finally, for each of these three cases, the second invariant of the deformation-rate tensor, II_d, which is a measure of the intensity of the rate of deformation, is shown in Figure 4-20. This invariant, II_d, is defined by the following equation:

$$II_d = \frac{1}{2} I_d^2 - \frac{1}{2} \sum_{i=1}^{3} \sum_{j=1}^{3} d_{ij} d_{ji} \qquad (4\text{-}4)$$

in which the subscripts "i" and "j" represent the component index of the deformation rate. Thus, the index is understood to run from 1 to 3 for the three dimensions of space. In Equation(4-4), the first invariant I_d is defined as

$$I_d = \sum_{i=1}^{3} d_{ii} \qquad (4\text{-}5)$$

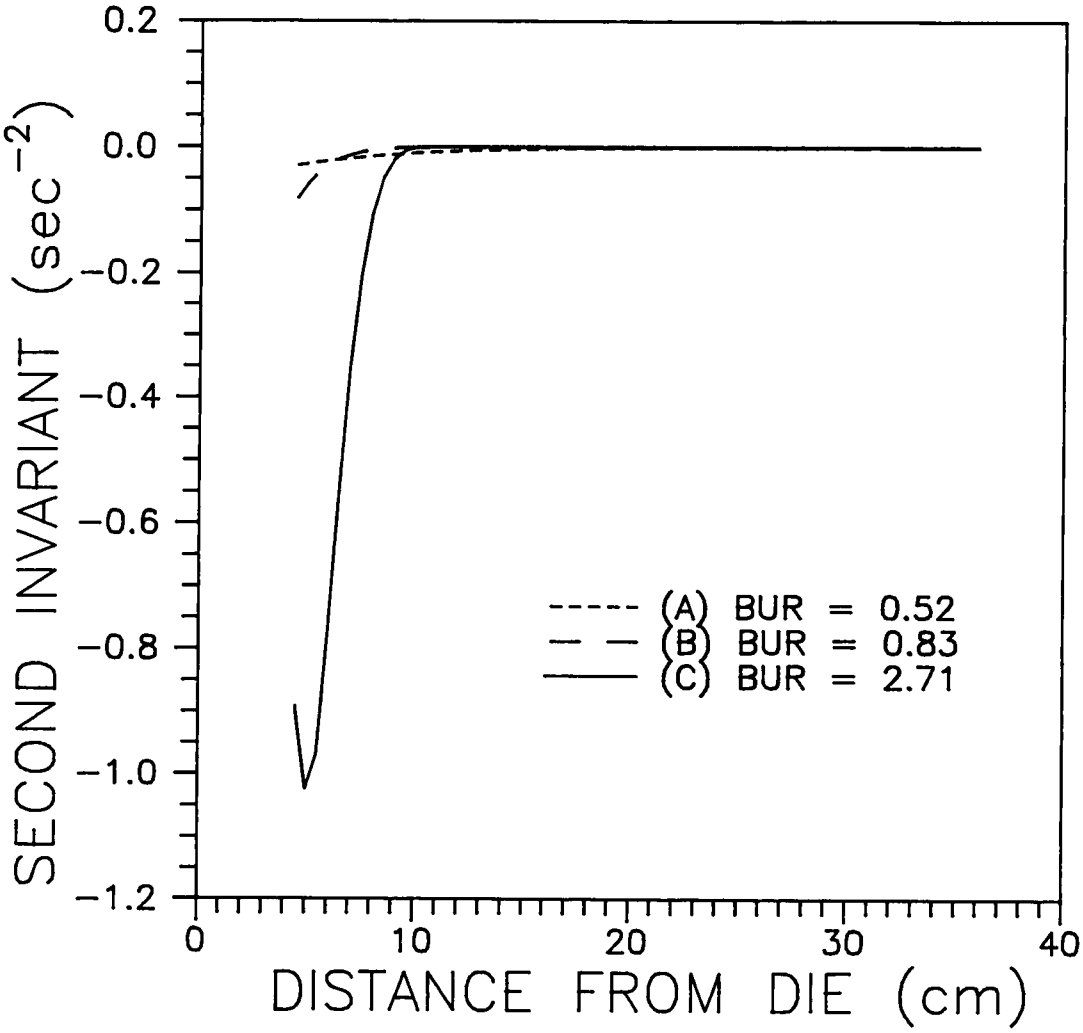

Figure 4-20 Calculated profiles of the second invariant deformation-rate tensor for three cases on basis of the deformation rates in the three principal directions for LDPE resin.

Hence, for the tubular film the second invariant of deformation-rate tensor II_d can be expressed by the following equation:

$$II_d = d_{11}d_{22} + d_{22}d_{33} + d_{33}d_{11} \qquad (4\text{-}6)$$

In other words, based on the three principal deformation rates (d_{11}, d_{22} and d_{33}), the second invariant value can be calculated using Equation(4-6). Thus, the resulting second invariants for three cases are shown in Figure 4-20. This figure indicates that case(C), which has the largest bubble among the three cases, shows the most intensive deformation rate (that is, the largest variation in II_d) occurring in the melt.

The same characteristics, as they were described and discussed in the preceding paragraphs for LDPE, can be also seen from the profiles of deformation rates and second invariant for the other polyethylene, LLDPE. For three cases, the deformation rates in each direction (d_{11}, d_{22} and d_{33}) are shown in Figures 4-21 ~ 4-23, respectively; the profiles of the second invariant (of the deformation tensor) are shown in Figure 4-24.

In summary, increasing the blow-up ratio (the other processing parameters being fixed) not only causes the

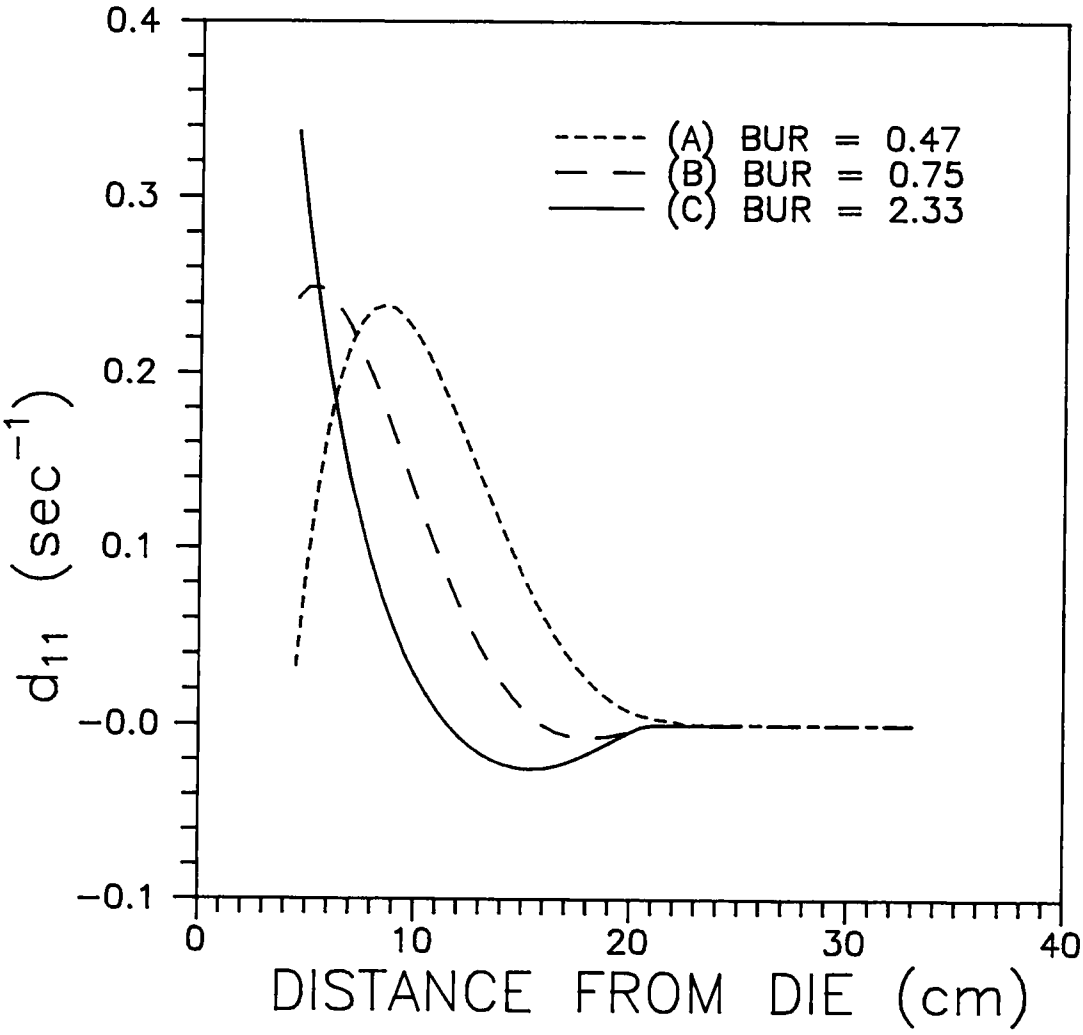

Figure 4-21 Calculated profiles of the deformation rates in the machine direction for three cases on basis of the on-line measured velocity profiles for LLDPE.

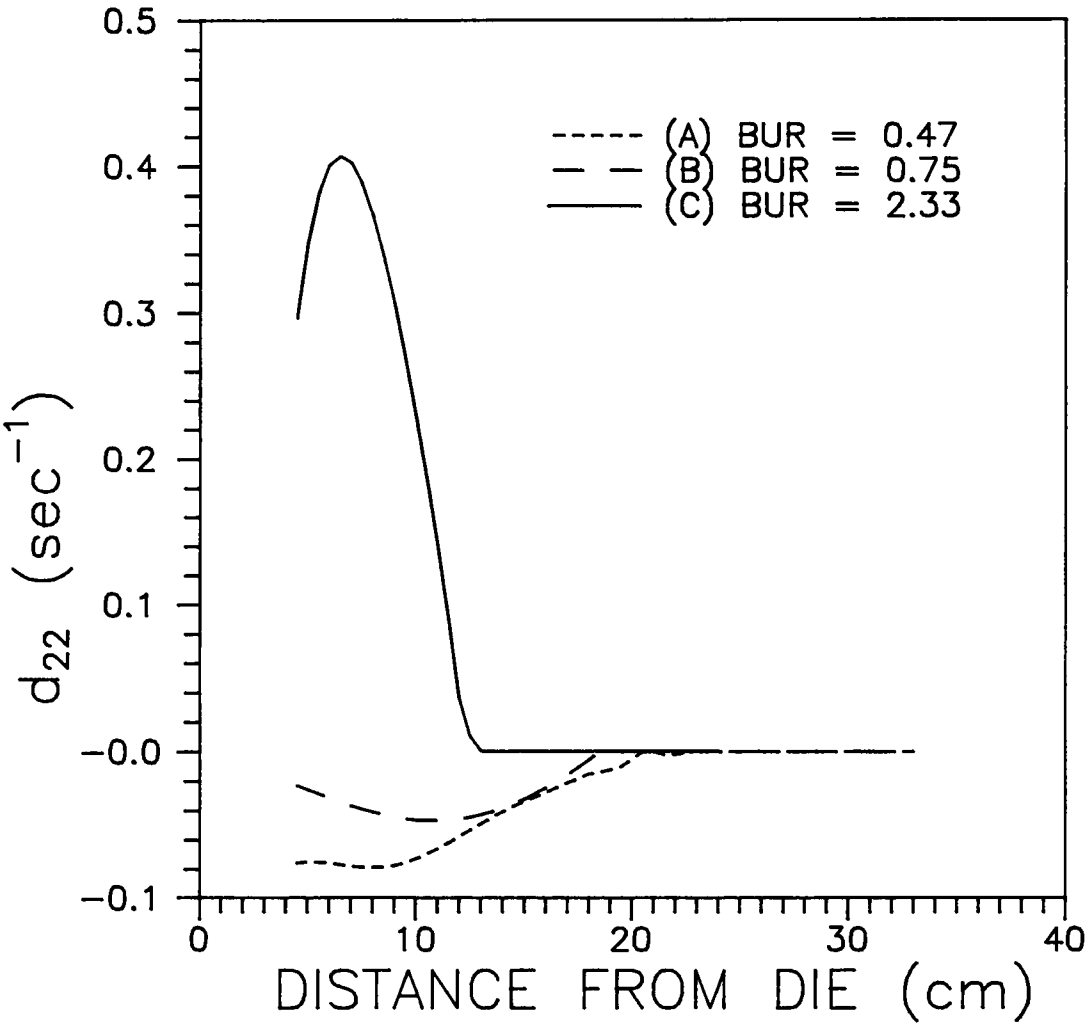

Figure 4-22 Calculated profiles of the deformation rates in the circumferential direction for three cases on basis of the on-line measured radius profiles for LLDPE.

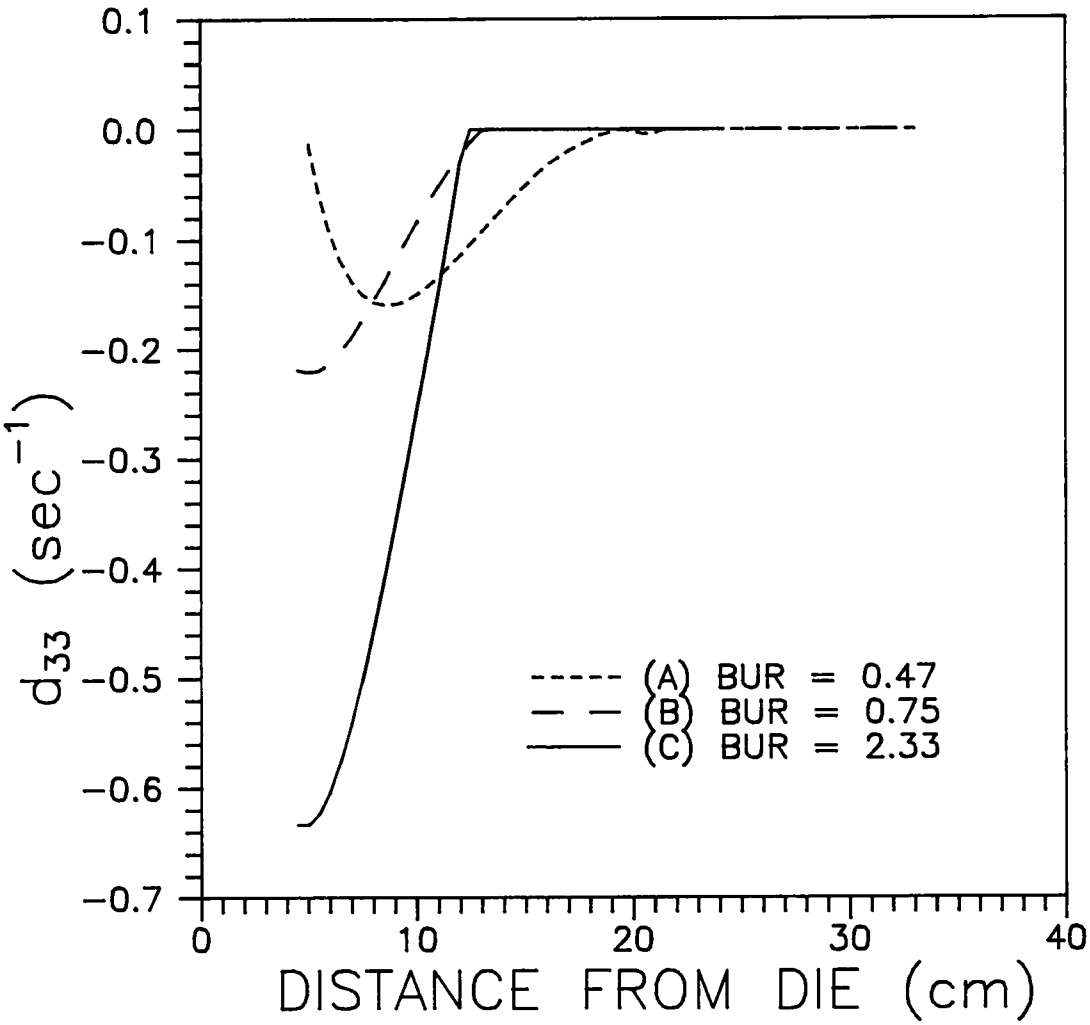

Figure 4-23 Calculated profiles of the deformation rates in the normal direction for three cases on basis of the on-line thickness profiles for LLDPE.

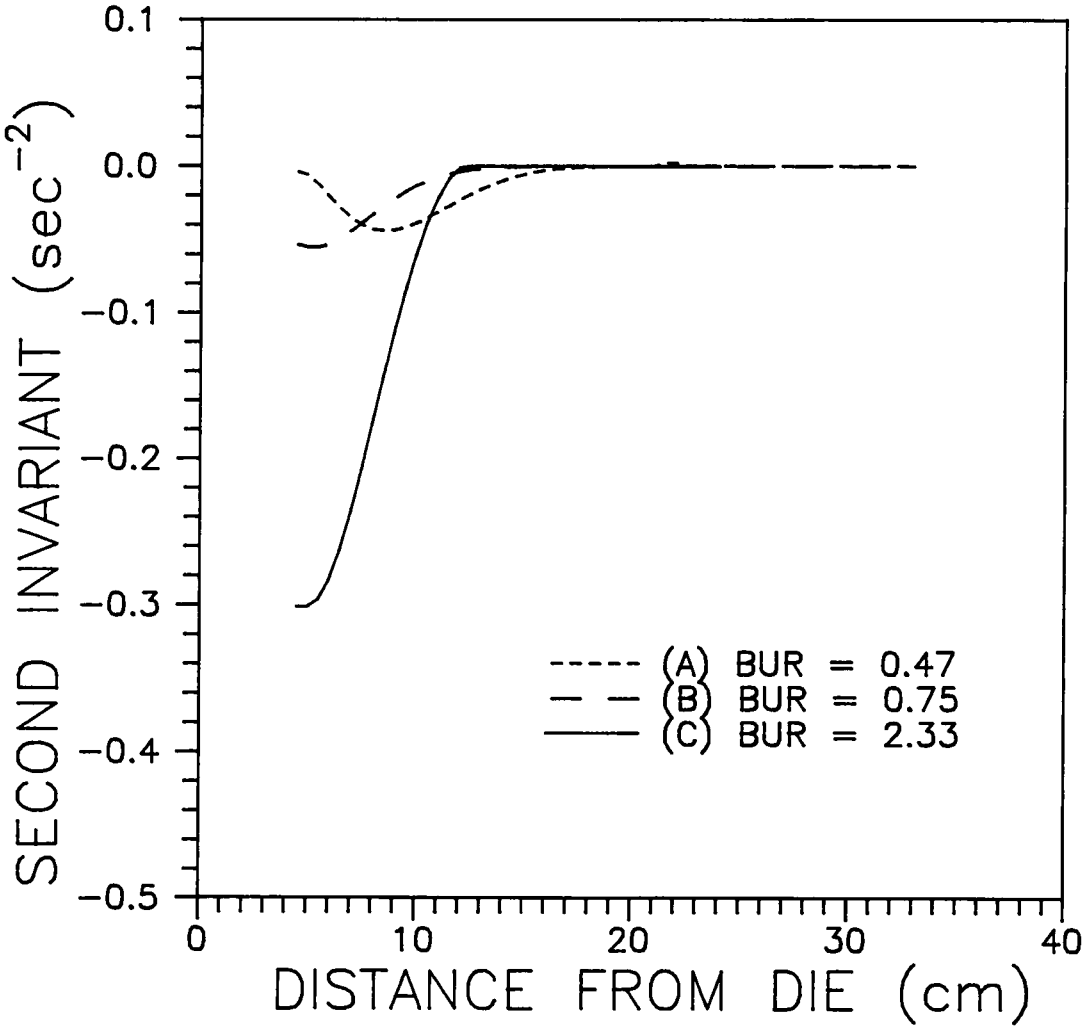

Figure 4-24 Calculated profiles of the second invariant deformation-rate tensor for three cases on basis of the deformation rates in the three principal directions for LLDPE resin.

deformation rate in the hoop direction to increase, but also causes the deformation rates in the other two principal directions to increase. Accordingly, the overall deformation rate of the melt (evaluated by II_d) increases with the blow-up ratio.

CHAPTER 5

THEORETICAL MODELLING OF RESULTS

The advantages of mathematical modelling are to provide deeper understanding of the physical system as well as to reduce the amount of experimental work required. Therefore, most importantly, a mathematical model must, at least, be able to qualitatively describe the behavior of the target physical system. The validity of a mathematical model can be first evaluated via qualitative comparisons to experimental observations. If the qualitative behavior of the model agrees with the target system, then it becomes possible to do quantitative comparisons and predictions.

Therefore, according to the above idea, firstly, the validity of the two existing mathematical models, that is, the model of Pearson and Petrie [3,4] and the model of the present author (as presented in his M.S. thesis [28]), were examined via qualitative comparisons to experimental observations. These results will be presented in Section 5.2. Then, in Section 5.3, quantitative comparison of the present model with experiment will be given because the predictions of the

present model agree with the basic trends of the experimental data in the prior qualitative examinations. Thirdly, a further exploration of the film blowing process via the present model will be carried out and will be presented in Section 5.4. Finally, a physical explanation of the differences between these two models and an attempt to resolve the difficulties of the Pearson-Petrie model will be given. Following this scheme, the detailed results and discussion will be given in the following sections.

5.1 GOVERNING SYSTEM EQUATIONS

Based on both the Pearson-Petrie model and the present model, computer simulations for the film blowing process were carried out. In the mathematical simulations, the following assumptions were made on the basis of the literature cited in Chapter 2:

(1) The surface tension is negligible.

(2) The inertial and drag force become unimportant because of low take-up speed.

(3) The gravitational force may be neglected.

(4) The heat transfer between the inner surface of the film and the inflating air inside the bubble is negligible.

(5) The heat transfer between the film and the environment is primarily controlled by convection and radiation, and heat conduction through the film can be neglected.

(6) The viscous dissipation is small enough to be neglected.

Under these assumptions, two sets of governing system equations can be obtained, depending how one sets up the physical problem. The earlier analysis of Pearson and Petrie, in which the force balances are based on thin-shell theory, led to the governing system equations, as expressed by Equations(2-58) ~ (2-60), (2-63) and (2-67). On the other hand, in the author's M.S. thesis, direct force and energy balances on a locally cylindrical bubble are made; and the final system equations were given by Equations(2-67) and (2-76) ~ (2-78).

All of the governing system equations are first-order ordinary differential equations. Thus, they can be integrated simultaneously by using the fourth-order Runge-Kutta numerical method [97] with the following initial conditions:

at Z = 0 (at the die exit):

$H = H_o$ (the die gap)

$R = R_o$ (the radius of the annular die)

$T = T_o$ (the extrusion temperature)

$X = 0$ (the weight-fraction crystallinity)

$\theta = 0$ (the angle between the bubble profile and the Z-axis)

It should be noted that an issue in the literature regards the initial condition in θ (for the Pearson-Petrie model). In the latest study of Ashok and Campbell [30] and the author's prior study [28], θ was assumed to be zero at the die exit; on the other hand, to avoid this condition Pearson and Petrie [4] (and also other investigators [69,82]) started their analyses at the frost line (where θ was assumed to be zero) and worked backwards in Z. However, comparing the results of these analyses, these differing approaches do not change the qualitative nature of the Pearson-Petrie solution. Hence, $\theta = 0$ was here taken to be one of the initial conditions.

A BASIC computer program was developed to carry out the numerical integration. The take-up force in these two models was adjusted until the desired take-up speed was met. The numerical scheme is illustrated in Figure B-1 in Appendix B.

5.2 QUALITATIVE COMPARISON OF RESULTS OF THE PEARSON-PETRIE MODEL AND THE PRESENT MODEL

For the purpose of a qualitative examination of the two existing models, the model of Pearson and Petrie and the present model, the theoretically predicted effects of inflation pressure, extrusion temperature, and melt viscosity on the bubble radius were carried out. Since the bubble size is the most intuitive and accurately measurable quantity, the final radius can be used as a way to qualitatively judge the validity of these two models.

5.2.1 The Pearson-Petrie Model

As described in Chapter 2, the original mathematical model for the film blowing process was first set down by Pearson and Petrie [3,4] and their analysis has been widely used in all subsequent work. Although much effort has been devoted to computer simulation using their model, few investigations can support the theoretical predictions with experimental data. The lack of systematic comparisons is probably due to the complexities of the analysis and the data collection. Therefore, in this section computer simulations based on the Pearson-Petrie model are carried out; most importantly, the results of the theoretical predictions will

be qualitatively examined by comparing to the experimental observations previously presented.

Before theoretical modelling is carried out, two major material equations need to be chosen: namely, the rheological equation and the crystallization rate equation (because the resins used in this study (polyethylenes) are semi-crystalline). The detailed discussion about these two material equations will be given in the next section, Section 5.3. Here, in this section, for simplicity, the following two equations, Equations(5-1) and (5-2), are chosen for viscosity η and crystallization rate constant K, respectively:

$$\eta = \alpha 1 \exp\left(\frac{\beta 1}{T}\right) \exp\left[\alpha 2 \left(\frac{X}{X_f}\right)^{\beta 2} \right] \qquad (5\text{-}1)$$

in which T is the temperature of melt (in units of Kelvin); X and X_f are the crystallinity at temperature T and the ultimate crystallinity, respectively;

$$K = K_o \exp\left[\frac{-U^*}{R(T-T_\infty)}\right] \exp\left[\frac{-C_3}{T\Delta T}\right] \qquad (5\text{-}2)$$

in which R is the universal gas constant, $U^* \approx 1500$ cal/mol, is the activation energy for segmental jump rate in polymers; $T_\infty = T_g - 30$ (K); $\Delta T = T_m^o - T$. The equilibrium melting point T_m^o for polyethylene is 141±0.5 °C [98]. Equations of the form of

Equations(5-1) and (5-2) have been successfully used in the simulation of the melt spinning process [89,99].

Although the detailed description and determination of the other parameters in Equations(5-1) and (5-2) will be given in Section 5.3, the numerical values of these parameters used in this section for examining the behavior of the models are summarized in Table 5-1. In order to obtain adequate and reasonable numerical values for the required parameters, all of the values are estimated either on the basis of practical experimental data or on the basis of published results from the literature. For example, the rheological constants $\alpha 1$ and $\beta 1$ are estimated from the measured complex viscosity of LDPE at the frequency of 10^{-1} rad/sec, at various temperatures, as shown in Figure 3-1; the parameters in Equation(5-2), K_o and C_3, are taken from the literature [99]. The other required physical parameters, such as heat of fusion, density and heat capacity, for polyethylene can be also obtained from the literature [100-104]. The heat of fusion ΔH_f is assumed to be 66 cal/g. The density (in g/cm^3) in the molten state is

$$\rho_{am} = [\ 1.135 + 0.00104(T-273)\ ]^{-1} \qquad (5-3)$$

The density (in g/cm^3) in the solid state is

Table 5-1 Summary of the numerical values of parameters used in the qualitative simulations (in Section 5.2) using the Pearson-Petrie model and the present model.

PROCESSING PARAMETERS	MATERIAL PARAMETERS
Die Radius R_o: 0.746 cm	α_1: 9.577 poise
Die Gap H_o: 950 μm	β_1: 4,476 K
Die Temperature T_o: 190 °C	α_2: 13.5
Mass Flow Rate W: 0.15 g/sec	β_2: 0.4
Air Temperature T_{air}: 49 °C	X_f: 0.445
Room Temperature T_r: 30 °C	K_o: 2,670 sec^{-1}
Heat Transfer Coeff. U: 0.001 $cal/cm^2sec°C$	C_3: 85,000 K^2

$$\rho_{solid} = \left\{ \frac{1}{\rho_{am}} + X\left[\frac{595-0.837(T-273)}{599-(T-273)} - \frac{1}{\rho_{am}} \right] \right\}^{-1} \quad (5\text{-}4)$$

For the heat capacity (in cal/g^{o}C) of polyethylene, we have

$$C_p = 0.49 + 0.000867(T-273) \quad (5\text{-}5)$$

In all of these equations T is in units of Kelvin.

(A) Relationship of Pressure and Blow-up Ratio

Under a fixed take-up condition in which a take-up speed 12.5 cm/sec is assumed, the predicted relationship between inflation pressure and the blow-up ratio is shown in Figure 5-1. The predicted ΔP vs. BUR curve indicates an unexpected (inverse) pressure effect on the radius of the tubular film; that is, increasing the inflation pressure causes the blow-up ratio to decrease. This phenomenon has been reported in several other investigations [4-6,29,30,87]; however, no satisfactory explanation was given. Furthermore, most importantly, the entire shape of the predicted curve, qualitatively speaking, is different from that of the experiments, as shown in Figures 4-1 ~ 4-5. That is, the prediction of the Pearson-Petrie model on the point of pressure versus blow-up ratio substantially deviates from the physical picture of the actual process.

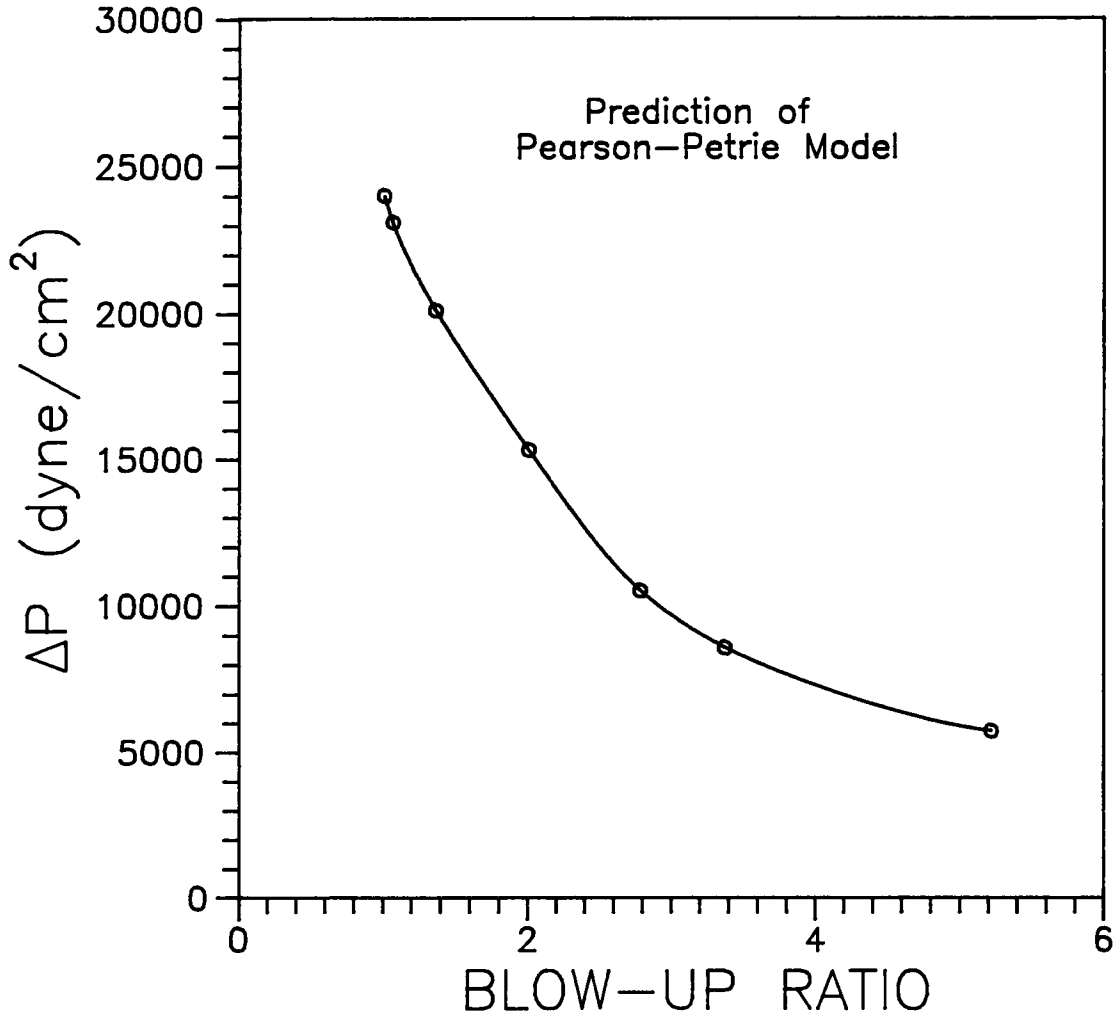

Figure 5-1 Theoretically predicted relationship between the inflation pressure and the blow-up ratio using the model of Pearson and Petrie.

(B) Influence of Extrusion Temperature

Three different extrusion temperatures, 180 ^{o}C, 190 ^{o}C, and 200 ^{o}C, are used in the computer simulation. The predicted radius profiles for these three die temperatures are shown in Figure 5-2. It can be seen that at an extrusion temperature of 200 ^{o}C, the highest temperature, the predicted radius is smaller than the other two. In other words, the Pearson-Petrie model predicts that the blow-up ratio will be increased by lowering the extrusion temperature for a fixed pressure. However, as was shown in Figure 4-4 in Chapter 4, the experimental observations indicate that the final radius decreases with a decrease of the die temperature for a fixed ΔP. Hence, it is obvious that the qualitative trend (predicted by the Pearson-Petrie model) on the matter of the influence of extrusion temperature on radius is opposed to that of experiments.

(C) Influence of Melt Viscosity

Changing the viscosity (that is, changing the pre-exponential coefficient $\alpha 1$ in Equation(5-1)) by factors of 0.8 and 1.5, respectively, the predicted effect of viscosity on the bubble radius can be obtained. The calculated radius profiles for three different melt viscosities are shown in

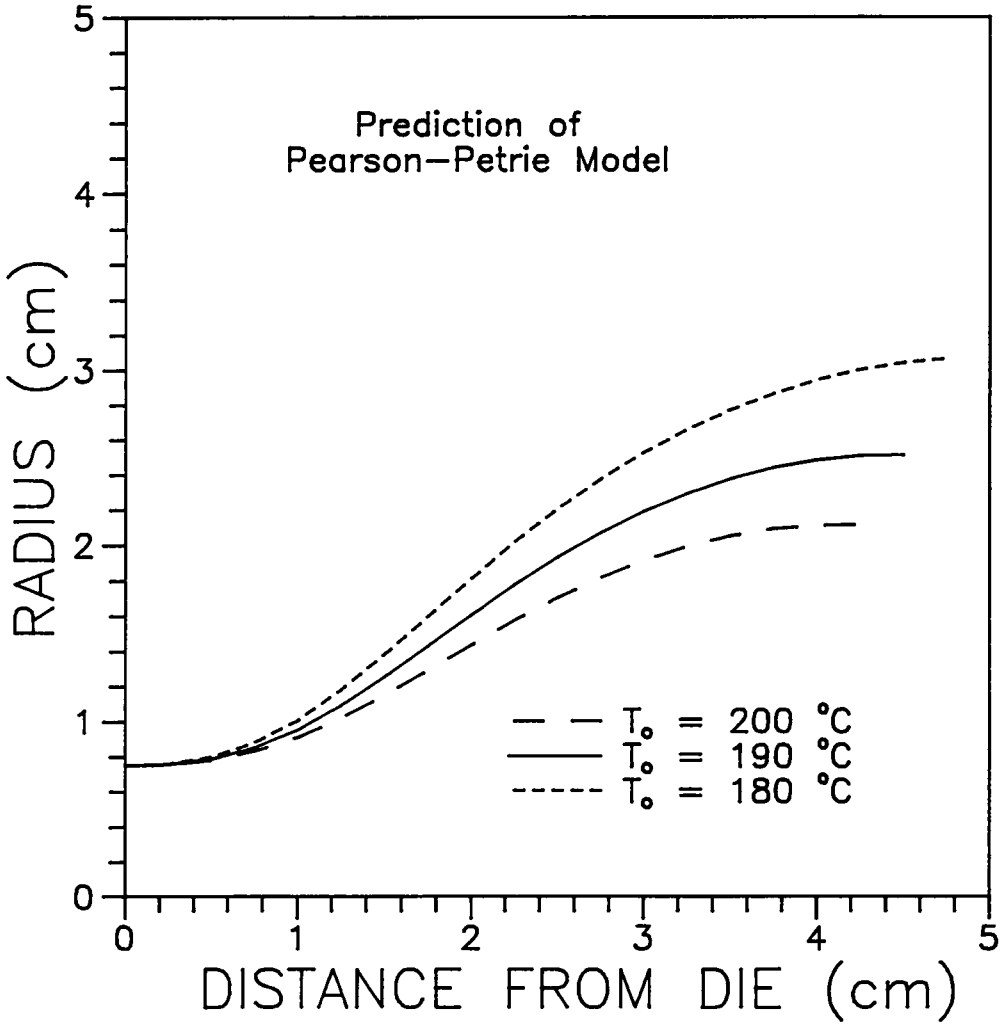

Figure 5-2 Theoretically predicted effect of the extrusion temperature on the bubble radius using the model of Pearson and Petrie.

Figure 5-3. Figure 5-3 indicates that when the inflation pressure is fixed, the melt with a higher viscosity gives a larger bubble. The same prediction result was also reported in the study of Ashok and Campbell [30].

The above prediction result is against one's physical intuition about the physical meaning of "viscosity". That is, according to the physical meaning of viscosity, the melt with a higher viscosity will give a smaller bubble rather than a larger bubble as predicted. This reasoning can be supported by both the sets of experimental data in this study and in the literature [26]. Firstly, in Chapter 4, Figure 4-4 shows that for a fixed ΔP a smaller bubble was obtained by lowering the extrusion temperature; most importantly, lowering the extrusion temperature is equivalent to an increase in melt viscosity because the melt viscosity is strongly dependent on temperature. Furthermore, this reasoning (based on the physical meaning of viscosity) can be supported by the experimental data in the literature [26] as well. In the study of Wagner [26], it was observed that to reach the same range of BUR the required ΔP increases with a decrease in the melt index. It is well-known that the melt with a lower melt index has a higher viscosity. Thus, the same physical picture (that is, for a fixed ΔP the melt with higher viscosity gives the smaller bubble) can be drawn from Wagner's observations.

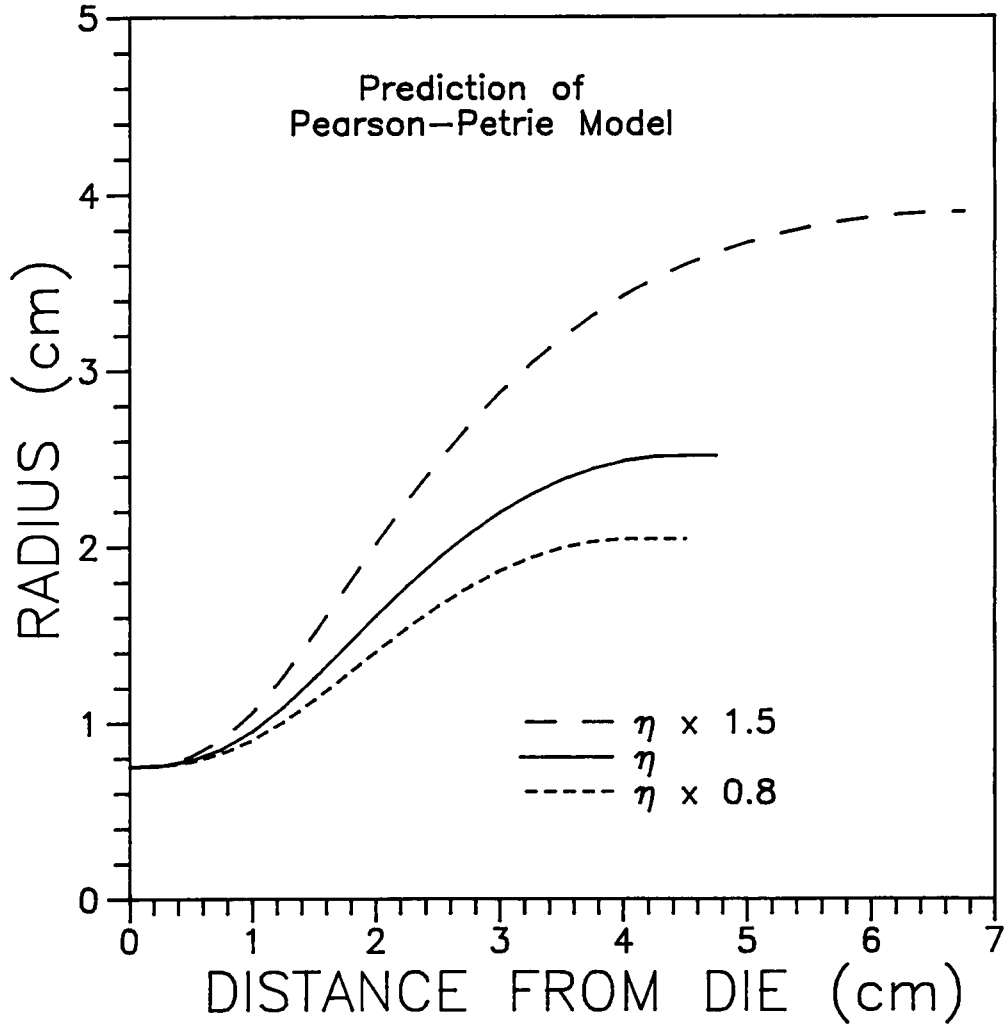

Figure 5-3 Theoretically predicted effect of the melt viscosity on the bubble radius using the model of Pearson and Petrie.

Therefore, it is obvious that on the question of the influence of melt viscosity on the radius (for a fixed inflation pressure) the prediction of the Pearson-Petrie model is contrary to the physical picture.

5.2.2 The Present Model (Newly Proposed Model)

For the purpose of comparison, the present mathematical model, newly proposed in the author's M.S. thesis [28], will now be examined using the same numerical values for the processing parameters and the material parameters as were used in the preceding section (see Section 5.2.1). A Newtonian rheological model is being used here.

(A) Relationship of Pressure and Blow-up Ratio

The predicted relationship between the pressure and the blow-up ratio is shown in Figure 5-4. This figure shows an "intuitive" pressure effect on the blow-up ratio; that is, a higher inflation pressure causes a larger bubble. This "intuitive" pressure effect can also be found in most of the experimental data, as shown in Figures 4-1 ~ 4-5 in Chapter 4. Beside this agreement, the degree of sensitivity of BUR to ΔP also qualitatively agrees with experimental observations. That is, the final bubble radius is more sensitive to an increase of pressure in the region of higher blow-up ratio.

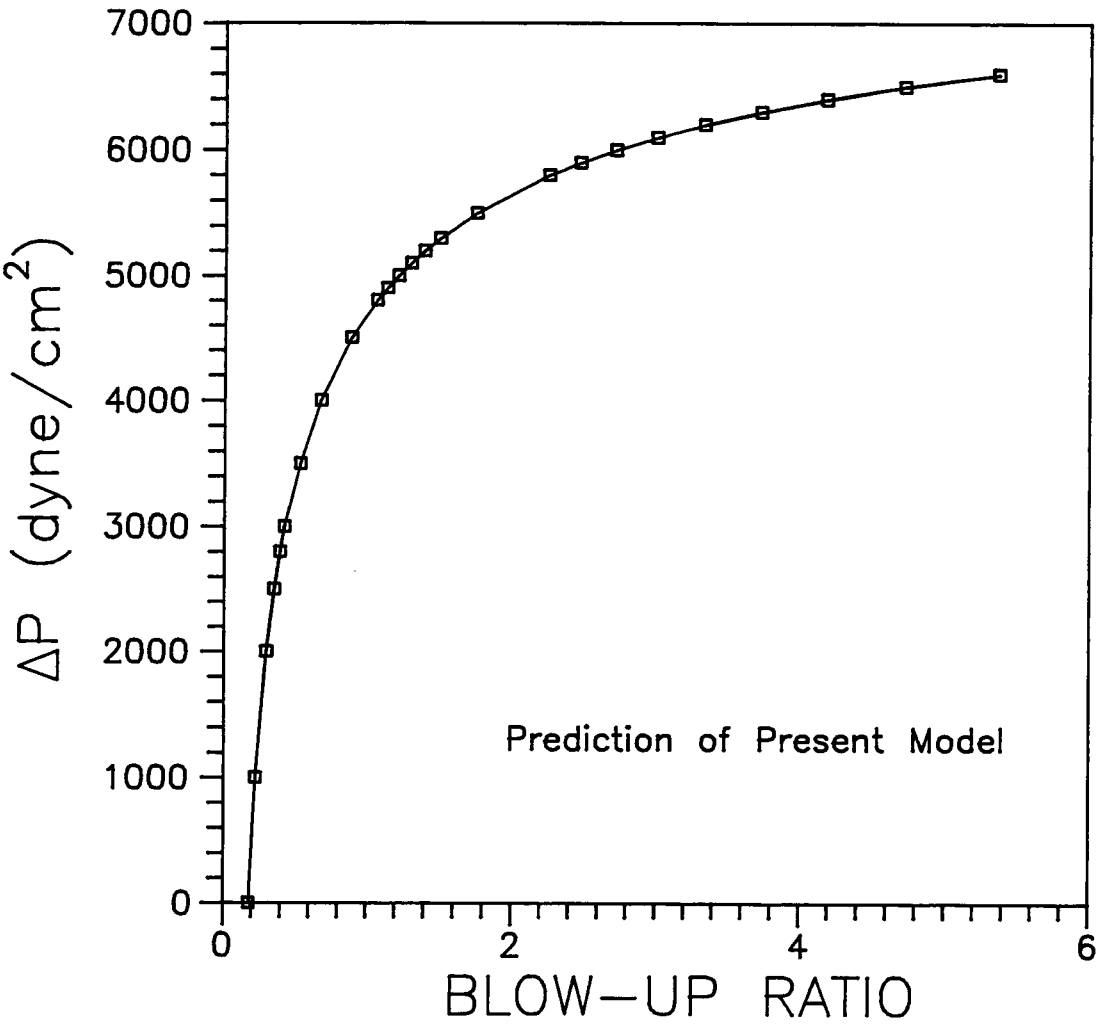

Figure 5-4 Theoretically predicted relationship between the inflation pressure and the blow-up ratio using the present model.

However, it should be noted that the curve in Figure 5-4 does not show the "slightly inverse" pressure effect which was observed in the region of high blow-up ratio, as shown in Figures 4-1 ~ 4-4. This small disagreement is likely due to the over-simplified assumption of a Newtonian fluid in the simulation. The phenomenon of deformation thinning (pseudo plastic) nature of polymer melt during processing is well-known [89-91]. Therefore, it is believed that this small disagreement will be improved by replacing the Newtonian viscosity equation with a deformation-thinning model. Further analysis concerning this point will be given in a later section, Section 5.4.

(B) Influence of Extrusion Temperature

Three different extrusion temperatures, 180 ^{o}C, 190 ^{o}C, and 200 ^{o}C, are used to examine the prediction of the present model. The predicted radius profiles at these three die temperatures are shown in Figure 5-5. This figure indicates that the final bubble radius increases with increase of the extrusion temperature for a fixed internal pressure. This trend of prediction, qualitatively speaking, agrees with that of the experimental results, as shown in Figure 4-4 in Chapter 4.

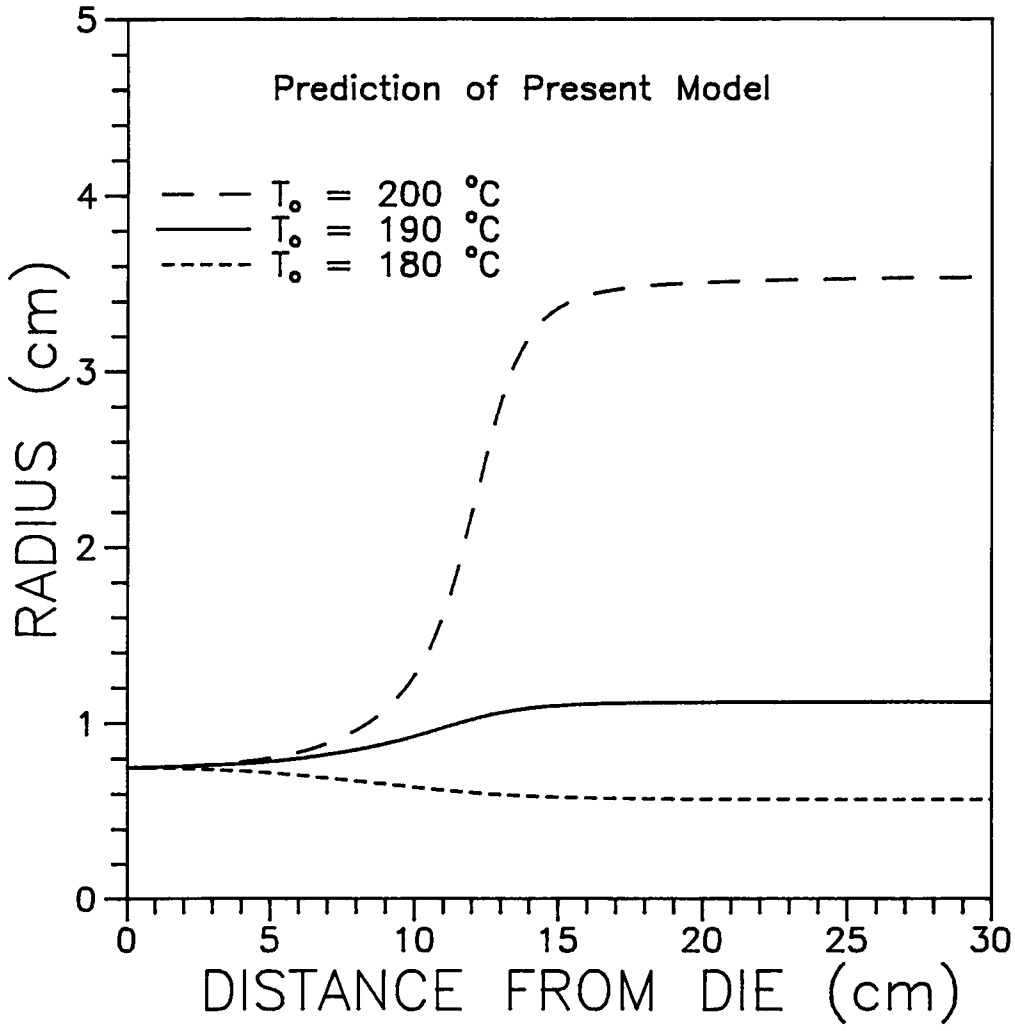

Figure 5-5 Theoretically predicted effect of the extrusion temperature on the bubble radius using the present model.

(C) Influence of Melt Viscosity

The predicted effect of melt viscosity on the bubble radius is shown in Figure 5-6, in which the viscosity values are changed by factors of 0.8 and 1.5. This figure indicates that for a fixed inflation pressure a melt with a lower viscosity will be blown into a larger bubble. It should be noted that this prediction (by the present model) is opposite to that of the Pearson-Petrie model. Most importantly, furthermore, this prediction of the present model qualitatively agrees with the actual physical picture (which was described in detail and discussed in Section 5.2.1).

5.2.3 Summary

The validity of a model can be evaluated via qualitative comparisons to experimental observations. The above comparisons for the Pearson-Petrie model indicate that the predicted effects of inflation pressure, extrusion temperature and melt viscosity on the radius are contrary to the experimental observations. On the other hand, however, the qualitative comparisons show that the predictions of the present model are satisfactory. Therefore, a further quantitative test of the present model will be carried out in the next section. By this means, applicability of the present model can be further examined.

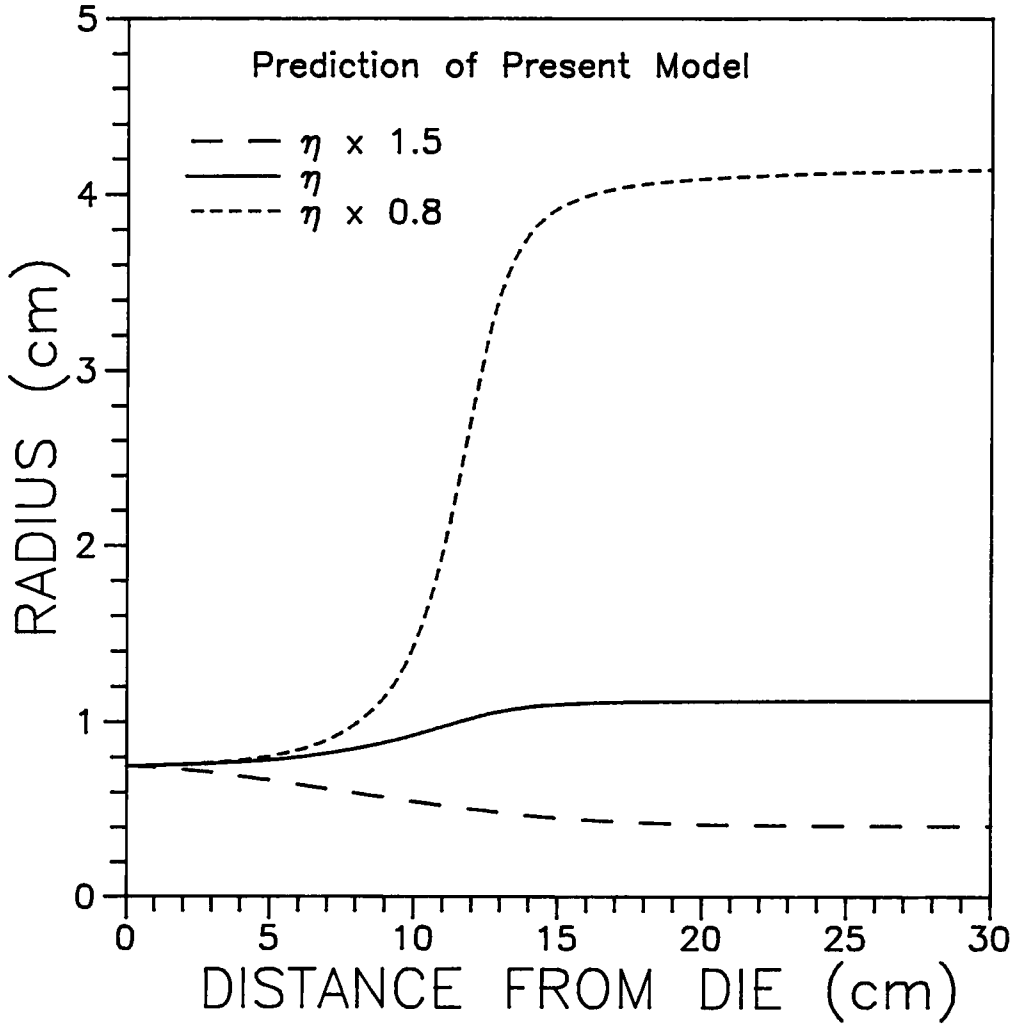

Figure 5-6 Theoretically predicted effect of the melt viscosity on the bubble radius using the present model.

5.3 QUANTITATIVE COMPARISON OF THE PRESENT MODEL WITH DATA

Since the present model has shown the ability to qualitatively describe the film blowing process, it is now important to do a quantitative check. In the following detailed quantitative checks, the actual processing conditions, such as the mass flow rate, the extrusion temperature, the measured inflation pressure and the take-up speed will be used as input parameters for the simulation; then, the calculated profiles of radius, thickness and velocity will be compared to the on-line data.

5.3.1 Simulation of Radius, Thickness and Velocity Profiles

Before carrying out calculations to simulate the bubble during processing, certain parameters need to be estimated.

(A) Heat Transfer Parameters

The physical and mechanical properties of the final product are strongly dependent on the thermal history during processing. However, the heat transfer process (mechanism) in the blown film process is highly complex. The tubular melt is cooled by blowing external air along the bubble surface. It is obvious that the heat transfer involved during processing

is dominated by forced convection. Unfortunately, it seems not possible to obtain an analytical expression for the forced convection problem because it depends on the surface geometry and the transport properties of the fluid (such as viscosity, velocity, and density) [105]. If extensive data on air temperature, air velocity, and melt temperature were collected, it might be possible to construct an empirical correlation without an analysis. However, collecting such extensive data was beyond the scope of the present work. Hence, in order to concentrate on the capability of the present model, the on-line measured temperature profiles, where they are available, were used as the input parameter. Where they are not available, an empirical interpolation scheme was used, as will be discussed latter.

(B) Melt Viscosity

Since the phenomenon of deformation thinning is well-known [40,89-91], it is reasonable to use a deformation-thinning model to describe the rheological behavior. A widely used viscous thinning model [106-108], is expressed by the following equation:

$$\eta = \frac{\eta_o}{1 + [\, a\lambda |II_d|^{1/2} \,]^b} \qquad (5\text{-}5)$$

where η is the shear melt viscosity, λ is the relaxation time, II_d is the second invariant of the rate-of-strain tensor, **b** is the slope of the shear viscosity curve in the region of high shear rate, and **a** is an adjustable (empirical) factor. The parameter for the zero-shear viscosity, η_o, can be estimated from the asymptotic value of shear viscosity at small deformation rates. Furthermore, η_o may be expressed in the form of an Arrhenius type equation, which describes the temperature dependence; the crystallinity dependence was assumed to be of a form that produces a rapid viscosity increase with crystallization as described earlier.

$$\eta_o = \alpha 1 \exp\left(\frac{\beta 1}{T}\right) \exp\left[\alpha 2 \left(\frac{X}{X_f}\right)^{\beta 2} \right] \qquad (5\text{-}6)$$

where $\alpha 1$ and $\beta 1$ can be estimated from the curve of zero-shear viscosity versus temperature; X and X_f are the weight-fraction crystallinity and the ultimate crystallinity, respectively; $\alpha 2$ and $\beta 2$ are empirical factors which weight the influence of crystallinity. This type of viscosity equation was successfully used by Lambach [109] and by Hood [99] in the simulation of the melt spinning of polyethylene. A similar form has also been used by other investigations [6,40,89,91,110,111].

Based on the above statements, shear viscosity data are needed for estimating the parameters of **b**, $\alpha 1$ and $\beta 1$ in Equations(5-5) and (5-6). However, it should be noted that the rheological data for the three polyethylenes, as shown in Figures 3-1 ~ 3-3, are the "complex viscosity", $|\eta^*|$, (actually the magnitude of the complex viscosity), as measured by a parallel-plate oscillatory rheometer, rather than the steady shear viscosity. Cox and Merz [112] reported that curves of shear viscosity (η_s) versus shear rate (γ) are often nearly the same as curves of the magnitude of the complex viscosity ($|\eta^*|$) versus frequency (ω). There is not a basic physical understanding of this equivalent, although it seems to work quite well in most cases [113-119]. Finally the Cox-Merz rule can be expressed as:

$$\eta_s(\gamma) = |\eta^*(\omega)| \qquad (\omega = \gamma) \qquad (5\text{-}7)$$

According to the experimental data published in the literature [113-118] for linear and branched polyethylenes, it is found that the complex viscosity and the shear viscosity are in good agreement. Therefore, the thinning factor **b** in Equation(5-5) can be estimated from the slope of the complex viscosity curve in the region of high frequency; the factors $\alpha 1$ and $\beta 1$ can be

determined by the asymptotic value of complex viscosity at small deformation rate and the corresponding temperatures.

For LDPE, LLDPE, and HDPE, the values of factor **b** were estimated from the extreme right of the complex viscosity curves and are listed in Table 5-2. For determination of the factors of $\alpha 1$ and $\beta 1$, an asymptotic value of complex viscosity at low frequencies is needed. Because all of the complex viscosity curves in Figures 3-1 ~ 3-3 do not show clear plateaus, the complex viscosity values at ω = 0.1 rad/sec (that is, the lowest frequency measured) were taken as the asymptotic values. For each polyethylene, the complex viscosity values (at ω = 0.1 rad/sec) at various temperatures (that is, 160 ^{o}C, 170 ^{o}C, 180 ^{o}C, and 190 ^{o}C) are shown in Figure 5-7. Thus, the values of $\alpha 1$ and $\beta 1$ for these three polyethylenes can be determined by linear regression and are listed in Table 5-2.

The numerical values of the other adjustable factors in Equations(5-5) and (5-6) were obtained during the simulations, as will be discussed later; for completeness, however, values for $\alpha 2$, $\beta 2$, and $\mathbf{a}\lambda$ are shown now in Table 5-2. Since the effect of crystallinity on melt viscosity is not well known and is difficult to quantify, the factors of $\alpha 2$ and $\beta 2$ were adjusted so as to terminate the change of bubble radius at the frost line. For the three polyethylenes, the numerical values

Table 5-2 Summary of the numerical values of parameters used in the quantitative simulations (in Section 5.3) for the three polyethylenes.

Resin Type	α_1 (poise)	β_1 (K)	α_2 (-)	β_2 (-)	b (-)	$a\lambda$ (sec)	X_f (-)	K_o (sec^{-1})	C_3 (K^2)
LDPE	9.577	4,476	13.5	0.4	0.68	4.68	0.445	2,670	85,000
LLDPE	131.446	2,961	13.5	0.2	0.51	0.20	0.562	296,559	13,100
HDPE	337.575	2,746	13.5	0.2	0.55	5.10	0.731	2,231	62,000

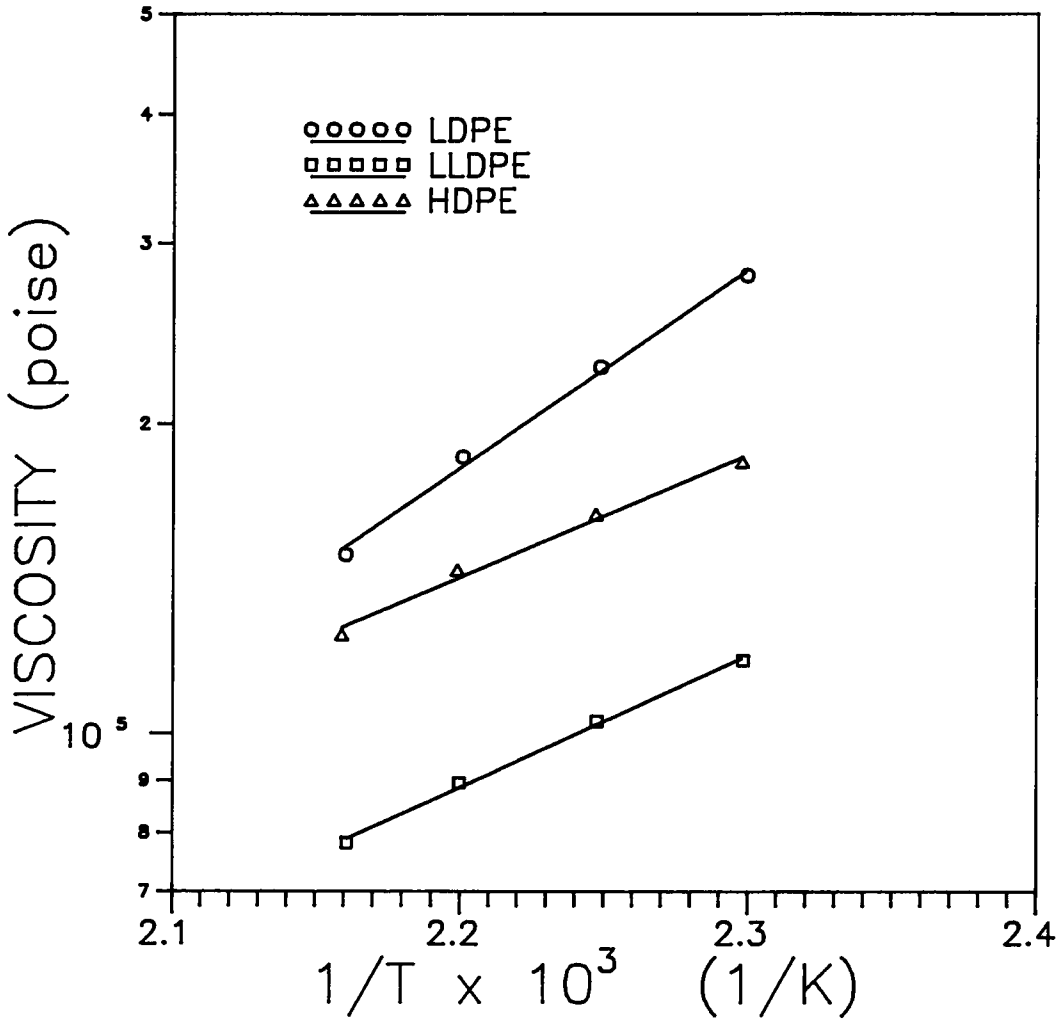

Figure 5-7 Complex viscosity values (at ω = 0.1 rad/s) at various temperatures for the three polyethylenes.

of the factor $a\lambda$, which is one of the factors controlling non-linearity of melt viscosity, were adjusted in order to obtain an optimum fitting of the overall on-line data.

Finally, the final weight-fraction crystallinity X_f in Equation(5-6) can be obtained from density by the following equation

$$X_f = \left(\frac{\rho-\rho_a}{\rho_c-\rho_a}\right)\left(\frac{\rho_c}{\rho}\right) \qquad (5-8)$$

where ρ_a and ρ_c are the theoretical densities of amorphous and crystalline phases, respectively. At 23 °C, ρ_a = 0.863 g/cm^3 and ρ_c = 1.000 g/cm^3 are taken for polyethylene [104]. The obtained values of X_f for LDPE, LLDPE, and HDPE are summarized in Table 5-2.

(C) Crystallization Kinetics

Since polyethylene is a semi-crystalline material, consideration of the crystallinity change needs to be included in the modelling. The crystallinity change along the machine direction can be estimated by Equation(2-67), in which the crystallization rate constant, K, can be expressed by a more complete form [89,91,99,120]:

$$K = K_o \exp\left[\frac{-U^*}{R(T-T_\infty)}\right] \exp\left[\frac{-C_3}{T\Delta T+C_o T^2 f_a{}^2}\right] \qquad (5-9)$$

in which f_a is the amorphous orientation factor; C_o is an empirical factor which is intended to account for the effect of molecular orientation on the crystallization rate.

The values of the parameters, K_o and C_3, in Equation(5-9) were obtained from Hood's study [99] involving quiescent crystallization of various polyethylenes. In Hood's study, the reported values of K_o and C_3 for the resins which have nearly the same densities as those used in this study were taken and shown in Table 5-2.

Furthermore, the stress-induced crystallization parameter, C_o, which characterizes the enhancement of crystallization rate due to orientation, is assumed to be zero. This assumption is based on two considerations. Firstly, comparing the measured take-up stresses in melt spinning and in film blowing [14,109], it is found that the stress in the melt during spinning is much higher (more than 50 times greater) than that in film blowing. Secondly, the value of C_o is difficult to quantify; usually, it is empirically given in modelling [91,99]. Therefore, for reasons of simplicity, the orientation term in Equation(5-9) is omitted.

Finally, based on the numerical values listed in Table 5-2, simulations of the profiles of bubble radius, thickness

and velocity were carried out. In the simulation, iterations (by adjusting the take-up force) were required in order to meet the desired take-up speed, that is, the experimentally pre-set take-up speed. The numerical values for the rheological parameter $a\lambda$ and for the crystallinity parameters $\alpha 2$ and $\beta 2$ were chosen to fit the radius profile data. These numerical values were shown previously (Table 5-2).

For LDPE, comparisons between the on-line data and the simulation results are shown in Figures 5-8 ~ 5-10. In Figure 5-8, for each case (that is, case(A), case(B) and case(C) defined in Section 4.5), the calculated radius profiles (as shown by a solid line) are compared to the on-line data (as shown by the discrete data points connected with a dashed line). It can be seen that there is a very good agreement between them. Following the same definitions for the symbols used in Figure 5-8, it can be seen that there still are good agreements between the predictions and the experimental results for the film thickness and velocity, as shown in Figures 5-9 and 5-10, respectively.

For LLDPE, comparisons between the on-line data and the simulation results for radius, thickness and velocity profiles are shown in Figures 5-11 ~ 5-13, respectively. In Figure 5-11, for three cases using LLDPE, the calculated radius profiles (as shown by solid lines) are compared to the on-line

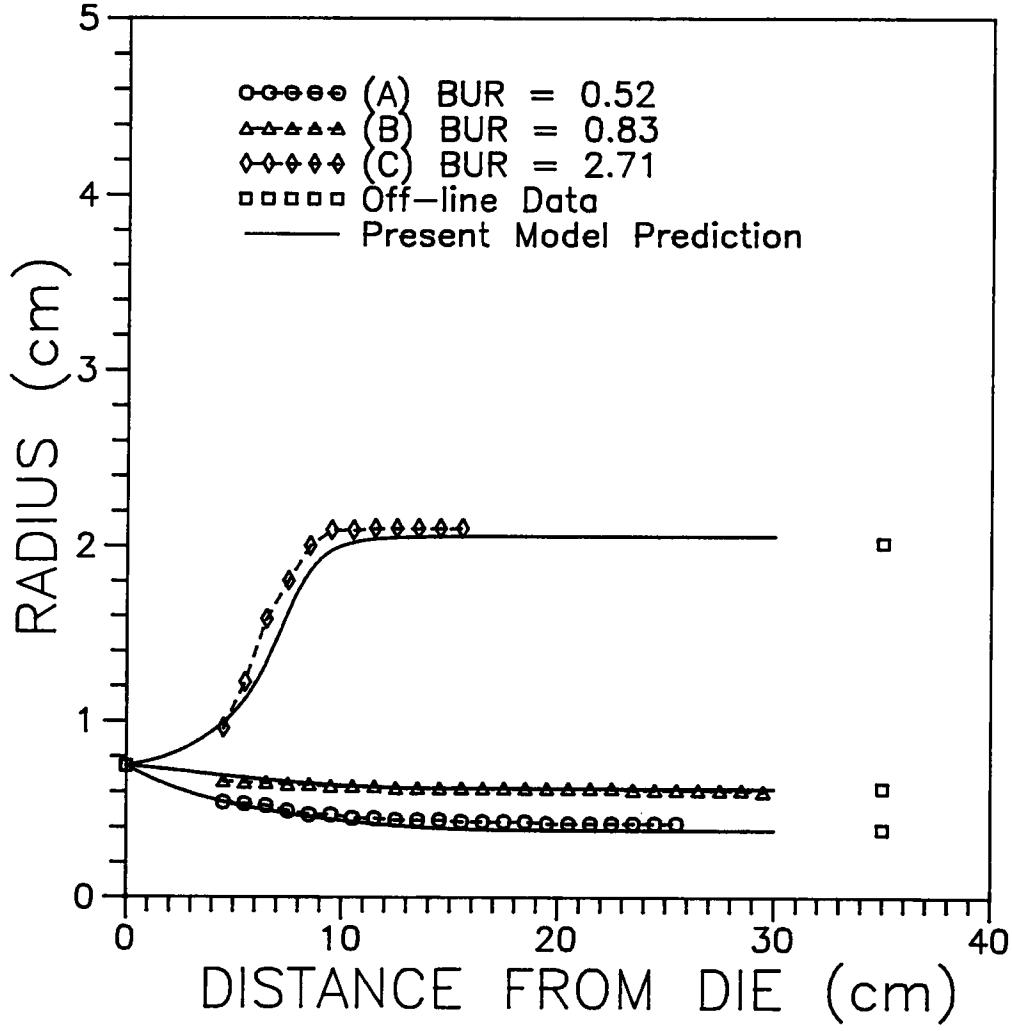

Figure 5-8 Comparisons of the predicted radius profiles to the on-line measured data for the three cases using LDPE.

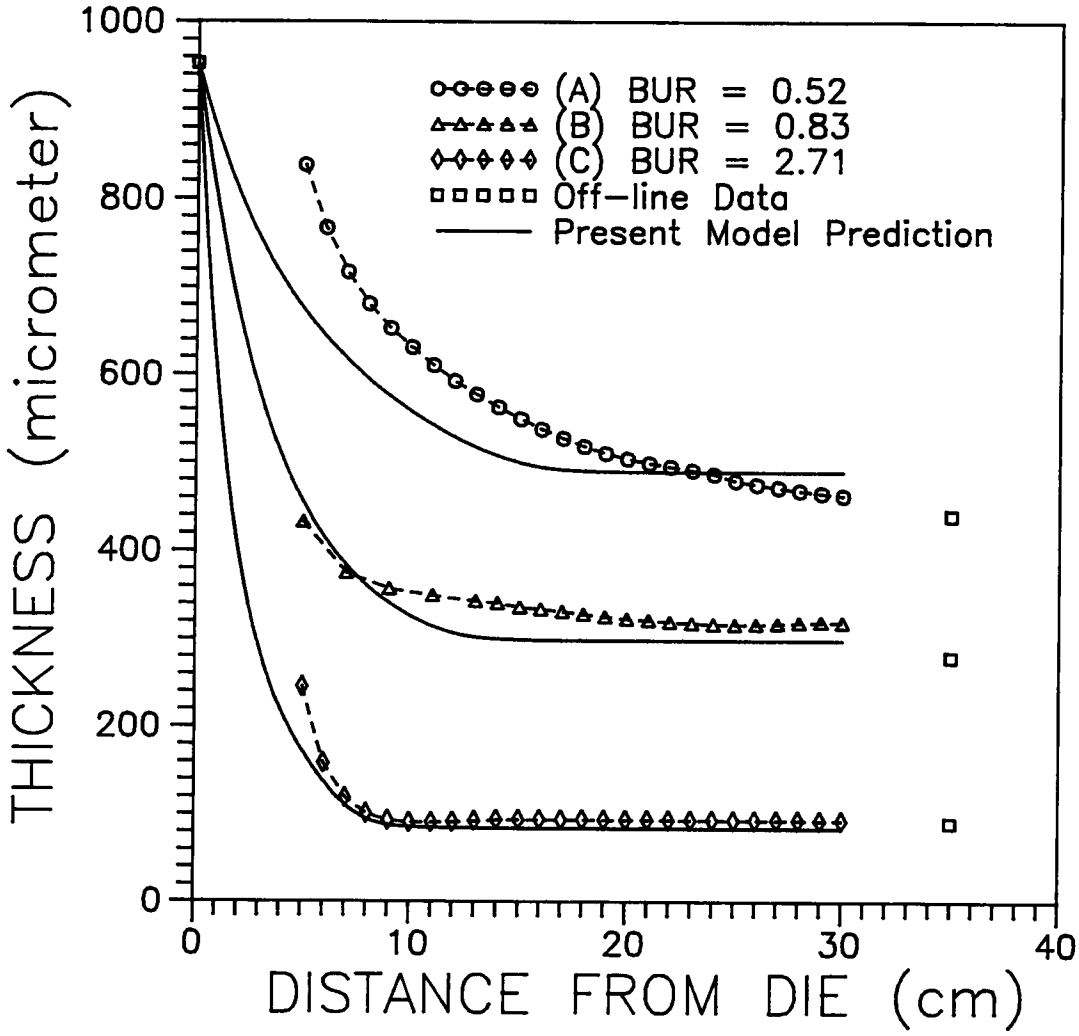

Figure 5-9 Comparisons of the predicted thickness profiles to the on-line data for the three cases using LDPE.

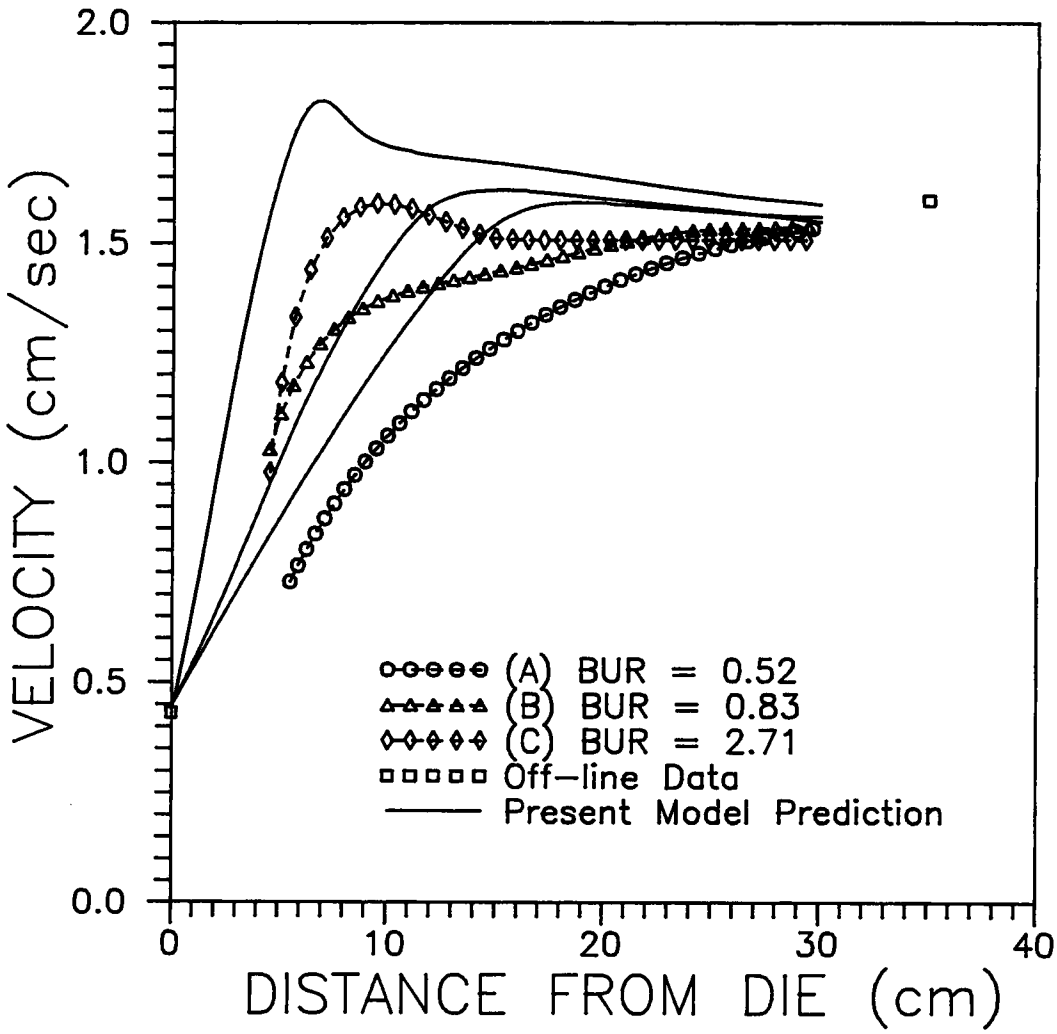

Figure 5-10 Comparisons of the predicted velocity profiles to the on-line measured data for the three cases using LDPE.

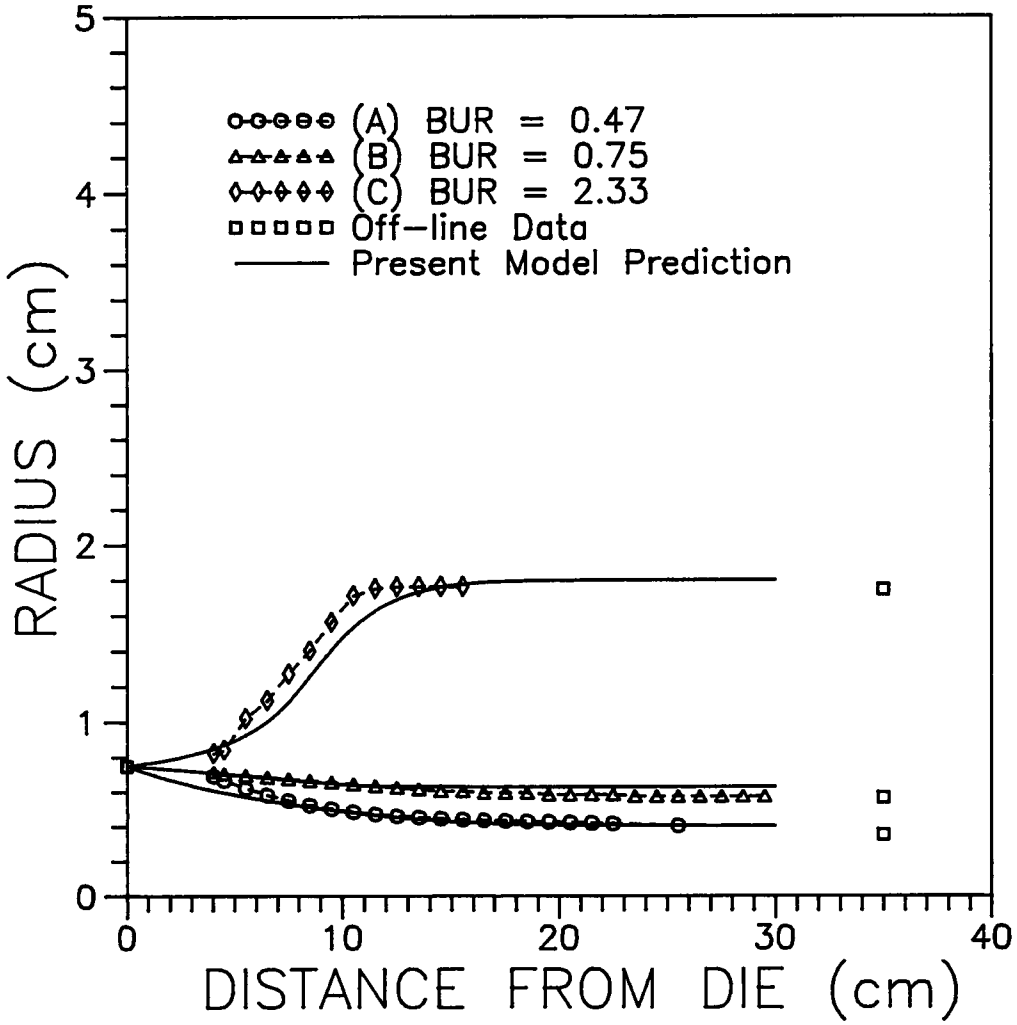

Figure 5-11 Comparisons of the predicted radius profiles to the on-line measured data for the three cases using LLDPE.

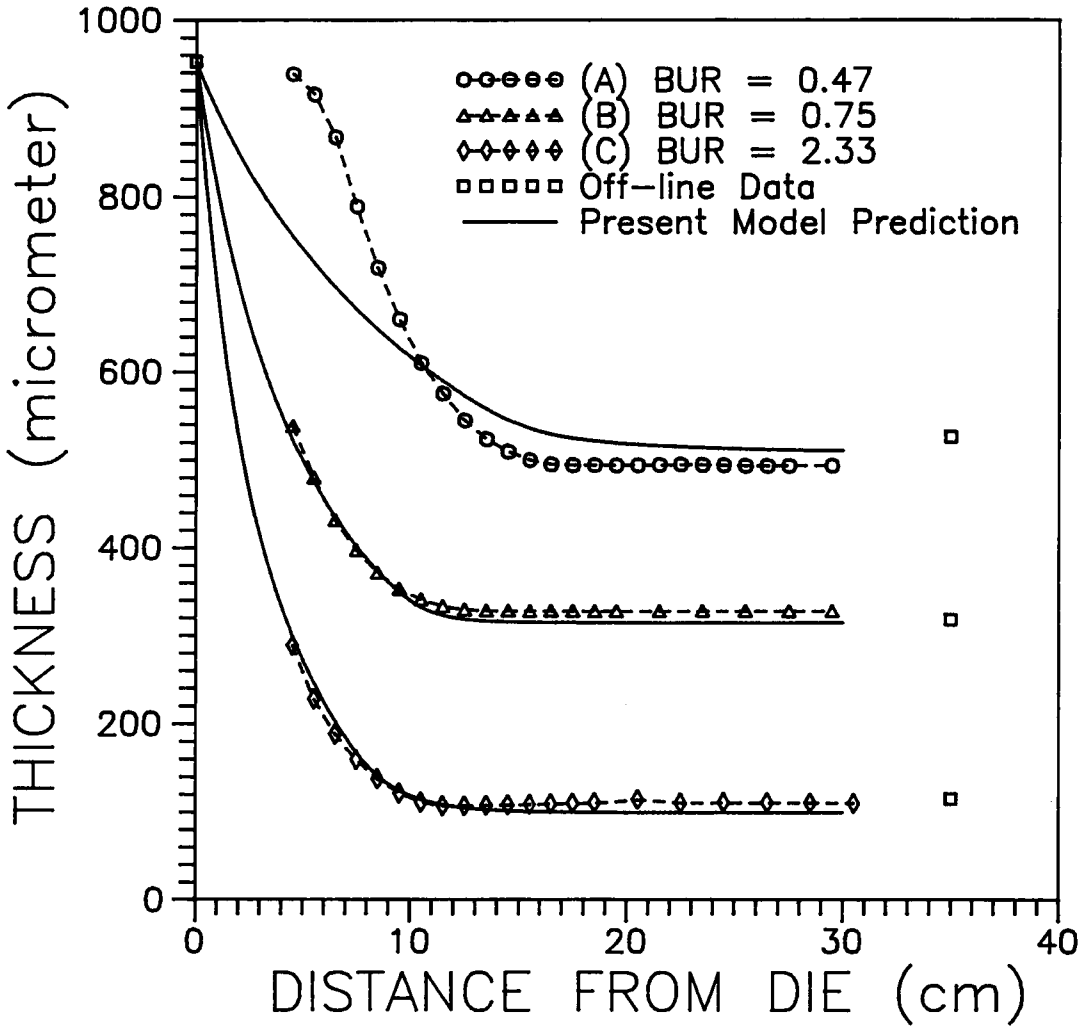

Figure 5-12 Comparisons of the predicted thickness profiles to the on-line data for the three cases using LLDPE.

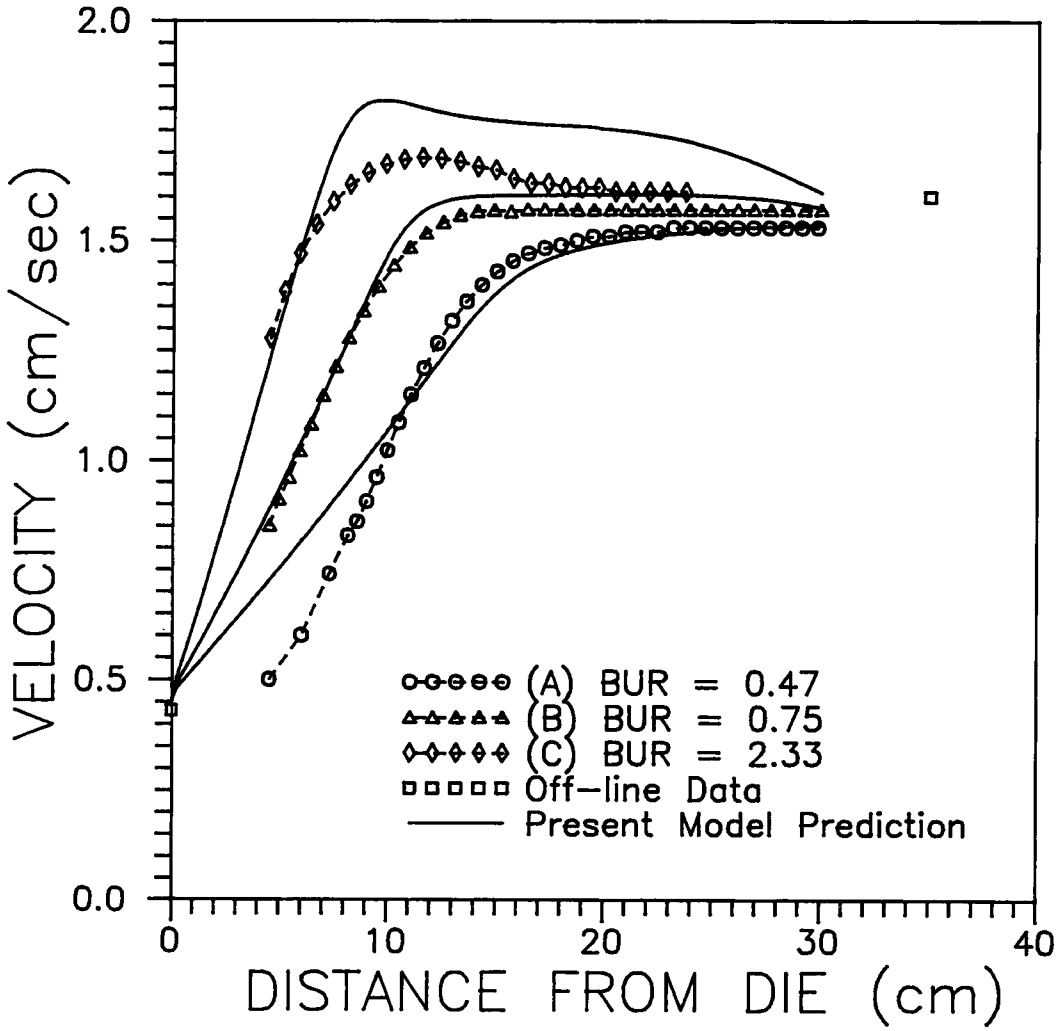

Figure 5-13 Comparisons of the predicted velocity profiles to the on-line measured data for the three cases using LLDPE.

data (as shown by the discrete data points connected with dashed lines). It can be seen that there is a very good agreement between them. Moreover, both Figures 5-12 and 5-13 also show that the simulated profiles of the film thickness and velocity are in good agreement with the on-line measured data for each case.

5.3.2 Simulation of Inflation Pressure vs. Blow-up Ratio

It should be noted that the calculated profiles of radius, thickness and velocity in the preceding section, Section 5.3.1, are based on on-line measured temperature profiles. In the case of generating an entire curve of pressure versus blow-up ratio, appropriate parameters for the heat transfer process must be interpolated between the measured temperature profiles. For simplicity, an empirical cooling-rate factor ζ will be introduced in the following paragraphs for the purpose of interpolation of the temperature profiles.

(A) Estimation of Cooling-rate Factor ζ

Without the effect of the latent heat of crystallization, it is assumed that the temperature distribution along the machine direction can be described by the following empirical equation:

$$\frac{T - T_{ao}}{T_o - T_{ao}} = \exp[\ -\zeta Z\ ] \qquad (5\text{-}10)$$

where T is the local temperature of the film at the distance of Z (cm) above the die; ζ is an empirical cooling-rate factor; T_o is the extrusion temperature; T_{ao} is the cooling-air temperature at the nozzle of the cooling ring. Thus, according to Equation(5-10), the cooling-rate factor, ζ, can be determined from the measured film temperatures T, the measured cooling-air temperature T_{ao}, and the pre-set die temperature T_o. For all of the six on-line temperature profiles of LDPE and LLDPE (as shown in Figures 4-11 and 4-12 in Chapter 4), the extrusion temperatures were all controlled at 190 ^oC; and the measured air temperature at the nozzle of the cooling ring was 58 ^oC. Hence, for the temperature data of each run, the part of the data, which is prior to the occurrence of an significant temperature plateau (crystallization), can be re-plotted in the way of $\ln\left(\frac{T - T_{ao}}{T_o - T_{ao}}\right)$ versus Z (the distance above the extrusion die), as shown in Figures 5-14 and 5-15 for LDPE and LLDPE, respectively. Within experimental scatter, all of the dimensionless temperature curves in these two figures are approximately linear. The scattering of data points, as shown in both Figure 5-14 and 5-15, is probably due to fluctuations

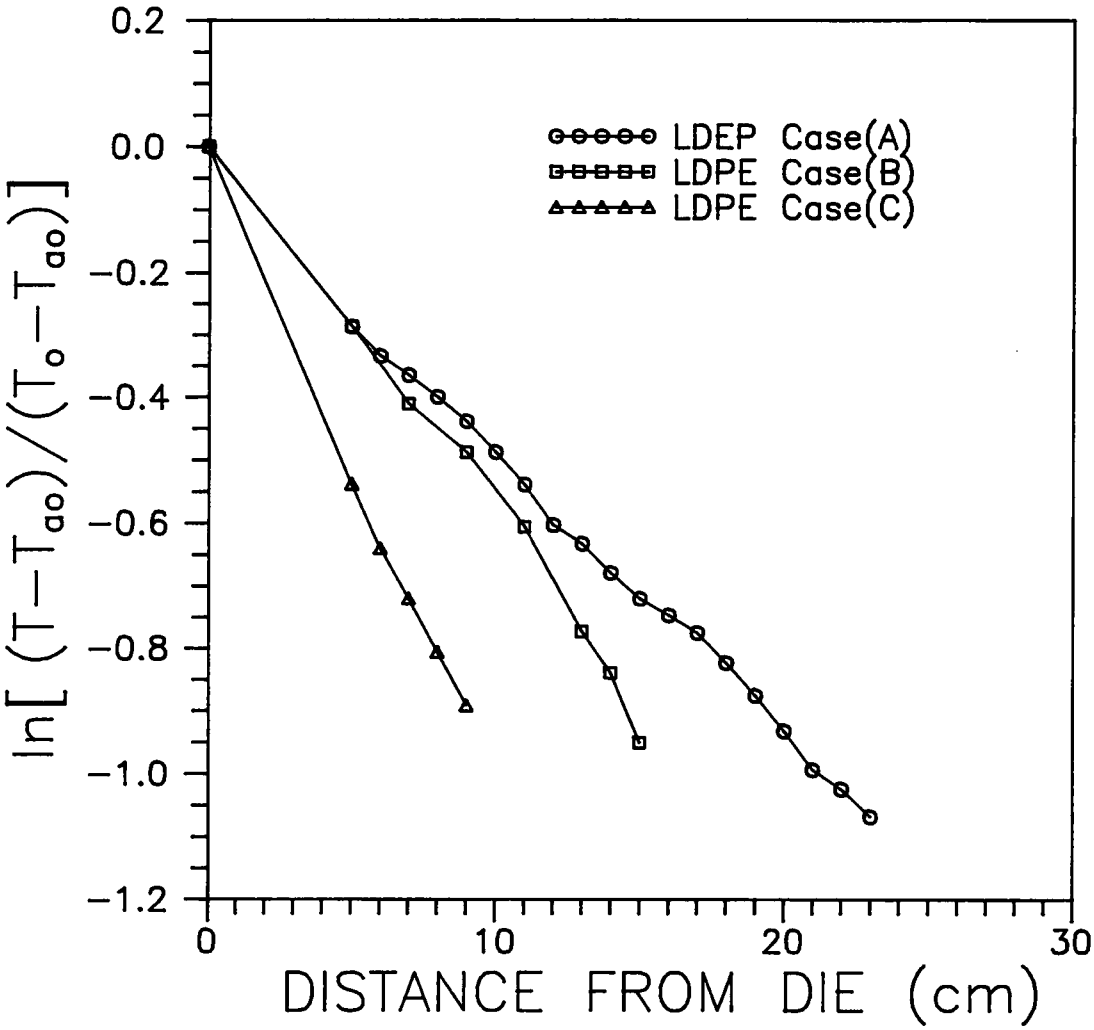

Figure 5-14 Dimensionless temperature profiles generated by Equation(5-10) for the three cases using LDPE.

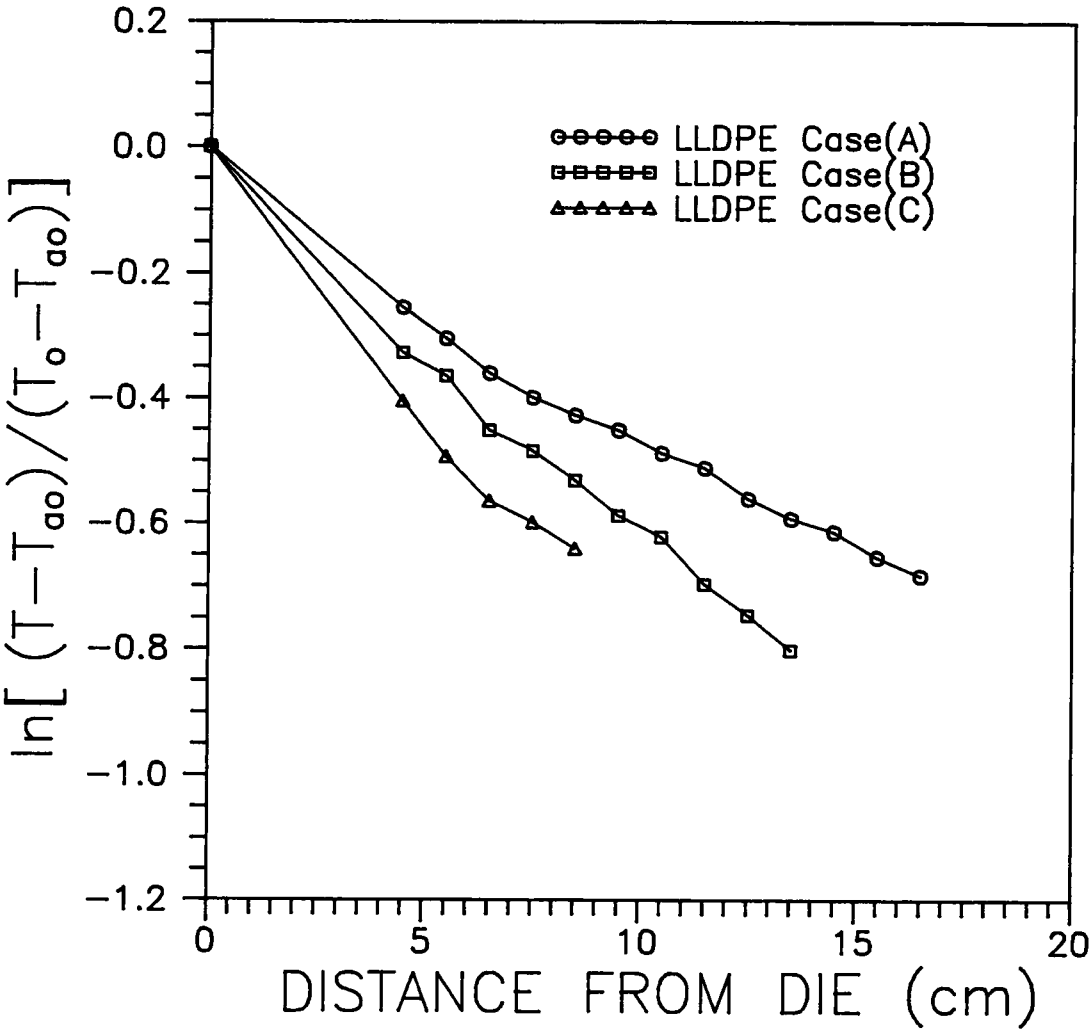

Figure 5-15 Dimensionless temperature profiles generated by Equation(5-10) for the three cases using LLDPE.

in the film temperature during processing, which are indicated by the degree of smoothness of the original temperature profiles in Figures 4-11 and 4-12. As a matter of fact, a significant fluctuation in the film temperature (up to ±6 ^{o}C) has been reported in another investigation [7]. These fluctuations are probably due to the non-uniformity of the surrounding cooling air and possible minor variations of the melt flow rate and the extrusion temperature. Therefore, according to the shape of the curves in Figures 5-14 and 5-15, it will be reasonable to assume that the cooling-rate factor ζ is constant for each run. That is, the value of ζ for each case can be determined from the slope of each curve in Figures 5-14 and 5-15. However, due to the scattering, the data points for each run will be bracketed by two straight lines, as shown in Figures 5-16 and 5-17 (for LDPE and LLDPE, respectively), to obtain a possible range of the ζ value for each run. Furthermore, associating the obtained ζ values with the corresponding final bubble radius, it is very interesting to note that the cooling-rate factor, ζ, is strongly dependent on the bubble size, as shown in Figure 5-18. Finally, this figure provides the following empirical equation:

$$\zeta = 2.781 \times 10^{-2} \ln(R_L) + 7.613 \times 10^{-2} \qquad (5\text{-}11)$$

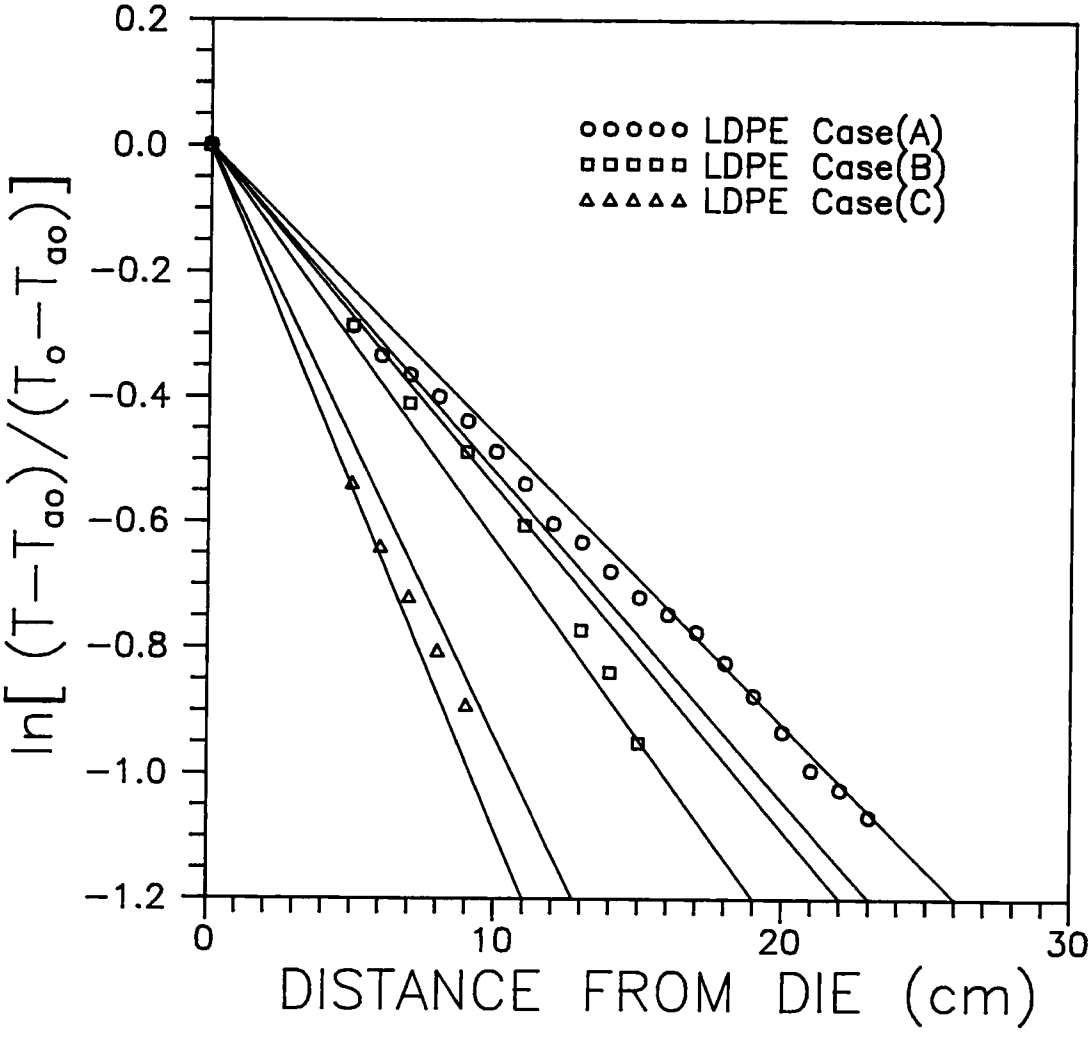

Figure 5-16 Ranges of the dimensionless temperature profiles for the three cases using LDPE.

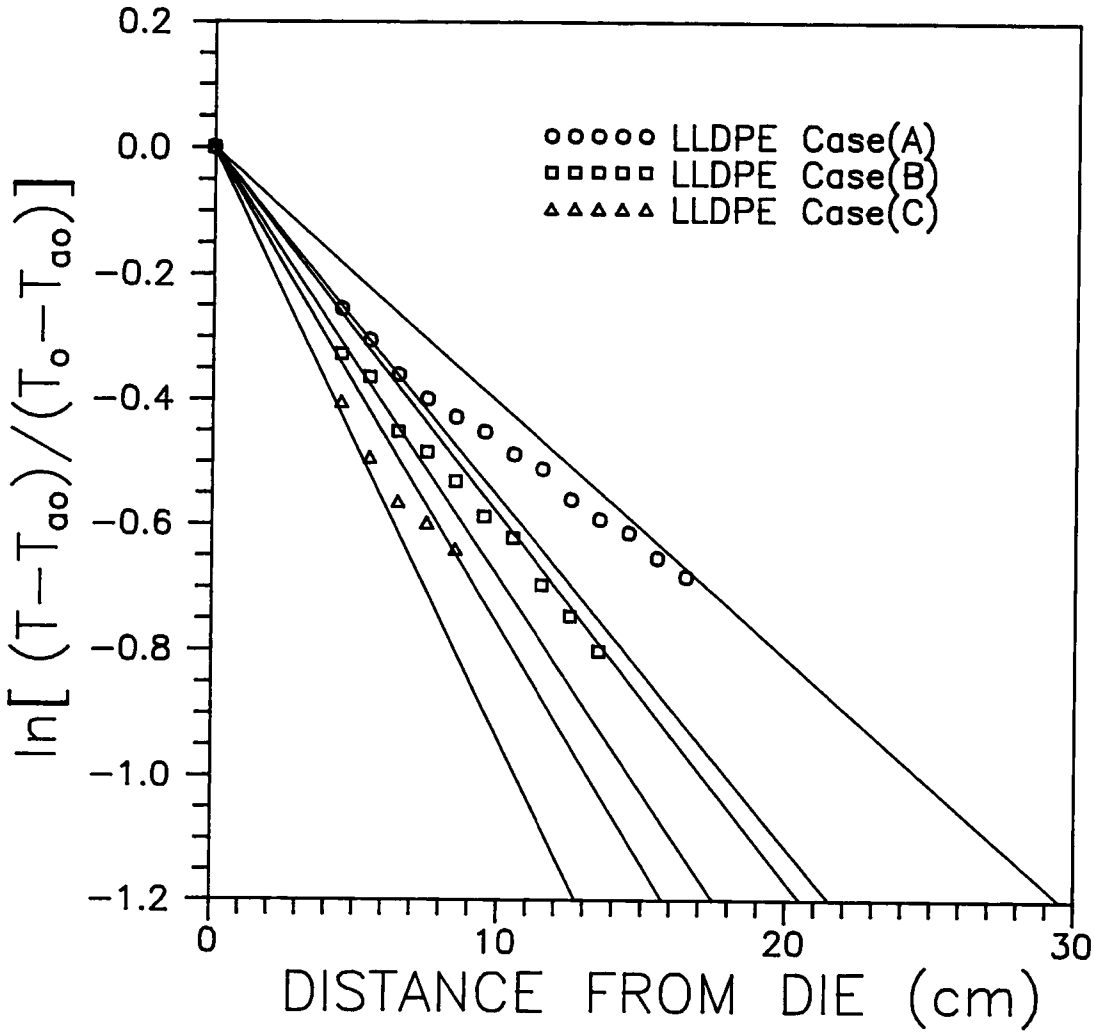

Figure 5-17 Ranges of the dimensionless temperature profiles for the three cases using LLDPE.

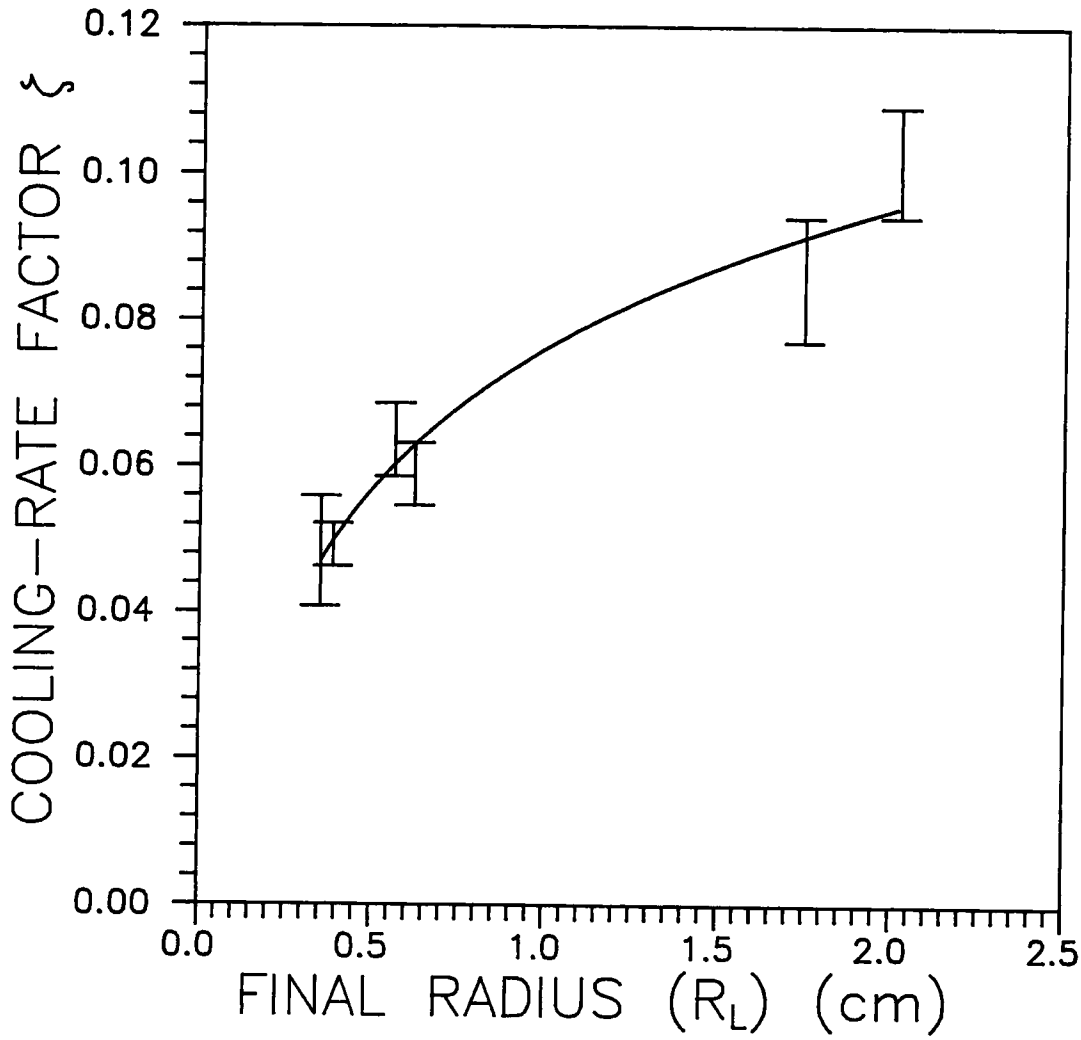

Figure 5-18 Empirical relationship between the cooling-rate factor ζ and the final bubble radius R_L.

where ζ is the cooling-rate factor (in units of cm^{-1}) and R_L is the final radius of the bubble (in units of cm).

Therefore, according to the assumption of Equation(5-10), the first two terms on the right-hand side of the energy balance equation, Equation(2-75), can be replaced with the cooling-rate factor ζ by inserting Equation(5-10) into the following equation:

$$-U(T-T_{air}) - \varepsilon\sigma(T^4-T_r^4) = \left(\frac{WC_p}{2\pi R}\right)\frac{dT}{dZ} \qquad (5\text{-}12)$$

Thus, the resulting expression for energy balance is

$$\left(\frac{WC_p}{2\pi R}\right)\frac{dT}{dZ} = \left(\frac{WC_p}{2\pi R}\right)[-\zeta(T_o-T_{ao})\exp(-\zeta Z)] + \left(\frac{W\Delta H_f}{2\pi R}\right)\frac{dX}{dZ} \qquad (5\text{-}13)$$

where T_o and T_{ao} are 190 °C and 58 °C for this study, respectively. Finally, a first-order temperature differential equation can be obtained

$$\frac{dT}{dZ} = [-132\zeta \exp(-\zeta Z)] + \left(\frac{\Delta H_f}{C_p}\right)\frac{dX}{dZ} \qquad (5\text{-}14)$$

Thus, Equation(2-78), one of the system governing equations, can be replaced with the empirical equation, Equation(5-14). Hence, incorporating Equation(5-14) with Equations(2-67), (2-

76) and (2-77), computer simulation of the entire curve of pressure versus blow-up ratio can be carried out. However, in simulation, it should be noted that the empirical cooling-rate factor ζ in Equation(5-14) is correlated to the final bubble radius (R_L) by Equation(5-11). Therefore, an initially guessed R_L value will be required for calculation; and iterations for adjusting the prior guessed R_L are needed until it meets the final radius calculated by the model.

For three polyethylenes, LDPE, LLDPE, and HDPE, the simulated curves of ΔP vs. BUR are compared to their corresponding experimental data, as shown in Figures 5-19, 5-20 and 5-21, respectively. The numerical values used in simulation are the same as that listed in Table 5-2. From these three figures, it can be seen that, generally speaking, the predicted curves show reasonably good agreement with the experimental results. These comparisons indicate that the present model is able to describe the actual relationship between the inflation pressure and the bubble size.

However, making a detailed quantitative comparison, some discrepancy between predictions and experiments can be seen in Figures 5-19 ~ 5-21. This discrepancy is attributed to the over-simplified assumption for the film temperature (that is, the use of the empirical cooling-rate factor, ζ).

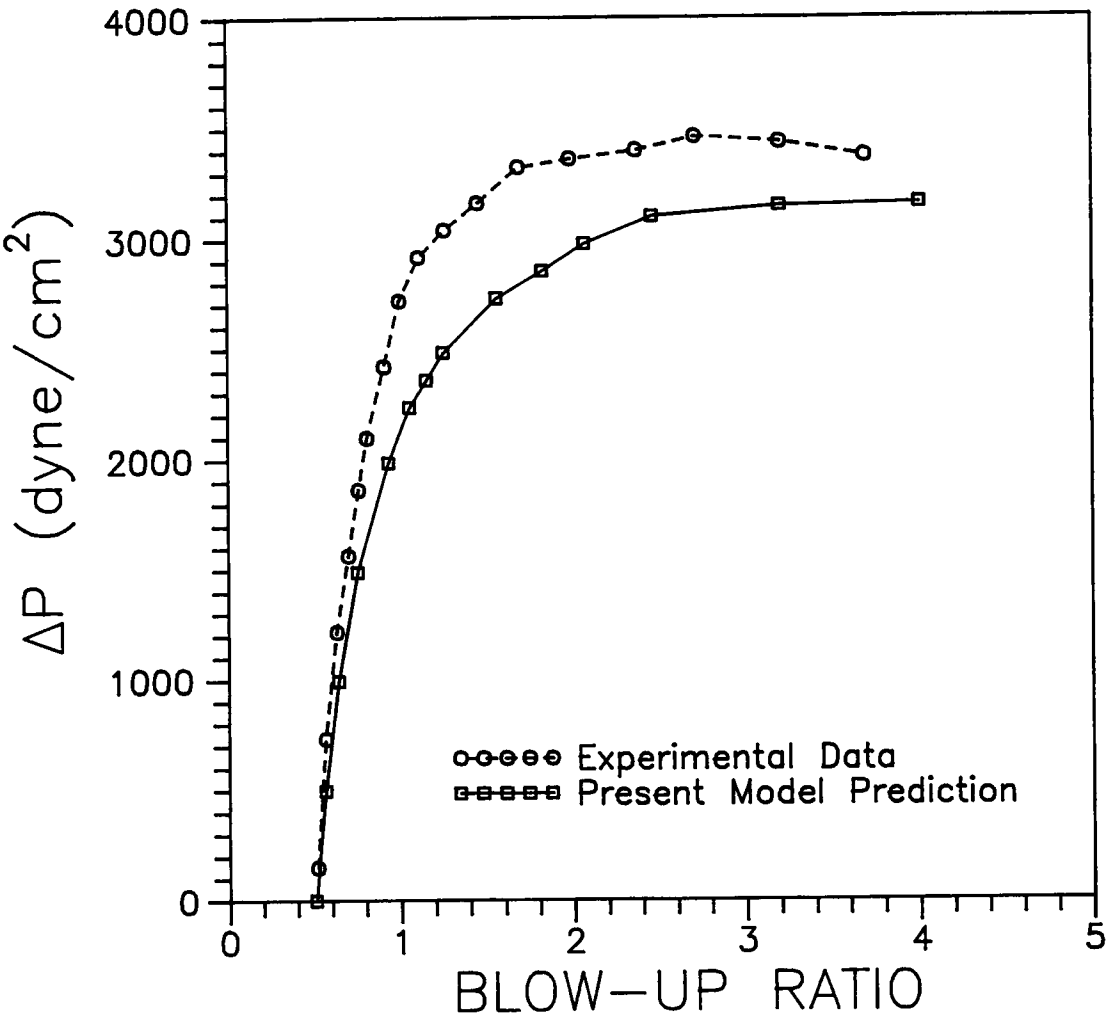

Figure 5-19 Comparison of the predicted ΔP vs. BUR curve to the experimental data for LDPE using the present model.

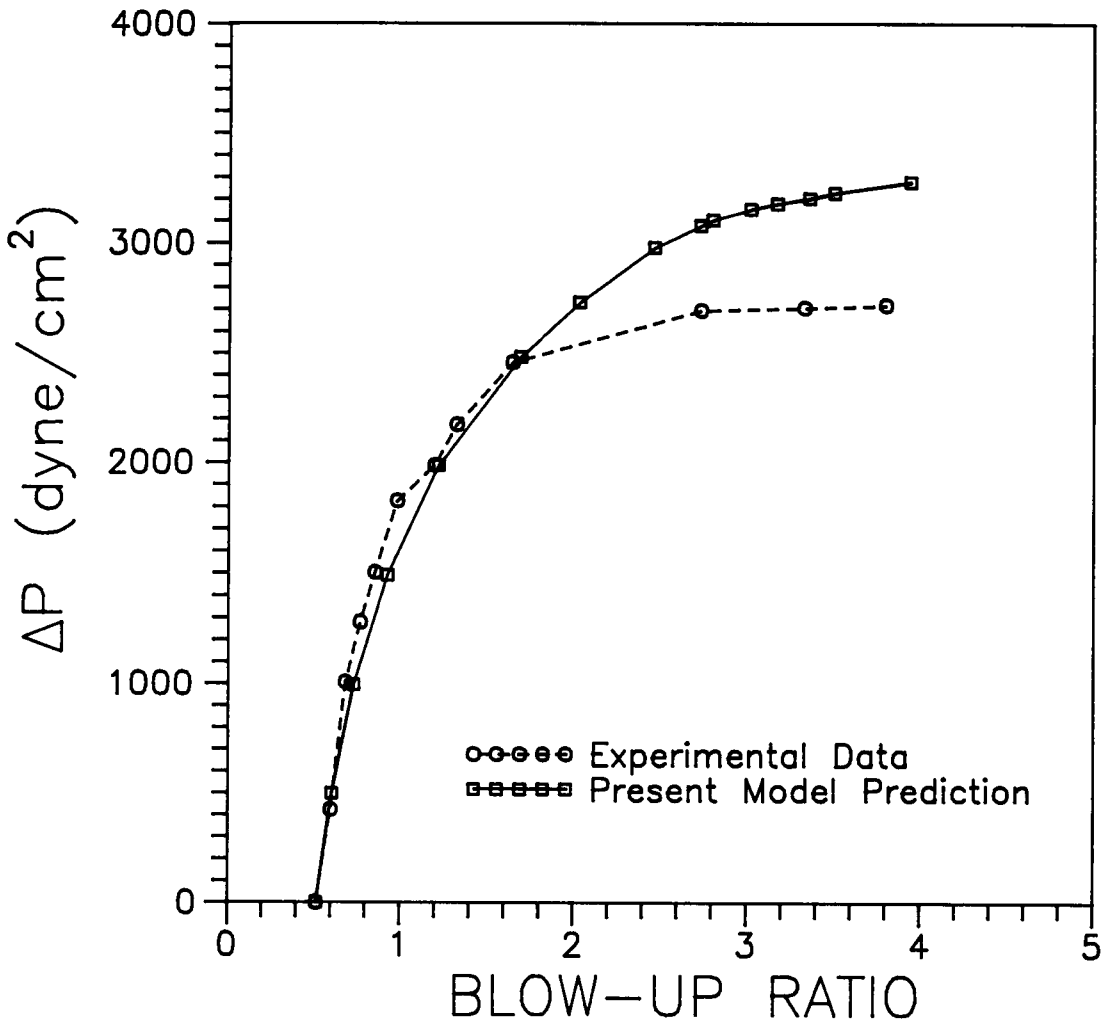

Figure 5-20 Comparison of the predicted ΔP vs. BUR curve to the experimental data for LLDPE using the present model.

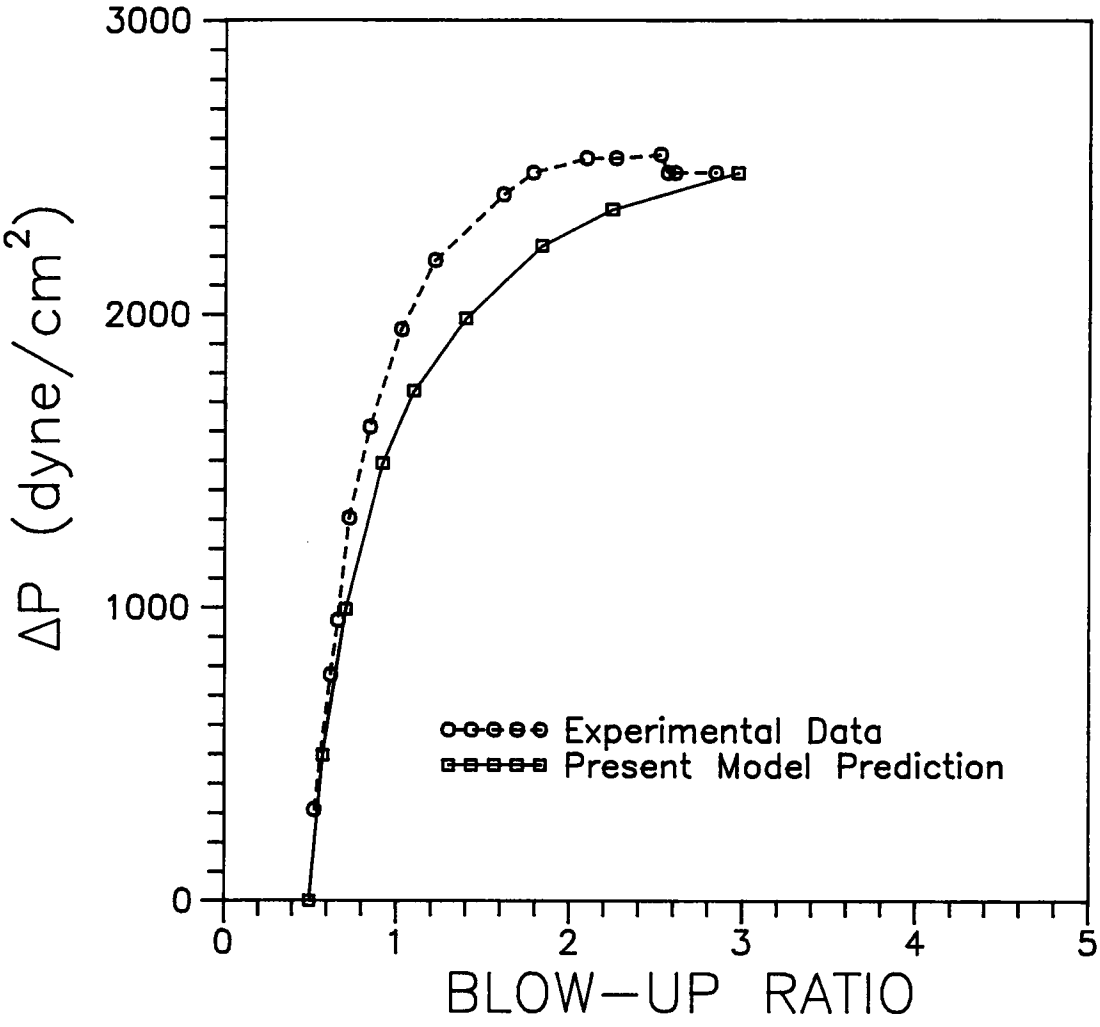

Figure 5-21 Comparison of the predicted ΔP vs. BUR curve to the experimental data for HDPE using the present model.

5.3.3 Comparison of Viscosity Used in Model to Complex Viscosity

The two preceding sections, Sections 5.3.2 and 5.3.3, have shown that the prediction of the present model and the experimental data are in a good agreement. It is important to check whether the viscosity values used in the calculation in the two preceding sections are of reasonable magnitude. Hence, the measured complex viscosity curves (equivalent to the shear viscosity by the Cox-Merz Rule), as shown in Figures 3-1 ~ 3-3 for three polyethylenes, will be used as a basis of comparison. The curve of shear viscosity versus shear rate generated by Equation(5-5), which is used in the present modelling to describe the rheological behavior, will be compared to the measured complex viscosity data.

To carry out the calculation of Equation(5-5) for the case of shear viscosity, the second invariant of deformation-rate tensor for simple shear flow will be required. According to the definition of deformation rate, Equation(2-25), the following expression for the simple shear flow can be obtained:

$$d_{12} = d_{21} = \gamma \qquad (5\text{-}15)$$

where γ is the shear rate, the subscripts "1" and "2" represent the flow direction and the transverse direction, respectively. Thus, following the definition of the second invariant of deformation-rate tensor II_d, Equation(4-4), the following can be obtained

$$II_d = -\gamma^2 \qquad (5\text{-}16)$$

for the case of simple shear flow. Thus, based on Equation(5-16) and the associated rheological parameters listed in Table 5-2, the shear viscosity curves can be generated by Equation(5-5). Taking the temperature of 190 ^{o}C, for example, the calculated shear viscosity curves for LDPE, LLDPE and HDPE are shown by the solid lines in Figures 5-22, 5-23 and 5-24, respectively. All of these three figures indicate that the shear viscosity curves generated by Equation(5-5) are of the same order of magnitude as the measured complex viscosity data which is shown by the circle points connected with dashed lines. Especially, Figure 5-23, for the material of LLDPE, shows a very good agreement between the two curves.

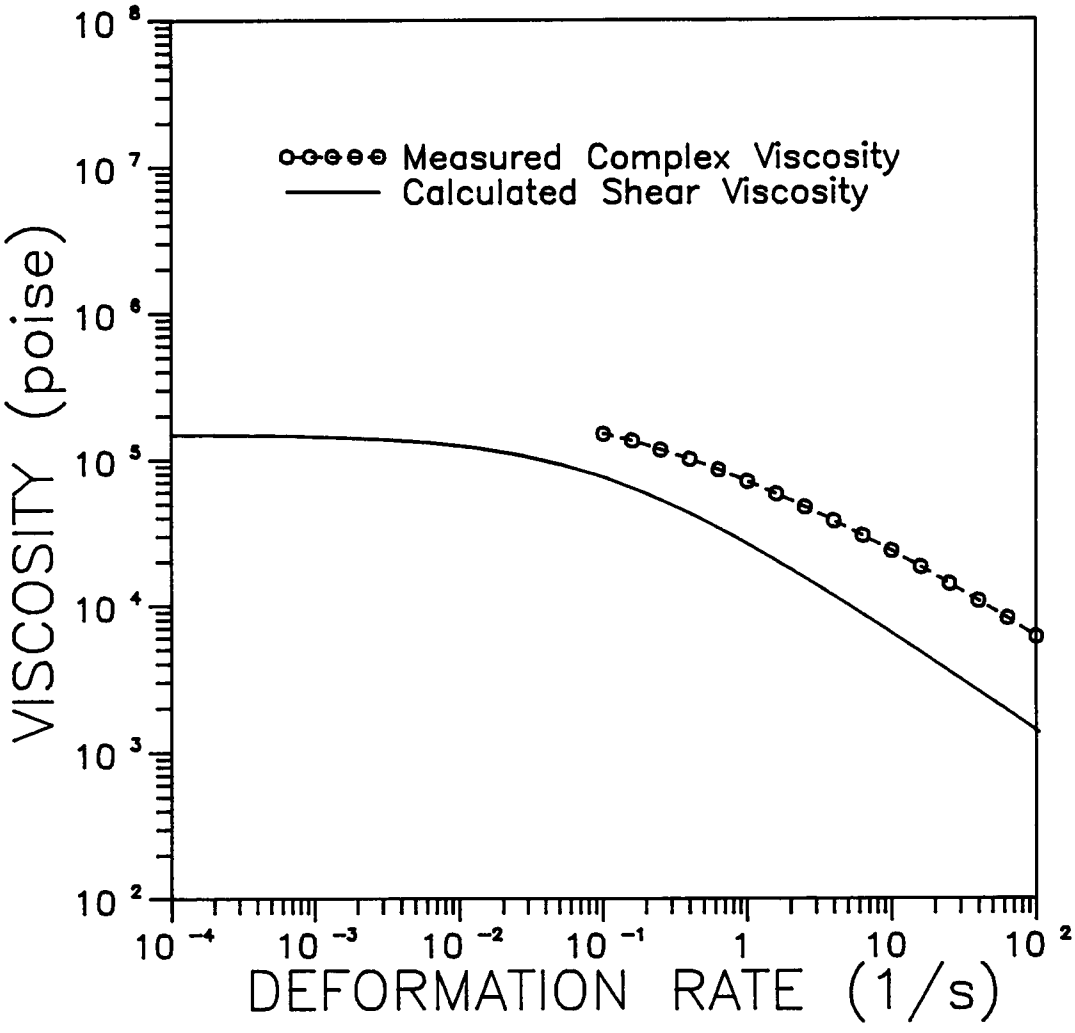

Figure 5-22 Comparison of the shear viscosity generated by the rheological equation to the measured complex viscosity for LDPE.

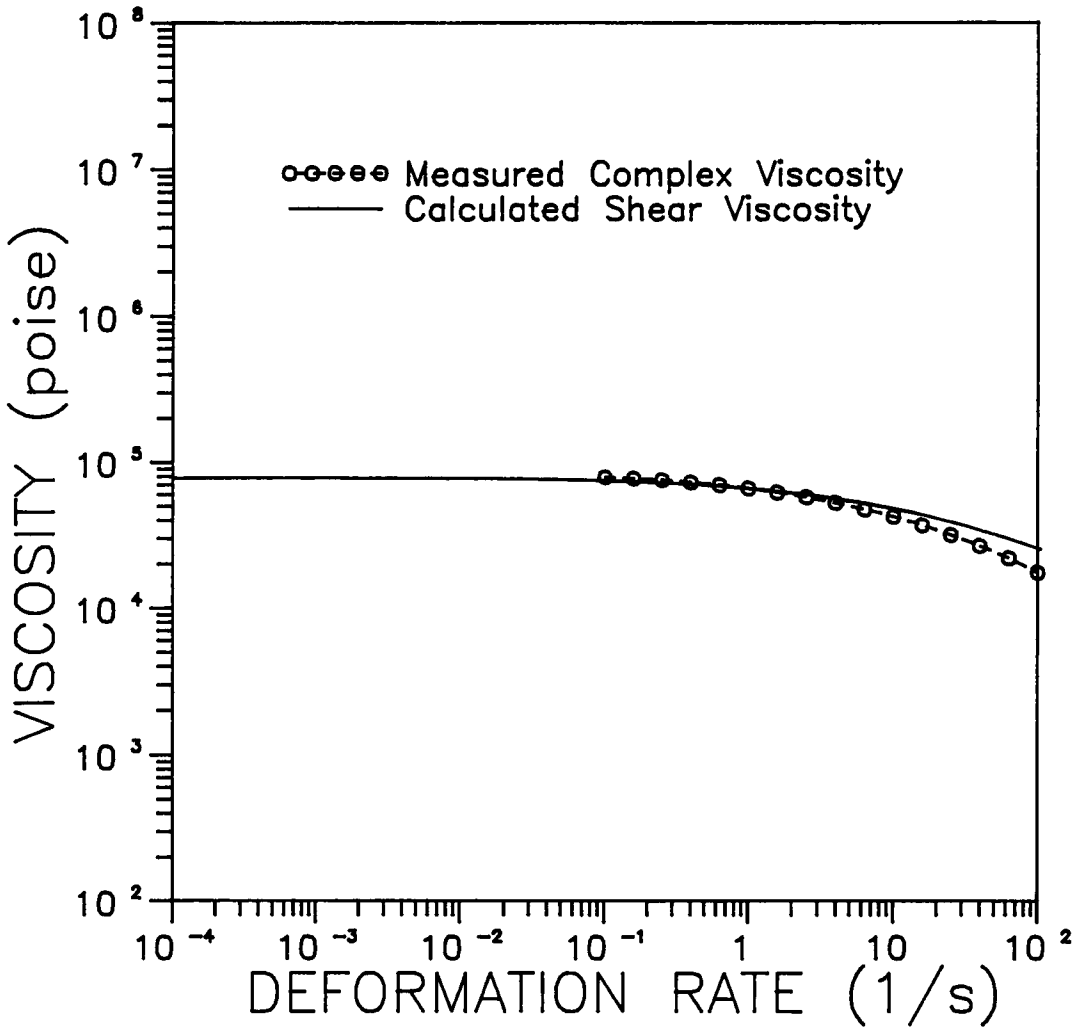

Figure 5-23 Comparison of the shear viscosity generated by the rheological equation to the measured complex viscosity for LLDPE.

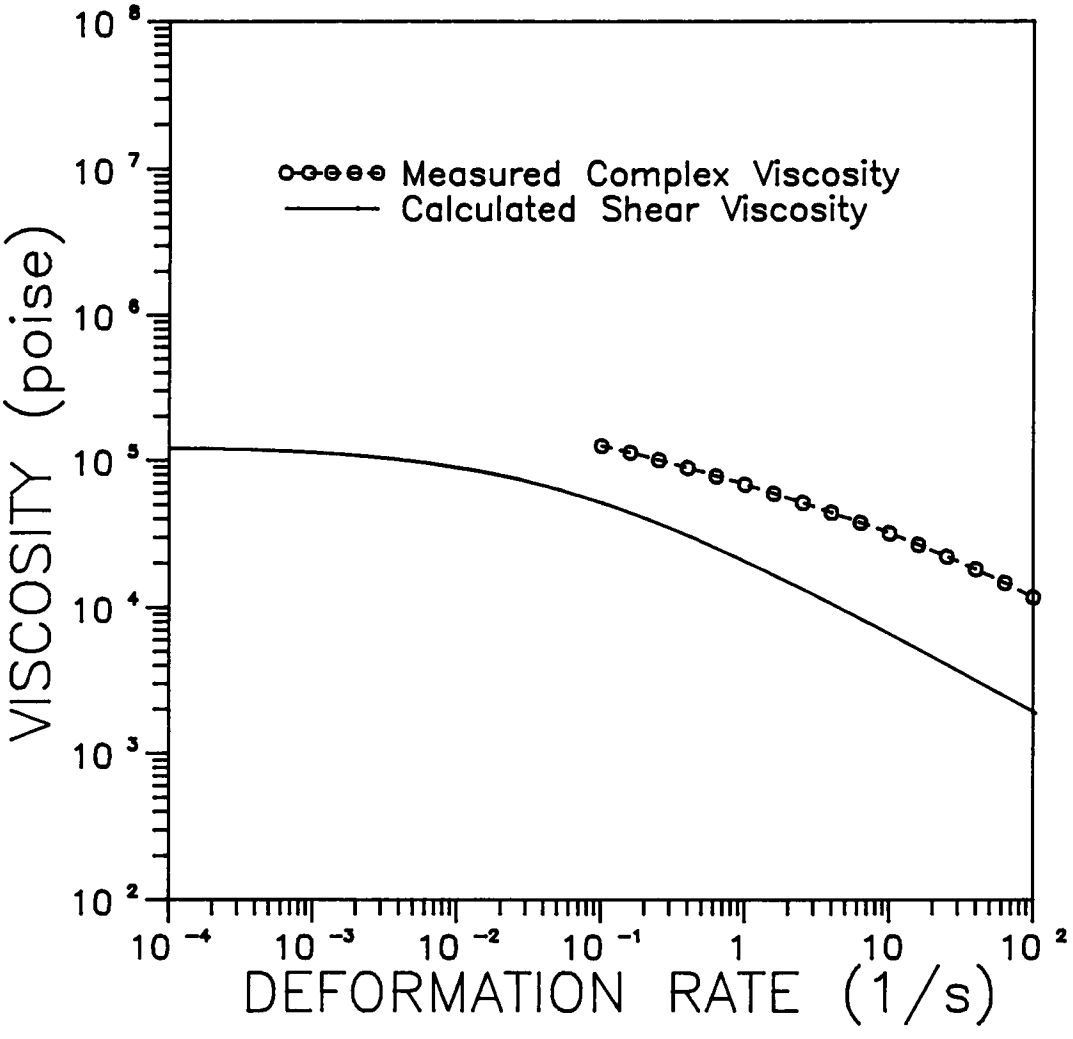

Figure 5-24 Comparison of the shear viscosity generated by the rheological equation to the measured complex viscosity for HDPE.

5.4 FURTHER IMPLICATIONS OF THE PRESENT MODEL

The preceding section, Section 5.3, has shown that the present model is able to quantitatively describe both the general picture — the pressure vs. blow-up ratio curve and the detailed profiles of radius, thickness and velocity very well. In this section, the implications of the present model will be further explored. The effects of the rheological properties (such as the viscosity and the thinning), and the processing parameters (such as the extrusion temperature and the external cooling rate) will be investigated. The theoretical results in the present section are supported by the experimental observations in the range where they are available, but the discussion here considers more general results.

In order to make the prediction meaningful and close to the practical physical picture, the numerical values of the material and processing parameters will be similar to those used previously (for the three polyethylenes). The numerical values used in this section are summarized in Table 5-3, in which the definition of the symbols are the same as before. It should be noted that in order not to complicate the overall picture, the heat transfer coefficient U (in the energy balance, Equation(2-51)) is assumed to be a constant, i.e., U

Table 5-3 Summary of the numerical values of parameters used in the further qualitative simulations (in Section 5.4) using the present model.

PROCESSING PARAMETERS	MATERIAL PARAMETERS
R_o: 0.746 cm	α_1: 9.577 poise
H_o: 950 μm	(α_1: 9.577, 6.385, 14.366 poise in Section 5.4.4)
T_o: 190 °C	β_1: 4,476 K
(T_o: 170, 190, 210 °C in Section 5.4.3)	α_2: 13.5
W: 0.15 g/sec	β_2: 0.4
T_{air}: 49 °C	aλ: 5.0 sec
T_r: 30 °C	b: 0.75
U: 0.001 cal/cm^{2}sec°C	(b: 0.60, 0.70,0.75 in Section 5.4.2)
(U: 0.5, 1.0, 2.0 x10^{-3} cal/cm^{2}sec°C in Section 5.4.5)	X_f: 0.445
TUR: 4.0	K_o: 2,670 sec^{-1}
(TUR: 1.0, 2.0, 4.0, 8.0 in Sections 5.4.1 and 5.4.2)	C_3: 85,000 K^2

= 1.0 x 10^{-3} (cal/cm^2sec^{o}C). This is a typical value estimated from the present study and also from earlier investigations [6,14,27,28,30]. Based on this assumption, the influence of take-up speed, melt viscosity, extrusion temperature, and cooling rate on the relationship between inflation pressure and bubble radius will be examined.

5.4.1 Influence of Take-up Ratio

The take-up ratio (TUR), defined as the ratio of the final axial velocity (i.e., the take-up speed) to the initial velocity at the die exit, is one of the important processing parameters. It not only controls the stretch ratio in the machine direction, but also interacts with the other key parameters, such as the inflation pressure and the bubble radius. In this sub-section, the melt is simply assumed to be a Newtonian fluid; further investigation for a thinning fluid will be given in the next sub-section. Thus, for the Newtonian fluid, the numerical values of the thinning parameters, **b** and **a**λ, are equal to zero.

Figure 5-25 shows the predicted ΔP vs. BUR curves under the four different take-up ratios, 1.0, 2.0, 4.0, and 8.0. It can be seen that the entire ΔP vs. BUR curve shifts upwards when the take-up ratio increases. That is, to obtain a desired bubble radius the required inflation pressure

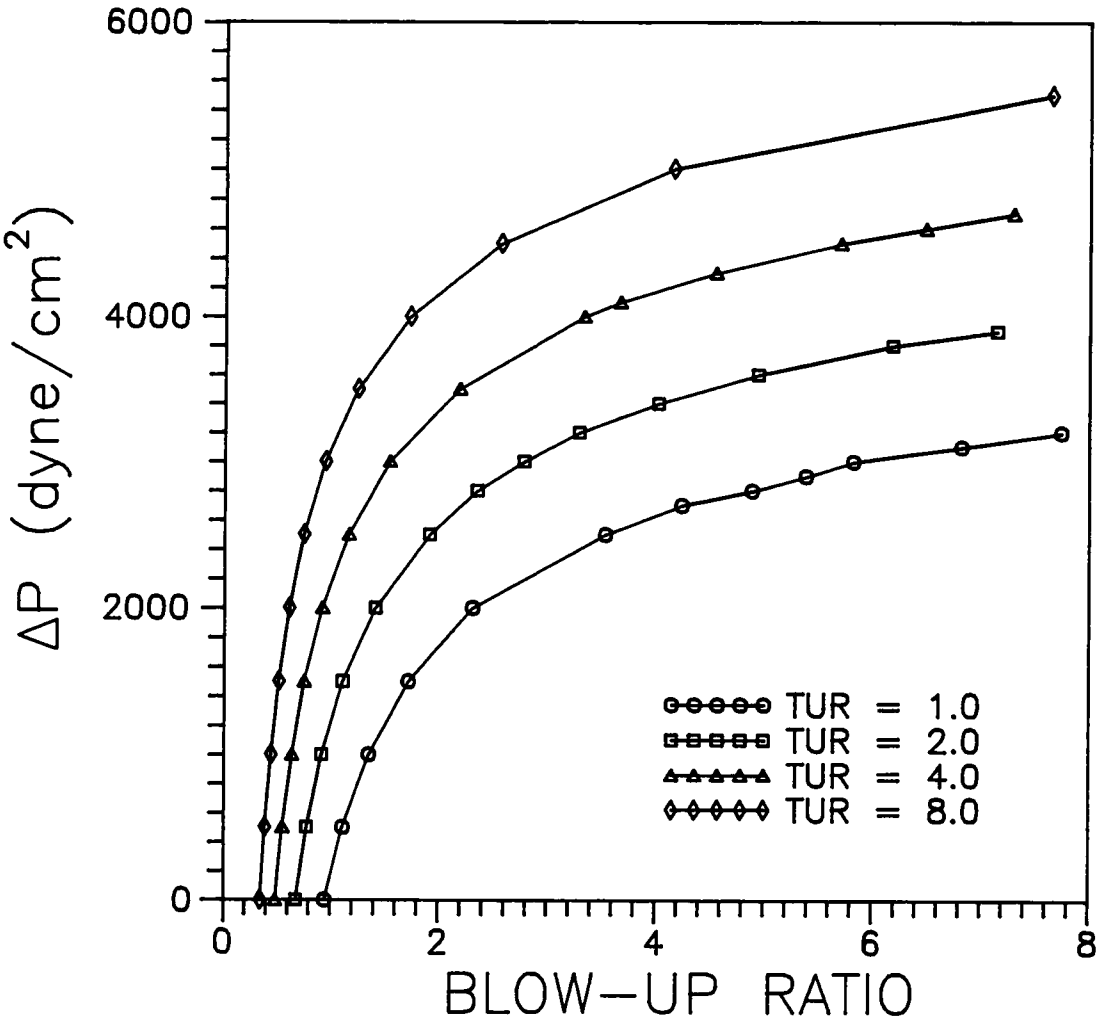

Figure 5-25 Theoretically predicted ΔP vs. BUR curves at various take-up ratios for a Newtonian fluid using the present model.

increases with the take-up speed. In other words, there is a competition between the pressure and the stretch ratio: to achieve a certain fixed radius a higher pressure is required to prevent the larger contraction in the hoop direction caused by the higher stretch ratio in the machine direction. According to this reasoning, for a fixed pressure, a lower blow-up ratio (i.e., a smaller bubble) will be expected at a higher take-up ratio. This expectation is shown in Figure 5-25. Furthermore, most importantly, this predicted trend can be supported by the experimental data: the order of the predicted ΔP vs. BUR curves for different take-up ratios in Figure 5-25, qualitatively agrees with the experimental observations for the various take-up speeds, as shown in Figures 4-1, 4-2 and 4-3 in Chapter 4 for LDPE, LLDPE, and HDPE, respectively.

Two disagreements in the above comparison are worth noting. One is that none of the predicted curves in Figure 5-25 show the slight inverse pressure effect (the downturn) which was observed during processing, as indicated in Figures 4-1 ~ 4-3. The other is that none of the predicted curves in Figure 5-25 crosses over the others, which can be seen in some of the experimental results, as shown in Figure 4-1 for LDPE (in which the curve at TUR = 5.1 obviously crosses over the others). These two disagreements are most likely due to the

over-simplified assumption of a Newtonian fluid. Therefore, a thinning fluid will be considered in the following paragraphs.

5.4.2 Influence of Viscous-thinning Factor

From the expression of Equation(5-5), it can be seen that the thinning factor **b** is the slope of the shear viscosity curve at a high shear rate. That is, the magnitude of the factor **b** represents the degree of "thinning" of the melt under a certain deformation rate: a higher **b** value causes a larger viscosity drop at a certain fixed deformation rate. Hence, it is essential to examine the effect of **b** on the relationship between the inflation pressure and the bubble radius. Therefore, three **b** values are chosen: 0.60, 0.70, and 0.75. For these three values, the predicted ΔP vs. BUR curves at different take-up ratios (TUR = 1.0, 2.0, 4.0, and 8.0) are shown in Figures 5-26, 5-27 and 5-28, respectively. The value of $\mathbf{a}\lambda$ is assumed to be 5.0; this value remains the same for all of the cases.

It should be emphasized that the only difference between the curves in Figure 5-25 and the curves in Figures 5-26 ~ 5-28 is the rheological equation: the former are predicted using a Newtonian viscosity equation; the latter are predicted using a viscous-thinning equation. Comparing Figures 5-26 ~ 5-28 to

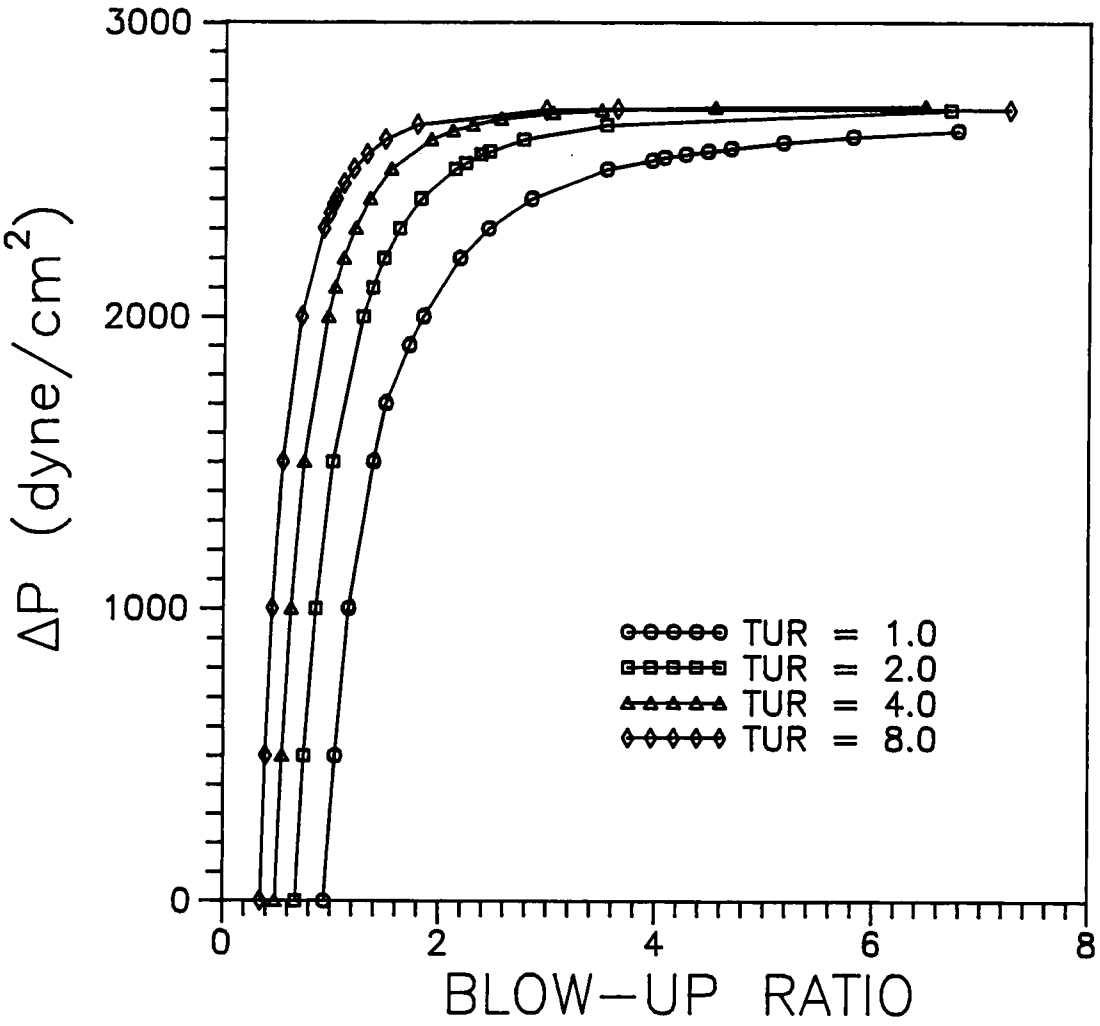

Figure 5-26 Theoretically predicted ΔP vs. BUR curves at various take-up ratios for a deformation-thinning fluid (**b** = 0.60) using the present model.

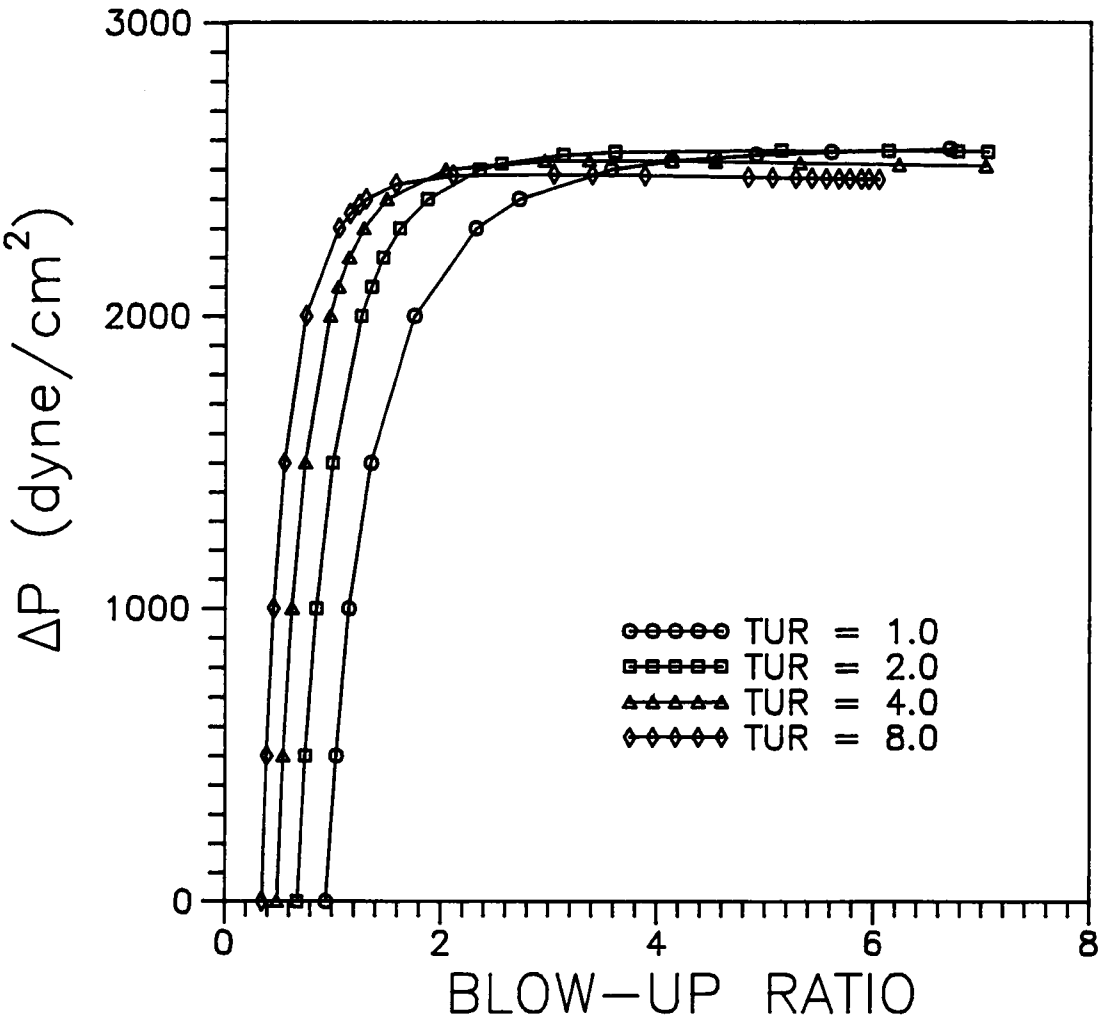

Figure 5-27 Theoretically predicted ΔP vs. BUR curves at various take-up ratios for a deformation-thinning fluid (**b** = 0.70) using the present model.

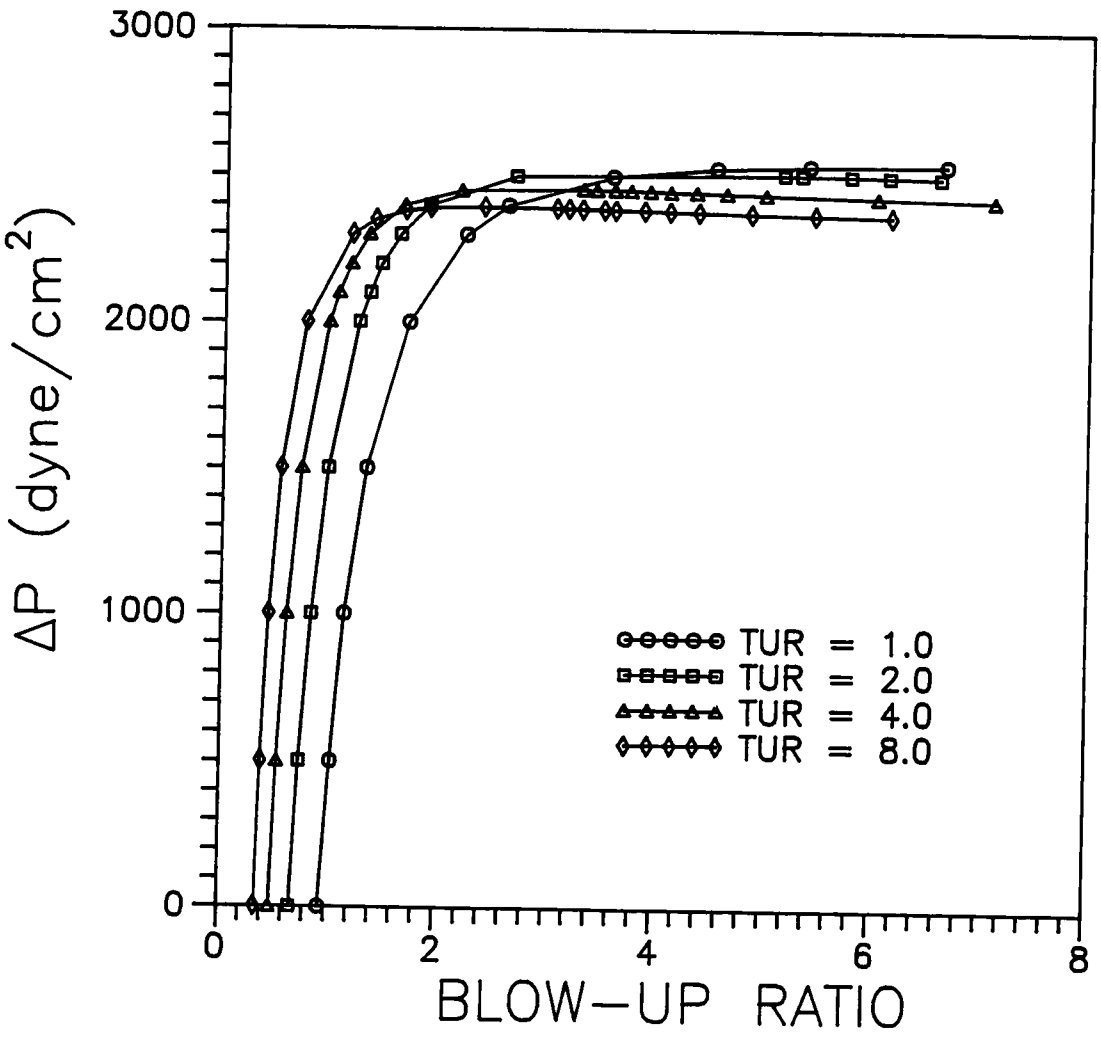

Figure 5-28 Theoretically predicted ΔP vs. BUR curves at various takeup ratios for a deformation-thinning fluid (**b** = 0.75) using the present model.

Figure 5-25, several important features can be observed and are summarized in the following statements.

(i) Generally speaking, introduction of a deformation-thinning factor into the viscosity equation does not change the overall shape of the ΔP vs. BUR curve or the order of the curves for various take-up ratios, especially in the region of low blow-up ratio (that is, BUR < 2). Quantitatively speaking, the introduction of the deformation-thinning effect causes the entire set of ΔP vs. BUR curves to shift downwards. The range of ΔP in Figure 5-25 is about from 0 to 5600 (dyne/cm^2); however, the range of ΔP in Figure 5-26 ~ 5-28 is about from 0 to 2700 (dyne/cm^2). This phenomenon is attributed to the fact that to achieve a certain fixed radius a lower pressure is sufficient for a melt with a lower viscosity, which is induced by the external deformation. Furthermore, the curve with a higher take-up ratio shows a larger amount of shift. Thus, for example, it can be seen that the gap between the curves for different take-up ratios in Figure 5-26, especially in the region of higher blow-up ratio (BUR > 2), is smaller than that shown in Figure 5-25. Based on the same reasoning, the case of a higher take-up ratio must

have a larger viscosity drop, which is caused by a higher deformation rate.

(ii) An obvious cross-over between the curves for different take-up ratios can be seen from Figures 5-26 ~ 5-28; however, this phenomenon is not shown in Figure 5-25. Furthermore, comparing these three figures (i.e., Figures 5-26 ~ 5-28) this cross-over phenomenon between curves is becoming more obvious with an increase of the thinning effect. For the case of **b** = 0.75, as shown in Figure 5-28, the order of the ΔP curves at high blow-up ratio (that is, BUR > 3.6 for this case) is completely opposite not only to that in the Newtonian case (Figure 5-25), but also to the original order at low blow-up ratio (BUR < 1.5). As was discussed in the preceding paragraph, this also can be reasoned by the interaction between the deformation rate, the non-linearity of the melt viscosity, and the required inflation pressure for reaching a certain bubble radius.

Most importantly, this predicted trend qualitatively agrees with the data. From the **b** values, as listed in Table 5-2, which were taken from the measured complex viscosity curves, it can be seen that LDPE has the highest **b** value and LLDPE has the lowest. Examining the experimental data for ΔP versus BUR shown

in Figures 4-1 and 4-2 in Chapter 4 for LDPE and LLDPE, respectively, the predicted cross-over trend as a function of **b** is indeed found in the experiments.

(iii) Some of the curves in Figures 5-26 ~ 5-28 show a slight inverse pressure effect on the bubble radius in the region of high blow-up ratio (that is, to produce a larger bubble the required pressure is smaller); however, none of the curves in Figure 5-25 does. The predicted inverse pressure effect (the downturn) can be seen clearly by expanding the y-axis scale from the three original figures, as shown in Figures 5-29, 5-30 and 5-31 for **b** = 0.60, 0.70, and 0.75, respectively. Moreover, the cross-over phenomenon discussed in the preceding sub-section can be seen in these figures with expanded y-axis scale as well.

For the case of **b** = 0.60, as indicated in Figure 5-29, only the curve at TUR = 8.0 (the highest take-up ratio) shows the inverse pressure effect. Furthermore, for the cases of **b** = 0.70 and 0.75 (with the larger thinning effect), not only the curves for TUR = 8.0 show the inverse pressure effect but also the curves for lower take-up ratios (such as TUR = 2.0 and 4.0). Therefore, based on this predicted trend, it can be realized that the inverse pressure effect is also due to

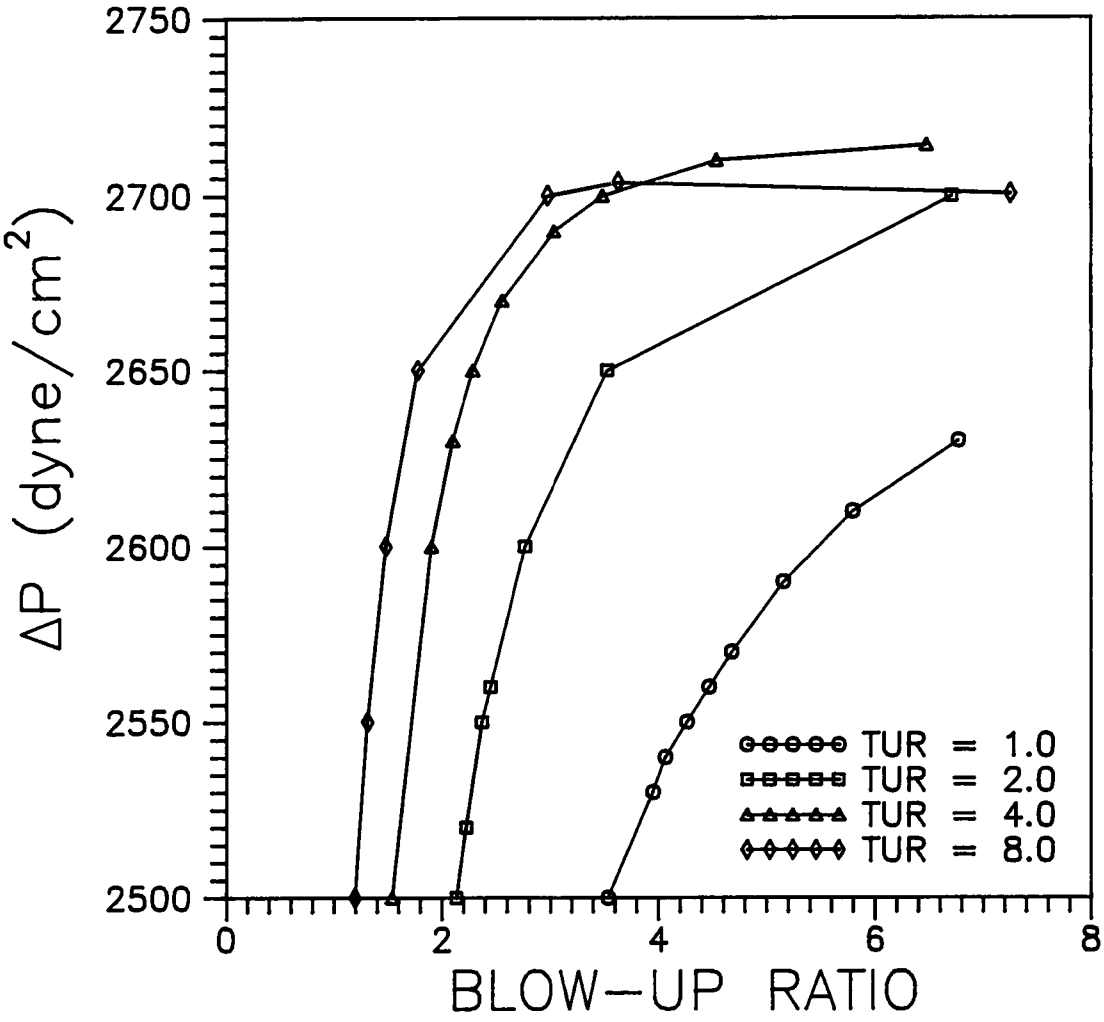

Figure 5-29 An enlargement of a part of the curves in Figure 5-26 (**b** = 0.60) with an expanded y-axis scale.

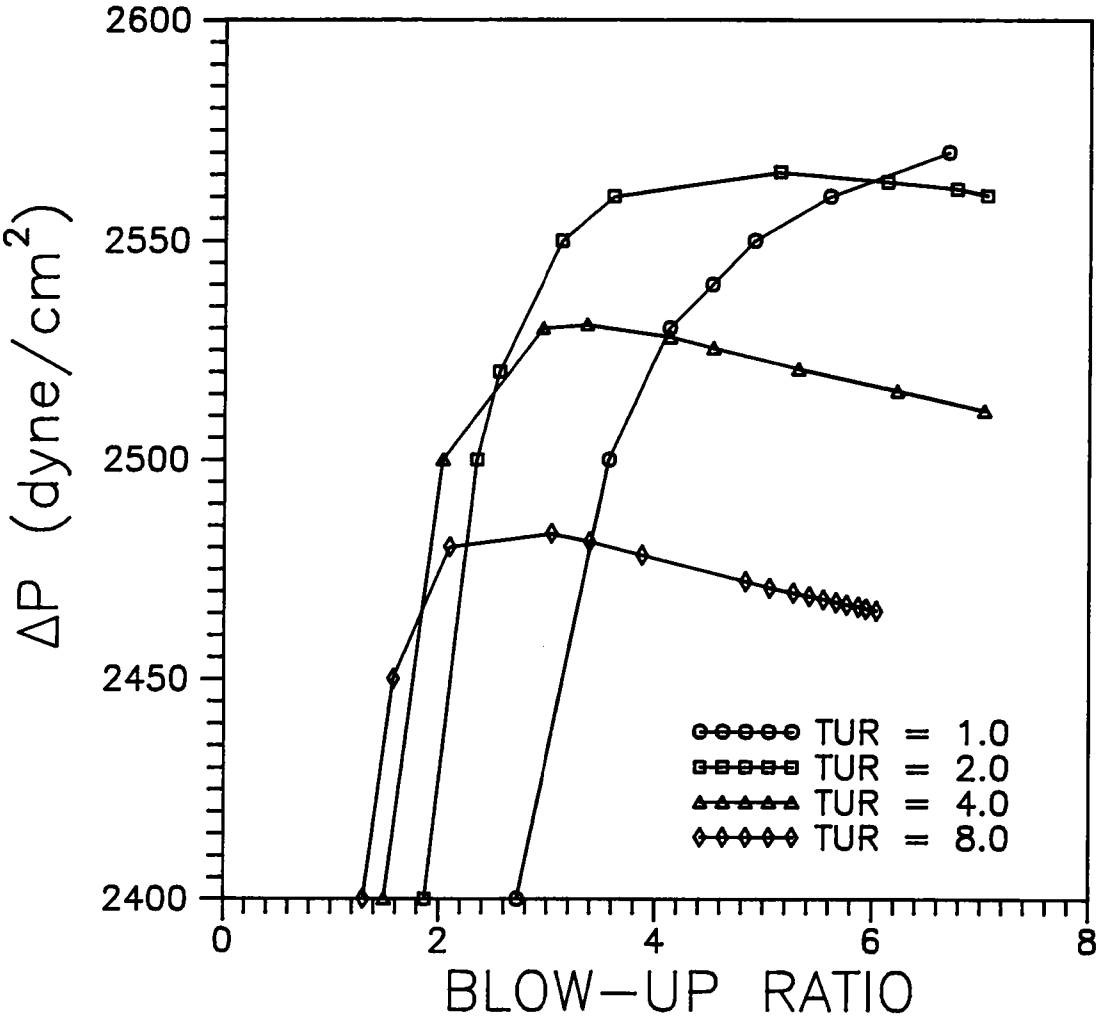

Figure 5-30 An enlargement of a part of the curves in Figure 5-27 (**b** = 0.70) with an expanded y-axis scale.

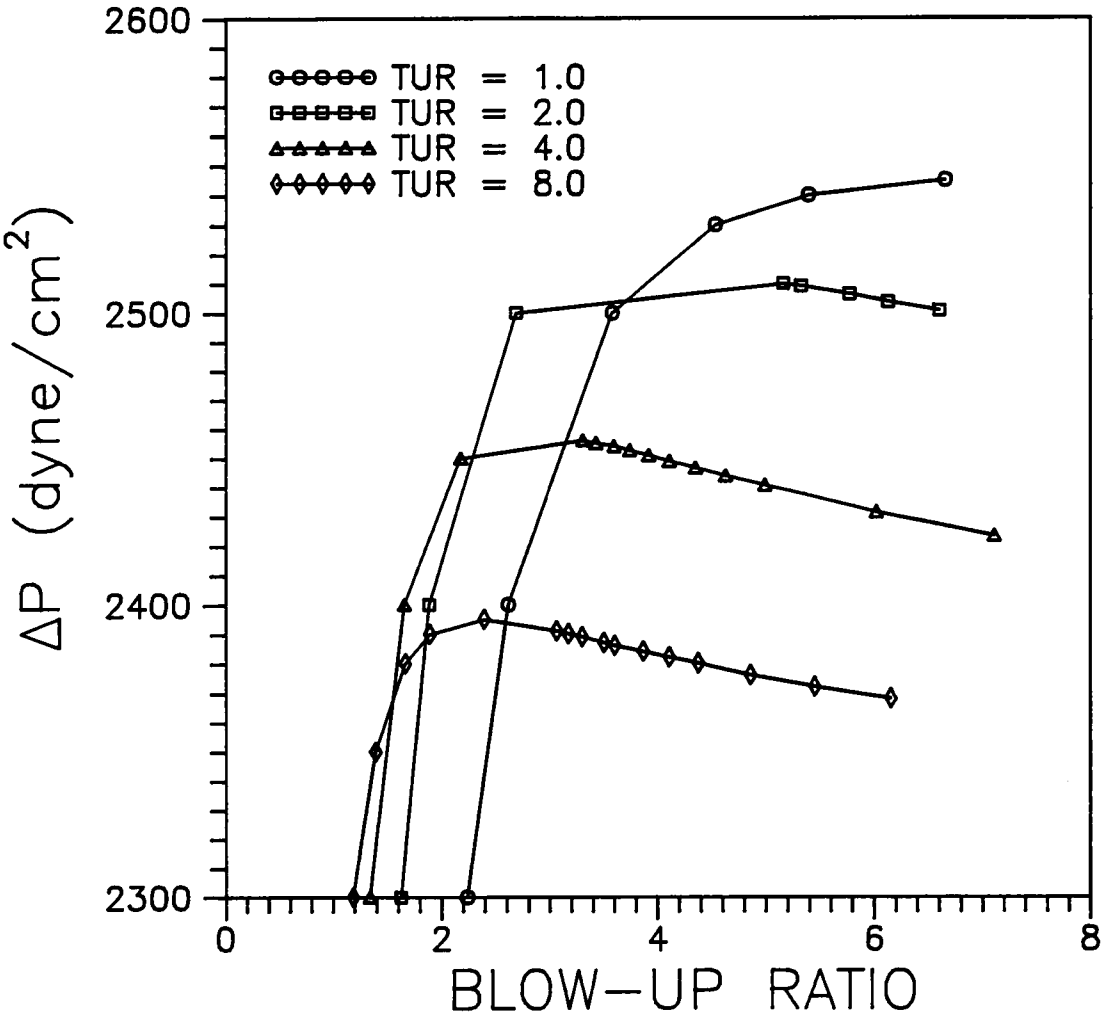

Figure 5-31 An enlargement of a part of the curves in Figure 5-28 (**b** = 0.75) with an expanded y-axis scale.

the effect of deformation thinning. Moreover, the take-up ratio for starting the inverse-pressure phenomenon depends on the degree of non-linearity of viscosity (i.e., the degree of deformation thinning) of the material. That is, for a material with a higher **b** value the inverse pressure effect may be observed in a lower take-up ratio region (compared to a material with a lower **b** value).

This theoretical prediction (discussed in the preceding paragraph) can be supported by the experimental observations. As it was listed in Table 5-2, experimental data shows that among the three polyethylenes LDPE has the largest **b** value, and LLDPE has the lowest. Hence, according to the experimental observations, LLDPE only shows an clear inverse-pressure effect at the highest take-up ratio (that is, TUR = 7.3), as shown in Figure 4-2 in Chapter 4. On the other hand, LDPE shows an obvious inverse-pressure effect even at very low take-up ratios (that is, TUR = 1.8 and 2.6), as indicated in Figure 4-1 in Chapter 4. However, it should be noted that for LDPE the on-line measured inverse-pressure effect may or may not occur at the higher take-up ratios (TUR = 4.1 and 5.1 in Figure 4-1) because the bubble broke at high take-up ratios during

processing (thus, the experimental data was not obtained).

Furthermore, it should be noted that the theoretical ΔP vs. BUR curve for TUR = 1.0 in each figure (Figures 5-29 ~ 5-31) does not show the inverse pressure effect. This is attributed to the fact that for the case of very low take-up ratio (i.e., low deformation rate) the viscosity drop caused by deformation is not high enough to onset the inverse pressure effect.

According to the above discussion, it can be concluded that the "mixed" experimental observations in the literature [11,14,25-28] on the relationship between the inflation pressure and the bubble radius (as previously described in Chapter 1 and discussed in Section 2.6 in Chapter 2) are not really "mixed". They can be all be explained by the predictions shown in Figures 5-26 ~ 5-31. For example, the experimental data published by Wagner [26], as shown in Figure C-1 in Appendix C, qualitatively agrees with the present model predictions as shown in Figure 5-28. Furthermore, the measured inverse-pressure effect in the BUR region about 1.4 ~ 4.6 reported by Kwack and Han [25], as shown in Figure C-2 in Appendix C, also qualitatively agrees with the model predictions in Figure 5-31. Therefore, the mixed experimental

observations in the literature have to do with what type of material is used and what range of take-up ratio and blow-up ratio is observed.

5.4.3 Influence of Extrusion Temperature

The extrusion temperature, one of the important processing parameters, directly affects the rheological properties of melt and is also associated with other processing parameters. Hence, the effect of the extrusion temperature on the relationship between inflation pressure and bubble radius needs to be investigated.

Three different die temperatures (T_o), 170 ^oC, 190 ^oC, and 210 ^oC, are chosen for model simulation. For completeness, the deformation thinning effect is included in the viscosity equation, in which the factors $\mathbf{a}\lambda$ and $\mathbf{b}$ are assumed to be 5.0 and 0.75, respectively, for these three cases (T_o = 170 ^oC, 190 ^oC and 210 ^oC). The numerical values for the other required parameters for the simulation are the same as that listed in Table 5-3.

For the three extrusion temperatures (170 ^oC, 190 ^oC, and 210 ^oC), the predicted curves of ΔP versus BUR are shown in Figure 5-32. For these three cases, the take-up ratios remain the same, TUR = 4.0. From the order of the curves shown in Figure 5-32, it can be seen that to reach a pre-

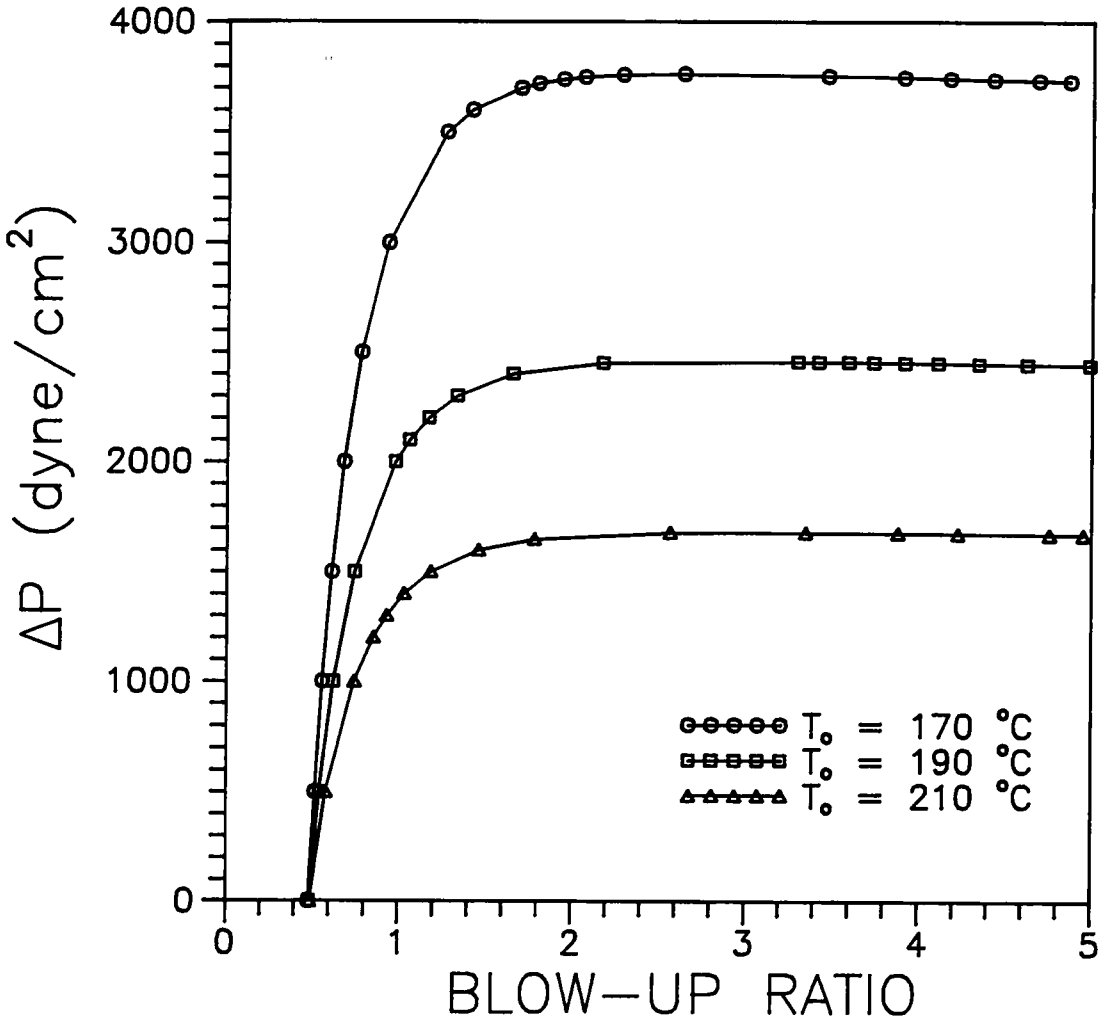

Figure 5-32 Theoretically predicted ΔP vs. BUR curves for various extrusion temperatures using the present model.

determined blow-up ratio, the required inflation pressure increases with decreasing extrusion temperature. This is attributed to the fact that the melt viscosity is strongly dependent on the temperature, as demonstrated by Figures 3-1 ~ 3-3 in Chapter 3. Hence, for the case of a lower extrusion temperature, the melt will have a higher viscosity; thus, a higher internal pressure is required to inflate the bubble to a certain radius.

Most importantly, compared to the experimental data, as shown in Figure 4-4 in Chapter 4, the order of the predicted curves in Figure 5-32 agrees with the experimental observations.

5.4.4 Influence of Magnitude of Viscosity

The magnitude of the melt viscosity is strongly influenced by the molecular weight, as reviewed in Section 2.3 of Chapter 2. Therefore, it is essential to understand the effect of the magnitude of the melt viscosity.

Changing the viscosity (i.e., the pre-exponential coefficient $\alpha 1$ in Equation(5-6)) by factors of 1.5 and $(\frac{1}{1.5})$, respectively, the predicted curves of ΔP versus BUR are shown in Figure 5-33 (that is, TUR = 4.0). Comparing the three curves in Figure 5-33, it can be seen that to reach a certain blow-up ratio a melt with a higher viscosity needs a higher

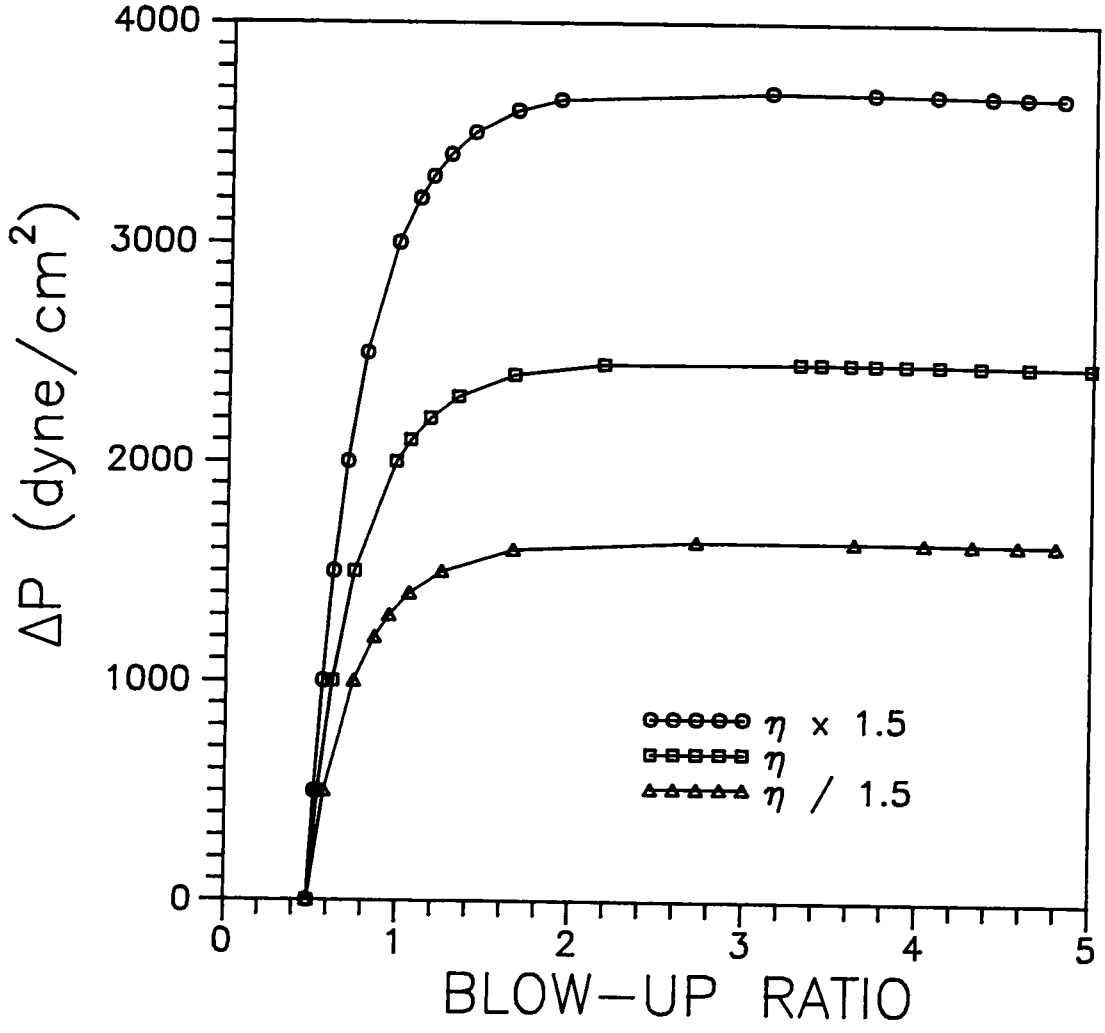

Figure 5-33 Theoretically predicted ΔP vs. BUR curves for various viscosity magnitudes using the present model.

inflation pressure. It needs to be emphasized that this predicted trend can be supported by the experimental observations in both this study (see Figure 4-4 in Chapter 4) and Wagner's investigations [26] (as previously described and discussed in Section 5.2.1).

Furthermore, the comparison of Figure 5-32 and Figure 5-33 can be used to support the reasoning that increasing the extrusion temperature is equivalent to decreasing the magnitude of the melt viscosity. This reasoning was used as a basis of interpretation of the results in Chapter 4 and in the previous sections of this chapter (that is, Section 5.2.1). The temperature-dependent part of the viscosity equation used for Figure 5-32 and Figure 5-33 can be expressed as:

$$\eta_T = 9.58 \exp\left[\frac{4476}{T}\right] \qquad (5\text{-}17)$$

where η_T represents the temperature dependent viscosity and T is in units of Kelvin. Thus, it can be found that the magnitude of η_T is decreased by a factor of about 1.5 when the die temperature is raised from 190 ^{o}C to 210 ^{o}C, and the magnitude of η_T is increased by a factor of about 1.5 when the die temperature is lowered from 190 ^{o}C to 170 ^{o}C. Therefore, the three curves in Figure 5-32 are expected to be approximately equivalent to the that in Figure 5-33. This

expectation is supported by combining these two figures, as shown in Figure 5-34.

5.4.5 Influence of External Cooling Rate

In practice, the film blowing process is non-isothermal and the external cooling rate is one of the key processing parameters. Hence, the effect of cooling rate will be examined using the present model.

The cooling rate of the film is primarily controlled by the external heat convection, which is usually described by the heat transfer coefficient. Therefore, changing the heat transfer coefficient U by factors of 0.5 and 2.0, respectively, the resulting ΔP versus BUR curves are shown in Figure 5-35 (at a fixed take-up ratio, 4.0). This figure indicates that for a fixed inflation pressure, a larger bubble can be obtained by decreasing the cooling rate. More importantly, this predicted trend qualitatively agrees with the experimental observations, as shown in Figure 4-5 in Chapter 4, in which different air flow rates were used.

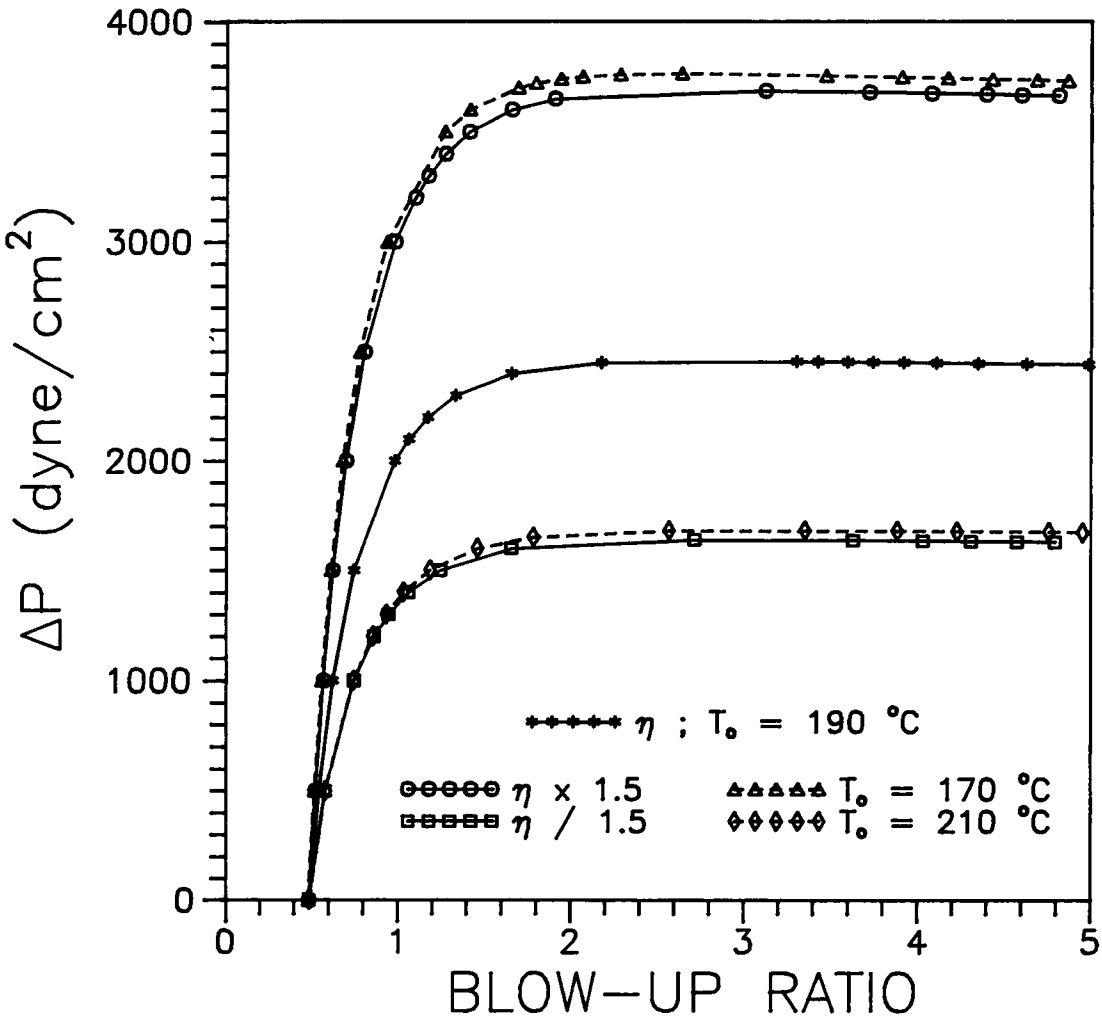

Figure 5-34 Comparisons of the predicted ΔP vs. BUR curves using various viscosity values to that using various extrusion temperatures.

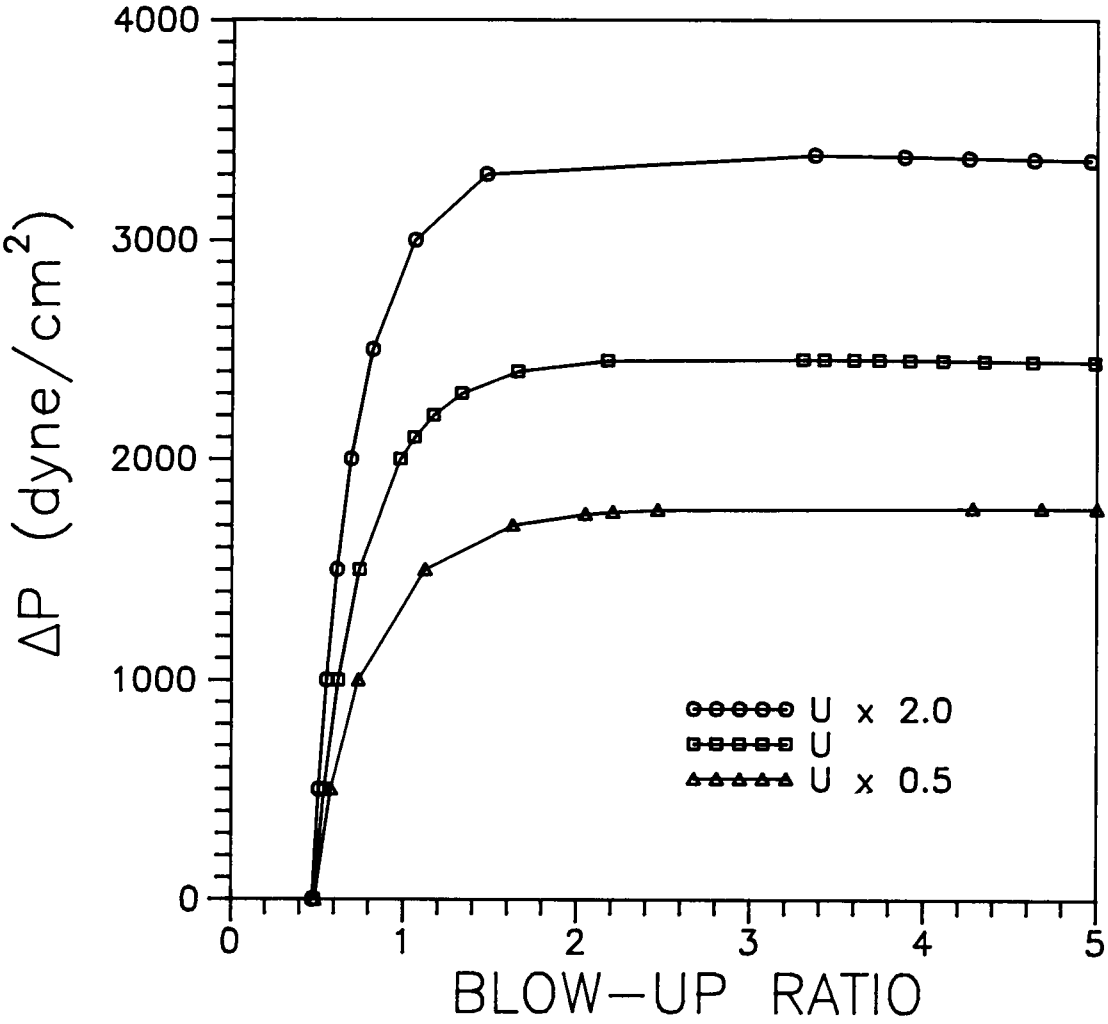

Figure 5-35 Theoretically predicted ΔP vs. BUR curves for various magnitudes of heat transfer coefficients using the present model.

5.5 RECONSIDERATION OF THE PEARSON-PETRIE MODEL

The results presented in the previous sections show that the present model is able to describe the blowing process correctly, but the Pearson-Petrie model is not. But from a theoretical point of view, since the Pearson-Petrie model is a more general formulation, it should include the present model as a special case. The problem in passing from the Pearson-Petrie model to the present model will be discussed.

5.5.1 Key Difference between Two Existing Models

Comparing the Pearson-Petrie model and the present model, the key difference is in the force balance equation in the circumferential direction. For the hoop direction, the force balance in the Pearson-Petrie model is based on thin-shell theory [3,4,75], as expressed by the following equation:

$$\Delta P = \frac{H\sigma_{11}}{R_1} + \frac{H\sigma_{22}}{R_2} \qquad (5\text{-}18)$$

where σ_{11} and σ_{22} are the normal stresses in the machine direction and in the hoop direction, respectively. The expressions for the two principal radii of curvature, R_1 and R_2 (in the machine and the hoop directions, respectively), are obtained through geometrical relationships as follows:

$$R_1 = \frac{-\sec^3\theta}{\frac{d^2R}{dZ^2}} \qquad (5\text{-}19)$$

$$R_2 = \frac{R}{\cos\theta} \qquad (5\text{-}20)$$

where θ is the angle between the tangent direction and the Z-axis, as illustrated in Figure 2-5 in Chapter 2. However, in the present model the hoop direction balance is derived from a "quasi-cylindrical" approach:

$$\Delta P = \frac{H\sigma_{22}}{R} \qquad (5\text{-}21)$$

where σ_{22} is the normal stress in the hoop direction, and H and R are the local thickness and radius of the bubble, respectively. Comparing Equation(5-18) to Equation(5-21), it can be found that there is one additional term, $\frac{H\sigma_{11}}{R_1}$, in Equation(5-18), which is the consideration of the effects of the normal stress, σ_{11}, in the machine direction. Thus, the hoop-direction force balance in the Pearson-Petrie model, Equation(5-18) can be reduced to the form of that of the present model, Equation(5-21), by omitting the effects of σ_{11}. Based on this comparison, Equation(5-18) appears to be a more general formulation; however, it failed to describe the actual

processing correctly. Therefore, the role of the term, $\frac{H\sigma_{11}}{R_1}$, needs to be examined.

5.5.2 Influence of the Term $\frac{H\sigma_{11}}{R_1}$

(A) Influence on the Inflation Pressure

This term, $\frac{H\sigma_{11}}{R_1}$, can be estimated from the known shape of the bubble. Using the analysis result of the present model, the importance of this term can be revealed by introducing a new variable ΔP_{eff} which is given by the following equation.

$$\Delta P_{eff} = \Delta P - \frac{H\sigma_{11}}{R_1} = \frac{H\sigma_{22}}{R} \qquad (5\text{-}22)$$

where ΔP_{eff} is the "effective pressure". That is, it is the net pressure which is balanced by the normal stress built up in the circumferential direction. Therefore, the relative magnitudes of the terms $\frac{H\sigma_{11}}{R_1}$ and ΔP can be observed.

Since the results in the previous sections have shown that the present model is able to fit the experimental data very well (essentially the same as the data), the model will be used to calculate ΔP_{eff}. Four arbitrarily chosen bubble profiles, namely case(a), case(b), case(c) and case(d), can be

obtained on the basis of the present model, as shown in Figure 5-36; the associated ΔP values for these four radius profiles are 1490, 2484, 2856 and 3105 dyne/cm^2 (that is, 0.60, 1.00, 1.15, and 1.25 inches of water), respectively. Thus, based on each of the radius profiles in Figure 5-36, the effective pressure, ΔP_{eff}, for each case can be determined using Equations(5-19) and (5-22).

The computed effective pressures, ΔP_{eff}, along the machine direction for case(a), case(b), case(c) and case(d) are all shown in Figure 5-37. It can be seen that the overall average of each ΔP_{eff} curve is constant (that is, the constant value of ΔP for each corresponding case). However, an obvious variation of ΔP_{eff} value can be seen from the curves for case(c) and case(d). This fluctuation is occurring in the region where the bubble radius is changing. Furthermore, according to the expression of Equation(5-19), it can be seen that a bubble with a higher blow-up rate (that is, a higher value of $\frac{d^2R}{dZ^2}$) will cause a higher variation on ΔP_{eff}, as indicated by the curve for case(d) in Figure 5-37. It should be emphasized that even for the case(d), which has the largest effect of the term of $\frac{H\sigma_{11}}{R_1}$ on ΔP, there is only about a 5.5% variation from the constant value of ΔP.

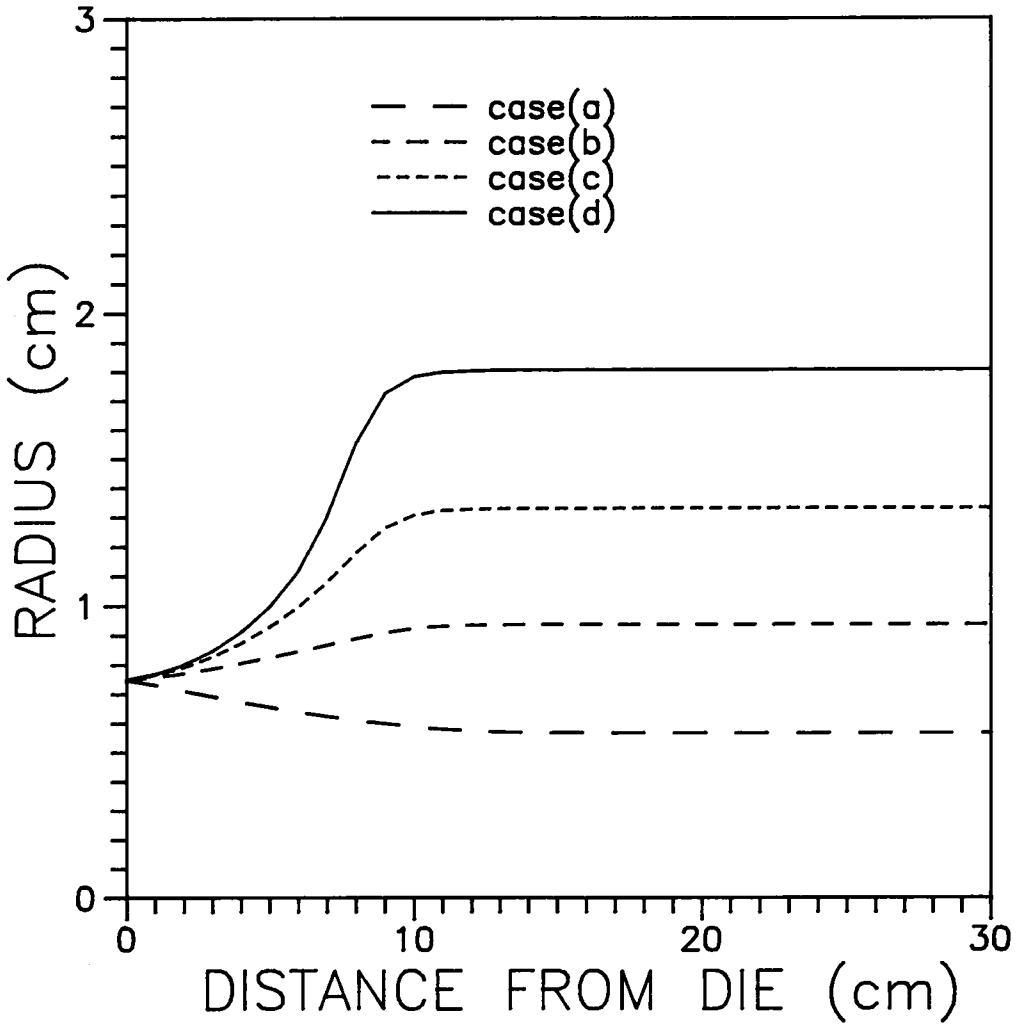

Figure 5-36 Calculated radius profiles using the present model for the four chosen cases.

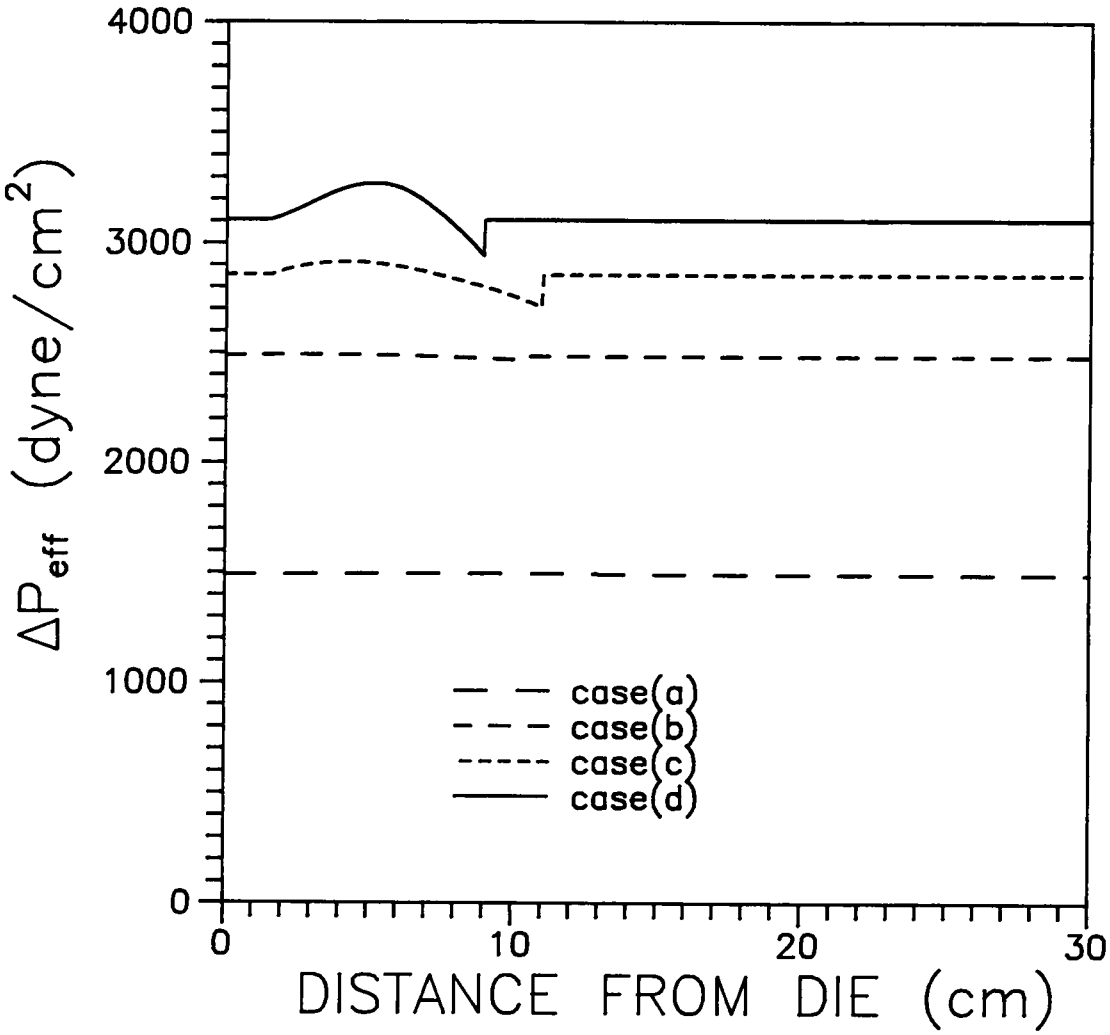

Figure 5-37 Calculated profiles of the effective pressure, ΔP_{eff}, along the Z-axis.

(B) Influence on Overall Simulation

The influence of the term $\frac{H\sigma_{11}}{R_1}$ on the overall model predictions can be further evaluated by replacing the constant ΔP with the ΔP_{eff} curve (which includes the effect of the normal stress in the machine direction) in the present model. Thus, the effect of the term $\frac{H\sigma_{11}}{R_1}$ on the overall simulation results can be found. To carry out the simulation on the basis of ΔP_{eff}, it should be noted that the use of ΔP_{eff} in the simulation is based on the assumption that the shape of the bubble is known *a priori*. Thus, for this case it is more logical that the take-up force be adjusted to force the calculated final radius to the known value, rather than forcing the velocity (as was done in the previous sections).

The comparison of the bubble profiles predicted by using the four ΔP_{eff} curves (in Figure 5-37) to that originally predicted by the four constant ΔP values (as previously shown in Figure 5-36) is shown in Figure 5-38. Figure 5-38 indicates that for case(d) (that is, the case which has the largest radius) there is a very slight difference between the radius profiles predicted by using constant ΔP and by using the effective pressure, ΔP_{eff}. However, there is no perceivable difference for the other three radius profiles (case(a), case(b) and case(c)). Furthermore, the comparisons for the associated thickness, velocity and temperature

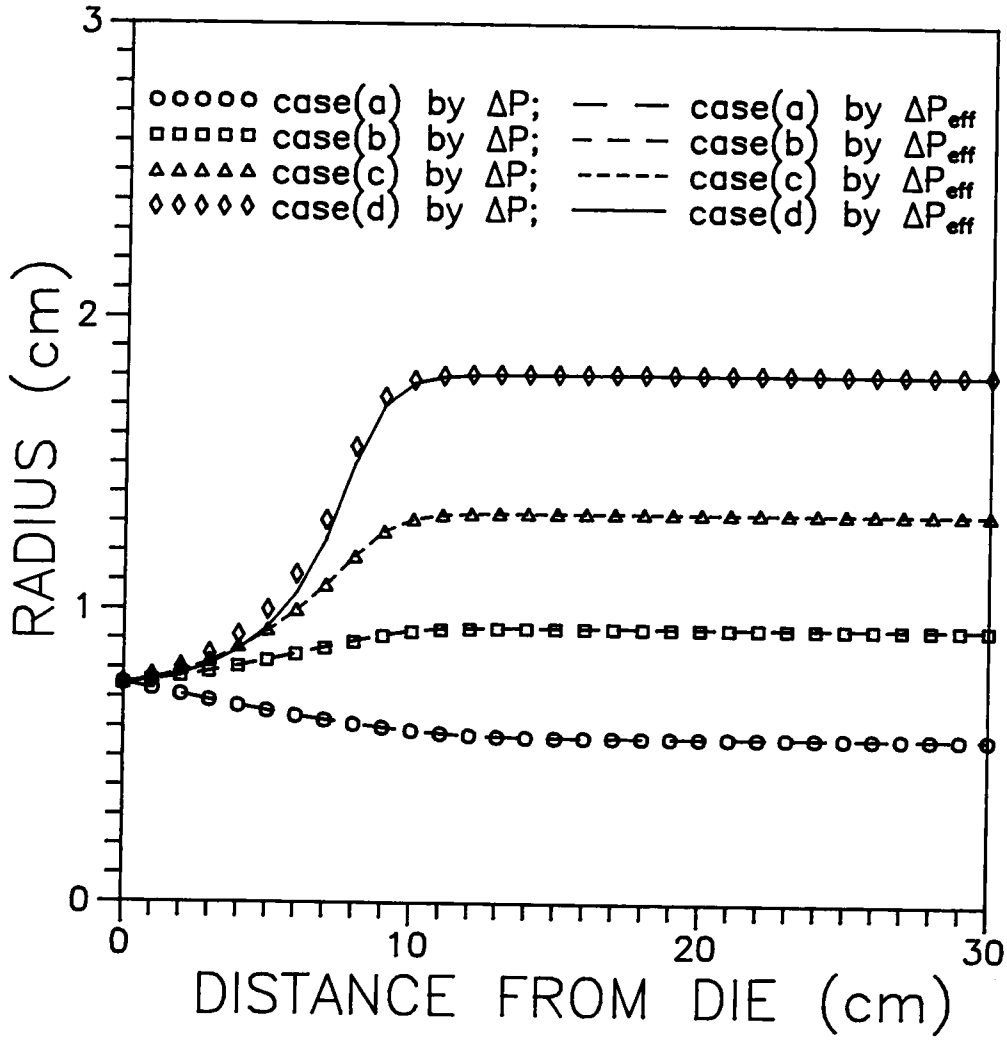

Figure 5-38 Comparisons of the predicted radius profiles using ΔP to that using ΔP_{eff} for the four cases.

profiles for these four cases are shown in Figures 5-39, 5-40 and 5-41, respectively. For the thickness, velocity and temperature profiles, case(a), case(b) and case(c) show no detectable difference between the profiles predicted by using ΔP and by using ΔP_{eff}. However, for case(d), although noticeable differences can be seen in Figures 5-39 ~ 5-41, even so, the general characteristic of the analysis does not change: that is, the effect of inflation pressure on blow-up ratio is still intuitive (increasing inflation pressure increases blow-up ratio) unlike the predicted counter-intuitive pressure effect using the Pearson-Petrie model.

Finally, according to the discussion in the preceding paragraphs, it can be concluded that $\frac{H\sigma_{11}}{R_1}$ is not the dominant term in the hoop direction balance when the shape of the bubble is known *a priori*.

5.5.3 Nature of Thin-Shell Theory

Thin-shell theory, upon which the Pearson-Petrie model is based, has traditionally been used to design *solid* vessels. The shape of the vessel is known *a priori* and it was in that spirit that the calculations of the previous section (involving ΔP_{eff}) were made: that is, the shape of the bubble is taken as given and the velocity and thickness come out as results. In that context there are not substantial

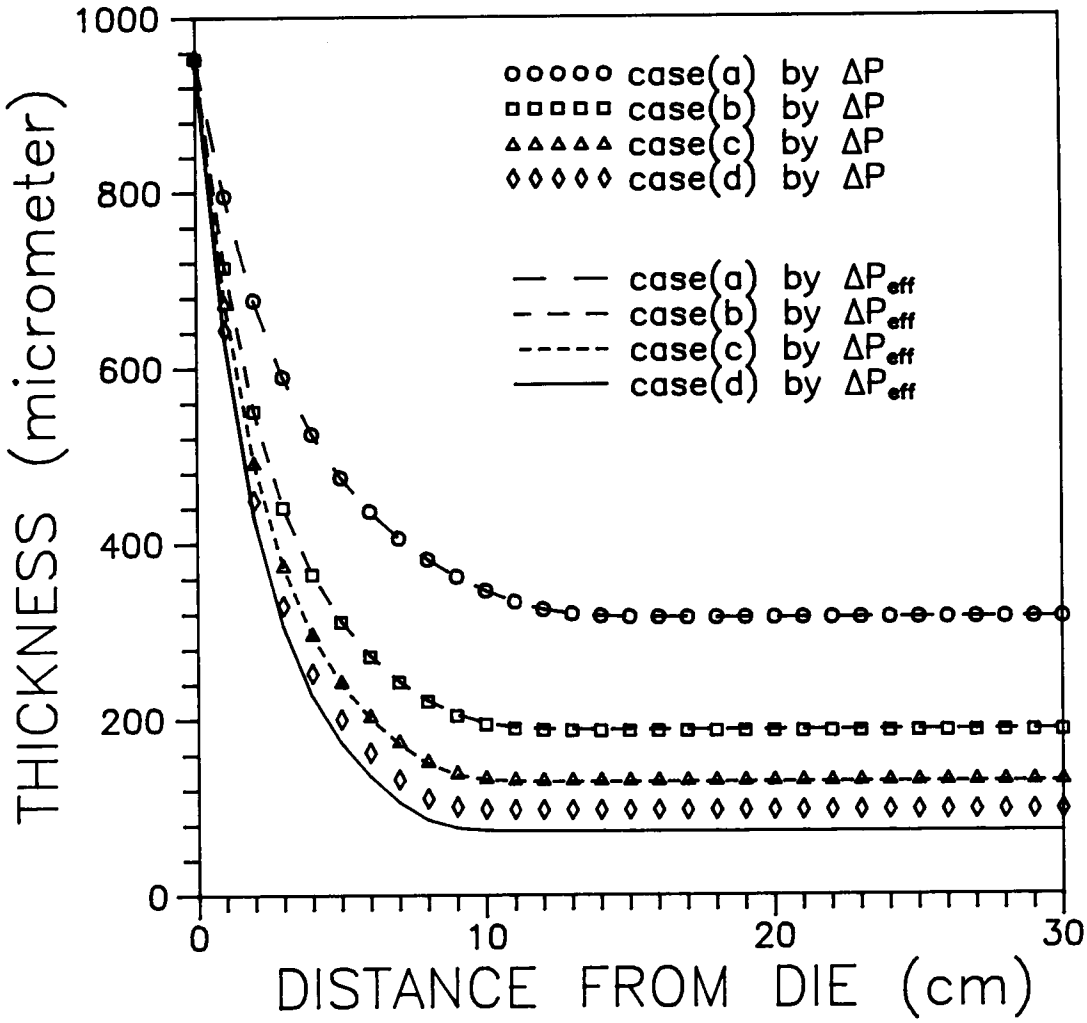

Figure 5-39 Comparisons of the predicted thickness profiles using ΔP to that using ΔP_{eff} for the four cases.

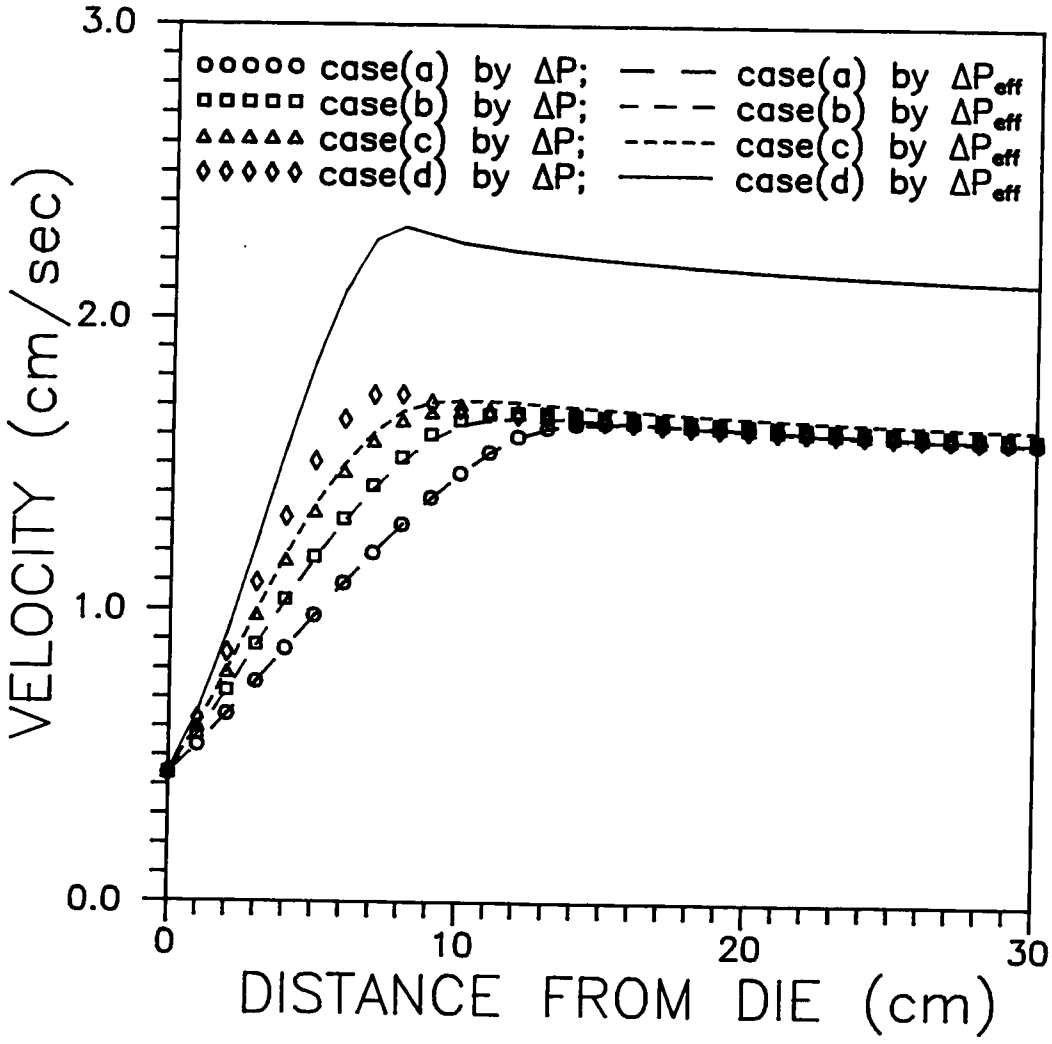

Figure 5-40 Comparisons of the predicted velocity profiles using ΔP to that using ΔP_{eff} for the four cases.

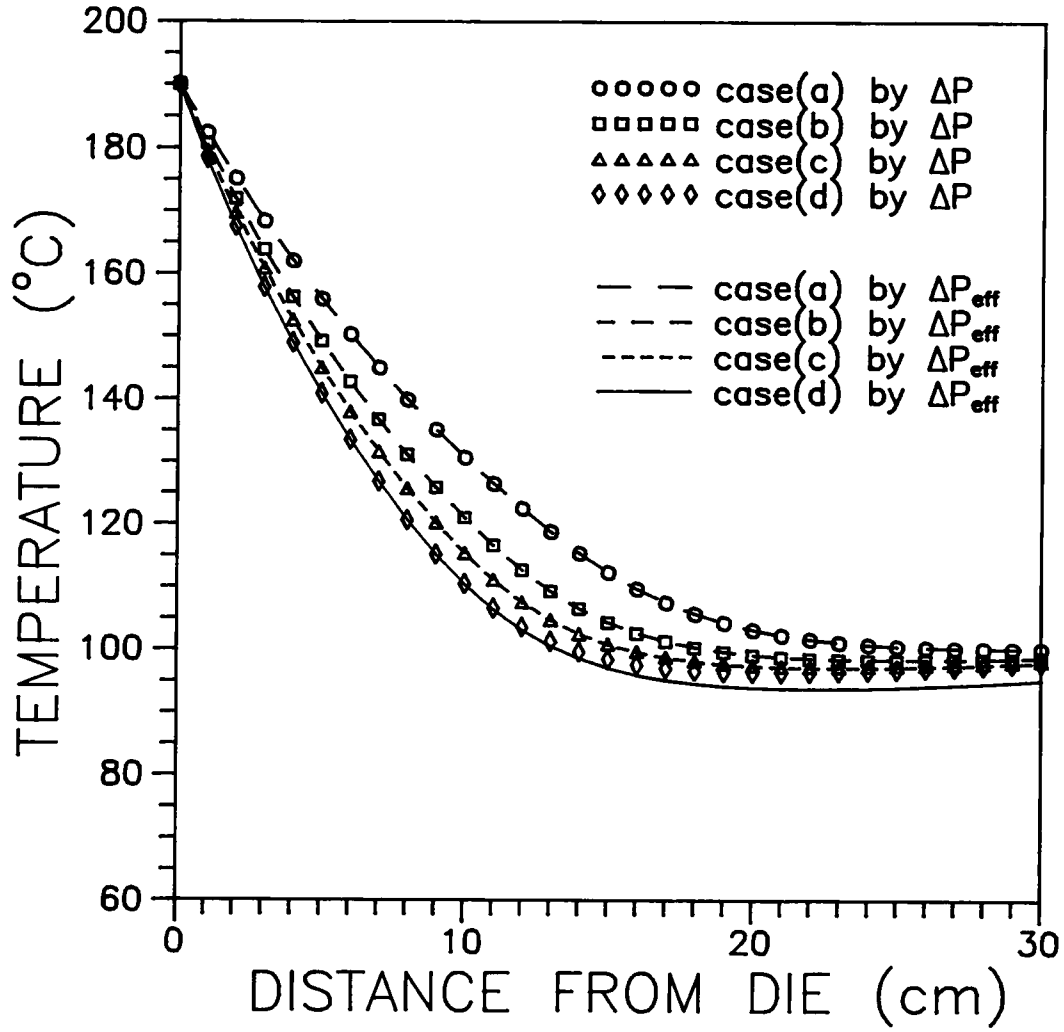

Figure 5-41 Comparisons of the predicted temperature profiles using ΔP to that using ΔP_{eff} for the four cases.

differences between the Pearson-Petrie model and the present model.

If, however, the Pearson-Petrie model is used to solve a free-boundary fluid mechanics problem — i.e., to *determine* the shape of the bubble — then substantial differences appear. That was the point made in Section 5.2: the Pearson-Petrie model predicts a counter-intuitive effect of inflation pressure on blow-up ratio, in contrast to an intuitive effect from the present model. The mathematical difference is that one drives the finite difference solution of the Pearson-Petrie equations by the very term (the second derivative term $\frac{d^2R}{dZ^2}$) which makes the two models different. Local differences between ΔP and ΔP_{eff}, minor when the shape was known *a priori*, are now of major concern: even the qualitative nature of the solution changes. In the same vein, inspection of the equations (Equations (2-58) and (2-60)) at $Z = 0$ and $\Delta P = 0$ shows that the Pearson-Petrie equations, when used to drive the solution forward, give a bubble of increasing radius.

With the help of Prof. Gary Harrison [121], possible shortcomings of the Runge-Kutta integration scheme were considered. By inspecting the form of the equations and by changing the step size, he concluded that the Runge-Kutta scheme used herein is satisfactory. An issue in the

literature regards the initial condition in θ (taken as $\theta = 0$ at $Z = 0$ in the present work and also by Ashok and Campbell [30]); to avoid this condition Pearson and Petrie [4] (and also other investigators [69,82]) started their analyses at the frost line and worked backwards in Z. These differing approaches do not, however, change the qualitative nature of the Pearson-Petrie solution — i.e., one see the counter-intuitive effect in all cases.

If the numerical scheme is not at fault, one needs to reconsider the physics of the problem. It is hard to fault the assumptions of thin-shell theory (that there be no shear stresses and that the radii of curvature be large compared with the thickness). The key must lie somehow in whether one is solving a solid mechanics problem or a fluid mechanics problem. It is difficult to see why there should be a difference. Finally it must be said that a fully satisfactory explanation is lacking at the present time.

CHAPTER 6

CONCLUSIONS

The major conclusions of the present work on tubular film blowing are as follows:

1. Experimental studies for three polyethylenes (low density, linear-low density, and high density polyethylenes, all having a melt index of 1.0) were carried out. The measurements included the effect of the inflation pressure (ΔP) and the take-up ratio (TUR) on the blow-up ratio (BUR) at various extrusion temperatures and cooling-air flow rates; and detailed on-line radius, velocity and temperature measurements for the first two materials. The essential features of these data are:

(a) With the exception of certain limited regimes, the effect of inflation pressure on blow-up ratio is the so-called "intuitive" one: that is, increasing the inflation pressure causes the blow-up ratio to increase.

(b) A useful way to present data is in the form of plots of ΔP versus BUR with TUR as the parameter. Such

plots show generally that an increase in ΔP is associated with an increase in BUR (the intuitive effect); and that curves with high values of TUR lie above those with low TUR. However, at a certain value of blow-up ratio (typically about 2 or 3), the ΔP vs. BUR curves become flat and, in some cases at least, show a downturn (a "counter-intuitive" effect). Moreover, they cross-over: that is, curves with high values of TUR lie below those with low values of TUR. Shortly after these complicated effects are seen, the bubbles become unstable and break.

(c) Extending the range of the processing conditions, by changing the extrusion temperature and the air flow rate, did not change the relationship of inflation pressure to blow-up ratio, as described in the above paragraphs. That is, the intuitive pressure effect existed in the region of low blow-up ratio and the counter-intuitive effect was observed in the high blow-up ratio region.

(d) The three polyethylenes showed essentially the same type of behavior. However, compared to the other two materials, the low density polyethylene was more stable in the plateau regions of the ΔP curves, which is possibly due to the elasticity of the melt.

(e) All of the on-line collected profiles (that is, the radius, the velocity, the thickness and the temperature) showed that at the position of the observed frost line, the film radius, thickness and velocity almost stopped changing, and an occurrence of a temperature plateau (or at least an obvious decrease in the cooling rate) appeared.

(f) The deformation rates in the three principal directions (that is, the machine, the circumferential and the normal directions) can be obtained from the collected on-line profiles of radius, thickness and velocity. The results show that increasing the blow-up ratio not only causes the deformation rate in the hoop direction to increase but also causes the deformation rate in the machine direction to increase. This phenomenon is due to a decrease in the frost-line height with increasing the blow-up ratio. Furthermore, the absolute value of the second invariant (of deformation-rate tensor) increases with an increase in the blow-up ratio.

2. According to the qualitative comparisons with the experimental observations, the model of Pearson and Petrie showed obvious difficulties in describing the results. These

difficulties include the effects of inflation pressure, extrusion temperature and melt viscosity on the bubble radius.

3. A "quasi-cylindrical" model for the tubular film geometry, using a deformation-thinning viscosity constitutive equation, satisfactorily explains the essential features of the experimental data, including the so-called intuitive and counter-intuitive pressure effects and the cross-over effect noted above (see item 1(b)). Also the effects of extrusion temperature and cooling rate are explainable (see item 1(c)).

4. The "mixed" experimental observations in the literature on the relationship between inflation pressure and blow-up ratio are not really mixed. They have to do with the type of material (that is, the rheological non-linearity) that is used and the range of take-up ratio and blow-up ratio involved.

5. Thin-shell theory, which underlies the model of Pearson and Petrie, contains an extra term compared with the present model — a term having to do with curvature in the axial direction. Inclusion of this term causes a number of difficulties, a major one being the counter-intuitive pressure effect. Thin-shell theory is normally used for solid vessels,

for which the shape is known *a priori*. If the shape of the bubble is assumed to be known *a priori*, there are not major differences between the Pearson-Petrie model and the present model. But if one tries to use the former model in a fluid mechanics manner — to predict the shape of the bubble — the counter-intuitive and other difficulties arise. The reason for this difference is not fully understood.

LIST OF REFERENCES

LIST OF REFERENCES

1. R. R. Knittel, in "Modern Plastics Encyclopedia," R. J. Martino, Ed., Mc Graw-Hill, New York (1992).

2. R. A. Weeks, in "Modern Plastics Encyclopedia," R. J. Martino, Ed., Mc Graw-Hill, New York (1991).

3. J. R. A. Pearson, and C. J. S. Petrie, J. Fluid Mech., 40, 1 (1970).

4. J. R. A. Pearson, and C. J. S. Petrie, J. Fluid Mech., 42, 609 (1970).

5. C. D. Han and J. Y. Park, J. Appl. Polym. Sci., 19, 3277 (1975).

6. T. Kanai and J. L. White, J. Polym. Eng., 5, 135 (1985).

7. B. Cao, P Sweeney and G. A. Campbell, ANTEC, New York, 35 (1989).

8. R. Farber and J. Dealy, Polym. Eng. Sci., 14, 435 (1974).

9. E. Fisher, Kunststoffe, 70,541 (1980).

10. R. K. Gupta, A. B. Metzner and K. F. Wissbrun, Polym. Eng. Sci., 22, 172 (1982).

11. C. D. Han and J. Y. Park, J. Appl. Polym. Sci., 19, 3257 (1975).

12. C. D. Han and R. Shetty, Ind. Eng. Chem., Fundam., 16, 49 (1977).

13. T. A. Huang and G. A. Campbell, ANTEC, Washington, D.C. (1985).

14. T. Kanai and J. L. White, Polym. Eng. Sci., 24, 1185 (1984).

15. G. Menges and W. O. Predohl, Polym. Eng. Sci., 15, 394 (1975).

16. T. Nagasawa, T. Matsumura, S. Hoshino and K. Kobayashi, Appl. Polym. Symp. 20, 275 (1973).

17. H. H. Winter, Pure and Appl. Chem., 55, 943 (1983).

18. D. R. Holmes and R. P. Palmer, J. Polym. Sci., 31, 345 (1958).

19. P. H. Lindenmeyer and S. Lustig. J. Appl. Sci., 9, 227 (1965).

20. W. F. Maddams and J. E. Preedy, J. Appl. Polym. Sci. 22, 2721 (1978).

21. W. F. Maddams and J. E. Preedy, J. Appl. Polym. Sci. 22, 2739 (1978).

22. W. F. Maddams and J. E. Preedy, J. Appl. Polym. Sci. 22, 2751 (1978).

23. K. J. Choi, J. E. Spruiell and J. L. White J. Polym. Sci.: Polym. Phys. Ed. 20, 27 (1982).

24. J. R. Dees and J. E. Spruiell, J. Appl. Polym. Sci., 18, 1053 (1974).

25. T. H. Kwack and C. D. Han, J. Appli. Polym. Sci., 35, 369 (1988).

26. M. H. Wagner, Kunststoffe, 68, 362, (1978).

27. M. H. Wagner, Rheol. Acta, 15, 40 (1976).

28. C. C. Liu, M.S. Thesis, University of Tennessee, Knoxville, 1991.

29. J. R. A. Pearson, and C. J. S. Petrie, Plast. Polym., 38,85 (1970).

30. B. K. Ashok and G. A. Campbell, Intern. Polymer Processing, 7, 240 (1992).

31. T. A. Huang and G. A. Campbell, Advances in Polymer Technology, 5, 181 (1985).

32. L. Mandelkern, Rubber. Chem. Technol., 32 (1959).

33. R. F. Westover, in "Processing of Thermoplastic Material," E. C. Bernhardt Ed., Kreiger, New York (1974).

34. R. Farber, M. Eng. Thesis, Mc Gill University, Montreal (1973).

35. W. Ast, Kunststoffe, 63, 427 (1973).

36. M. H. Wagner, Ph.D. Dissertation, University of Stuttgart (1976).

37. T. A. Huang and G. A. Campbell, J. Plastic Film & Sheeting, 2, 30 (1986).

38. M. Pivovonsky and M. R. Nagel, "Tables of Blackbody Radiation Functions," Macmillan, New York (1961).

39. N. Hajji, Ph.D. Proposal, The University of Tennessee, Knoxville, May (1989).

40. N. Hajji, Ph.D. Dissertation, University of Tennessee, Knoxville, 1992.

41. T. G. Fox and P. J. Flory, J. Am. Chem. Soc., 70, 2384 (1948).

42. T. G. Fox and P. J. Flory, J. Phys. Chem., 21, 581 (1950).

43. P. A. Small, Ad. Polym. Sci., 18, 1 (1975).

44. F. J. Bueche, Chem. Phys., 40, 484 (1964).

45. G. Atalla and D. Romanini, Rheo. Acta, 22, 471 (1983).

46. D. Constantin, Polym. Eng. Sci., 24, 268 (1984).

47. D. Acierno, D. Curto, F. P. La Mantia and A. Valenza, Polym. Eng. Sci., 26, 28 (1986).

48. F. P. La Mantia and D. Acierno, Polym. Eng. Sci., 25, 279 (1985).

49. C. D. Han, Y. J. Kim, H. K. Chuang and T. H. Kwack, J. Appl. Polym. Sci., 28, 3435 (1983).

50. C. D. Han and T. H. Kwack, J. Appl. Polym. Sci., 28, 3399 (1983).

51. T. H. Kwack and C. D. Han, J. Appl. Polym. Sci., 28, 3419 (1983).

52. J. R. A. Pearson, "Mechanical Principal of Polymer Melt Processing", Pergamon Press, London (1966).

53. R. I. Tanner, "Engineering Rheology," Clarendon Press, Oxford (1985).

54. S. Middleman, "Fundamental of Polymer Processing", Mc Graw Hill, New York (1977).

55. D. Acierno, J. N. Dalton, J. M. Rodriguez and J. L. White, J. Appl. Polym. Sci., 15, 2395 (1965).

56. I. Chen, G. E. Haggler, L. E. Abbott, J. N. Dalton, D. C. Bogue, and J. L. White, Trans. Soc. Rheol. 16, 473 (1972).

57. C. D. Han and R. R. Lamonte, Trans. Soc. Rheol., 16, 447 (1972).

58. C. D. Han and L. Segal, J. Appl. Polym. Sci., 14, 2973 (1970).

59. M. Zida, Rheol. Acta, 8, 89 (1969).

60. C. D. Han, "Rheology in Polymer Processing," Academic Press, New York (1976).

61. H. Yamane, Ph.D. Dissertation, University of Tennessee, Knoxville, 1985.

62. R. R. Knittel, in "Modern Plastics Encyclopedia," R. J. Martino, Ed., Mc Graw-Hill, New York (1990).

63. T. Kanai, Intern. Polymer Processing, 1, 137 (1987).

64. C. D. Han and J. Y. Park, J. Appl. Polym. Sci., 19, 3291 (1975).

65. W. Minoshima, Ph.D. Dissertation, University of Tennessee, Knoxville, 1983.

66. W. Minoshima and J. L. White, J. Non-Newtonian Fluid Mech., 19, 275 (1986).

67. P. A. Sweeney, G. A. Campbell, and F. A. Feeney, Intern. Polymer Processing, 7, 229 (1992).

68. Y. L. Yeow, J. Fluid Mech., 75, 577 (1976).

69. J. J. Cain and M. M. Denn, Polym. Eng. Sci., 28, 1527 (1988).

70. K. J. Choi, J. L. white and J. E. Spruiell, J. Appl. Polym. Sci., 25, 2777 (1980).

71. T. Alfrey, S. P. E. Trans., 5, 68 (1965).

72. C. J. S. Petrie, Rheol. Acta, 12, 92 (1973).

73. C. J. S. Petrie, AIChE J., 21, 275 (1975).

74. W. Ast, Kunststoffe, 64, 146 (1974).

75. V. V. Nonozhilov, "The Theory of Thin Shells", Noordhoff, Groningen (1959).

76. S. Timoshenko and S. Woinowsky-Krieger, "Theory of Plates and Shells," Mc Graw-Hill, New York (1959).

77. C. J. S. Petrie, Plast. Polym., 42, 259 (1974).

78. G. Menges and W. Predohl, Plastverarbeiter Bd., 23, 338 (1972).

79. E. R. G. Eckert and R. M. Drake, "Heat and Mass Transfer," 2nd ed., Mc Graw-Hill, New York (1959).

80. J. R. Holman, "Heat Transfer," 5th ed., Mc Graw-Hill, New York (1981).

81. B. Cao and G. A. Campbell, AIChE. J., 36,420 (1990).

82. X. L. Luo and R. I. Tanner, Polym. Eng. Sci., 25, 620 (1985).

83. C. J. S. Petrie "Film Blowing, Blow Moulding and Thermoforming," in "Computational Analysis of Polymer Processing," J. R. A. Pearson and S. M. Richardson Eds., Applied Science Publishers, New York: Elsevier Science Publishing Co. (1983).

84. R. K. Gupta, Ph.D. Thesis, University of Delaware (1981).

85. G. A. Campbell and B. Cao, "Blown Film Simulation, A Severe Test for Rheological Models," in "Polymer Rheology and Processing," A. A. Collyer and L. A. Utracki, Eds., Elsevier Science Publishing Co., New York (1990).

86. K. S. Yoon and C. W. Park, Poly. Eng. and Sci., 32, 1771 (1992).

87. S. M. Alaie and T. C. Papanastasiou, Intern. Polymer Processing, 8, 51 (1993).

88. Operation for PROBEYE Thermal Video System Series 3000, Hughes Aircraft Company.

89. J. Zhou, M.S. Thesis, University of Tennessee, Knoxville, 1988.

90. R. M. Patel, M.S. Thesis, University of Tennessee, Knoxville, 1988.

91. R. M. Patel, Ph.D. Dissertation, University of Tennessee, Knoxville, 1991.

92. F. T. Trouton, Proc. R. Soc., A77, 426 (1906).

93. H. J. Kang and J. L. White, Intern. Polymer Processing, 7, 38 (1992).

94. L. E. Dowd, Soc. Plast. Eng. J., 28, 22 (1972).

95. D. Al-Sammerrai and N. K. Al-Nidawy, "Polyethylene: Synthesis, Properties, and Uses" in "Handbook of Polymer Science and Technology," N. P. Cheremisinoff, Eds., Marcel Dekker, Inc., New York, Vol. 2 (1989)

96. L. H. Sperling, "Introduction to Physical Polymer Science," John Wiley & Sons, New York, pp. 207 (1986).

97. J. C. Butcher, "Numerical Analysis of Ordinary Differential Equations," John Wiley & Sons, New York (1987).

98. K. H. Illers and H. Hendus, Makromol. Chem., 113, 1 (1968).

99. L. S. Hood, M.S. Thesis, University of Tennessee, Knoxville, 1990.

100. B. Wunderlich and M. Dole, J. Polym. Sci., 24, 201 (1957).

101. R. G. Griskey and G. N. Foster III, S. P. E. Ann. Tech. Conf., 26, 546 (1968).

102. L. Mandelkern, Rubber. Chem. Technol., 32 (1959).

103. R. F. Westover, in "Processing of Thermoplastic Material," E. C. Bernhardt Ed., Kreiger, New York (1974).

104. G. T. Davis, R. K. Eby and J. P. Colson, J. Appl. Phys., 41, 4316 (1970).

105. F. P. Incropera and D. P. DeWitt, "Fundamentals of Heat and Mass Transfer," 3rd ed., John Wiley & Sons, New York (1990).

106. D. C. Bogue, Ind. Eng. Chem. Fund., 5, 253 (1966).

107. D. C. Bogue and J. L. White, "Engineering Analysis of Non-Newtonian Fluid", NATO Agardograph, #144 (1970).

108. "C-FLOW, User's Guide," Advanced CAE Technology, Inc., New York (1989).

109. J. L. Lambach, M.S. Thesis, University of Tennessee, Knoxville, 1988.

110. R. M. Patel, J. Bheda and J. E. Spruiell, J. Appl. Polym. Sci., 42, 1671 (1991).

111. J. Shimizu, N. Okui and T. Kakutani, in "High Speed Fiber Spinning," A. Ziabicki and H. Kawai Eds., John Wiley and Sons, New York (1985).

112. W. P. Cox and E. H. Merz, J. Polym. Sci., 28, 619 (1958).

113. Y. P. Khanna, Polm. Eng. Sci., 31, 440 (1991).

114. S. Venkatraman, M. Okano, and A. Nixon, Polym. Eng. Sci. 30, 308 (1990).

115. H. C. Booij, P. Leblans, J. Palmen, and G. Tiemersma-Thoone, J. Polym. Sci.: Polym. Phy. Ed., 21, 1703 (1983).

116. D. S. Kalika and M. M. Denn, J. Rheol., 31, 815 (1987).

117. R. M. Schulken, R. H. Cox, and L. A. Minnick, J. Appli. Polym. Sci., 25, 1341 (1980).

118. L. A. Utracki and R. Gendron, Soc. Rheol., 28, 601 (1984).

119. J. M. Dealy and K. F. Wissbrun, "Melt Rheology and Its Role in Plastics Processing," Van Nostrand Reinhold, New York (1990).

120. K. Katayama and M. G. Yoon, in "High Speed Fiber Spinning," A. Ziabicki and H. Kawai Eds., John Wiley and Sons, New York (1985).

121. G. Harrison, Visiting Professor, University of Tennessee, Knoxville; Professor, Department of Mathematics, College of Charleston; personal communication (1992).

APPENDICES

APPENDIX A

For LLDPE and LDPE, a combination of the on-line measured profiles of radius, velocity, temperature and thickness, and the on-line observed frost line height for each of case(A) and case(B) will be shown in the following figures, in which the vertical dashed lines represent the position of the observed frost line. Similar data for case(C) for both materials was shown in the body of this dissertation in Chapter 4.

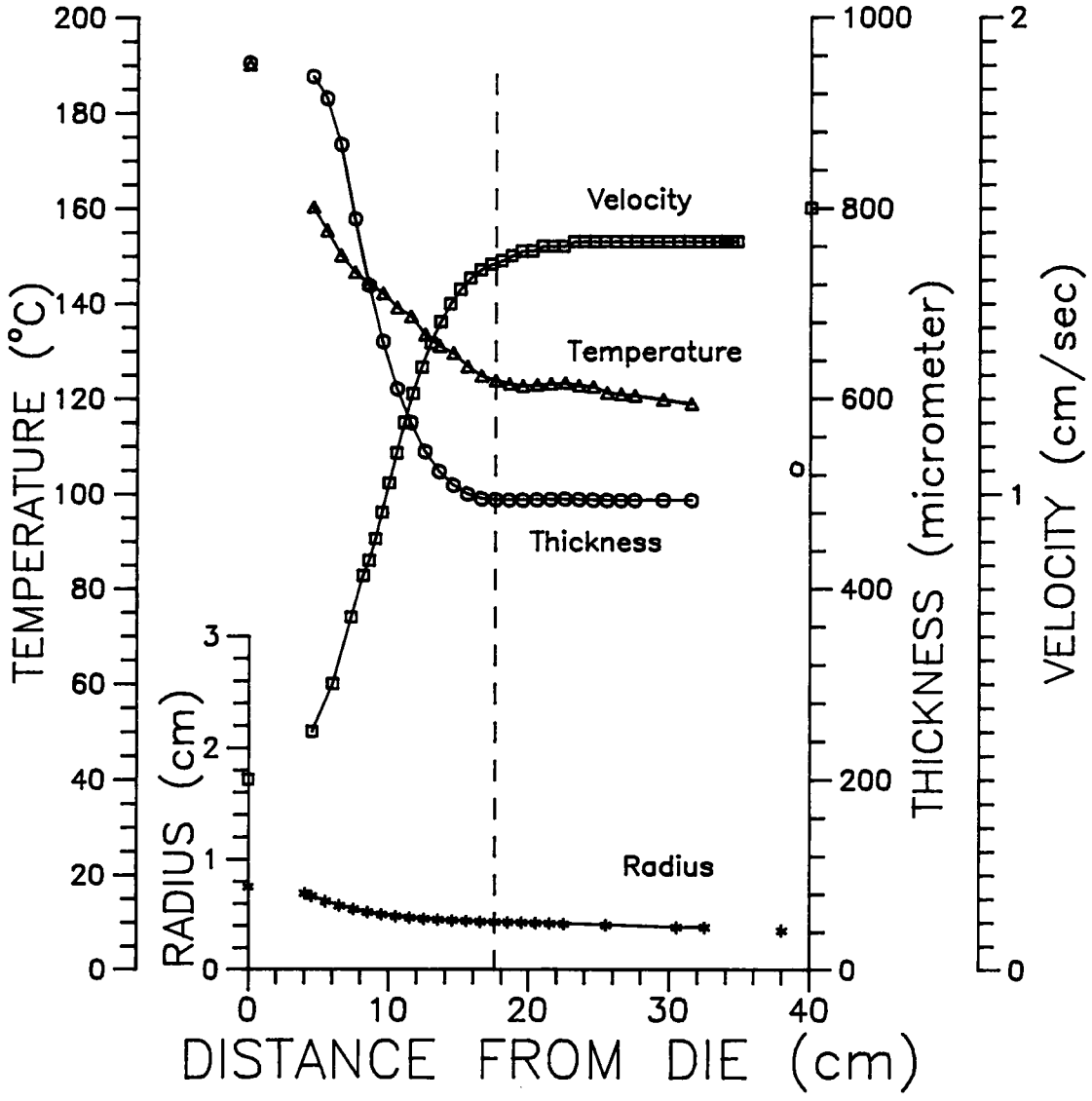

Figure A-1 Combination of the on-line profiles of radius, velocity, temperature and thickness, and the on-line observed frost line height for case(A) using LLDPE resin.

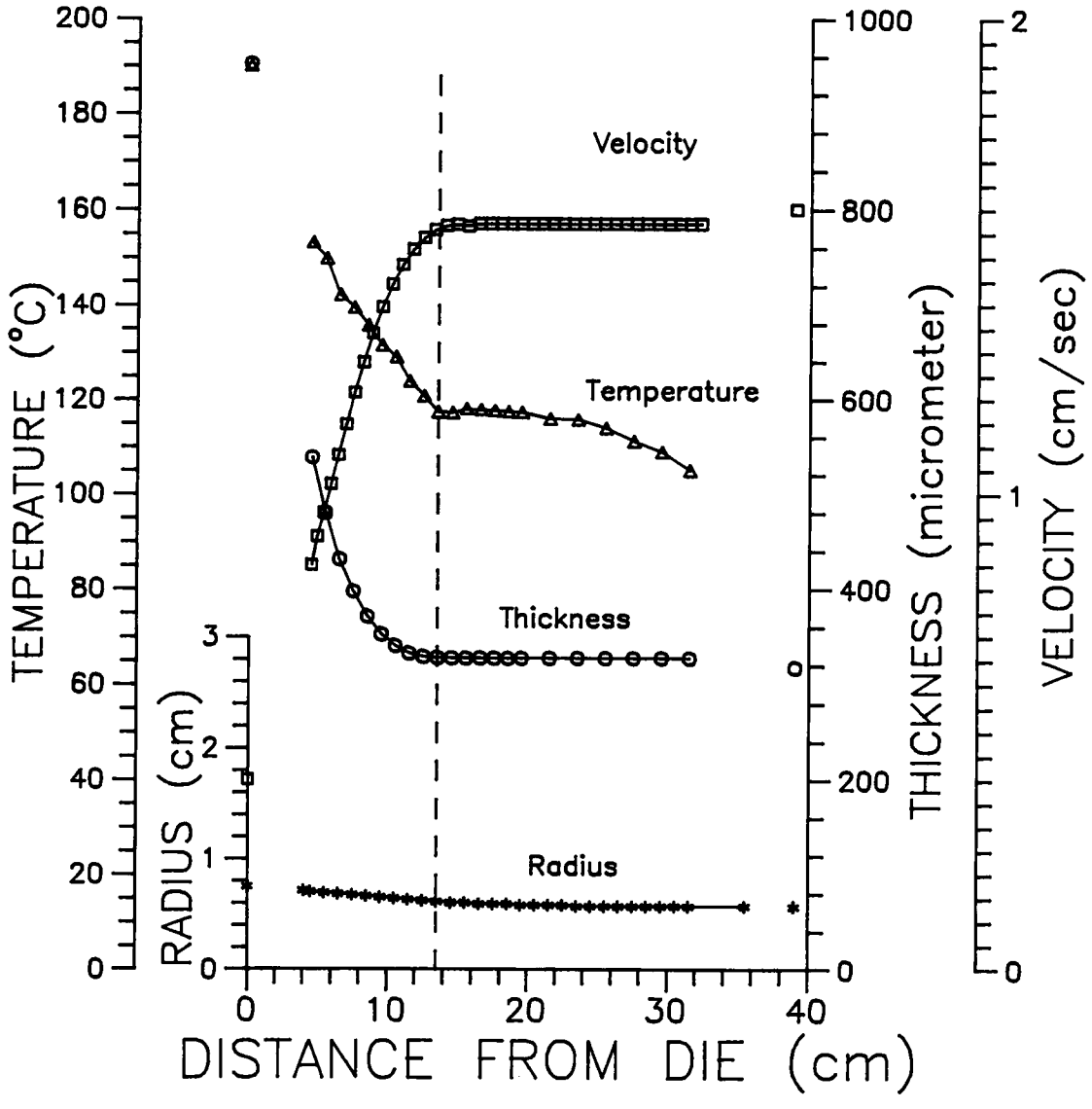

Figure A-2 Combination of the on-line profiles of radius, velocity, temperature and thickness, and the on-line observed frost line height for case(B) using LLDPE resin.

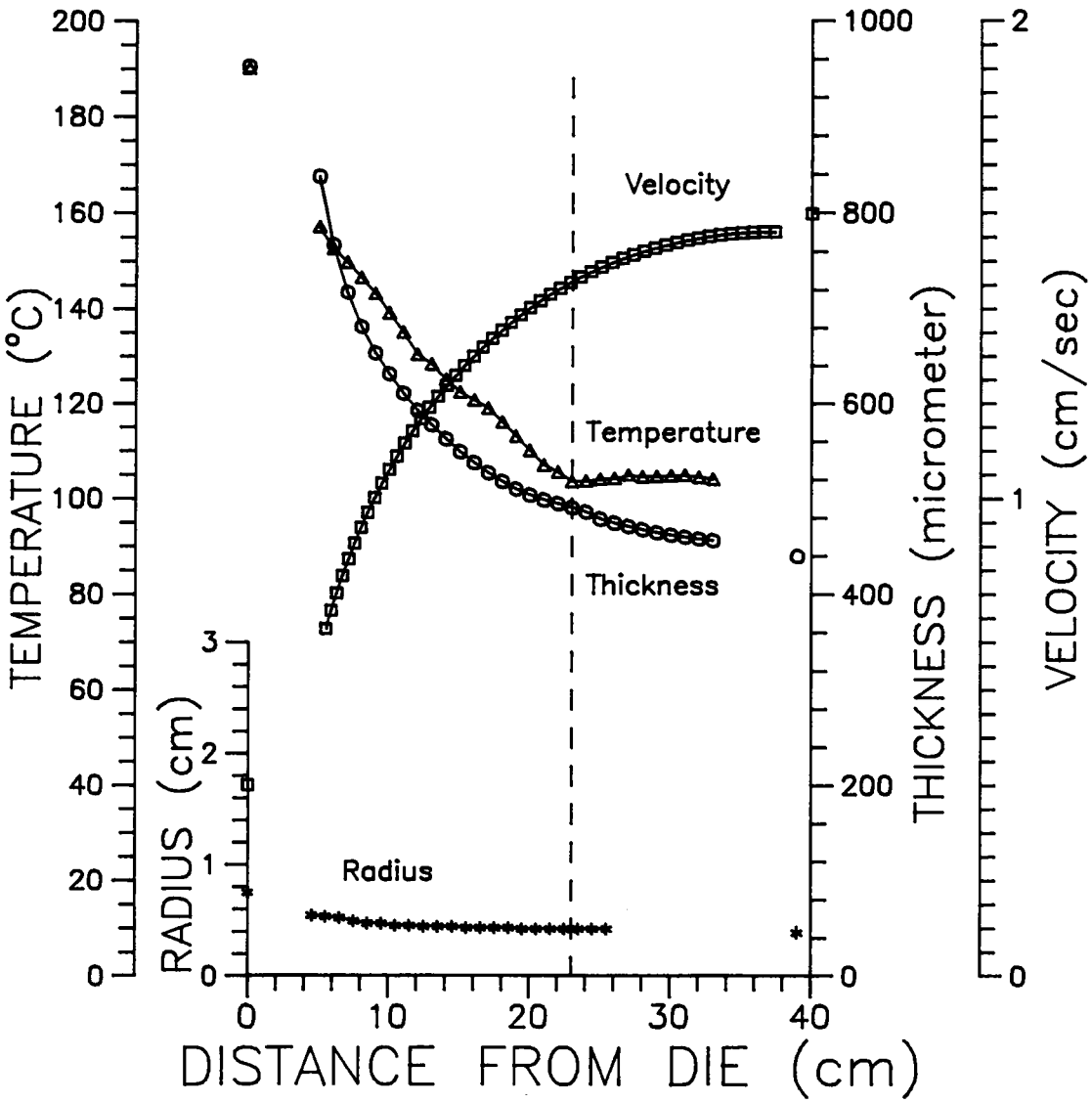

Figure A-3 Combination of the on-line profiles of radius, velocity, temperature and thickness, and the on-line observed frost line height for case(A) using LDPE resin.

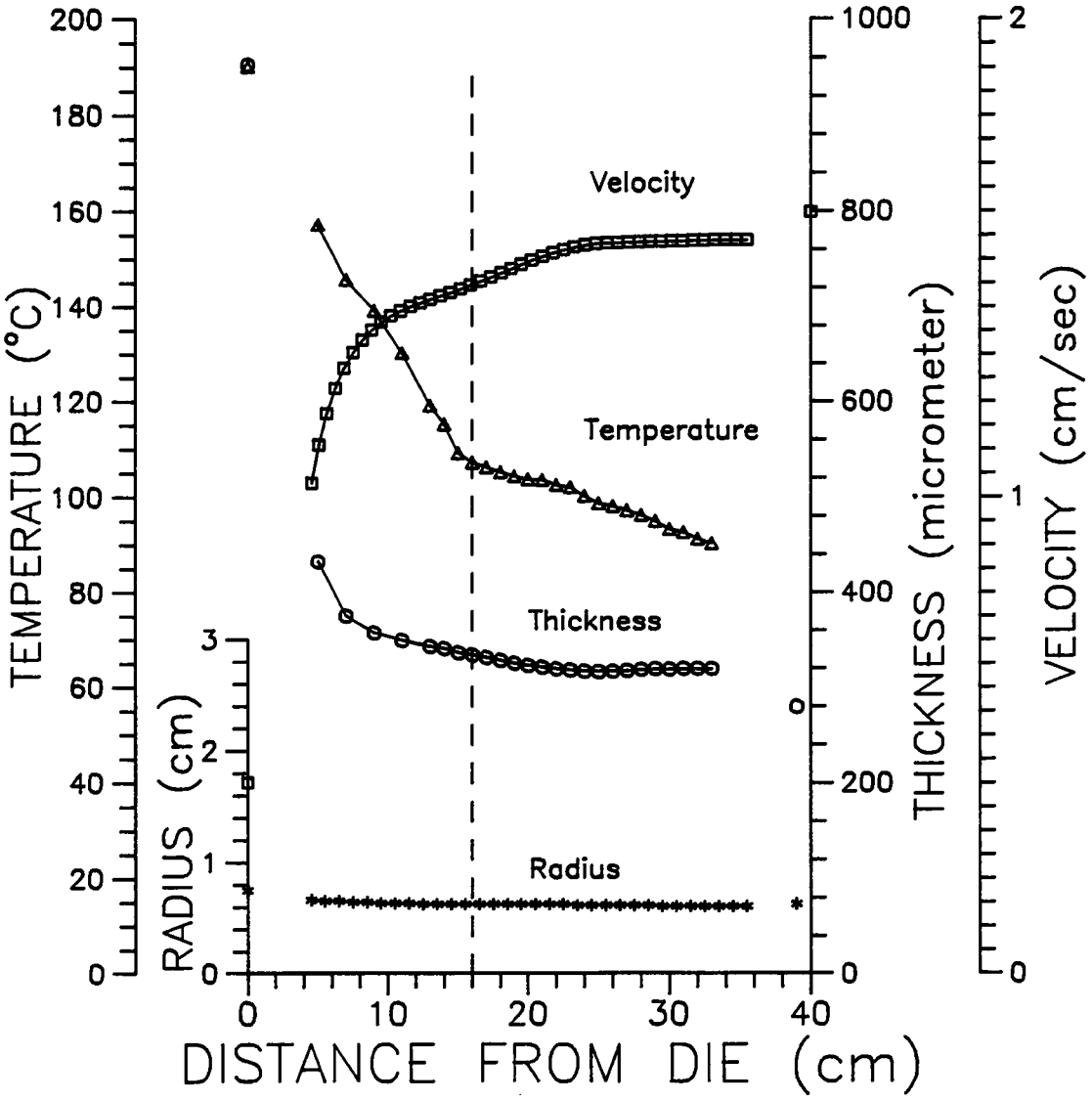

Figure A-4 Combination of the on-line profiles of radius, velocity, temperature and thickness, and the on-line observed frost line height for case(B) using LDPE resin.

APPENDIX B

The governing equations of the mathematical models as discussed in Section 5.1 in Chapter 5 can be integrated simultaneously by using the fourth-order Runge-Kutta numerical method. The algorithm used in the numerical scheme is illustrated in Figure B-1. The detailed BASIC computer programs are available upon request to the author or to the author's major professor.

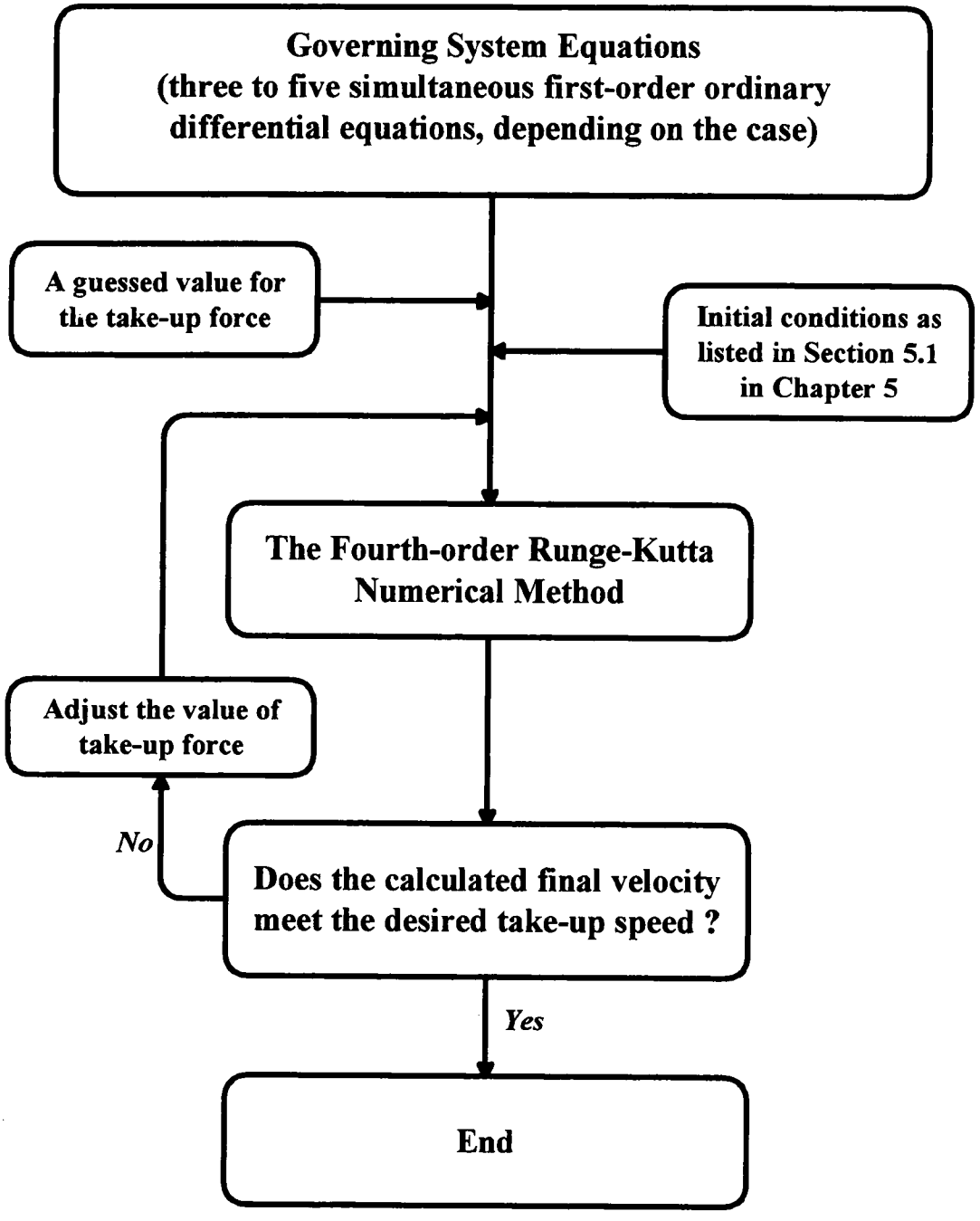

Figure B-1 Schematic diagram of the numerical scheme used to solve the governing equations of the mathematical models.

APPENDIX C

Some typical experimentally observed relationship between the inflation pressure and the blow-up ratio in the literature [25,26] are shown in this section. The essential features of these published experimental results, as shown in Figures C-1 and C-2, can be qualitatively explained by the present model, which includes the so-called "intuitive" and "counter-intuitive" pressure effects, and the order of ΔP curves of various take-up ratios depending on the magnitude of blow-up ratio, and the cross-over phenomenon between ΔP curves. The detailed discussion concerning these features was given in Section 5.4.2 in Chapter 5.

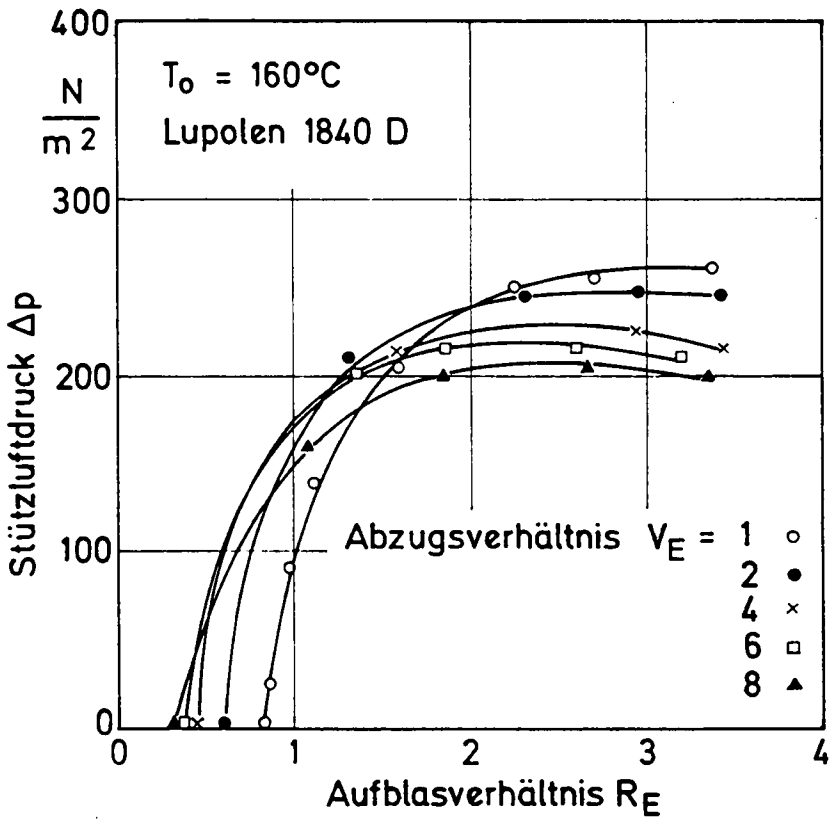

Figure C-1 Inflation pressure ΔP as a function of blow-up ratio (R_E) and take-up ratio (V_E) for low-density polyethylene [26].

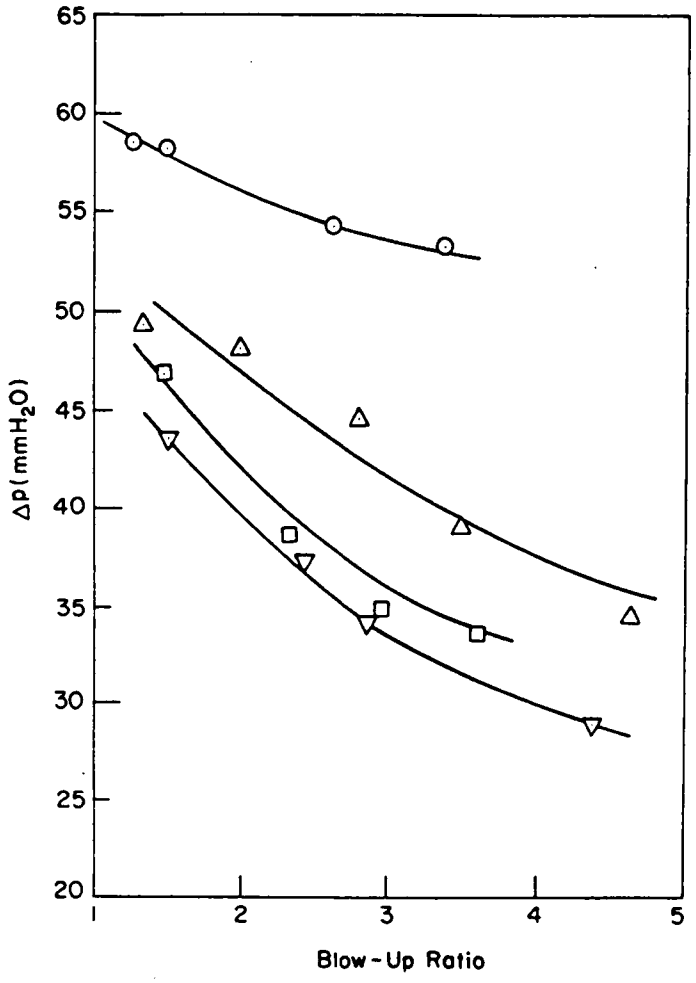

Figure C-2 Effect of blow-up ratio on the bubble pressure of the high-pressure low-density polyethylene at various take-up ratios: (○) 3.98; (Δ) 9.86; (□) 15.61; (∇) 21.44 [25].

VITA

Cheng-chien Liu (劉 誠 健) was born in Taiwan, Republic of China, on October 19, 1963. From September 1981 to June 1985, Mr. Liu studied in the Chemical Engineering Department at the Tatung Institute of Technology in Taipei, Taiwan and received a Bachelor degree of Science. During his undergraduate studies, he won several scholarships, including the Chinese Technical Service Association Scholarship, the Future College Teacher Scholarship of the Tatung Institute of Technology and the Academic Achievement Scholarship of the Tatung Company. Fulfilling the compulsory military service requirement, he served as a Second Lieutenant from 1985 to 1987, and then he worked as a teaching associate in the Department of Chemical Engineering at the Tatung Institute of Technology for one year.

He received Master of Science in Polymer Engineering in August 1991. He continued for a doctorate degree in the same program. The degree of Doctor of Philosophy was awarded in August 1994.

He is a member of the Society of Plastic Engineers.